Investigation of Aneurysm Formation: a macro-structural approach

UNIVERSITY of PORTSMOUTH

Serena de Gelidi

School of Engineering

University of Portsmouth

This dissertation is submitted for the degree of

Doctor of Philosophy

March 2016

To my parents, my strong roots

To José Antonio, the travel companion of a lifetime

Acknowledgements

A couple of years ago I would have not believed possible for me to go through a doctoral degree. It has been a long journey with so many people. Some of them travelled with me every single day, others supported me for short periods. However, all of them contributed, directly or indirectly, to this dissertation. This page represents my spontaneous flow of thoughts, purposely free from academic conventionalism.

I want to thank my parents, for their unconditional support, their love and for the strength I inherited from them. My immense gratitude goes to José Antonio for his encouragement in the darkest days and his smile in the happiest days. I am sure the completion of this degree relies on him, who daily holds my hand. I also thank my sisters and the rest of my family for their kindness. I wish to acknowledge the closest friends along this path: Vincenzo as we created a solid bond by starting together this adventure, Valentina for being the gift I was waiting for, Marco F. the playfellow, Georgios for sharing hundreds of coffee breaks, Marco P. an amazing new entry, Thirumavalavan and Shafini the best office mates, Diego and Francesco for their long-time friendship.

I would like to express my great appreciation to Dr. Andrea Bucchi, who provided me the opportunity to start the doctoral degree and has guided me from the very first day. I am grateful to Prof. Jie Tong for her suggestions and her sympathy. I would also like to acknowledge Dr. Gianluca Tozzi for his critical point of view on the experimental procedures. I wish to thank Mr Colin Lupton for his numerous suggestions and technical assistance. I am obliged to Dr. Ivan Carubelli, Dr. Gaetano Burriesci and Dr. Benyamin Rahmani, without their availability I could have not performed part of the experimental campaign. Finally, a special recognition goes to David and Robert, who showed me the effectiveness of diplomacy.

Abstract

Among the cardiovascular diseases, the leading cause of death in Europe, is related to the aortic aneurysm. Despite several studies focus on its rupture risk, limited attention is reserved to aneurysm formation. The main purpose of this research study is to assess, from the macro-structural point of view, whether an aneurysm may be instigated in healthy model of aorta inflated by a supra-physiological pressure. In addition, a physiologic systolic pressure is applied to estimate the overall arterial response. The mechanical characterization of the healthy descending aorta is accomplished by means of uniaxial and equi-biaxial tensile tests performed on porcine tissue. Since no standard experimental protocol is available for soft tissues, a complete methodology based on up-to-date techniques is detailed. Several computational analyses have been performed to highlight the impact on numerical predictions of the pre-conditioning frequency, the sample shape and the sample thickness measurement. Furthermore, the fitting of experimental responses appears definitely crucial for numerical predictions. Several strain-energy functions are compared as part of the isotropic modelling based on uniaxial mechanical responses. In addition, a Fung orthotropic FE model is generated based on equi-biaxial mechanical behaviour. A cylindrical and a more physiologic FE geometry are compared, emphasizing how a different design leads to consistent differences in wall stress and radial stretch predictions. This study suggests that aneurysm formation is unlikely to be caused by supra-physiological pressure in a healthy model of descending aorta. Isotropic models predict the bulge appearance in the abdominal district only for

selected mechanical responses. However, a localized geometric imperfection could lead to aneurysm formation in the thoracic district.

Declaration

Whilst registered as a candidate for the above degree, I have not been registered for any other research award. The results and conclusions embodied in this thesis are the work of the named candidate and have not been submitted for any other academic award.

Serena de Gelidi

March 2016

Contents

List of Figures

List of Tables

Chapter 1

Introduction

1.1 Background

1.1.1 The cardiovascular system

The cardiovascular system is composed of the heart, blood vessels and blood. The heart is a muscular pump, which contraction ensures the blood flows from the right atrium to the right ventricle and then is pumped to the lungs to receive oxygen. Successively, the blood flows from the lungs to the left atrium, then to the left ventricle. A systolic pressure ($\sim 120 mmHg$) drives the blood into the systemic circulation, supplying all organs and body regions (Figure 1.1). Such pressure progressively decreases along the arterial tree, reaching a minimum in the right atrium (0-3 mmHg). Typically, the whole amount of blood ($\sim 5l$) is pumped through the heart approximately in one minute, being the flow rate directly proportional to the pressure and inversely proportional to the vessel resistance (Guyton & Hall, 2000). In addition, the larger the vessel diameter the lower is the resistance.

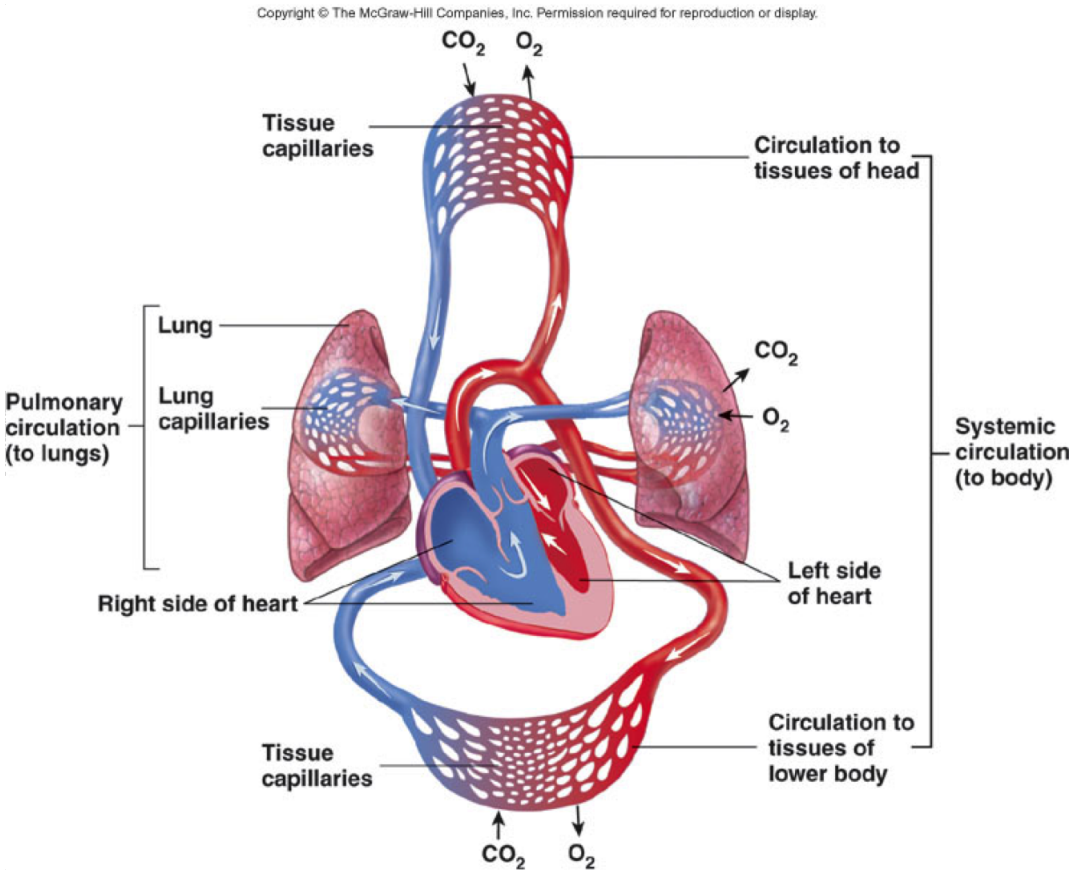

Figure 1.1 Schematic model of the cardiovascular system, showing the systemic and pulmonary circulations.

The cardiovascular system executes essential functions for the body. Firstly, it distributes O_2, nutrients, water and hormones throughout the body. Moreover, CO_2 and metabolic waste products are transported from the tissues to the lungs and excretory organs. Finally, such system contributes to body thermoregulation and to the infrastructure of the immune system (Aaronson *et al.*, 2012).

1.1.2 Cardiovascular diseases

Any abnormal function of the cardiovascular system is defined as cardiovascular disease. Cardiovascular disease is the leading cause of death in Europe, and despite recent decreases in mortality rates in many countries, it is still responsible for over 4 million deaths per year, close to half of all deaths in Europe. In 2014, 51% of deaths were

recorded among women and 42% among men (Nichols *et al.*, 2014). Cardiovascular diseases kill over 160,000 individuals every year in the United Kingdom and still represent the greatest cause of mortality in women (British Heart Foundation, 2014). Furthermore, over 40,000 premature deaths of individuals under 75 years of age are caused by such diseases with more than two thirds of these occurring in men (British Heart Foundation, 2014). Aortic aneurysm is ranked, depending on the race, as the 8th or 10th most frequent cause of death in US (Heron, 2015).

Aiming to reduce the mortality, the treatment of such pathologies has a considerable impact on economy. The first line of defence against the cardiovascular diseases is screening of risk groups. In addition, a sizeable part of the direct costs can be attributed to the drugs needed by the patients. However, these strategies sometimes are not effective, or the disease cannot be handled any more with medication. Thus, minimum-invasive procedures need to be performed (Sommer, 2010). As an example, the endovascular aneurysm repair (EVAR) procedure consists of two small incisions in the groin to expose the femoral arteries. The sheathed Dacron or PTFE (polytetrafluoroethylene) graft and stents are fed through these arteries by catheters until the graft is positioned correctly along the aneurysmal segment of aorta. Removal of the sheath, with or without balloon expansion, allows fixing mechanisms to attach firmly the graft to the arterial wall, allowing blood to pass through it and remove pressure from the diseased aortic wall (Greenhalgh *et al.*, 2004). In spite of these advances, surgery may be needed for several reasons: the catheter cannot be placed reliably, the patient has multivessel disease, the lesion is at a difficult location or a previously implanted stent has failed (Sommer, 2010). Therefore, annual costs for screening, drugs, minimum-invasive procedures and surgeries exceeded £6.8 billion in 2012/13 (British Heart Foundation, 2014).

As the procedures outlined above affect the vessels mechanically, it is essential to understand the mechanical behaviour of the vessel wall in order to improve the outcome of such treatments.

1.1.3 Anatomy of arteries

Arteries are deputed to transport blood from the heart to the capillary networks throughout the body. The microstructure of the arteries varies with: the location along the vascular tree (Tanaka & Fung, 1974), the age (Erbel & Eggebrecht, 2006), the species (Mello *et al.*, 2004) and the localized vascular adaptations (Rowley *et al.*, 2011). However, all arterial walls are composed of three concentric layers: the *intima*, the *media* and the *adventitia*.

The *intima* consists of a thin layer of endothelial cells, lining the innermost of the arterial wall. Its extreme smoothness and normal chemical composition prevent the adhesion of platelets. Endothelial cells are usually flat and elongated in the direction of blood flow; exceptions occur near bifurcations, wherein the blood flow is complex and the cells are often polygonal in shape (Davies & Tripathi, 1993; Galbraith *et al.*, 1998). Furthermore, the endothelium of blood vessels produces chemicals that affect blood pressure such as nitric oxide (NO), which is a vasodilator, and the peptide endothelin, that stimulates vessel contraction (Scanlon & Sanders, 2011). A significant thickening and hardening of the blood vessel is generally observed with aging, leading to a pathological *intima* affected by arteriosclerosis (Holzapfel *et al.*, 2000).

The *media* is the middle layer of the artery, separated from the *intima* and *adventitia* by the internal and external elastic lamina respectively. The internal lamina is essentially a fenestrated plane of elastin that allows the transport of H_2O, nutrients, and electrolytes across the wall. The *media* contains smooth muscle cells that are embedded in an extracellular plexus of elastin and collagen (primarily types I, III, and V) as well as an aqueous ground substance matrix containing proteoglycans. Strength and resilience of this composite layer are a result of the smooth muscle cells, elastin and collagen fibrils arranged in spirals (Holzapfel *et al.*, 2000). The smooth muscle is affected by the chemicals produced by the endothelium. Hence, the relaxation of smooth muscle generates the dilation of the vessel and a lower pressure. Conversely, the contraction of

the muscle layer increases the blood pressure (Scanlon & Sanders, 2011).

The *adventitia*, the outermost layer, consists primarily of dense network of type I collagen fibres elastin, nerves, fibroblasts and fibrocytes. Helical structures of wavy collagen fibrils stabilize and reinforce the arterial wall, surrounded by loose connective tissue (Holzapfel *et al.*, 2000). Similarly to the epicardium of the heart, the collagenous *adventitia* serves primarily as a protective cover of the artery (Humphrey, 2002). Furthermore, the *adventitia* provides the nutrition with the arterial and venous *vasa vasorum* (Erbel & Eggebrecht, 2006). Holzapfel et al. (Holzapfel *et al.*, 2000) provided an effective model of a healthy elastic artery (Figure 1.2) in order to represent the fibres arrangement in each layer.

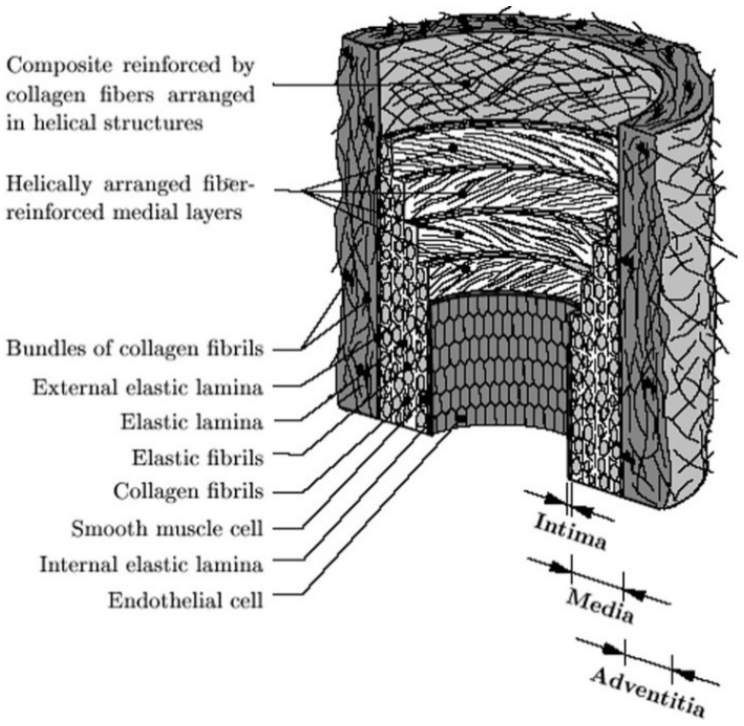

Figure 1.2 Schematic model of the major components of a healthy elastic artery composed of three layers: *intima*, *media* and *adventitia* (Holzapfel *et al.*, 2000).

Mechanical properties of the arterial wall depend on the distributions, orientations, and interconnections of the intramural constituents. Histology reveals that smooth muscle in the *media* tends to be oriented circumferentially, whereas type I collagen in the

adventitia tends to be oriented axially. Therefore, arteries are anisotropic (Humphrey, 2002).

The largest systemic artery is the aorta, which consists of the ascending portion, the so-called arch, and the descending thoracic and abdominal segments (Figure 1.3). The aortic diameter decreases with the distance from the aortic valve and increases with age (Nienaber & Fattori, 1999). Although aortic dimension should be normalized to body size (Nienaber & Fattori, 1999), the diameter of the thoracic segment is about 3 cm, tapering to about 2 cm in the abdomen (O' Gara, 2003).

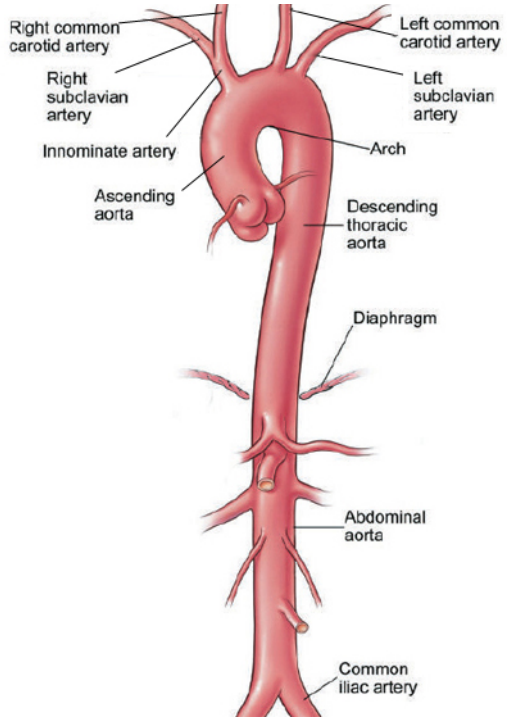

Figure 1.3 The whole aorta consists of the ascending region, the arch and the descending region, which is referred as thoracic in the upper section and as abdominal below the diaphragm (Website 2).

Aorta experiences a complex mechanical loading due to the pulsatile blood flow ejected by the left ventriculum: axial tension, radial stretch and, limited for the ascending segment, torsion (Humphrey, 2002). Thus, an appropriate mechanical response is required to carry and distribute oxygenated blood to all arteries. Since 1800 the aortic mechanics has fascinated researchers (Roy, 1881), aiming to understand the mechanical behaviour in healthy and pathological conditions.

A micro-structural degeneration of aortic wall layers impairs its mechanical response and leads to severe pathologies. Among the major cardiovascular diseases are accounted: the aortic dissection (generating the presence of extraluminal blood within the layers) and aneurysms (Nienaber & Fattori, 1999).

1.2 Aneurysm: definition and incidence

An aneurysm (from Greek: ἀνεύρυσμα, meaning widening) is a permanent and irreversible localised enlargement of an artery. The problem associated to the bulge appearance consists in a weakening of the aortic wall that leads to a progressive dilatation, which, if left untreated, may result in rupture and death (Nordon *et al.*, 2009). Furthermore, aneurysm is generally asymptomatic (Sakalihasan *et al.*, 2005) and often detected as an incidental finding on ultrasonography, computed tomography (CT) or magnetic resonance imaging (MRI) performed for other purposes (Aggarwal *et al.*, 2011). An example of aneurysm imaging obtained by CT is reported in Figure 1.4.

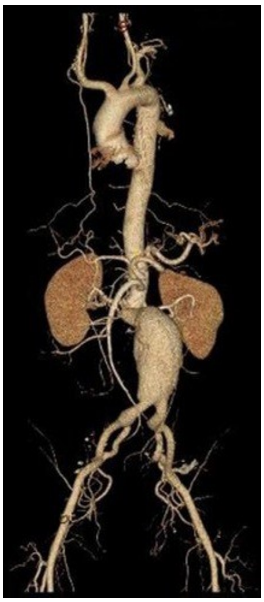

Figure 1.4 Volume rendered CT angiogram of an abdominal aortic aneurysm (Website 1).

The incidence of abdominal aortic aneurysms (AAA) is approximately 7% of over 65-year population. Furthermore, the highest prevalence of AAA (5.9%) was found in

white male smokers between 50 and 79 years (Voitle *et al.*, 2015).

The main diameter of the aneurysm has been well-established in the literature to correlate with its rupture risk. However, recently it has been suggested that the rate of expansion is most useful in monitoring small AAAs. Despite similar initial diameters, AAAs with higher expansion rates may be more likely to rupture (Khan *et al.*, 2015). Currently, the diagnosis of AAA carried out by NHS (National Health Service, 2014) depends on the measurement of its antero-posterior diameter of the aorta determined by means of ultrasound (Scott, 2002), as showed in Figure 1.5.

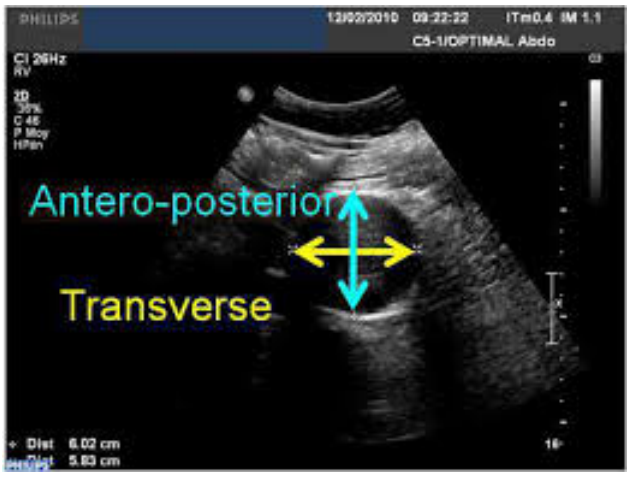

Figure 1.5 Ultrasound cross-sectional view of an abdominal aneurysm to measure its largest diameter (Rouet *et al.*, 2010).

Whether the diameter measures between 3 *cm* and 4.4 *cm*, an annual scan is performed to check the rate of expansion. A size comprised between 4.5 *cm* and 5.4 *cm* requires scans to be repeated every three months to record further enlargement. Lastly, above a dimension of 5.5 *cm* surgeons usually recommend an endovascular or open surgical treatment.

Although US recommendations are similar to UK (National Health Service, 2014), symptomatic aneurysms or fast enlarging ones may be recommended to repair despite their diameters (Khan *et al.*, 2015).

As a support of the presented procedure, Scott (Scott, 2002; Scott *et al.*, 1998) showed that substantial reductions in aneurysm-related mortality could be achieved by the

implementation of a population-screening programme. However, the outcome of screening may be controversial as people with large aneurysms do not necessarily die from them, but the surgical repair may result in postoperative mortality (Brady *et al.*, 2000). Since the surgery is aimed at increasing life expectancy, there is therefore a duty upon clinicians to identify any other life-limiting pathology and to treat this where possible. Moreover, perioperative mortality is directly related to patients preoperative physiological status (Hallett Jr., 2000). Thus, surgeon decision appears not easy to take. The effect of the hospital admission for ruptured AAA has been recently estimated in UK: the overall mortality rate is counted to be 67.5%. However, 41.6% of the patients did not undergo surgery (Ozdemir *et al.*, 2015). In addition, a recent study highlighted a lower in-hospital mortality in the USA compared to England, in spite of similar post operative mortality rates (Karthikesalingam *et al.*, 2014).

In England and Wales, ruptured AAAs count 6000 deaths per year, making this the 10th leading cause of death in men over 55 years of age (Anjum *et al.*, 2012). Despite mortality from AAA has declined since the late 1990s, from 40.4 per 100 000 population in 1997 to 25.7 per 100000 population in 2009 (Anjum & Powell, 2012), elective hospital admissions for aneurysm repair have actually increased in patients aged over 75 years (Rudarakanchana & Jenkins, 2014).

1.2.1 Hypotheses about the formation

Despite smoking has been found to be a major risk factor (Anjum & Powell, 2012) and the use of tobacco has been reduced world-wide, the incidence of AAA is increasing. This has led to uncertainty as to the significance of risk factors generally associated to aneurysm pathogenesis (Nordon *et al.*, 2009). A number of other aspects, such as age, sex and ethnicity may predispose to aneurysm formation. In addition, a family history of atherosclerosis or hypertension requires a significant attention by clinicians (Aggarwal *et al.*, 2011). Although there is evidence for a genetic predisposition to

AAA formation demonstrated by both familiar and segregation observational studies, no single gene has yet emerged as the key to understanding this relationship. Furthermore, it is considered unlikely that a single gene polymorphism will hold the key to aneurysm formation (Sandford *et al.*, 2007).

Nowadays, advances in imaging diagnostic tools and endovascular therapies have increased the detection and the repair of unruptured asymptomatic aneurysms respectively (Seibert *et al.*, 2011). However, the pathogenesis remains unclear as findings from different biological studies are contrasting. It is believed that AAA results from progressive degeneration of the aortic wall due to degradation of the extracellular matrix (Rein *et al.*, 2011). Arterial elastin becomes fragmented and degraded during aging. Hence, loss of elastin and smooth muscle stimulates a turnover of collagen, commonly observed during the enlargement of an AAA (Humphrey & Holzapfel, 2012). The remodelling stage of the aortic wall is mainly regulated by matrix metalloproteinase, serine and cathepsin proteases. Proteolytic degradation and remodelling of elastin and collagen are associated with weakening and dilatation of the aneurysm, making the aneurysm more prone to rupture (Hellenthal *et al.*, 2012). The essential problem in assigning a clear causality lies in the availability of aortic tissue for histologic analysis (Nordon *et al.*, 2009). Since the tissue removed after surgery represents the end-stage disease, it appears difficult to capture experimentally the initiating factor for aneurysms. Furthermore, the experimental testing of soft tissue cannot rely on any standard protocol. Therefore, published data are hardly comparable due to considerable differences in sample preparation and mechanical testing. Despite most recent studies attempt to characterise healthy thoracic tissue by means of an up-to-date procedure (Peña *et al.*, 2015), no detailed study has corroborated every aspect of such methodology.

Analytical approaches (Ohm law, Poiseuille law, ...) generally give great insight into the physical interpretation of basic physiology (Guyton & Hall, 2000). However,

analytical solutions are generally unfeasible for more complicated conditions, such as cardiovascular diseases. Therefore, computational simulations appear advantageous to address aneurysm formation, growth, modelling and rupture.

Computational studies have established that the magnitude of the wall shear stress (WSS) of well-developed aneurysms is significantly lower than that of the healthy artery (Shojima, 2004). Since the WSS modulates gene expressions and the cellular functions of the vessel wall, excessively low values may induce the structural fragility of the aneurysmal wall (Shojima, 2004). As a result, a burst may be predicted. On the other hand, despite findings about the role of WSS in aneurysm development appear inconsistent, the initiation of intracranial aneurysms in artificial arterial bifurcation has been associated to high WSS (Meng *et al.*, 2014). It has been observed that as the aorta remodels itself during aneurysm formation, the axial stress becomes very significant. In addition, associated shape changes depend on many factors, such as local areas of inflammatory-based elastin degradation, position of other organs to block growth in a certain direction, uncontrolled hypertension and presence of intraluminal thrombus (Khan *et al.*, 2015). Though such factors appear more significant to evaluate the AAA rupture risk (Gasser *et al.*, 2014), the overall wall stress of the blood vessel increases substantially compared to the healthy configuration (Khan *et al.*, 2015).

However, existing CFD simulations (Meng *et al.*, 2006, 2007) assumed the blood to be a newtonian fluid and the arterial wall was modelled as rigid. The onset and progression of cardiovascular disease have been linked, among other, to hemodynamics. However, there is evidence that physiological activity is dependent on variables such as stress and strain within the tissue (Sommer, 2010).

Therefore, there is the need to investigate the relation between a supra-physiological inflating pressure and the biomechanical response of the aorta, modelled as hyper-elastic material, as possible cause for aneurysm formation. Such modelling appears challenging due to aortic complexity and highly nonlinear behaviour.

Recently, computational simulations have investigated the bifurcation from a membrane

tube configuration subject to axial loading and internal pressure attempting to justify aneurysm formation (Alhayani *et al.*, 2013). The material properties of such model originated from speculative values based on published data. As a result, the formation of the bulge in the anisotropic model appeared analogous to the one predicted in the isotropic design. The buckling behaviour of arterial models based on experimental data has been simulated on healthy and aneurysmal arteries (Lee *et al.*, 2014).
However, it appears that so far no model, based on experimental data acquired by means of up-to-date protocol, has investigated the bulging of the aorta.

1.3 Aim of this research

The overall purpose of this research study is to assess, from the macro-structural point of view, whether an aneurysm may be instigated in an healthy model of aorta inflated over a certain threshold of pressure. This research focuses on the descending segment, being more commonly affected by aneurysm formations (Voitle *et al.*, 2015). A particular emphasis is given to the understanding of aortic mechanical properties. Since no standard procedure is available to perform experimental tests on hyper-elastic materials, a complete up-to-date protocol has been set up by means of rubber samples and used on aortic samples. Successively, the wall stress values generated by physiologic pressure at rest and in supra-physiologic conditions are estimated. An isotropic FE modelling is compared to anisotropic material design. Lastly, the impact of some experimental measurements (e.g. thickness) or feature (e.g. pre-conditioning) on numerical predictions is explored.
Therefore, this research covers two main areas: the scrupulous collection of experimental data sets and the design of finite element (FE) models to predict aneurysm formation in the aorta. For this purposes, uniaxial and biaxial tensile tests have been performed on samples of porcine aortas by means of up to standard facilities. The obtained mechanical responses have been fitted by isotropic and anisotropic material

models well-established in literature. Finally, FE models have been developed to predict the pressure values that may lead to aneurysm formation.
As additional outcomes of the present work, a novel experimental approach is suggested to characterise the aneurytic tissue, as well as an original integration of its behaviour in a FE model to predict aneurysm rupture.

1.4 Organization of the thesis

The present thesis is structured in eight chapters to illustrate the progress of the research performed. An extensive literature review of uniaxial and biaxial tests is reported in *Chapter 2* to set the scene of the proposed experimental protocols. Furthermore, the theoretical framework for the applied mathematical models is provided. Finally, the main modelling features adopted in the state of art for aortic FE design are illustrated. *Chapter 3* presents the methods for the acquisition and the processing of the experimental data collected for development of the aortic model. The experimental tests were carried out at the University of Portsmouth and at the University College of London (UCL). A consistent number of tools to post-process the data (e.g. thickness, stress-strain response, material fitting parameters, ...) have been created by means of Matlab scripts. *Chapter 4* shows and discuss the results obtained from all the experimental testing procedures detailed in *Chapter 3*.
The implementation process of FE models in Abaqus is described in *Chapter 5*. The numerical predictions generated by such computational models are listed and discussed in *Chapter 6*. In *Chapter 7*, overall findings are critically reviewed and the concluding remarks are presented. Lastly, preliminary FE models, which outcomes determined the design of experimental planar biaxial tests, are described in the Appendix.

Chapter 2

Literature review

The main purpose of this chapter consists in reviewing the state of art in order to offer a consistent basis to justify the present research. Besides, the first Section (2.1) introduces briefly continuum mechanics fundamentals and recaps the isotropic and anisotropic constitutive models available in literature to describe a hyper-elastic behaviour (Section 2.2). In addition, Section 2.3 summarizes the current experimental techniques adopted to characterize rubber-like materials. Thus, the state of art concerning rubber and aortic experimental testing is reviewed, with a particular remark about the storage of soft tissues. Finally, the finite element method is introduced in section 2.4, pointing out the principles of the algorithm and its existing applications in the aneurysm field of study. A separate note is dedicated to the modified Riks method.

2.1 Continuum mechanics basics

In this section, basic concepts, principles, and findings from continuum mechanics that are essential to describe the mechanical behaviour of hyper-elastic materials, such as aortic tissue, are presented.

A *body* is defined as a collection of material particles. Hence, a body *configuration* consists in the specification of the positions of each constitutive particle at a particular

time *t*. Motion can be defined, therefore, as a sequence of configurations parametrized by time.

Despite its molecular nature, the macroscopic response of a homogeneous body can be approximated by assuming locally averaged properties. Hence, stresses and strains can be described by continuous functions. The position of a body in a reference configuration, at time $t = 0$, relative to a coordinate system is defined by a position vector **X**. Similarly, the position of the same body in a current configuration, at time *t*, is identified by a position vector **x** (Figure 2.1).

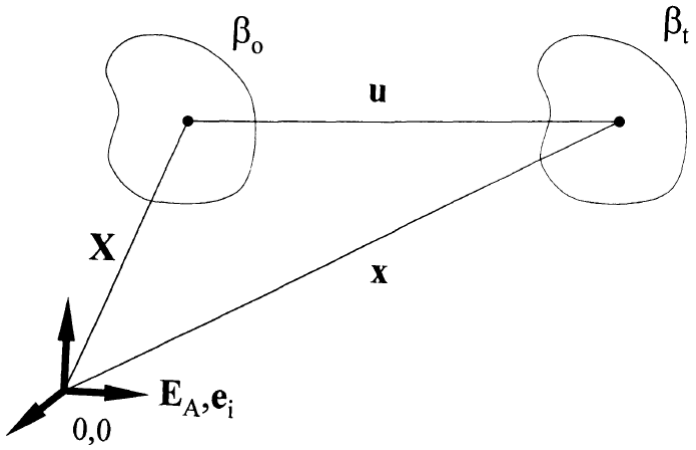

Figure 2.1 A rigid body motion from the reference configuration (β_0) to the actual one (β_t) (Humphrey, 2002).

Therefore, the displacement vector ***u*** for each material particle is given by:

$$\mathbf{u} = \mathbf{x} - \mathbf{X} \tag{2.1}$$

A generic differential line segment d**X** in the reference configuration (β_0) turns into the vector segment d**x** in the current configuration (β_t). This transformation of vectors is accomplished by the deformation gradient **F**, being a tensor defined as follows:

$$d\mathbf{x} = \mathbf{F}d\mathbf{X} \tag{2.2}$$

Furthermore, **F** can be expressed by polar decomposition as:

$$\mathbf{F} = \mathbf{R}\,\mathbf{U} = \mathbf{V}\,\mathbf{R} \tag{2.3}$$

where **R** represents the rotation tensor, **U** and **V** are defined as the stretch tensors in the reference and in the current configuration respectively. An alternative to the two-points and not symmetric tensor **F** is offered by the right Cauchy-Green tensor **C**:

$$\mathbf{C} = \mathbf{F}^T\mathbf{F} = \mathbf{U}^T\mathbf{R}^T\mathbf{R}\,\mathbf{U} = \mathbf{U}^2 \tag{2.4}$$

This tensor is defined *right* due to the position of the measure **F** with respect to its transpose. In the absence of motion ($\mathbf{x} = \mathbf{X}$) the deformation gradients **F** and **C** correspond to the *identity* tensor **I**. The eigenvalues of the right Cauchy–Green deformation tensor **C** are the square of the principal stretches (λ_i^2). The stretch ratio λ represents the ratio of the deformed length L divided by the initial length L_0.
Unfortunately, these tensors are not independent of any rigid body motion (i.e. rotation, translation). Alternatively, the deformations can be described by the Green-Lagrange strain tensor, which equals 0 when there is no deformation. This symmetric tensor is defined as:

$$\mathbf{E} = \frac{1}{2}(\mathbf{C} - \mathbf{I}) \tag{2.5}$$

In the soft tissue literature, the tensor **E** is the most common finite strain measure, due to the simplicity of the constitutive formulations. Specific circumferential and axial components can be defined under three simplifying assumptions: plane strain mode that neglects out-of-plane deformation, uniform radial expansion and the vessel wall approximated as a membrane. The circumferential strain $\mathbf{E}_\theta$ can be expressed in terms of the deformations in cylindrical coordinates:

$$\mathbf{E}_\theta = \frac{1}{2}\left[\left(\frac{R}{R_0}\right)^2 - 1\right] \tag{2.6}$$

where R_0 is the vessel radius at a reference time and R represents the radius measured at any other time in the cardiac cycle. Similarly, the axial Green-Lagrange strain $\mathbf{E}_Z$ is given by:

$$\mathbf{E}_Z = \frac{1}{2}\left[\left(\frac{L}{L_0}\right)^2 - 1\right] \tag{2.7}$$

where L_0 is the axial length at a reference time and L represents the actual length.

Whether a physical body is loaded by external forces, an internal loading state is generated, which is generally described by the notion of stress (Holzapfel, 2000).

The Cauchy stress tensor (σ), also known as the *true* stress, represents a contact force density measured in the current configuration per unit of current area. Both the force components and the normal to the area have fixed directions in space. Practically, if a stressed body is subjected to a pure rotation, the actual values of the Cauchy stress components will change. What was originally a uniaxial stress state might be transformed into a full tensor with both normal and shear stress components. Furthermore, the configuration of the body after the deformation appears difficult to appreciate experimentally. Therefore, it appears convenient to relate the measured forces to the reference configuration.

The first Piola-Kirchhoff stress represents indeed a multiaxial generalization of *engineering* stress, being defined as the force in the current configuration acting on the original area. The first Piola-Kirchhoff stress tensor $\mathbf{P}$ transforms outward unit normal $\mathbf{n}$ into the traction vector $\mathbf{t}^n$ such that:

$$\mathbf{t}^n = \frac{df}{dA} = \mathbf{P}\cdot\mathbf{n} \tag{2.8}$$

Similarly to tensor $\mathbf{F}$, the first Piola-Kirchhoff is an unsymmetric tensor. In the reference configuration, a symmetric tensor can be defined considering a fictitious force f^* that is applied on the oriented area NdA. The fictitious force is designated ad follows:

$$df^* = \mathbf{F}^{-1} df = df \mathbf{F}^{-T} \tag{2.9}$$

Hence, we can define a new traction vector $\mathbf{t}^{*n}$

$$\mathbf{t}^{*n} = \frac{df^*}{dA} = \mathbf{S} \cdot \mathbf{n} \tag{2.10}$$

where $\mathbf{S}$ is the second Piola-Kirchhoff stress tensor, being symmetric tensor that exists in the reference configuration (Humphrey, 2002). Stress tensor $\mathbf{S}$ has to be regarded as a pure numeric quantity, for which there is no possibility of a physical interpretation (Balzani, 2006). The second Piola-Kirchhoff stresses components in the circumferential ($\mathbf{S}_\theta$) and axial ($\mathbf{S}_Z$) directions are respectively given by:

$$\mathbf{S}_\theta = \frac{P r_i}{h \left(\frac{R}{R_0} \right)^2} \tag{2.11}$$

and

$$\mathbf{S}_Z = \left(\frac{L_0}{L} \right)^2 \left[\frac{F}{\pi (r_o^2 - r_i^2)} + \frac{P r_i^2}{h (r_o + r_i)} \right] \tag{2.12}$$

where F is the axial force, h the wall thickness, r_i the inner radius, r_o the outer radius and P is pressure (Pandit *et al.*, 2005).

2.2 Hyper-elastic behaviour

The relation between the stress and the strain in a body subjected to certain forces represents the main application of the elasticity theory. Hooke's Law describes a linear relationship between the stress and small strain values. However, large deformations are described by means of different expressions (Figure 2.2). In this work, arteries are modelled as rubber-like materials due to their common stress-strain response.

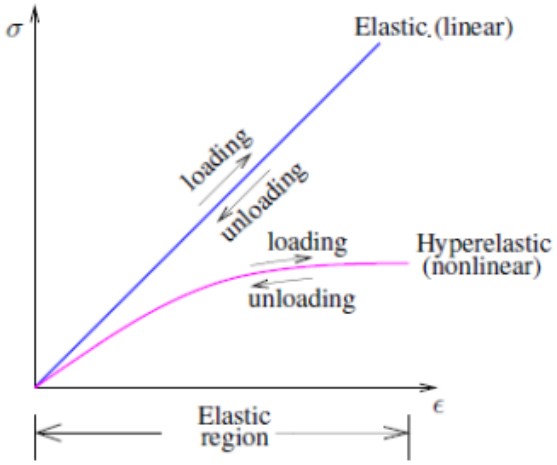

Figure 2.2 Elastic stress-strain responses: linear (blue), hyper-elastic (pink) (Garcia *et al.*, 2005).

Hyper elasticity is the capability of a material to experience large elastic strain due to small forces, without permanent deformations. Truesdell defined hyper elasticity as a special case of elasticity (Truesdell, 1963).

A hyper-elastic material, also called Green-elastic, is characterized by a nonlinear behaviour, as its answer to the load is not directly proportional to the deformation. In 1860, Neumann introduced a general stored-energy function and derived from it the general constitutive equation of hyperelasticity (Truesdell & Noll, 1965). Such strain-energy function W indicates the recoverable energy stored in such material as it deforms (Humphrey, 2002). During an isothermal deformation, W is associated with the free energy per unit undeformed volume. During an iso-entropic deformation, W corresponds to the internal energy per unit undeformed volume (Taber, 2004). Therefore, the Cauchy stress can be expressed by the derivative of W with respect to a stretch component λ_i as follows:

$$\sigma_i = -p + \lambda_i \frac{dW}{d\lambda_i} \tag{2.13}$$

where p is the hydrostatic pressure. Furthermore, W can be expressed as a function of principal stretches or strain invariants. This aspect will be clarified in Section 2.2.2. Constitutive models are meant to describe the response of a material to applied loads.

This reaction depends on the internal constitution of the material. Historically, several constitutive models have been published to characterize the mechanical response of rubber-like materials and arterial walls. These formulations are reviewed in Sections 2.2.2 and 2.2.3.

2.2.1 Analogy with rubber materials

Rubber-like materials exhibit an elastic behaviour in a wide range of strain. This feature is exploited, in the biomechanical field, to obtain an isotropic version of a constitutive model for arterial wall mechanics. Since the collagen fibres of soft tissues are not active at low stresses, the mechanical response is assumed to be isotropic (Holzapfel *et al.*, 2005). Additionally, the use of synthetic materials facilitates the setting up of novel experimental techniques aiming at a more precise and reliable characterisation of biological tissues. This is mainly due to minor constraints on storage and sample preparation, as well as availability and consistency in their mechanical properties, which makes them advantageous to implement or refine various experimental techniques. Moreover, rubber minimizes the effect of material variability, which is quite extensive in biological tissue. Rubber-like materials also exhibit viscoelasticity, which accounts for a combined viscous, or fluid-like, and elastic, or solid-like, behaviour (Humphrey, 2002). Thus, hydrated tissues are characterized by creep and relaxation, which are time-dependent phenomenons. As a consequence of viscoelasticity, the Mullin's effect, which will be presented in Section 2.3.2, needs to be taken into account.

Rubbers have been widely adopted to reproduce and study aortic disease, such as aneurysm. Schurink et al. (Schurink *et al.*, 1998) created a rubber model of aneurysm to study the effect of endoleakage, frequently observed after endovascular repair of abdominal aortic aneurysm. Holzapfel et al. (Holzapfel *et al.*, 2002, 2005) affirmed that arteries share a thermomechanical behaviour similar to rubber-like materials. In order to clarify the effect of the intraluminal thrombus on the transmission of pressure, Hinnen

et al. (Hinnen *et al.*, 2005) modelled saccular aneurysms made of elastic vulcanized rubber. Aiming to identify aneurysm sites of rupture, Doyle et al. (Doyle *et al.*, 2009a,b) implemented silicone experimental models. In order to study the wave reflection along the arteries, Segers & Verdonck (Segers & Verdonck, 2000) replicated the human arterial tree adopting handmade tapering rubber tubes.

Therefore, rubber materials have been frequently adopted to mimic in vitro the behaviour of the arterial wall.

2.2.2 Isotropic models

Isotropic constitutive models are based on the idea that the response of the rubber-like material is the same in all directions. Therefore, the fibrous nature of an arterial wall is neglected. This approach has been extensively used to simplify the modelling of arterial tissue (Doyle *et al.*, 2007; Isaksen *et al.*, 2008; Kobielarz & Jankowski, 2013; Lally *et al.*, 2004; Scotti *et al.*, 2008; Wang & Li, 2011).

Among the hyper elastic isotropic models, Mooney (Mooney, 1940) presented the earliest significant phenomenological theory of large elastic deformation. However, Mooney's theory is generally known by Rivlin's formulation (Rivlin & Saunders, 1951) based on invariants. Isotropic formulations are often expressed in function of strain invariants, which are defined as follows:

$$\begin{aligned} I_1 &= \lambda_1^2 + \lambda_2^2 + \lambda_3^2 \\ I_2 &= \frac{1}{\lambda_1^2} + \frac{1}{\lambda_2^2} + \frac{1}{\lambda_3^2} \\ I_3 &= \lambda_1^2 \lambda_2^2 \lambda_3^2 \end{aligned} \tag{2.14}$$

The third invariant I_3 describes the volume change during the deformation. Since the change in volume of rubber-like materials is negligible compared with the change in shape (Treloar, 1943), the simplifying assumption of incompressibility is usually

adopted (Treloar, 2005). Thus, for an incompressible material it follows that $I_3 = 1$. Therefore, Rivlin & Saunders (Rivlin & Saunders, 1951) proposed a constitutive relation based explicitly on the first and second invariants:

$$W = C_{10}(I_1 - 3) + C_{01}(I_2 - 3) \tag{2.15}$$

where C_{10} and C_{01} are material parameters obtained via fitting.
Yeoh (Yeoh, 1993) formulation accounts only the first invariant, as follows

$$W = C_{10}(I_1 - 3) + C_{20}(I_1 - 3)^2 + C_{30}(I_1 - 3)^3 \tag{2.16}$$

where C_{10}, C_{20} and C_{30} are fitting coefficients. The model will normally be stable whether the parameters C_{10} and C_{30} are positive and C_{20} is negative. Although dW/dI_2 is finite, Yeoh suggested to neglect it as it is generally sufficiently small. The simplest constitutive model is the Neo-Hookean model (Treloar, 1943), which can be viewed as a simplification of the previous model:

$$W = C_{10}(I_1 - 3). \tag{2.17}$$

The *eight chain model* presented by Arruda and Boyce (Arruda & Boyce, 1993) adopts an invariant and a stretch:

$$W = \mu \sum_{i=1}^{5} \frac{C_i}{\lambda_m^{2i-2}} (I_1^i - 3^i) \tag{2.18}$$

where μ is a material parameter function of the initial shear modulus μ_0, C_i are related to the series expansion form of the inverse Langevin function and λ_m is the locking stretch. Other strain energy functions are function of the first and second invariant

implicitly, such as Ogden (Ogden, 1972):

$$W = \sum_{i=1}^{N} \frac{\mu_i}{\alpha_i}(\lambda_1^{\alpha_i} + \lambda_2^{\alpha_i} + \lambda_3^{\alpha_i} - 3) \tag{2.19}$$

where μ_i and α_i are temperature-dependent material parameters that allow a good fit of the theoretical description to the experimental data (Ogden, 1972). In Abaqus, the factor multiplying the sum of deviatoric principal stretches is different, being $2\mu_i/\alpha_i^2$.

Rubber shows strain-hardening at large strains as the long flexible molecular strands that comprise the material cannot be stretched indefinitely. Therefore, Gent's strain-energy function (Gent, 1996) takes into account this feature in the following form:

$$W = -C_1 I_m \ln\left(1 - \frac{I_1}{I_m}\right) + C_2 \ln\left[\frac{I_2 + 3}{3}\right] \tag{2.20}$$

where I_m represents the maximum stretch ratio.
Marlow's strain-energy function (Marlow, 2003) is defined differently from the previous ones. The nominal uniaxial stress $\tau_1(\varepsilon)$ is integrated over the strain interval [0,ε^*]:

$$W(\varepsilon) = \int_0^{\varepsilon^*} \tau_1(\varepsilon)\,\mathrm{d}\varepsilon. \tag{2.21}$$

Similarly to Yeoh, Delfino et al. (Delfino *et al.*, 1997) neglected the second invariant, assuming the arterial wall to be isotropic and homogeneous by means of the following exponential strain-energy function:

$$W = \frac{C_1}{C_2}\left[e^{\frac{C_2}{2}(I_1-3)} - 1\right] \tag{2.22}$$

where C_1 and C_2 are the material constants. Another approach, formulated as regression of experimental data, has been introduced by Raghavan & Vorp (Raghavan & Vorp,

2000) to describe the mechanical behaviour of the AAA wall:

$$W = C_1(I_1 - 3) + C_2(I_1 - 3)^2 \tag{2.23}$$

Recently, Volokh (Volokh, 2008) argued that the energy increase of a material should be limited as the idea of intact materials at increasing strains is unphysical. Therefore, the average bond energy ϕ is assumed to be the material failure energy in the following general expression:

$$\varphi(W) = \phi - \phi e^{\frac{-W}{\phi}} \tag{2.24}$$

where $\varphi(W = 0) = 0$ and $\varphi(W = \infty) = \phi$. In the case of the *intact* material behaviour, $W \ll \phi$, we have $\varphi(W) \approx W$.

The reviewed formulations are the most common strain-energy functions encountered in literature to describe isotropic hyper-elastic materials also in the context of biological tissue.

2.2.3 Anisotropic models

Despite several biomechanical studies are based on isotropic assumptions, a couple of strain-energy functions take into account the anisotropic nature of soft tissues. Histology indeed highlights the anisotropic nature of arterial walls due to the constitutive framework of collagen that carries the load, as already mentioned in Section 1.1.3.

In a seminal paper, Fung et al. (Fung *et al.*, 1979) represented the artery as a membrane, which constitutive model depends only on the circumferential and axial deformations. The exponential form of the strain-energy function has been preferred to analyse systematic variations due to different factors, such as the age, the influence of drugs or the effect of hypertension. Furthermore, the derivation of the expression for strains

in terms of stresses is shown being easier compared to a polynomial constitutive form. Hence, the three-dimensional stress-strain behaviour of a soft tissue can be described by a strain-energy function W that is exponential in terms of the Green strain:

$$W = \frac{C}{2}\left[e^{Q(E)} - 1\right] \tag{2.25}$$

being C a model constant having units of stress, and Q a polynomial function of the components of E, including linear, quadratic, and cubic terms. Materials that are described by equation 2.25 are generally called *Fung elastic* (Humphrey, 2002). Over years, however, experience revealed that it was actually better to neglect the linear and the cubic terms (Fung, 1993). Hence, Q assumes a quadratic form:

$$Q = a_1 E_{\theta\theta}^2 + a_2 E_{ZZ}^2 + 2a_4 E_{\theta\theta} E_{ZZ} \tag{2.26}$$

where a_i are dimensionless material model constants. In particular, parameters a_1 and a_2 quantify the material stiffness along the normal strain directions, while a_4 is related to the shear stiffness (Ma *et al.*, 2007; Pandit *et al.*, 2005). In order to expand such strain-energy function in terms of the nine strain components, Q can be written in the following form:

$$\begin{aligned} Q = {} & a_1 E_{\theta\theta}^2 + a_2 E_{ZZ}^2 + a_3 E_{RR}^2 + 2a_4 E_{\theta\theta} E_{ZZ} + 2a_5 E_{ZZ} E_{RR} + 2a_6 E_{\theta\theta} E_{RR} \\ & + a_7 E_{\theta Z}^2 + a_8 E_{\theta R}^2 + a_9 E_{ZR}^2 \end{aligned} \tag{2.27}$$

where R, θ, Z are polar coordinates in the radial, circumferential and axial directions respectively (Fung *et al.*, 1979). As a result, second Piola-Kirchhoff stress components S_{ij} can be expressed as partial derivatives of W:

$$S_{ij} = \frac{\partial W}{\partial E_{ij}} \tag{2.28}$$

being E_{ij} the components of the Green-Lagrange strain tensor **E**. It is well known that most soft tissues exhibit hysteresis (Lee *et al.*, 1967; Rickaby & Scott, 2013), and thus they are not strictly elastic. However, the loading and unloading curves become repeatable following multiple cycles of testing. Hence, Fung proposed that such behaviour can be separately assumed to behave elastically in loading and unloading, defining a pseudoelastic behaviour (Fung *et al.*, 1979). In this way, quantification of the stress-strain relations in loading and unloading simply requires separate sets of the material parameters. At this point it is important to note that Fung's approach, like most in solid mechanics, is phenomenological. The equation 2.25 acts as a quantitative descriptor based on macro observations of tissue behaviour, not a detailed analysis of the microstructure or detailed information on the mechanical behaviour of the individual constituents (Humphrey, 2002).

An approach able to capture the nature of such constituents, is based on the idea of including an anisotropic contribution to the initial isotropic problem. Hence, the strain-energy function would take the form $W = W_{isotropic} + W_{anisotropic}$. The isotropic component accounts for the elastin-dominated ground matrix modelled as a Neo-Hookean model, and the anisotropic component takes into account the collagen represented by the Fung model. Hence, Holzapfel et al. (Holzapfel *et al.*, 2000) proposed to represent the strain-energy stored in a composite material reinforced in two preferred directions indicated by the invariants I_4 and I_6. Both invariants can also be expressed as a function of the main stretches as follows:

$$\begin{aligned} I_4 &= \lambda_1^2 \cos^2 \theta_1 + \lambda_2^2 \sin^2 \theta_1 \\ I_6 &= \lambda_1^2 \cos^2 \theta_2 + \lambda_2^2 \sin^2 \theta_2 \end{aligned} \tag{2.29}$$

where λ_i are the principal stretches, θ_1 and θ_2 represent the fibres directions. This constitutive model, intended as phenomenological and not as a structural model, is referred

as the *Holzapfel-Gasser-Ogden (HGO) model*, which has been recently (Holzapfel *et al.*, 2005) reformulated as follows:

$$W = \mu(I_1 - 3) + \frac{k_1}{2k_2}\left(e^{k_2\left[\rho(I_4-1)^2+(1-\rho)(I_1-3)^2\right]} - 1\right). \tag{2.30}$$

In the equation 2.30, the first invariant I_1 characterizes the isotropic mechanical response of the elastin. Positive parameter k_1 has stress dimensions, while k_2 is dimensionless. The $\rho \in [0,1]$ parameter is also dimensionless and accounts for the fibres dispersion. However, ρ has no histological meaning (García *et al.*, 2011).

Despite numerous isotropic and anisotropic constitutive models have been listed, the practical use of some of them (Delfino *et al.*, 1997; Gent, 1996; Volokh, 2008) may be complicated, being not implemented in standard software (e.g. Abaqus). Furthermore, depending on the available stress-strain data, an higher polynomial order (Ogden, 1972; Yeoh, 1993) may offer a more accurate fitting compared to first order (Treloar, 1943). Finally, further analyses, such as the observation of fibres direction (Holzapfel *et al.*, 2005), are required ahead certain fitting procedure. Thus, the choice of the strain-energy function, which will be carefully addressed in Chapters 5 and 6, relies on multiple factors.

2.3 Experimental data available

Nowadays, generic tensile tests are performed by automatic machines, able to measure simultaneously multiple parameters, such as force, displacement, temperature, number of cycles, test speed rate and duration. Nonetheless the improved technology, the adopted testing methodology remains a critical aspect for the proper characterization of rubber-like materials. In the following sections 2.3.1 the measuring techniques explored during this research are presented. Furthermore, the state of art concerning experimental

testing of rubber materials and aortic tissues is reviewed in section 2.3.2. Finally, the current storage practice of soft biological tissues is presented in section 2.3.3.

2.3.1 Measuring techniques

Testing machines are designed to apply a force to a specimen in order to determine its strength and resistance to deformation. These machines are meant to drive a crosshead at a controlled rate, applying a tensile load to a specimen. The load-applying mechanism of the machines involved in this research is servo hydraulic (hydraulic pump and servo hydraulic valves) or electromechanical. Current testing machines use strain-gage load cells, arranged for tensile or compressive loading. Their output signal is the load, commonly indicated in N.

Aiming to produce the stress-strain plot of an experimental test, the values of displacement or strain need to be acquired as well. Therefore, three different options to measure the deformation of rubber-like materials are presented: the machine crosshead, the video-extensometer and the digital image correlation.

Machine crosshead

The machine crosshead measures the specimen elongation in the gage length. However, elastic deflections in components such as machine frame, load cell, grips and specimen ends contribute to the measured elongation. In order to calculate the displacement, the elongation value has to be related to the initial conditions during which the specimen is crimped in the testing machine, but no load is applied yet (ASM, 2004).

Video-extensometer

Several devices are available to evaluate the elongation of the region of interest within each sample. However, strain gages and clip-on extensometer are not the best option

for hyper-elastic materials, since they introduce a consistent damage in such samples. Furthermore, rubber-like specimens appear bended under the weight of the mentioned measuring systems. Therefore, optical devices are preferred to obtain strain measurement (ASM, 2004).

A video-extensometer provides non-contact, high-resolution measurement of tensile and compressive sample deformations. A full image video-camera is focussed on the test specimen upon which contrasting marks, also called targets, have been marked or attached (Figure 2.3).

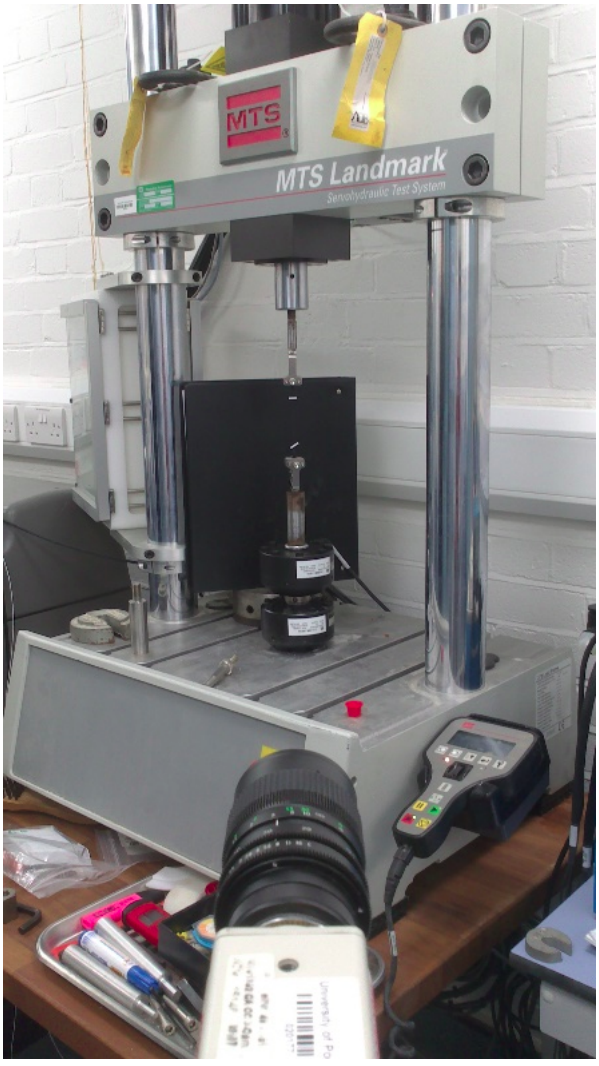

Figure 2.3 Video-extensometer focussed on the targets attached on sample surface.

The field of view depends upon the focal length of the lens fitted and the camera's distance from the specimen. The camera's chip (CCD or CMOS) confines any error in measurement to lens defects and to the distance between specimen and camera during testing. The selected target points are indicated on the monitor and the operator has to confirm the correct selection. Whether wrong targets are recognised, the operator can manually select the correct ones. The associated software ensures the distance between targets is continuously measured in real time during testing. Thus, the video-extensometer automatically calculates the measured extension as a percentage of the original length. Calibration is required exclusively to obtain actual extension values (Messphysiks Material testing GmbH).

Digital Image Correlation

Among the presented measuring techniques, Digital Image Correlation (DIC) is the most recent, being an effective and flexible optical tool to obtain full-field deformation measurement. In essence, the region being measured on a reference image is mathematically translated, rotated and deformed until the best fit to the region on the deformed image is obtained (Gao & Desai, 2010). Artificially applied speckle patterns or natural texture on a specimen surface are recorded during an experiment by means of two cameras. The speckle pattern is generally produced by randomly spraying can or airbrush. The spray method is generally used to paint randomly soft tissues surfaces in front of the CCD camera (Krehbiel & Berfield; O'Leary *et al.*, 2014; Zhang & Arola, 2004). Alternatively, nuclear staining can be obtained by means of ethidium bromide (Badel *et al.*, 2011). The quality of the speckle pattern affects the measured displacements (Pan *et al.*, 2008). The cameras should be positioned somewhat symmetrically about the specimen. Despite this exact angle between the cameras is not a severe requirement, a broad range of angles between 15° and 45° is generally suggested (Vic, 2007).

The DIC method requires that the region of interest in the reference image is specified, in order to create a virtual grid. To the extent of computing the displacements of a selected point P, a square reference subset of pixels from the reference image is chosen and used to track its corresponding location in the deformed image (Figure 2.4). A square subset, rather than an individual pixel, is selected for matching as a wider variation in grey levels can be more uniquely identified in the deformed image. To evaluate the degree of similarity degree between the reference subset and the deformed subset, a cross-correlation (CC) criterion or sum-squared difference (SSD) correlation criterion must be predefined. The matching procedure is completed through searching for the peak position of the distribution of the correlation coefficient.

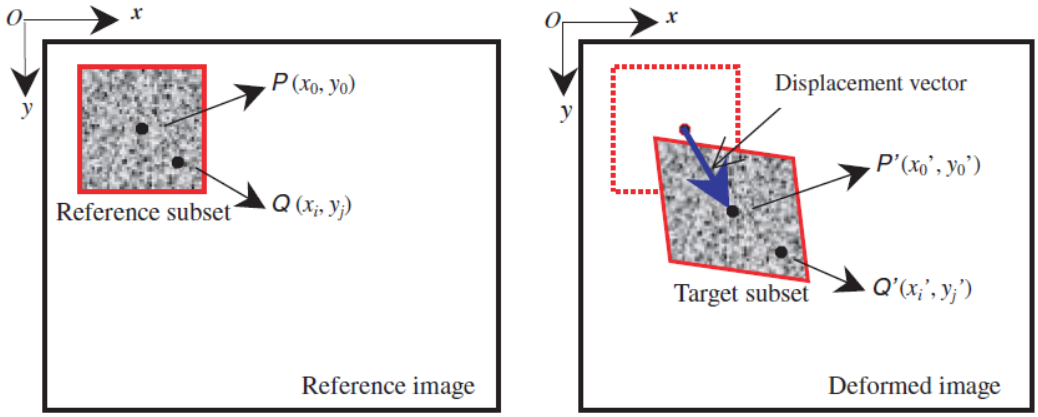

Figure 2.4 Basic principle of 2D DIC: the target subset of the undeformed image (left) is matched to the corresponding in the deformed image (right) by means of a cross-correlation criterion (Pan *et al.*, 2009).

Once the facets have been matched, the full-field displacement is automatically computed by tracking the change in position of points on digitized images. Subsequently, the strain field is obtained by derivation on displacement gradients (Palanca *et al.*, 2015). Similarly to the video-extensometer, each camera focus and aperture needs to be adjusted to the specimen. However, a supplemental light has to be carefully set, in order to avoid excessive or limited brightness. Furthermore, the DIC calibration process is more time consuming compared to video-extensometer. When the speckle pattern on sample surface does not fulfil all the requirements, no complete calibration can be achieved.

Hence, another sample needs to be prepared. An average time of 30 minutes may be needed for each sample subjected to DIC, while the video-extensometer halves such time.

Lastly, the operating principles of 3D-DIC are similar to 2D-DIC. Such extended analysis can be performed by using two or more cameras in stereoscopic vision (Palanca *et al.*, 2015).

As a conclusion of the present section, the region of interest of each measuring technique described in the present section is highlighted in Figure 2.5.

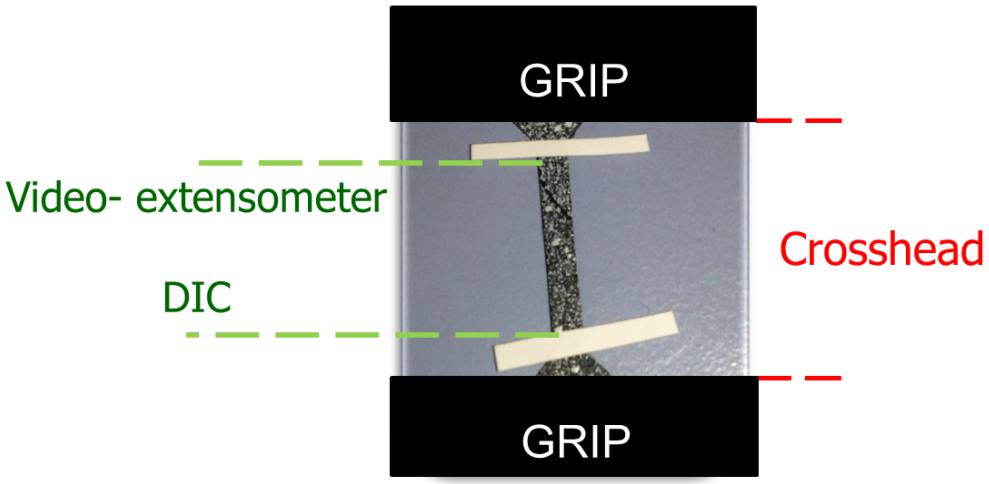

Figure 2.5 Comparison of area on which each measuring technique focus in order to estimate the elongation (crosshead, video-extensometer) or strain (DIC). Further details on the present picture will be given in Section 3.2.1.

2.3.2 State of the art

The uniaxial tensile test represents the preferred approach to obtain mechanical properties (Shergold *et al.*, 2006; Sokolis *et al.*, 2002; Vahapoglu *et al.*, 2011) due to its simple setup and to its limited cost compared to other more complex tests, such as indentation or inflation. However, a complete understanding of a material mechanical behaviour requires an additional biaxial test. Although this research is focussed on aortic wall tissue, rubber has been extensively adopted to implement the experimental procedures

that will be presented in Chapter 3. Therefore, in this Section a brief review about rubber-like materials precedes the actual literature of aortic tissue experimental testing.

In the history of rubber materials, Treloar is considered a pioneer, as he tested an 8% Sulphur vulcanized rubber strip (10 mm x 3 mm) in 1943 (Treloar, 1943). The sample was stretched by adding weights to a lower clamp and the deformed length was measured by a travelling microscope. As the test execution was manual, the rate of extension was not controlled. Similarly, Rivlin & Saunders (Rivlin & Saunders, 1951) tested a vulcanized rubber strip (50 mm x 8 mm), drawing two thin ink lines on it as references. The distance between the lines was measured by means of a cathetometer. Differently, Kawabata et al. (Kawabata *et al.*, 1981) performed a general biaxial test on a $115mm^2$ sample, clamped by nine chucks on each edge and simultaneously stretched by two servo controlled systems. The stretch ratio of the specimen along each direction was measured by a potentiometer. This work reports the biaxial experimental data set, from which uniaxial and pure shear data can be retrieved.
The technology available at that time clearly limited the acquisition of accurate experimental evidences. Nowadays, the limitation is represented by the methodology adopted to perform such tensile tests.

Mechanical pre-conditioning Hyper-elastic materials exhibit an appreciable change in their mechanical properties resulting from the first extension. Most of the softening appears after the first load: lower force values are recorded for the same applied stretch (Figure 2.6). After a few cycles, the material response is stable and repeatable, aside from a fatigue effect (Diani *et al.*, 2009). According to the damage model (Beatty & Krishnaswamy, 2000), a virgin material consists of a hard phase, made of cross-linked particles, and a soft phase, being the rubbery one. As the deformation of the virgin material progresses, a volume fraction of the initial hard phase is transformed into soft

phase. The *new* soft phase depends only on the maximum previous stretch (Beatty & Krishnaswamy, 2000). Hence, the softening is due to the breaking of the cross linked molecules (Bhowmick, 2008). This phenomenon, referred to as the Mullins effect, proves that a mechanical behaviour is unique after a certain pre-conditioning.

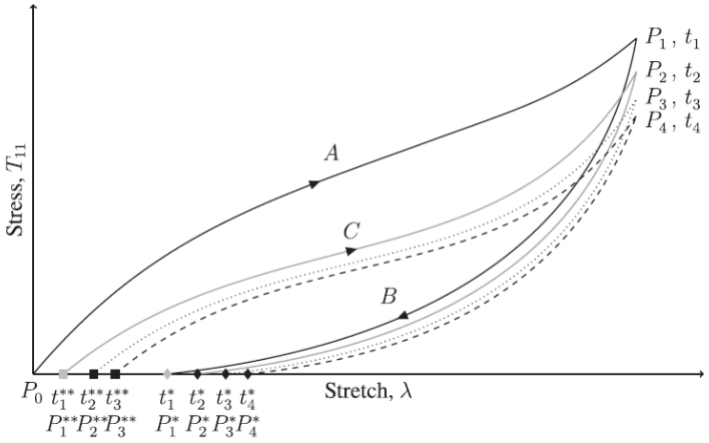

Figure 2.6 Typical softening behaviour of a biological specimen under tension. The process starts from an unstressed virgin state at P_0 and the loading path A and the unloading path B returning to the unstressed state. Reloading commences along the path C that lies below the path A. Unloading of the biological specimen from the point P_2 follows the grey path below path B. This phenomenon is referred as hysteresis (Rickaby & Scott, 2013).

However, the number of pre-conditioning cycles appears not to be standardized. Attempts to incorporate mandatory mechanical conditioning into ISO standards have met with resistance because trials with certain particular tests have failed to produce evidence that the effect is large enough to be significant (Brown, 2006). Although British standard (BS ISO, 2012) suggests tensile testing procedures for rubber, no exhaustive indication about the mechanical pre-conditioning (often referred to as *scragging*) procedure is reported. In order to improve the test reproducibility, the general recommendation consists of subjecting the test piece to *several* pre-conditioning cycles before taking stress–strain measurements (Luo *et al.*, 2010). Since 1995 the only recommendation available has been the number of pre-conditioning cycles and temperature to be used in the test series (BS 903-1, 1995; ISO 4664, 1998).

Furthermore, a number of studies reported the value of actuator speed selected for

the uniaxial tensile test. For example, Jerabek *et al.* (2010) elongated polypropylene specimens at 0.01 mm/s, Cox *et al.* (2008) stretched polydimethylsiloxane dumb-bells at 0.2 mm/s, ISO standard (ISO 37, 2005) suggests to test small dumb-bells at 3.33 mm/s, while Shergold *et al.* (2006) preferred to pull their silicone dumb-bells at 8.33 mm/s. Rarely, the value of frequency selected to perform the pre-conditioning is reported (Sahakaro & Beraheng, 2008).

Therefore, the experimental testing of hyper-elastic materials still remains critical: no complete standard protocol has been produced for rubber materials.

Mechanical testing of aortic tissue

The lack of a standard procedure for rubber becomes even more evident when it comes to hyper-elastic tissues. The mechanical characterization of aortic tissue remains highly heterogeneous.

Historically, Roy (1881) is considered the pioneer of uniaxial tests performed on human aorta, which anisotropy and elasticity have been documented. About a century later, Tanaka & Fung (1974) pointed out the importance of the pre-conditioning to overcome the Mullins effect and proved variations of mechanical properties along the aortic tree. Successively, several works attempted to characterize healthy (Holzapfel, 2006; Raghavan *et al.*, 1996) and aneurytic aortic tissue (Di Martino *et al.*, 2006; Raghavan *et al.*, 1996; Xiong *et al.*, 2008). However, the comparison of the obtained data remains challenging due to unique experimental procedures adopted in each study. Despite experimental data collected from rabbit (Sokolis *et al.*, 2006) and bovine aortas (Chow & Zhang, 2011) are available, only most recent studies regarding porcine and human aortas are reviewed in this section.

Sample shape and clamping While uniaxial tensile tests are mostly performed on strips (Holzapfel, 2006; Pierce *et al.*, 2015; Raghavan *et al.*, 2006) cut out of the

aortic tissue (Figure 2.7), a number of studies preferred dumb-bell shaped specimen (Iliopoulos *et al.*, 2009; Weisbecker *et al.*, 2012).

Additionally, there are no typical sample dimensions for aortic samples, as reviewed in Table 2.1.

Figure 2.7 Uniaxial tensile test performed on a strip cut longitudinally from human abdominal aneurytic tissue (Raghavan *et al.*, 2006).

Shape	Sample dimensions [mm]	Reference
Strip	25 x 5	Kobielarz & Jankowski (2013)
Strip	25 x 7	(Di Martino *et al.*, 2006)
Strip	30 x 5	(Holzapfel, 2006)
Strip	n.a. x 8	(Raghavan *et al.*, 2006)
Strip	20 x 5	(Xiong *et al.*, 2008)
Strip	25 x 25	(Lillie *et al.*, 2010)
Strip	17 x 3	(Maher *et al.*, 2012a)
Strip	15 x 4	(Pierce *et al.*, 2015)
Dumb-bell	approx. 24 x 12.7	(Mohan & Melvin, 1982)
Dumb-bell	35 x 10	(Iliopoulos *et al.*, 2009)
Dumb-bell	37.3 x 8.7	(Weisbecker *et al.*, 2012)

Table 2.1 Review of sample shape and dimensions adopted for uniaxial tensile testing of porcine or human aortic tissue. Dumb-bells dimensions are intended as length and width at the clamping region.

In addition, a few studies applied a mechanical pre-conditioning to aortic samples, but a limited number of them reported the number of cycles performed: 2 cycles (Duprey *et al.*, 2010), 3 cycles (Kobielarz & Jankowski, 2013), 4 or 5 cycles (Mohan & Melvin, 1982) or 10 cycles (Xiong *et al.*, 2008). Similarly to rubber materials, the range of crosshead speed values is wide: 0.017 mm/s (Holzapfel, 2006)(Balzani, 2006), 0.033 mm/s (Kobielarz & Jankowski, 2013), 0.05 mm/s (Xiong *et al.*, 2008), 0.083 mm/s (Pierce *et al.*, 2015) and 0.167 mm/s (Duprey *et al.*, 2010).

The displacement is generally recorded by means of a video-extensometer (Holzapfel, 2006; Kobielarz & Jankowski, 2013; Pierce *et al.*, 2015; Weisbecker *et al.*, 2012). However, when no clear detail is given it is assumed that the crosshead measurement is chosen.

Shape	**Gripping**	**Sample dimensions [mm]**	**Reference**
Square	Hooks	15 x 15	(Matsumoto *et al.*, 2009)
Square	Clips	Not specified	(Zemanek *et al.*, 2009)
Square	Hooks	20 x 20	(Tong *et al.*, 2011)
Square	Hooks	15 x 15	(Schriefl *et al.*, 2012)
Square	Not specified	20 x 20	(Zou & Zhang, 2012)
Square	Not specified	15 x 15	(Zeinali-Davarani *et al.*, 2013)
Square	Hooks	14 x 14	(O'Leary *et al.*, 2014)
Cruciform$*$	Clamps	55 x 55	(Virues Delgadillo, 2010)
Circular	Hooks	30 (diameter)	(Raghavan *et al.*, 2011b)

Table 2.2 Review of sample shape, gripping method and dimensions adopted for biaxial tensile testing of porcine or human aortic tissue. '$*$ ' dimensions include the clamping region.

Biaxial planar tests are usually performed on square shaped samples (Zeinali-Davarani *et al.*, 2013; Zemanek *et al.*, 2009). However, different methods are chosen to grip the

sample, as reviewed in Table 2.2. Clamps are convenient to clamp quickly each side of the sample. However, as detailed in the Appendix, they introduce significant boundary effects due to the sample squeezing. Such squeezing can be limited by choosing clips, which are also easy to manage. The main advantage of hooks consists into avoiding any sample squeezing, hence boundary effects are minimum. In spite of that, it is usually difficult to distribute equally the hooks on each side. However, a convenient and recent solution to this problem is presented in Section 3.2.4.

The experimental setup adopted to test some of the samples reviewed in Table 2.2 are showed in Figure 2.8.

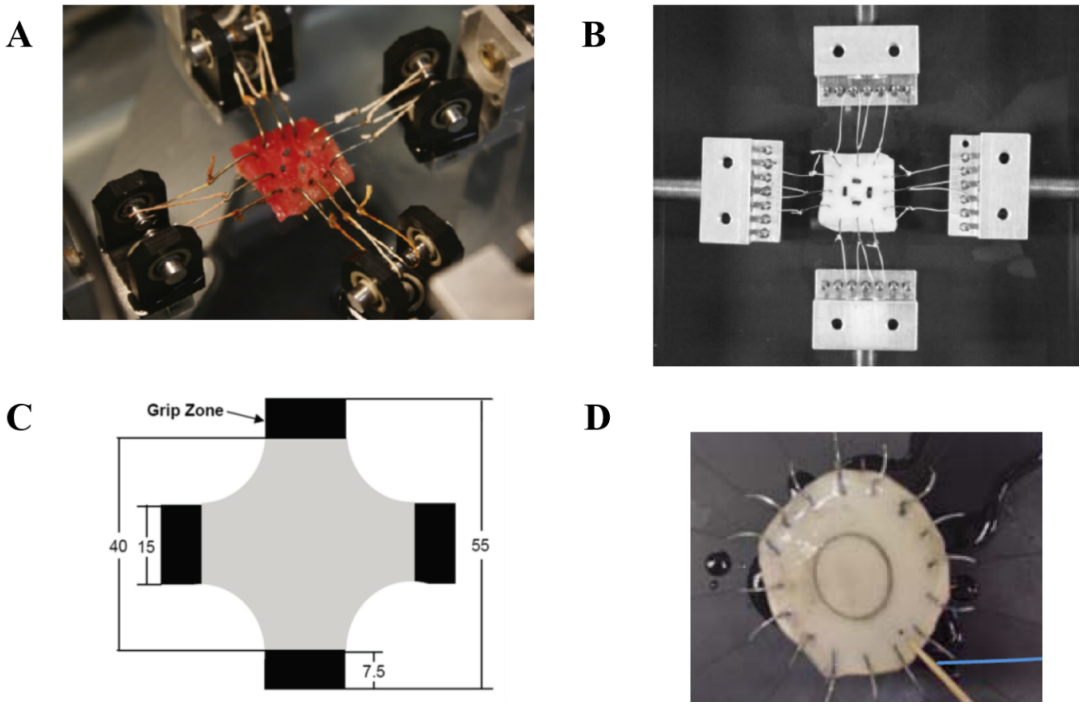

Figure 2.8 Review of experimental setups adopted in literature to investigate the mechanical biaxial behaviour of aorta. A) Square sample gripped by hooks (Tong *et al.*, 2011), B) Square sample gripped by hooks (Schriefl *et al.*, 2012), C) Cruciform sample clamped (Virues Delgadillo, 2010), D) Circular sample gripped by hooks (Raghavan *et al.*, 2011b).

Rarely, details about the pre-conditioning performed before biaxial tests are available in the open literature. As an exception, Zou & Zhang (2012) examined the behaviour of decellularized samples of porcine thoracic aorta by applying 8 cycles of pre-conditioning. The same number of cycles has been chosen by Zeinali-Davarani *et al.* (2013), while

O'Leary *et al.* (2014) performed 10 cycles on smaller specimens. Comparing the mechanical behaviour obtained during the first six cycles, Zemanek *et al.* (2009) concluded that no substantial change related to pre-conditioning occurs in equi-biaxial tests, where no preferential direction of applied force exists. Differently, the effect of pre-conditioning can be spotted for a pronounced alignment of the collagen fibres towards the applied force, achieved by uniaxial tests.

In order to apply selected stress values to stretch the sample, few tensile tests have been carried out in load control (Tong *et al.*, 2011), while other works adopted a displacement controlled protocol (O'Leary *et al.*, 2014; Schriefl *et al.*, 2012; Virues Delgadillo, 2010). Typically, a CCD camera was used to trace the position of the marker dots, placed in the central region, and determine the tissue strains in both directions throughout the biaxial deformation (Matsumoto *et al.*, 2009; Zemanek *et al.*, 2009; Zou & Zhang, 2012). However, other studies preferred the DIC applying a speckle pattern on the sample (O'Leary *et al.*, 2014).

Inflation and indentation Mechanical properties of materials can be collected also by other biaxial tests, such as inflation and indentation.

Inflation tests evaluate mainly the diameter variation in response to the internal pressure applied by a pump. In the investigations focused on arteries, Tyrode's solution (Vychytil *et al.*, 2010) or PBS (Lee *et al.*, 2012; Lillie *et al.*, 2010) was adopted to inflate the vessel. Although this test could be the closest to the actual *in vivo* conditions, no wall stress can be appreciated by only one camera (Lee *et al.*, 2012; Lillie *et al.*, 2010; Vychytil *et al.*, 2010). Differently, two cameras can capture the stress-strain behaviour of the sample (Kim & Baek, 2011). However, several additional details require attention: the chamber where the sample is located, the grips, the pipes carrying the liquid and the pump. Thus, the setup for inflation is definitely more complex compared to other experimental tests.

On the other hand, indentation tests may appear simpler to arrange. However, the shape of the indenter head is not obvious. In the state of the art, cylindrical (Karduna *et al.*, 1997; Sugita & Matsumoto, 2013) or spherical (Cloonan *et al.*, 2012; Cox *et al.*, 2008; Selvadurai & Yu, 2006) indenter heads have been adopted. Although different sizes of indenter heads have been compared (Cox *et al.*, 2008), it seems not clear which should be the ratio between the head and the sample dimension. Furthermore, it is expected that the indenter will induce the highest stress levels in the central part of the sample. Hence, the region of interest is restricted and influenced by the indenter head.
Therefore, planar biaxial tensile tests have been preferred.

Thickness measurement It is worth reviewing another aspect of experimental campaigns that highlights, once again, the lack of a standard protocol. Thickness measurement of soft tissues is notoriously difficult, since they can be easily squeezed, and affects the calculation of engineering stress, as it is adopted to estimate the undeformed cross-sectional area of the sample. Hence, the stress-strain curve, describing the tissue mechanical behaviour, can be severely affected. In addition, sophisticated numerical models often rely on mechanical responses obtained from experimental tests. Therefore, experimental data that will be imported in the model need to be acquired more rigorously.
Throughout experimental testing, force values are objectively measured by the load cell, while the evaluation of sample thickness is arbitrary with no universal methodology adopted. Typically, the thickness is assumed constant for all samples tested (Choudhury *et al.*, 2009) and rarely it is estimated for each specimen (Pierce *et al.*, 2015; Sokolis *et al.*, 2002). As a standard protocol is still missing, even some of the most recent studies do not specify the methodology adopted to evaluate the specimen thickness (Bailly *et al.*, 2014, 2012; Vahapoglu *et al.*, 2011). Currently, a variety of experimental methods are available to measure the thickness: laser micrometer (Di Martino *et al.*, 2006; Iliopoulos *et al.*, 2009; Sokolis *et al.*, 2002), video-extensometer (Holzapfel *et al.*,

2005; Weisbecker *et al.*, 2012), constant force thickness indicator (Choudhury *et al.*, 2009), digital calliper (Fitzpatrick *et al.*, 2010; Raghavan *et al.*, 2011a; Stemper *et al.*, 2007) or dial gauge (Sugita & Matsumoto, 2013). Similarly, no agreement has been reached to date about the reference configuration that should be used to measure the sample thickness, as they can be totally unloaded (Vande Geest *et al.*, 2006), loaded into grips (Raghavan *et al.*, 2011a) or sandwiched between metal plates (Sugita & Matsumoto, 2013) when the measurement is conducted.

Recently, Shang *et al.* (2015) emphasized that no universal measuring technique has been established for tissue specimens.

2.3.3 Storage of biological tissue

The tissue preservation for short periods is commonly achieved by means of temporary cold storage. However, in order to collect the most realistic experimental data, a refrigeration or freezing process has to be selected.

Stemper *et al.* (2007) investigated the effect of the storing process on tissue mechanical properties. Their results highlighted that sub failure stress, ultimate stress, and Young's modulus were decreased in refrigerated compared to fresh and frozen specimens of porcine descending aortas. Furthermore, no significant change in elastic modulus or sub failure and rupture stress and strain after freezing at $-20°C$ and $-80°C$ for 3 months.

Similarly, Virues Delgadillo (2010) concluded that the mechanical properties of porcine aortas were not significantly altered after preserving the tissues for two months in Krebs solution with dimethyl sulfoxide (DMSO) (at $-20°C$ or at $-80°C$) or in isotonic saline solution at $-20°C$.

Chow & Zhang (2011) observed that $4°C$ refrigeration led to a decreased initial slope and an increased stiff slope after 48 hours of storage. Conversely, the $-20°C$ and $-80°C$ storage conditions did not show changes in the initial slope. Therefore, with the purpose of limiting possible biochemical and microstructural changes in the artery due

to storage, they recommended freezing protocols ($-20°C$ or $-80°C$) over refrigeration ($4°C$).

Recently, O'Leary *et al.* (2014) concluded that despite minor changes of the tissue weight, no significant difference in biaxial mechanical properties can be observed before and after freezing at $-20°C$. Furthermore, no substantial difference has been noticed in relation to the storage time, as samples stored for up to one year were compared.

2.4 Finite Element Method

The behaviour of a generic system depends upon the geometry or domain of the system, the properties of the material, and the boundary, initial and loading conditions. The solution of complex systems is quite difficult to solve via analytical means. Therefore, most of the problems are nowadays solved using numerical methods. Among these, the methods of domain discretization championed by the Finite Element Method (FEM) is the most popular, due to its practicality and versatility.

The FEM is a numerical method seeking an approximated solution of the distribution of field variables in the problem domain that is difficult to obtain analytically. It is done by dividing the problem domain into several elements. Known physical laws are then applied to each small element, each of which usually has a very simple geometry.

2.4.1 Principles of the method

The classical displacement-based finite element formulation is well established in many commercial finite element codes. The results provided are generally accurate. An exception occurs for problems involving an incompressible hyper-elastic material. Let's consider a tridimensional body, consisting of an isotropic material and described by Young's modulus E and Poisson's ratio ν. The pressure (p) in the body is equivalent to

the negative average stress, defined as:

$$p = -\sigma_{av} = -\frac{1}{3}(\sigma_{xx} + \sigma_{yy} + \sigma_{zz}) \tag{2.31}$$

where σ_{xx}, σ_{yy} and σ_{zz} are the normal stresses. Equation 2.31 can be expressed as a function of volumetric strains as follows:

$$p = -\frac{E}{3(1-2\nu)}\varepsilon_V = -\kappa\varepsilon_V \tag{2.32}$$

where κ is the bulk modulus and ε_V is the volumetric strain. The volumetric strain is namely the ratio between the deformed volume and the original one. Therefore, ε_V is equivalent to the sum of principal strains ε_{xx}, ε_{yy} and ε_{zz}. When Poisson's ratio approaches 0.5, which happens for nearly incompressible materials, the bulk modulus κ tends to infinite and the volumetric strain to zero. Hence, a very fine finite element discretization is required to obtain good solution accuracy. However, it has been noticed that when $\nu = 0.499$ the stress prediction becomes very inaccurate even for fine mesh. In this case a mixed finite element formulation is required to avoid volumetric locking problems. In the analysis of almost incompressible behaviour, a formulation that *locks* leads to underestimated displacements, which affect the derived value of strains and, consequently, predicts very inaccurate stress values. Therefore, a decomposition of the stress tensor into a volumetric and a deviatoric component is performed to avoid the volumetric locking effect. Such decomposition was firstly introduced by Herrmann (Herrmann, 1965). Successively, an *hybrid* formulation was defined by interpolating displacements (u) and pressure (p) (Sussman & Bathe, 1987).

The basic problem in a general nonlinear analysis is to find the equilibrium state of a body corresponding to the externally applied loads (R) in the current deformed geometry. The principle of virtual work states that the external loads, applied to deform a body, are in equilibrium with the stresses developed within the material as an internal reaction.

The integral weak form of this principle constitutes the fundament of the finite element method.

A materially-nonlinear-only formulation, based on engineering stress and strain, is more effective for small displacements and strains. On the other hand, large displacements are typically modelled by means of a total Lagrangian formulation, which takes into account second Piola Kirchoff stress (S) and Green Lagrange strain (E). Furthermore the Lagrangian approach follows all particles of the body in their motion, hence it appears an effective analysis of solids and structures (Bathe, 1996).

Since hyper-elastic materials can be described by means of an incremental potential, the principal of virtual work is

$$R = \int S_{ij} \delta E_{ij} \, \mathrm{d}V \tag{2.33}$$

meaning that the variation of the integrated internal stress potential (S) must equal the variation of the external loading (R) potential (Sussman & Bathe, 1987). Therefore, the principle of virtual work expressed by the *u/p formulation* in total Lagrangian formulation assumes the form:

$$\begin{bmatrix} {}^{t+\Delta t}R \\ 0 \end{bmatrix} - \begin{bmatrix} {}^{t}_{0}F_u \\ {}^{t}_{0}F_p \end{bmatrix} = \begin{bmatrix} {}^{t}_{0}K_{uu} & {}^{t}_{0}K_{up} \\ {}^{t}_{0}K_{pu} & {}^{t}_{0}K_{pp} \end{bmatrix} \begin{bmatrix} U \\ P \end{bmatrix} \tag{2.34}$$

where R is the vector of load externally applied, F is the vector of equivalent nodal forces and K is the stiffness matrix (Bucchi & Hearn, 2013a). The stiffness matrix represents the finite element expression of the internal work, meaning geometric and material conditions at a discrete time, and is denoted as

$$K_{uu} = \int B^T C B \, \mathrm{d}V \tag{2.35}$$

B is often called strain matrix and C is a matrix of material constants. Normally, the strain for an element is calculated by taking the derivative of the displacement field, calculated by means of the shape functions N and nodal values of displacement $\varepsilon = Bu_i$. In order to prevent volumetric locking, a split in deviatoric and dilatational parts of the problem is needed. In formulating the u/p approach, the sub-matrix K_{uu} represents the deviatoric component, K_{up} the volumetric component, K_{pu} and K_{pp} arise from the weak form of equation 2.33. Furthermore K_{pp} is identically zero if the material is totally incompressible (Bucchi & Hearn, 2013a). This formulation can be extended to rubber-like materials, which exhibit nonlinear behaviour, by means of an incremental approach. An updated Lagrangian formulation determines the actual stresses (second Piola-Kirchhoff tensor **S**) and strains (Green-Lagrange tensor **E**) from the previous artificial step (Bathe *et al.*, 1975; Sussman & Bathe, 1987). Hence, the sub-matrix K_{uu} may in general be split into a linear K^L_{uu} and non-linear K^{NL}_{uu} contribution. K^L_{uu} is dependent upon the fourth-order constitutive elastic tensor C_{ijhk} and K^{NL}_{uu} is a function of the second Piola-Kirchhoff stress tensor **S**. In the u/p formulation the displacement and the pressure are approximated with a summation over an appropriate shape function H_i, as follows:

$$\begin{aligned} u &= \sum_{i=1}^{N} H_i^u u_i \\ p &= \sum_{i=1}^{N} H_i^p p_i \end{aligned} \tag{2.36}$$

where N represents the number of nodes defining each element used in the discretisation process, u_i and p_i represent the nodal value of displacement and pressure respectively. For a reliable analysis the polynomial shape functions H_i should satisfy the Ladyzhenskaya–Babuska– Brezzi (LBB) condition (Bathe, 2001). This condition requires the pressure shape function must be of a lower order than the displacement shape function. Consequently, unphysical oscillations, called *checkerboard* modes, that arise from

incompressibility may be avoided, for example, by means of a Taylor-Hood (Taylor & Hood, 1973) elements (Figure 2.9). An exhaustive list of elements satisfying the LBB condition is reported in Bathe's book (Bathe, 1996).

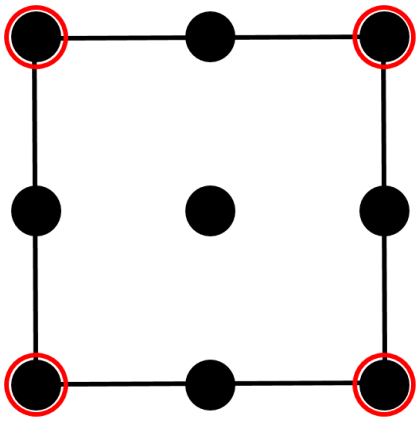

Figure 2.9 Quadrilateral Taylor-Hood discretization: velocity is evaluated in the filled black nodes, pressure in the red circled ones.

Another way to prevent volumetric locking is the adoption of either the *reduced* or *selective* integration: the integration scheme adopted is one order less accurate than the standard scheme. In particular, the *selective* approach applies full and *reduced* integration simultaneously, having decomposed the constitutive tensor in two parts. As an example, Abaqus C3D8 element implements such selective integration. Thus, the eight Gauss points usually needed for a linear brick are *reduced* to a single point. However, the reduced integration can cause unwanted behaviour of the element. This methodology reduces the rank of the total stiffness matrix, hence, this matrix can become singular. Therefore, modes that produce displacements, but require no forces can be observed. A spurious mode can be defined when a structure deforms without causing any stress in the material. This phenomenon is usually called *hour glassing* due to the typical shape of the deformed mesh resembling an hour-glass. As an example, *hour glass control* is included in Abaqus shell element S4R. A shell is defined as a solid medium geometrically defined by a midsurface immersed in the physical space and a parameter representing the thickness of the medium around this surface. When

the physical problem involves a solid thin in one direction, shell elements are usually adopted, being called *degenerated solid elements*. In other words, in shell analysis a modelling error in the transverse direction is accepted for a kinematic assumption in the same direction (Chapelle & Bathe, 2011).

Whether refined meshes of reduced-integration elements still show volumetric locking problems, the introduction of *hybrid* elements is recommended.

Generally, the choice of the element type depends on the specific problem to be investigated. However, as reviewed in Section 2.4.2, multiple implementations are available for analogous studies. Furthermore, as detailed in Section 6.2, challenging analyses may require alteration of boundary conditions or element type.

2.4.2 Application to aneurysm

Several finite element analysis have been carried out in order to predict stress distributions in abdominal aortic aneurysm (Isaksen *et al.*, 2008; Ma *et al.*, 2007) and evaluate its rupture potential (Doyle *et al.*, 2009a; Giannoglou *et al.*, 2006; Raghavan & Vorp, 2000).

Besides a limited number of studies treated the arterial wall as a linear elastic material (Giannoglou *et al.*, 2006; Torii *et al.*, 2006), the majority of finite element studies assumed the tissue to exhibit a nonlinear behaviour (Isaksen *et al.*, 2008; Rodríguez & Merodio, 2011; Scotti *et al.*, 2008).

In order to evaluate the differences associated with finite element modelling of abdominal aortic aneurysms, Doyle et al. (Doyle *et al.*, 2007) compared a linearly elastic model to nonlinear models. As a result, the most accurate stress distributions were obtained implementing nonlinear material properties. The arterial wall has been mostly modelled as isotropic (Delfino *et al.*, 1997; Gasser *et al.*, 2010; Giannakoulas *et al.*, 2005; Giannoglou *et al.*, 2006; Isaksen *et al.*, 2008; Raghavan & Vorp, 2000; Scotti *et al.*, 2008; Shang *et al.*, 2015; Wang *et al.*, 2002; Wang & Li, 2011).

Among the anisotropic formulations, even if the HGO model is often preferred (Alhayani *et al.*, 2013; Badel *et al.*, 2011; Holzapfel *et al.*, 2004; Rodríguez & Merodio, 2011; Rodríguez *et al.*, 2008), the Fung-type strain-energy function appears to be recently adopted to model the arterial wall (Avril *et al.*, 2010; Lee *et al.*, 2014; Ma *et al.*, 2007; Sun *et al.*, 2005). Recently, Ramachandran et al. (Ramachandran *et al.*, 2012) discussed the most appropriate material modelling choices to estimate the wall tension distribution, comparing Laplace law, Fung-type and isotropic polynomial strain-energy function. When the geometry is the only patient-specific information available, it has been concluded that the modelling choices have minimal impact on aneurysms wall tension evaluation (Ramachandran *et al.*, 2012).

In the state of the art, arterial walls are generally modelled by means of shell elements (Giannoglou *et al.*, 2006), assuming the tissue to be homogeneous, or by 3D elements (Alhayani *et al.*, 2013, 2014; Badel *et al.*, 2011; Lee *et al.*, 2014). In finite element analyses of realistic abdominal aortic aneurysms, Doyle *et al.* (2007) pointed out that the predictions carried out adopting 3D elements, i.e. cubic bricks, are more accurate compared to shell elements.

However, finite elements simulations rarely focus on the understanding of how aneurysm is instigated in arteries. As an example, Badel *et al.* (2011) simulated the inflation of a mouse carotid artery, modelled as a perfect cylinder, but no aneurysm was initiated. Historically, the topic of aneurysm formation has been addressed as a buckling problem from the macroscopic point of view. Han (2007) concluded that arteries may buckle and become tortuous due to high internal pressure even when the axial stretch ratio is below a certain value. The critical buckling pressure is proportional to the axial stretch ratio and wall stiffness. However, the arterial wall was modelled as thin and linear elastic. Fu *et al.* (2012) demonstrated that the aneurysm formation can be modelled as a bifurcation phenomenon induced by geometrical and material imperfections. The

initiation pressure is defined by two main features. First, the uniform inflation solution ceases to be stable as soon as the pressure reaches such value. Second, the near-critical bifurcated deformation is a bulge, of precisely the same form as observed experimentally (Fu *et al.*, 2008).

Lately, Lee *et al.* (2014) investigated the mechanical buckling and post-buckling behaviour of arteries in order to identify the interrelationship between artery buckling and aneurysms. A small initial bend of 1 degree along the central axis of the arteries was created as an imperfection to facilitate the buckling analysis. As a results of this study, buckling changes the shape and curvature of the aneurysmal wall surface which can lead to higher peak axial wall stresses and thus increase the risk of aneurysm rupture. The lateral deflection of arteries increased nonlinearly with increasing lumen pressure post-buckling. Further studies focused on the buckling mechanism being responsible for vessel tortuosity. Badel et al. (Badel *et al.*, 2013) showed that the tortuosity of veins is increased when their axial pre-stretch decreases and when their behaviour becomes more anisotropic. Alhayani et al. (Alhayani *et al.*, 2013) adopted the modified Riks method to instigate the bulge formation in isotropic, using Neo-Hookean strain-energy function, and anisotropic, using Holzapfel-type strain-energy function, arterial models. The coupling effect of fictious fibre orientation and elastic constants values trigger the aneurysm formation.

2.4.3 Riks method

The initiation of aneurysm concerns the stability of such hyper-elastic structure, as it is generally observed in rubber-like materials. Since the material parameters change along with the deformation, a nonlinear finite element analysis of the problem becomes necessary.

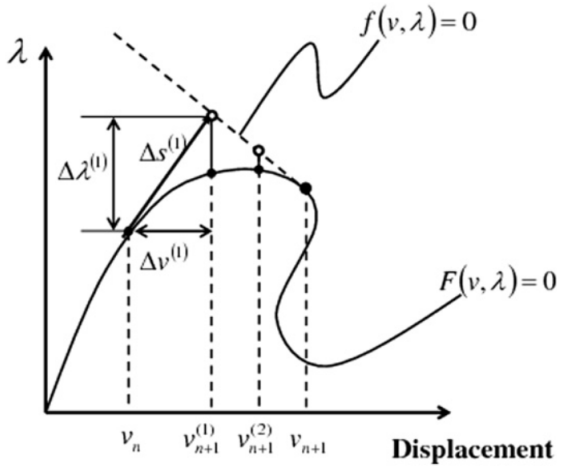

Figure 2.10 Typical unstable static response that shows a negative stiffness (Bucchi & Hearn, 2013a). The loading factor is indicated as λ, the arc length as s

In general non-linear static problems may be solved using the classical Newton–Raphson method. However, such problems sometimes involve buckling or collapse behaviour, where the load-displacement response shows a negative stiffness and the structure must release strain energy to remain in equilibrium (Figure 2.10).

Unfortunately the application of Newton–Raphson to this response is unsuitable. Following the load increase, the positive stiffness reduces, becoming zero in correspondence of the critical pressure. Beyond this crucial value, the structural stiffness is negative and further deformation is achieved with lower loads, inhibiting the Newton–Raphson approach.

Consequently, a different analysis needs to be carried out. A perturbation of the base state is performed to find nontrivial incremental displacement fields with arbitrary magnitudes as valid solutions to the problem. Such nontrivial incremental displacement fields are referred to as buckling modes. No distinction between geometry of the base state and the linearly perturbed configurations is made. In addition, the changes in surface traction and body forces during buckling are completely characterized by the change of the deformation gradient for any material point. Thus, the change in the applied tractions and body force intensities arises due to the change in geometry, while the magnitude of the applied forces is kept fixed. As an example, for a pressure load the

magnitude of the pressure remains constant but the surface normal changes as an effect of the deformation gradient. This algorithm is applicable when load magnitudes are governed by a single scalar parameter. The simulation starts applying a small trial force to determine the initial equilibrium state, known the initial undeformed configuration and solution. Successively, an increment of the force, which is treated as an unknown, is added to the previous value and solved simultaneously with deformation for the next equilibrium state along the path using iterative method (Zhao, 2008). The solution is obtained with a prediction stage and a correction stage. In the prediction stage a guess of the new equilibrium position is created and subsequently corrected using Newton–Raphson iterations until the new equilibrium position is reached. The load parameter is computed from the constraint condition: the error associated is reduced by forcing the solution to move along a particular curve (or straight line path).
Historically, different constraint conditions, showed in Figure 2.11, have been applied to solve such problem: load control, displacement control and arc length method.

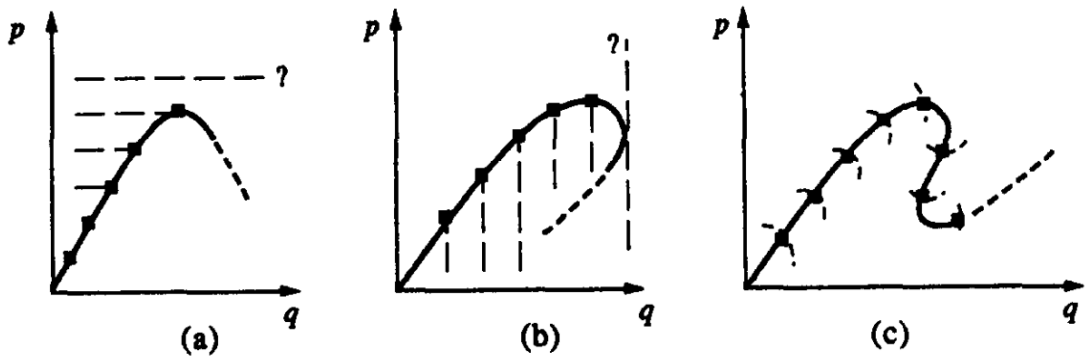

Figure 2.11 Geometrical representation of the three available methods to solve nonlinear load (p) vs displacement (q) response: a) load control, b) displacement control, c) arc length (Carrera, 1994).

The Riks method (Riks, 1979) allows development of the equilibrium path up to and beyond the limit point represented by the critical pressure using arc length control is a combination of pure load control and pure displacement control (Bucchi & Hearn, 2013a). Crisfield (Crisfield, 1981) introduced a sphere as nonlinear constraint around the last converged step. However such a sphere intersects the solution path in most cases

in two different points. Hence the solution has to be chosen (Wriggers, 2010). Therefore, a linearized version of the constraint equation has been proposed, consistent with the equilibrium equation, to be applied whenever the roots became complex (Schweizerhof & Wriggers, 1986).

A path following method such as the Riks algorithm is necessary to investigate the behaviour of a cylindrical hyper-elastic membrane subject to inflation. The solution path consists in a set of equilibrium points in the load-displacement space (Figure 2.10). Supposing a solution has been found at v_n, the increment size Δs along a path length is initially suggested by the user and adjusted by Abaqus automatic load incrementation algorithm (Dassault Systèmes, 2014). Hence, the equilibrium is checked as follows

$$R^i = (\lambda_0 + \Delta\lambda^i)P^i - I^i \tag{2.37}$$

where R represents the residuals, P the loading pattern and I the internal force generated by the stress. Whether the increment $i = 1$ has not converged, the solution moves along an orthogonal path, designated as $f(v, \lambda)$ (Dassault Systèmes, 2014). In addition, the load increment is scaled of a ρ factor

$$\rho^i = \frac{R^i P}{P^\star} \tag{2.38}$$

where $P^\star = \sqrt{P^N P^N}$, N being the degrees of freedom of the model. In order to cause the equilibrium search to be orthogonal to the last tangent, an additional update is implemented after each iteration

$$v^0 = v^i. \tag{2.39}$$

The modified Riks method is implemented in Abaqus and provides a load proportional factor (LPF), intended as a multiplier of the initial load applied. Beneath the maximum

LPF, the model is deforming under static equilibrium. The peak, instead, deals with the structural instability.

Chapter 3

Experimental Methodology

The current chapter introduces the materials adopted for experimental investigations in Section 3.1. In the following Section 3.2, the details of the testing protocols performed to characterise the mechanical behaviour of such materials are described. In order to assess the most reliable approach, a preliminary comparison between the measuring techniques, listed in Chapter 2, is reported. Subsequently, the collection of a complete and reliable data set is achieved by means of uniaxial and biaxial tensile tests. The flowchart shown in Figure 3.1 summarizes the sample preparation process, which will be detailed in the following sections.

Raw data are generally affected by noise, which can be limited but never fully suppressed. Thus, such data needs to be filtered. In addition, software for finite element analysis typically struggle to manage non-monotonic material behaviour. Therefore, the post-processing stage is described in Section 3.3.

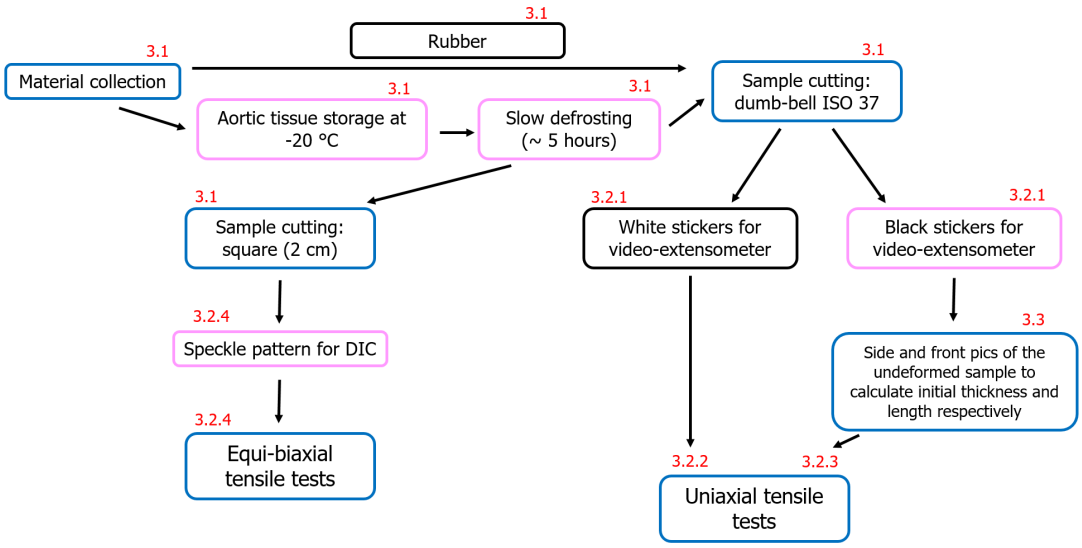

Figure 3.1 Preparation of rubber (black boxes) and aortic (pink boxes) samples. Red numbers indicate the Section in which each stage is detailed.

3.1 Materials

The present investigation considered the use of two different materials to be tested. Aiming to setup a robust experimental protocol and to test it on a generic hyper-elastic material, rubber has been adopted. As major advantages of this material, the sample preparation is simplified and the storage stage is neglected. Once the method has been detailed and verified, experimental tests have been carried out on aortic tissue.

A carbon filled rubber produced by Avon Rubber was available to execute the designed experimental protocol and to investigate the geometry effects on tensile responses. Therefore, samples shaped as strips and dumb-bells have been compared. In the state of the art, details concerning the methodology adopted to cut samples out of the harvested tissue are limited (Balzani, 2006). As the current experimental protocol is designed for aortic tissue, small specimens are required. The smallest standard available is described in Figure 3.2, being the dumb-bell type 4 of the International Standard (ISO 37, 2005).

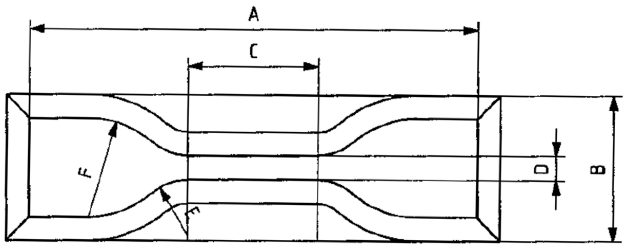

Reference	Dimension [mm]
A	35
B	6 ± 0.5
C	12 ± 0.5
D	2 ± 0.1
E	3 ± 0.1
F	3 ± 0.1

Figure 3.2 Standard cutter for preparation of dumb-bells (ISO 37, 2005).

Strip dimensions of 35 mm x 2 mm are analogous to the narrow part of the dumb-bell. In order to limit the variability introduced by a hand cutting process, a custom made die (Gibitre Instruments, Italy) has been used to cut standard dog-bone shaped specimens. Furthermore, this cutter has been adapted to be mounted on ESH servo-hydraulic testing machine to insure a faster and more accurate preparation process. Alternatively, strips have been hand–cut by means of a wet scalpel. It is worth notice that manual preparation of samples is currently encountered in literature (Fitzpatrick *et al.*, 2010). However, an additional step of calibre measurements was needed to carefully select the samples. Strips exceeding a tolerance of 1% in length and 10% in width have been discarded. The rubber thickness has been evaluated by means of microscopy measurements. As a result, the thickness, calculated as the average of 10 random samples, is assumed to be uniform and equal to 1.9 ± 0.4 mm.

In spite of its practical advantages, such rubber material cannot replicate the exact mechanical response of aortic tissue, being the main focus of the present study. However, the University of Portsmouth has no licence to store and test human tissue, since strict safety requirements need to be satisfied in the laboratories. In literature, porcine aortas are commonly preferred for the mechanical characterisation of arterial tissue (Lally *et al.*, 2004; Pandit *et al.*, 2005). This approach has been justified by the existing similarities between the human and porcine cardiovascular systems (Crick *et al.*, 1998;

Wolinsky & Glagov, 1969). Furthermore, porcine models are frequently used in the pre-clinical evaluation of medical devices (Maher *et al.*, 2012b).

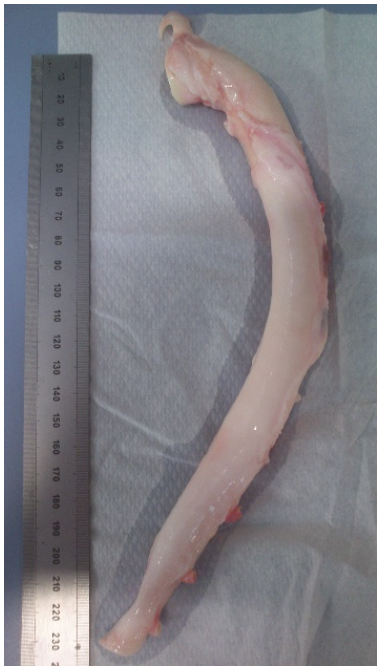

Figure 3.3 Porcine aorta previously stored in 0.9% saline solution at $-20°C$, slowly defrosted in the day of testing.

Therefore, porcine aortic tissue has been adopted in this study. In order to avoid substantial biochemical and microstructural changes, aortas have been harvested from Laverstoke park farm (Overton, UK) about one hour after the sacrifice and stored in 0.9% saline solution at $-20°C$ within 4 hours (Chow & Zhang, 2011; Stemper *et al.*, 2007). Successively, a slow defrosting procedure of about 5 hours has been carried out immediately prior to experimental testing procedures: samples have been placed firstly in the fridge and then exposed to room temperature.

As this study focus on the thoracic and abdominal tract of the descending aorta, the ascending aorta and the aortic arch have been cut away as shown in (Fig. 3.3). Hence, each aorta has been longitudinally cut along the posterior part, which was previously in contact with the vertebral column. Finally, aortic dog-bone shapes specimens have been cut by means of the die cutter, as showed in Figure 3.4.

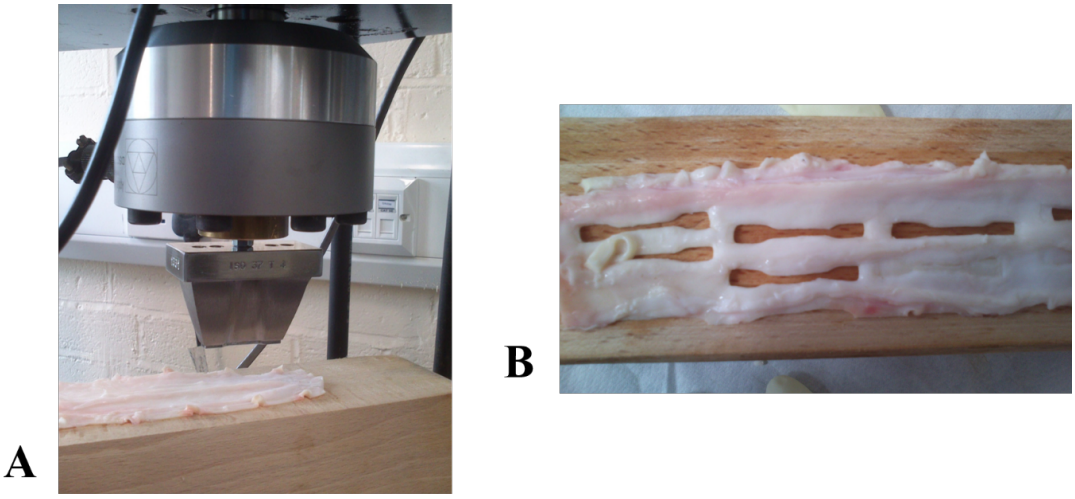

Figure 3.4 Preparation of aortic dog-bone samples. A) Dumb-bell cutter mounted on ESH servo-hydraulic testing machine. B) Longitudinal samples cut from abdominal aorta.

Longitudinal and circumferential samples have been cut out of thoracic aortas, while only longitudinal specimens are prepared from the abdominal segments, due to its reduced diameter. As consistent variations are observed along the aortic tree (Tanaka & Fung, 1974), the thickness has been estimated for each sample by means of the method described in Section 3.3.

Such sample preparation protocol has been applied also to specimens designed for biaxial tensile tests. As previously reviewed in Section 2.3.2, the majority of biaxial tests reported in literature were conducted on square specimens, clamped in different ways. Each square specimen (20 mm x 20 mm) has been cut by means of a steel guide die placed in a manual press (Figure 3.5).

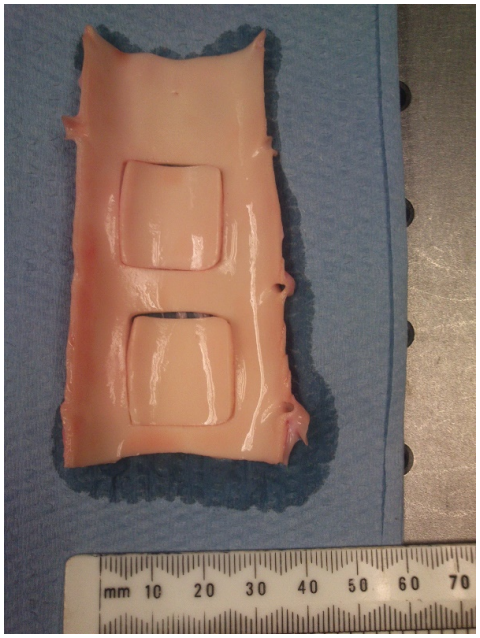

Figure 3.5 Preparation of aortic samples (20 mm x 20 mm) for biaxial tensile tests. Specimens are aligned to the circumferential and longitudinal direction.

3.2 Experimental tests

The following two sub-sections report the analysis of measuring techniques (Section 3.2.1) and the experimental tests conducted on rubber (Section 3.2.2) in order to consolidate the experimental protocol designed for biological materials. Last two sub-sections describe the experimental protocols applied to perform the uniaxial (Section 3.2.3) and biaxial tensile tests (Section 3.2.4) on aortic tissue.

3.2.1 Comparison between experimental techniques

A preliminary step in the mechanical characterisation of a generic hyper-elastic material consists of selecting a reliable technique to measure the sample strain. Therefore, the comparison of the measuring techniques previously described in Section 2.3.1 has been accounted as a fundamental step to design a robust standard protocol. Hence, the displacement achieved during uniaxial tensile tests has been simultaneously recorded by the machine cross-head, a video-extensometer and the DIC. This analysis has been

carried out for both rubber and aortic samples.

As explained in Section 2.3.1, the video-extensometer requires stickers to be applied on samples surface, thus the displacement between them is measured. Aiming to enhance the contrast, white stickers have been applied on black rubber specimens (Figure 3.6 A) placed in front of a black background (Figure 3.10). Conversely, black stickers have been applied on aortic sample (Figure 3.6 B) placed in front of a pale background.

Analogous attention has been given to DIC requirements. A speckle pattern of white opaque paint has been applied by means of an airbrush on the surface of rubber samples (Figure 3.6 A). On the other hand, black opaque paint has been applied on the aortic specimens (Fig. 3.6 B).

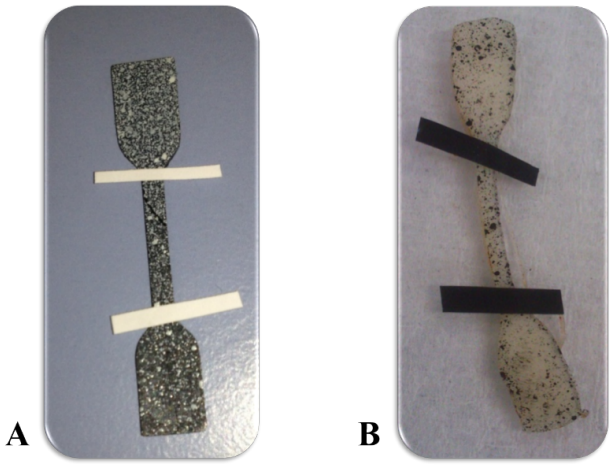

Figure 3.6 Undeformed dumb-bell samples. Stickers are required by the video-extensometer, while the speckle pattern is needed for DIC. A) Rubber specimen with white stickers and speckles. B) Aortic specimen black white stickers and speckles.

For each material, five samples have been tested by means of an MTS Landmark (MTS Systems Corporation, USA) equipped with a 2.5 kN load cell. Each sample has been gripped by Bose clamps Assy 3200 (Bose Corporation, USA) adapted for the MTS machine. The elongation speed was set at 0.1 mm/s (Cox *et al.*, 2008; Jerabek *et al.*, 2010; Sasso *et al.*, 2009). Through the test, the displacement has been measured by a Messphysik video-extensometer with a field of view ranging from 50 mm to 0.4 μm (Messphysik Materials Testing GMBH, Austria). The recording has been activated

before any movement of the crosshead and stopped manually after the end of the test. Furthermore, ten pictures have been taken during the test in order to be post-processed by Aramis software (GOM mbH, Braunschweig, Germany) for DIC. In order to avoid any kind of relaxation and ensure a good quality image for DIC, the cross-head has been stopped during the test for no more than 10 seconds each time and every 2 mm of displacement.
Strain values have been calculated on the same initial length for the video-extensometer and the machine cross-head. Post-processing of DIC produces strain fields from which the value in the middle of the region of interest has been extracted.

Thus, results obtained for rubber samples are reported in Figure 3.7. It can be seen that the video-extensometer (green triangle) is consistently estimating the minimum strain compared to the other techniques. Differently, DIC post-processing (red square) produces strain fields from which the strain value in the middle of the region of interest appear average or closer to the cross-head results.

Similarly, aortic results are shown in Figure 3.8. Differently from rubber outcomes, a wider difference between the strain obtained from the video-extensometer (green triangle) and the cross-head (blue rhombus) can be appreciated. Furthermore, DIC results (red square) appear closer to video-extensometer ones.

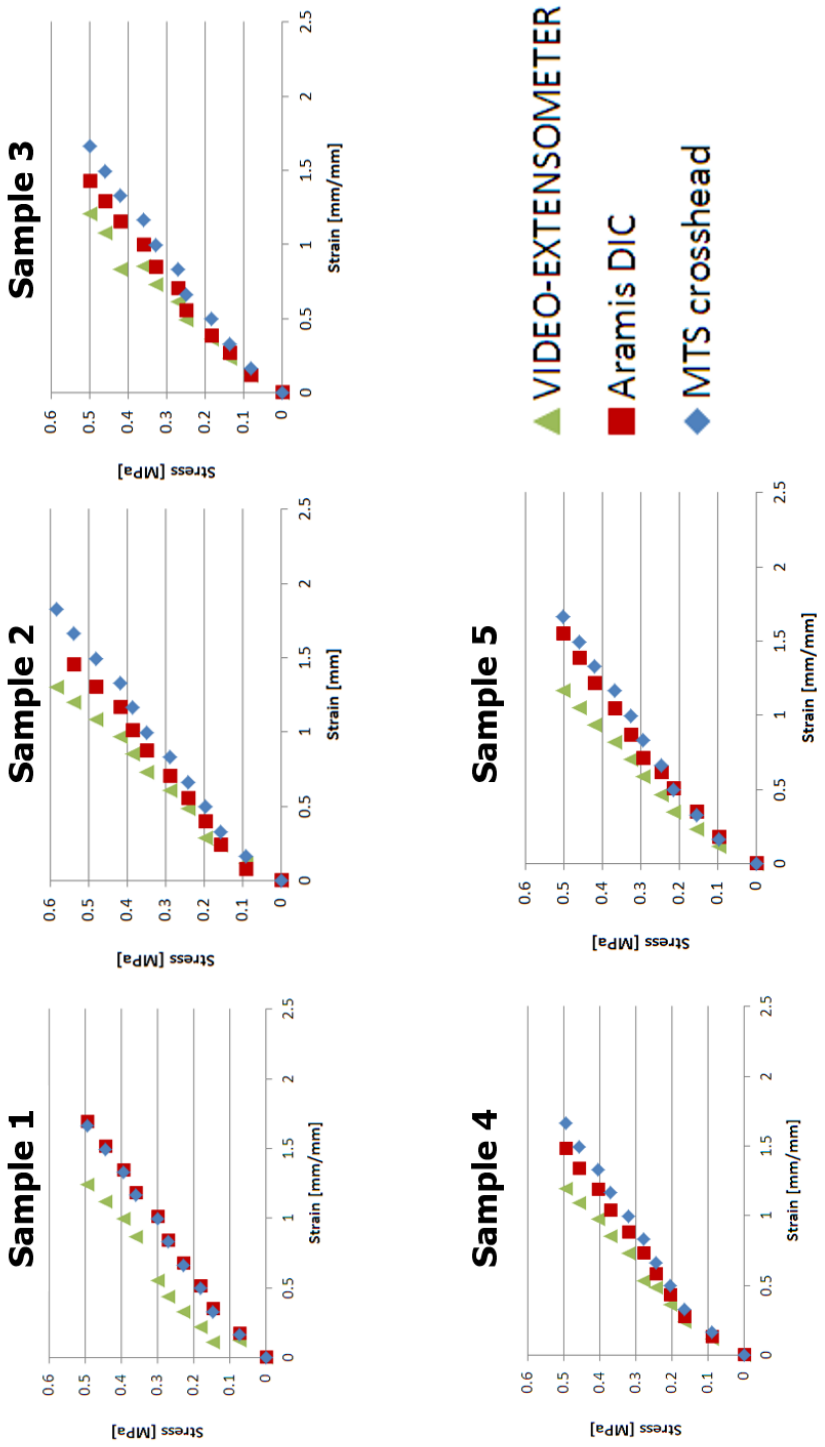

Figure 3.7 Stress-strain plot compare the use of three measuring techniques on five rubber samples: the video-extensometer (green triangle), the DIC (red square) and the testing machine (blue rhombus).

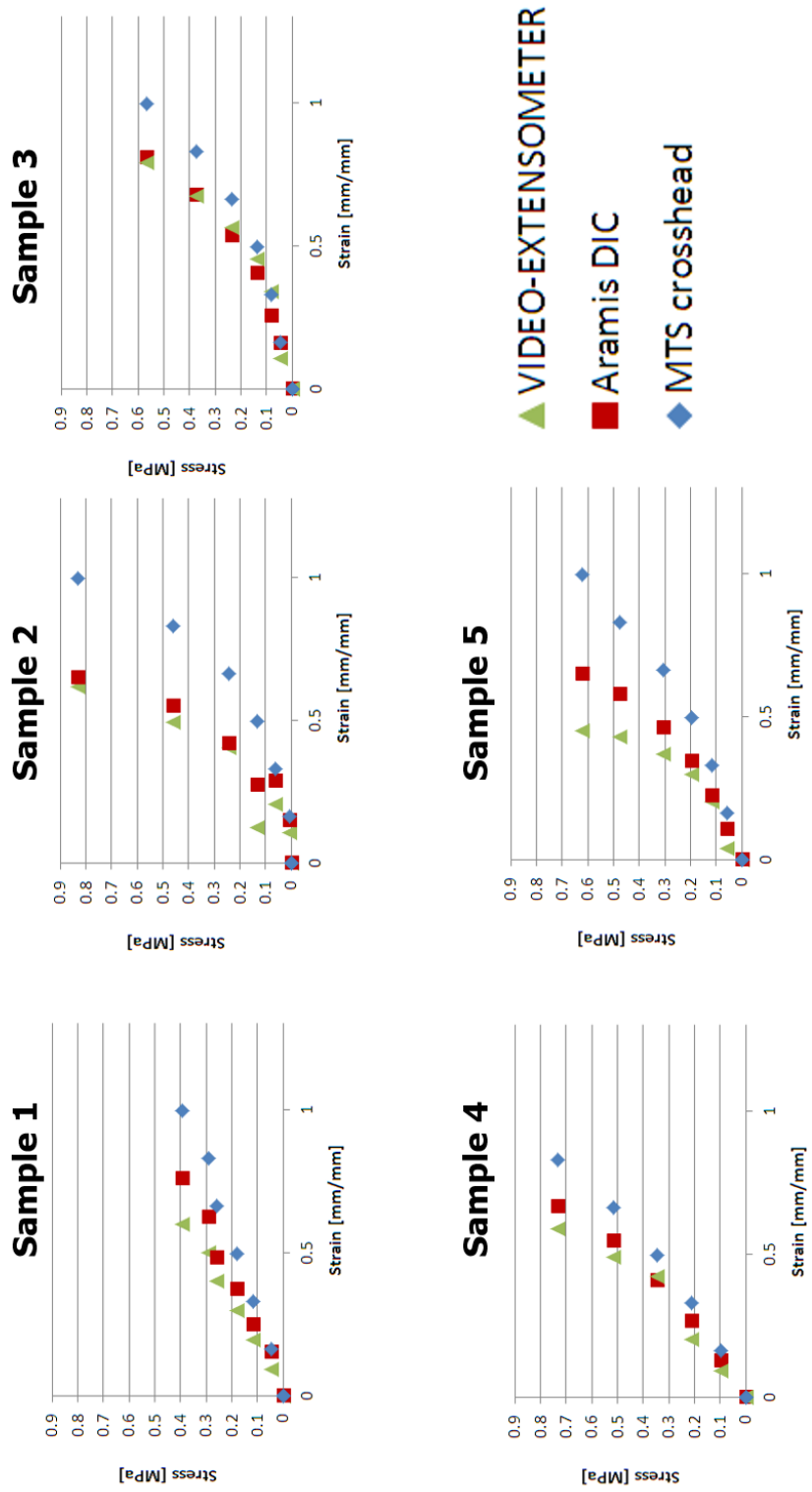

Figure 3.8 Stress-strain plot compare the use of three measuring techniques on five aortic samples: the video-extensometer (green triangle), the DIC (red square) and the testing machine (blue rhombus).

Analogous results were obtained by Krehbiel & Berfield (Krehbiel & Berfield) by comparing DIC to cross-head results for pig back skin.

The scatter appreciated between the measuring techniques can be explained observing that during such tests the video-extensometer and the DIC are focused on the same region of interest (ROI). On the other hand, since the initial length and the cross-sectional area between the grips do not correspond exactly to the same ROI, the difference appears consistent.

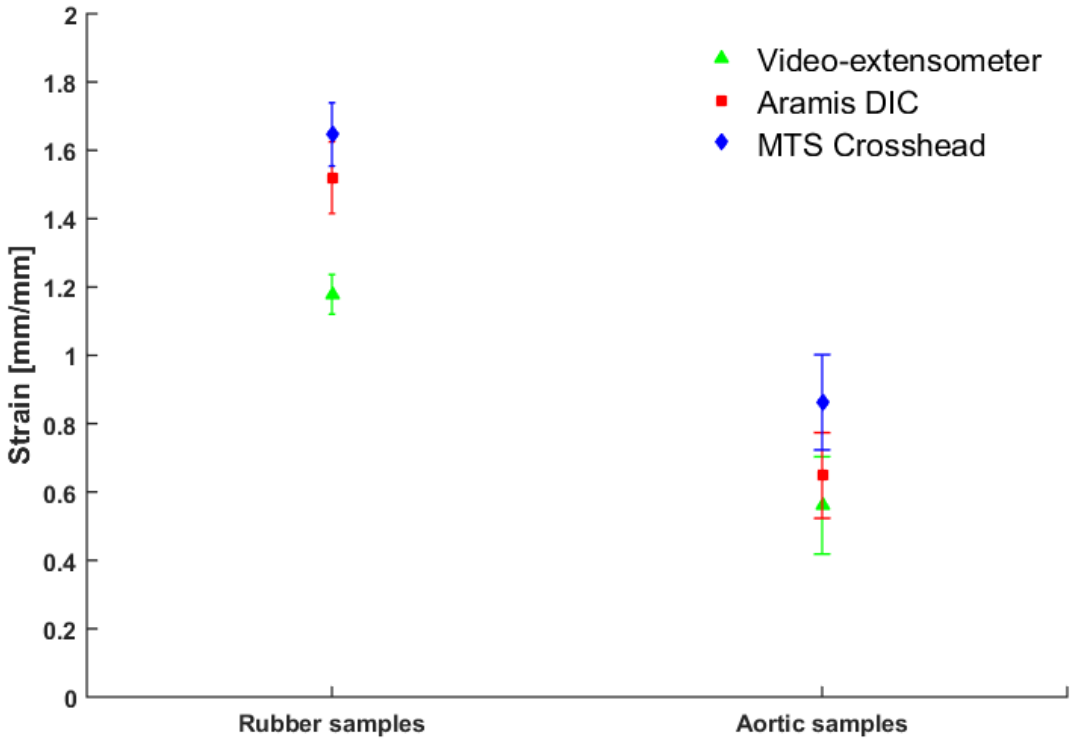

Figure 3.9 Mean strain (marker) and standard deviation (error bar) calculated for each measuring technique: the video-extensometer (green triangle), the DIC (red square) and the testing machine (blue rhombus).

The most promising results are obtained by DIC, as the strain computation field is mapped. However, DIC requires clearly more time to be carried out. The video-extensometer generates the minimum strain standard deviation for rubber samples, while no significant difference can be appreciated for aortic samples (Figure 3.9). Therefore, as its results have been evaluated close enough to DIC (Figure 3.8), the use

of the video-extensometer has been valued as the best compromise between accuracy and rapidity.

3.2.2 Trials on rubber: uniaxial tests

At the beginning, uniaxial tensile tests have been conducted on rubber to define all the details of the experimental protocol and to practice the whole procedure before testing aortic samples.

Rubber samples, prepared as previously described in Section 3.1, have been tested to comprehend their mechanical behaviour up to rupture. The same experimental setup referred in Section 3.2.1 has been employed (Figure 3.10).

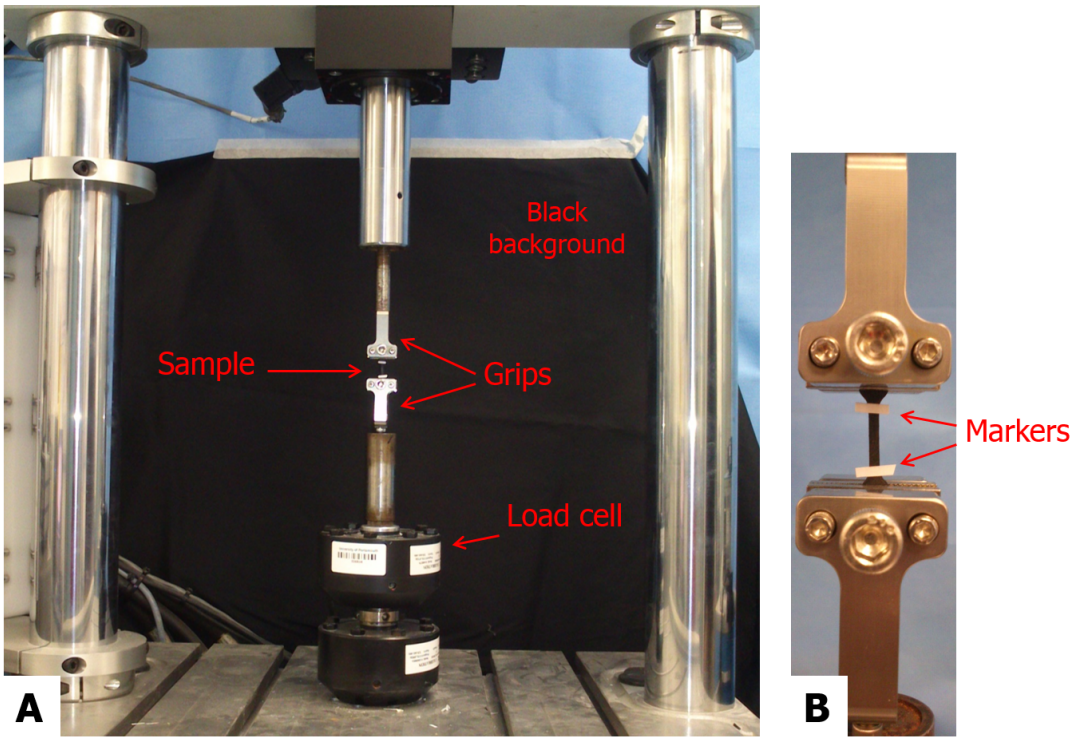

Figure 3.10 A) Experimental setup adopted for the uniaxial tensile tests on rubber sample. The sample was kept in position by grips (B) and tested uniaxially to failure. A video-extensometer was used to measure the displacement between the two white markers attached to the sample.

The video-extensometer was synchronized with the cross-head movement to capture the entire elongation process up to the rupture of each sample. Each test has been conducted

in displacement control at a constant cross-head speed of 0.2 mm/s. This value was calculated as the average of low speed rates adopted in literature, as described in Section 2.3.2 (Cox *et al.*, 2008; ISO 37, 2005; Jerabek *et al.*, 2010; Shergold *et al.*, 2006).
As the influence of pre-conditioning in the mechanical response of hyper-elastic materials has been often neglected, three different aspects have been analysed: the pre-conditioning frequency (f_P), the sample shape and the strain magnitude.
Firstly, the effect of frequency on the uniaxial tensile test has been explored. A pre-conditioning stage is carried out by means of a sinusoidal load waveform, whose strain amplitude is calculated as 10% of the maximum strain (7 mm/mm). This value has been retrieved from preliminary uniaxial tests performed without pre-conditioning. Furthermore, as recommended by British Standard (BS 903-1, 1995), 5 cycles of pre-conditioning, have been performed. In order to determine the influence of f_P on the mechanical stress-strain response, several values of frequencies have been tested on rubber strips: 0.01 Hz, 0.05 Hz, 0.075 Hz, 0.1 Hz, 0.2 Hz, 0.3 Hz, 0.4 Hz, 0.5 Hz, 0.6 Hz, 0.8 Hz, 1 Hz, 1.2 Hz, 1.4 Hz, 1.6 Hz and 2 Hz. Moreover, a test without pre-conditioning, intended as a control trial, has been carried out. Four specimens ($n = 4$) have been tested for each frequency.

The second aspect investigated is the role of sample shape on the material characterization. Therefore, in addition to the strips, dumb-bells have been tested at the following pre-conditioning frequencies: 0.2 Hz, 0.6 Hz, 0.8 Hz, 1 Hz, 1.4 Hz and 2 Hz. Similarly, a control test without any pre-conditioning has been performed.

In addition, a third aspect of the pre-conditioning process is explored: the strain magnitude. In two distinct tests, conducted at fixed preconditioning frequency of 0.2 Hz, two strain amplitudes are investigated: 20% and 8.5% of the maximum strain recorded. The engineering stress has been calculated taking into account the same cross-sectional area for both sample shapes.

3.2.3 Uniaxial tests on aortic tissue

Preliminary tests on aortic tissue showed reduced values of stress compared to results obtained from rubber. Therefore, a different facility, equipped with a smaller load cell, seemed appropriate to get more accurate results.
Aortic dumb-bells have been tested in displacement control on a high precision testing device specific for testing biological specimens (BOSE Electroforce 3200, Bose Corporation, Gillingham, UK), equipped with a 225 N load cell. The displacement has been determined by means of the Messphysik video-extensometer adopted in the previous tests. The contrast offered to the camera has been increased as presented in Section 3.2.1. The actual test has been conducted at a constant cross-head speed of 0.2 mm/s. This value has already been adopted in literature (Duprey *et al.*, 2010) and is consistent with the experimental work presented in Section 2.3.2.

The pre-conditioning stage of such samples is analogous to the one applied on rubber: a sinusoidal load waveform, which amplitude is 10% of the maximum strain (0.7 mm/mm). Furthermore, as recommended by British Standard for rubber materials (BS 903-1, 1995) and as average of the studies reviewed in Section 2.3.2, 5 cycles of pre-conditioning have been performed. Six thoracic and abdominal specimens have been tested for each frequency (Xiong *et al.*, 2008). In order to determine the influence of f_P on the mechanical stress-strain response, two frequencies have been selected: 1.2 Hz and 2 Hz. Such values are intended as an average resting (70 bpm) and exercising (120 bpm) heart rate respectively. Moreover, a control test, neglecting the pre-conditioning, is carried out.

The engineering stress has been calculated taking into account the undeformed cross-sectional area and assuming the specific thickness of each sample. Experimental data have been filtered by means of a Matlab (Mathworks, Massachusetts, US) script, which

reduces the number of experimental data to 40% of the original dataset performing a block average. The details of this script are reported in Section 3.3.

3.2.4 Equi-biaxial tests on aortic tissue

In order to achieve a complete mechanical characterisation of the aortic tissue, a biaxial test is required. Furthermore, it has been noted from the state of art that the majority of studies still prefer planar biaxial tests to indentation tests. As the biaxial testing protocol has been based on the study of preliminary FE configurations, the outcomes, justifying the experimental protocol, are showed in the Appendix.

Differently from tests performed in displacement control, force control analysis is quite challenging, thus rarely performed on soft tissue. However, such a test is required to achieve a correct equi-biaxial test, ensuring the same value of stress applied on each axis. Hence, the biaxial characterization has been performed in force control on a CellScale Biotester equipped with 23 N load cells. Despite the use of such an up-to-date facility, the force control mode limited the pre-conditioning options. Thus, a pre-conditioning of 5 cycles at 0.25 Hz has been applied. The actual tensile test has been conducted at 0.2 N/s.

Six samples tests have been tested for abdominal and thoracic aorta respectively. The sample anchorage has been studied by means of a preliminary FE analysis described in Section 7.3. The mounting system consists in a so-called BioRake placed on each side of the specimen: five equally spaced hooks pierce each side of the sample. Therefore the mounting is consistent and accurate (Figure 3.11 B). In addition, a high resolution (1280 x 960 pixels) CCD camera is placed on top of the sample to collect time synchronized images for post test analysis (Figure 3.11 A).

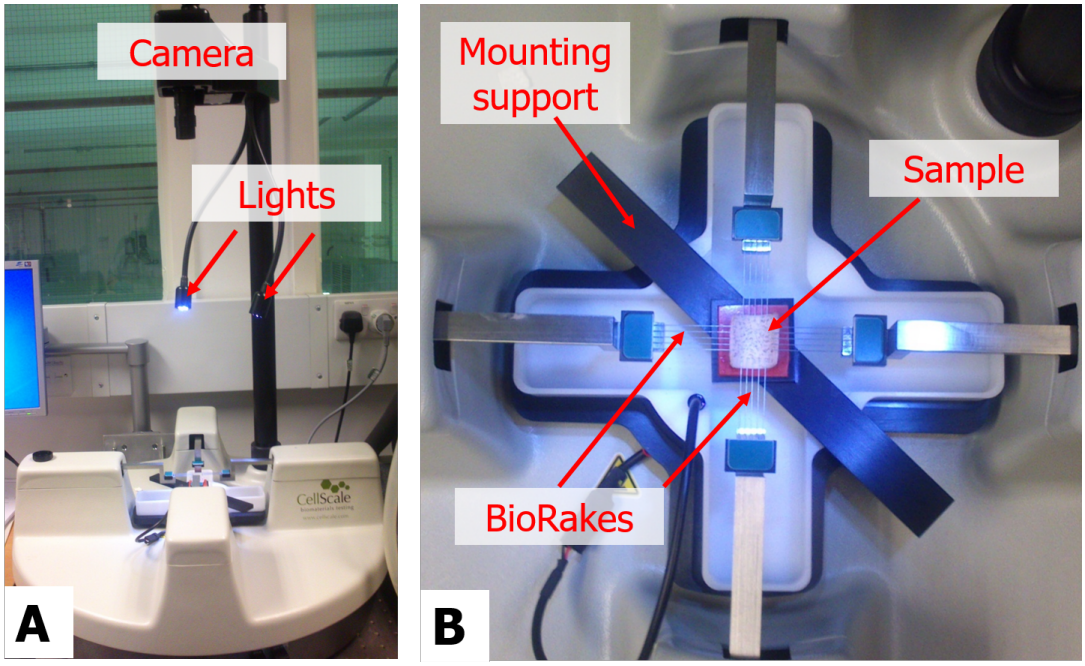

Figure 3.11 Experimental setup for planar equi-biaxial tests. A) CCD camera and additional lights are placed on top of the sample. B) Square sample of aortic tissue is hooked to each actuator by means of BioRakes.

The images have been collected throughout the test at 1 Hz rate by the CCD camera. Such images are automatically time-correlated with the force displacement data by the BioTester software. In order to perform DIC, a grid has been defined on the snapshot taken soon after the end of the pre-conditioning stage, intended as the undeformed configuration. The grid cuts out the hooks insertions on the sample (Figure 3.12). The software estimates the Green-Lagrange principal strain values performing a 16 points least squares average for each cell.

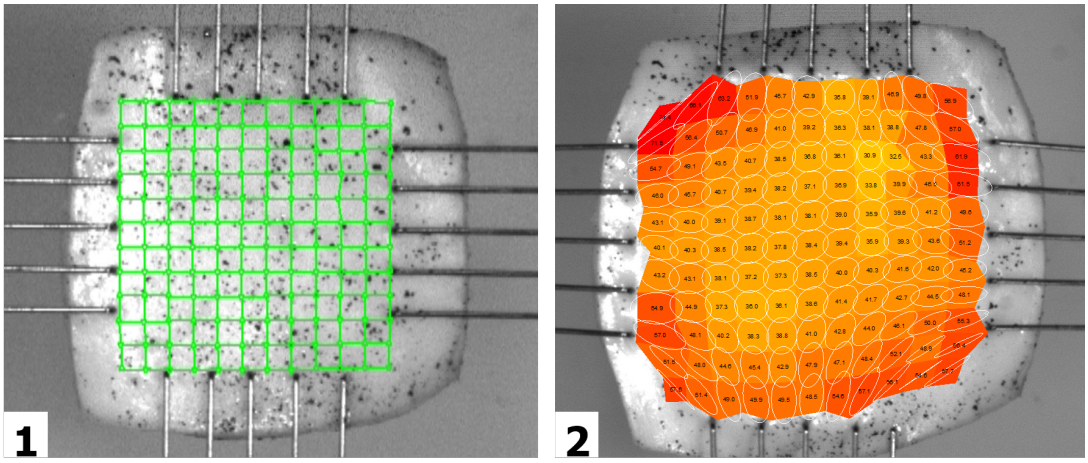

Figure 3.12 DIC on square sample. 1) A grid (11 x 11 cells) is designed on the undeformed configuration. 2) Strain values are mapped: a percentage value is calculated for each cell.

A sensitivity study has been conducted to evaluate the number of cells to take into account in order to average strain values for each frame. Similarly to uniaxial tests, the engineering stress has been calculated taking into account the undeformed cross-sectional area and assuming the specific thickness of each sample by means of the algorithm presented in Section 3.3.

3.3 Post-processing: Matlab scripts

As a result of uniaxial and biaxial tests described in Sections 3.2, force values are obtained from the testing machine, while displacement amounts have been acquired by the video-extensometer or strain values by DIC.

The calculation of engineering stress relies on the unloaded cross-sectional area with forces applied during tensile tests. Therefore, the width and the thickness of the sample are required. Being cut by a specific die, the tolerance of the width value has been assumed minimum and thus neglected.

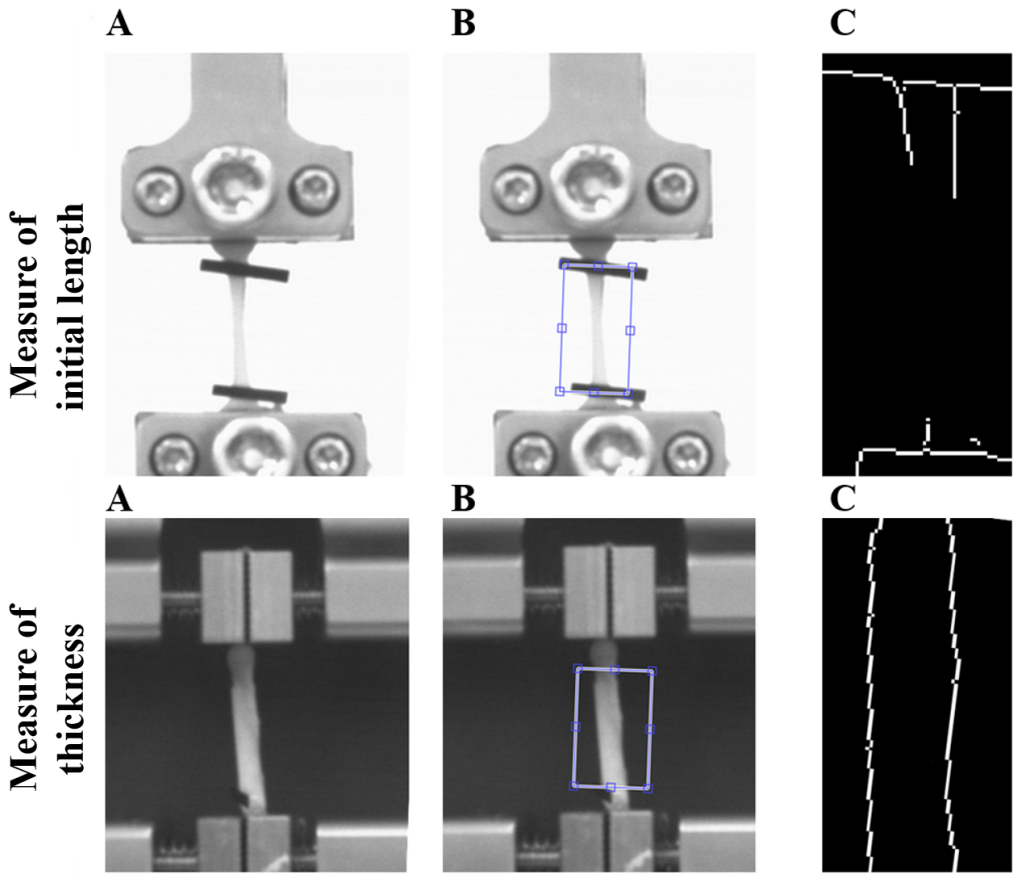

Figure 3.13 Steps of Matlab script used to measure the average thickness (bottom row) and the initial length (top row) of each sample: A) undeformed sample mounted between the grips, B) region of interest (ROI) selection and C) application of Sobel edge detection method on ROI.

Following the considerations presented at the end of Section 2.3.2, particular attention has been reserved to the thickness measurement of aortic tissue. Thickness and initial length were optically determined for each sample mounted between grips in the initial configuration, by means of an in house Matlab script (Mathworks, Massachusetts, US). In order to enhance the contrast of the region of interest (ROI) and to facilitate edges detection in the image segmentation, a black background was applied for the estimation of the thickness. Similarly, a white background was used to measure the initial length, as strips needed for the use of the video-extensometer were black. In both cases, Sobel edge detection method (Parker, 2010) was applied on the ROI, which was manually selected (Figure 3.13). Pixel conversion in *mm* was based on the grip dimensions,

previously measured by means of a digital caliper.

Despite the scrupulous attention for each experiment, the noise is unavoidable in such mechanical characterizations. Aiming to smooth the stress-strain plot and to obtain a monotonic curve to be imported in the finite element model, a post-processing step is required. Therefore, experimental data have been filtered by means of a Matlab script. In order to consider only the actual tensile test, the pre-conditioning cycles are cut out of the data-set. Stress-strain data are rounded to the second decimal digit and strain ordered. Successively, an average stress is calculated for intervals of strain of 0.05. In addition, experimental data are reduced of 40% compared to original data. An example of output obtained with such filter can be appreciated in Figure 3.14, where the reduction of the noise in the output (experimental data provided to FEM simulation) respect to the input signal (experimental raw data) is quite appreciable.

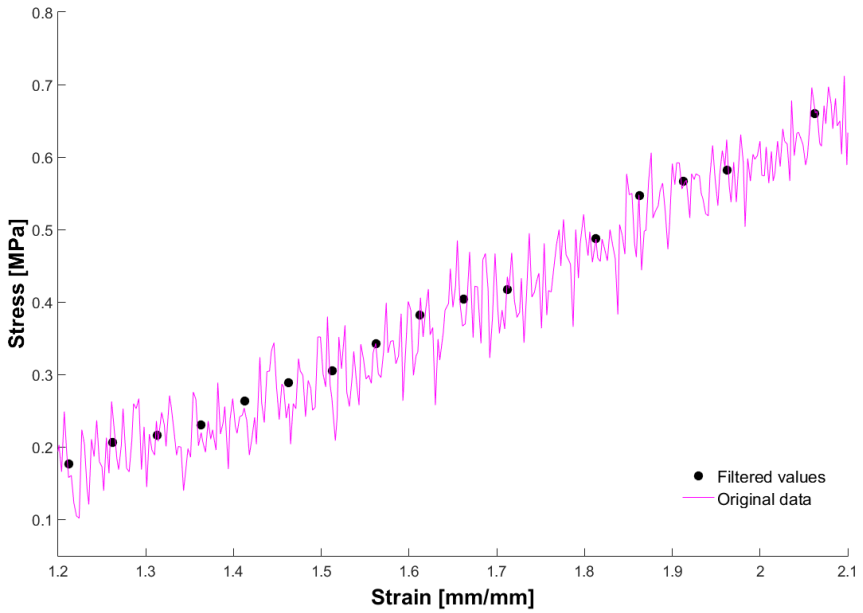

Figure 3.14 Block average filter (black dots) applied on untreated stress-strain data (continuous magenta line).

Furthermore, such script intends to produce a monotonic stress-strain response. As an example, no filtered value is displayed around the strain 1.78 or 2.2 in Figure 3.14,

where the filter calculated an average stress value inferior to the preceding strain interval. Thus, whether the noise is compromising the monotonicity of the curve, the filtered value is automatically removed.

At this point, a comparison between stress-strain curves is required to highlight significant differences in response to selected features of the experimental protocol, such as f_P. Therefore, a statistical tool widely adopted in literature (O'Leary *et al.*, 2014; Raghavan *et al.*, 2011b) appears to be the ANalysis Of VAriance (ANOVA). This evaluation consists in a generalized t-test applied to at least two groups of data. One-way ANOVA considers a single source of variation assigned to completely random samples cut from the same material (Wayne, 2009). As an example, this analysis can evaluate whether average stress or strains are significantly different because of the f_P applied.
ANOVA is based on three assumptions. First, the evaluated means are assumed to be normally distributed in each group. Second, the population variances in each group are considered equal. Lastly, the sampling is assumed to be random.
Therefore, ANOVA tests the null hypothesis for which the population means may be equal for all groups. In other words, the assumption states that there is no relationship between two phenomena. The null hypothesis is satisfied whether the observed differences in sample means are due to random sampling variation. The alternative hypothesis affirms that there are at least 2 group means that are significantly different from each other. Therefore, ANOVA returns a p-value below 0.05 whether the observed differences between sample means are due to authentic differences in the population means. This analysis is carried out by Matlab function *anova1*. Furthermore, an additional test is required to distinguish which specific groups differ from each other: Matlab function *multcompare* performs this task.

3.3.1 Data fitting

The mathematical modelling of hyper-elastic materials requires the accurate identification of fitting parameters from suitable experimental datasets. These constants are needed to match, in a least squares sense, theoretical and experimental stress values over the complete desired strain range (Bucchi & Hearn, 2013a; Sussman & Bathe, 2009). The fitting of experimental data is generally a critical aspect since it represents the bridge between the testing procedure and the numerical analysis. The material model used in a Finite Element (FE) analysis must accurately represent the physical behaviour of the material being used. The calibration process is challenging due to the complexity of material models. This step is especially delicate within the framework of soft tissue.

The difficulties arising in the fitting procedure are intrinsic to the considered problem, not to the specific choice of constitutive law. In limited cases uniqueness of material parameters may be achieved. However, non-uniqueness often occurs, and it may be reflected in numerical solutions. When, for example, polynomial models are adopted, high polynomial order ensures a better fitting to the data for an extensive range of deformations. However, numerical instabilities may arise from such a procedure. On the other hand, a nonlinear model often leads to the non-uniqueness of the optimal set of constants. Ogden *et al.* (2004) carried out a study of the fitting of stress-stretch equations to experimental data for rubber for incompressible isotropic hyper-elastic constitutive laws. As a result, Ogden suggested to carefully assess analytically the fitting of the material parameters before performing finite element studies. Hence, unclear physical meaning of numerical predictions may be prevented.

Therefore, data collected from the biaxial tests have been previously analysed to capture in a clear way the main qualitative features. A nonlinear regression has been performed to model the experimental data by the Fung model.

Following the biaxial tensile tests, second Piola-Kirchhoff stress (S) values have been calculated and Green-Lagrange strain (E) imported from DIC post-processing. Theoretical stress values in the circumferential direction has been calculated, according to literature presented in Section 2.2.3, as follows:

$$S_{\theta\theta} = \frac{\partial W}{\partial E_{\theta\theta}} = (2a_1 E_{\theta\theta} + 2a_4 E_{ZZ} + 2a_6 E_{RR}) \frac{C}{2} e^{Q(E)} \tag{3.1}$$

where Q is

$$\begin{aligned} Q(E) = {} & a_1 E_{\theta\theta}^2 + a_2 E_{ZZ}^2 + a_3 E_{RR}^2 + 2a_4 E_{\theta\theta} E_{ZZ} + 2a_5 E_{ZZ} E_{RR} + 2a_6 E_{\theta\theta} E_{RR} \\ & + a_7 E_{\theta Z}^2 + a_8 E_{\theta R}^2 + a_9 E_{ZR}^2 \end{aligned} \tag{3.2}$$

Similarly, the axial Second Piola-Kirchhoff stress is

$$S_{ZZ} = \frac{\partial W}{\partial E_{ZZ}} = (2a_2 E_{ZZ} + 2a_4 E_{\theta\theta} + 2a_5 E_{RR}) \frac{C}{2} e^{Q(E)} \tag{3.3}$$

As suggested in literature (Pandit *et al.*, 2005), the goal of the data fitting algorithm consists in determining the material constants C and a_i which minimize the square of the difference between theoretical (Equations 3.1 and 3.3) and experimental values of circumferential ($S_{\theta\theta}^{exp}$) and axial (S_{ZZ}^{exp}) stresses as:

$$Error = \sum_{i=1}^{N} \left[\left(S_{\theta\theta_i} - S_{\theta\theta_i}^{exp} \right) \right]^2 + \sum_{i=1}^{N} \left[\left(S_{ZZ_i} - S_{ZZ_i}^{exp} \right) \right]^2 \tag{3.4}$$

where N represents the total number of experimental points. This approach is justified by the fact that $S_{\theta\theta}^{exp}$ and S_{ZZ}^{exp} values are comparable.

Despite an excellent fitting of Equation 3.4 which can be obtained by means of Matlab *lsqcurvefit* function, it has been proved, as late outcome of this research, that such a result is not sufficient to fully implement a Fung modelling. In order to estimate parameters a_7, a_8 and a_9 it is necessary to take into account shear behaviour, which cannot be captured by the biaxial tensile tests described in Section 3.2.4, being the

sample aligned with circumferential and longitudinal directions (Zhou & Fung, 1997). Thus, in Chapter 7 it is reported and discussed how misleading is the literature about the Fung modelling.

Therefore, theoretical shear stress value are calculated analogously to Equations 3.1 and 3.3 (Zhou & Fung, 1997). As an example:

$$S_{\theta Z} = \frac{\partial W}{\partial E_{\theta Z}} = (2a_7 E_{\theta Z}) \frac{C}{2} e^{Q(E)} \tag{3.5}$$

Green-Lagrange shear strain and stress data have been determined by means of *synthetic* simple shear test. The principal stretches for this test (Ogden, 1997), sketched in Figure 3.15, are the following:

$$\lambda_1 = \lambda \qquad \lambda_2 = \frac{1}{\lambda} \qquad \lambda_3 = 1 \tag{3.6}$$

thus, the first invariant (I_1) can be calculated as reported in Equation 2.14. The amount of shear κ (Moreira & Nunes, 2013; Ogden, 1997) is hence defined as

$$\kappa = \tan(\phi) = \lambda - \frac{1}{\lambda}. \tag{3.7}$$

As a result, the Green-Lagrange shear strain (Fung, 1993; Vossoughi & Tözeren, 1998) is calculated as

$$E_{12} = \frac{1}{2}\lambda_1\lambda_2 \cos(\phi_F) = \frac{1}{2}\lambda_1\lambda_2 \cos\left(\frac{\pi}{2} - \phi\right) \tag{3.8}$$

where ϕ and ϕ_F are the angles showed in Figure 3.15. The angle ϕ is worked out from Equation 3.7 and principal stretches from Equation 3.6 substituted, thus

$$E_{12} = \frac{1}{2}\cos\left(\frac{\pi}{2} - \arctan(\kappa)\right). \tag{3.9}$$

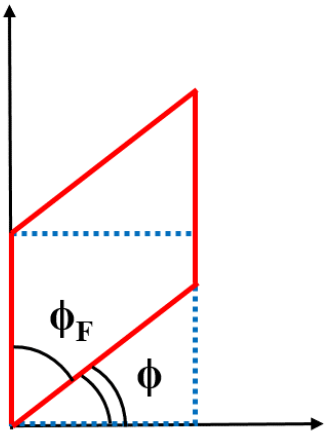

Figure 3.15 Sketch of a simple shear test transforming the original configuration (dashed blue) into the deformed one (red). The angle ϕ_F is needed to calculate Green-Lagrange shear strain.

As the Cauchy stress in simple shear tests (Nunes & Moreira, 2013) can be expressed as

$$\sigma_{12} = 2\kappa \frac{\partial W}{\partial I_1}, \tag{3.10}$$

biaxial data are fitted by Yeoh strain-energy function (Section 2.2.2) in Abaqus. This model has been selected because it is dependent on the first invariant and provides a good fitting of the experimental data. Thus, the fitting coefficients C_{10}, C_{20} and C_{30} are determined and Equation 3.10 becomes

$$\sigma_{12} = 2\kappa \left[C_{10} + 2C_{20}(I_1 - 3) + 3C_{30}(I_1 - 3)^2 \right]. \tag{3.11}$$

The Cauchy stress (σ) is related to the second Piola-Kirchhoff (S) of Equation 3.5 as follows

$$\mathbf{S} = J\mathbf{F}^{-1}\sigma\mathbf{F}^{-T} \tag{3.12}$$

where the deformation gradient $\mathbf{F}$ for simple shear deformation is

$$F = \begin{bmatrix} 1 & \kappa & 0 \\ 0 & 1 & 0 \\ 0 & 0 & 1 \end{bmatrix}. \tag{3.13}$$

Therefore, Equation 3.12 becomes

$$\mathbf{S} = 1 \begin{bmatrix} 1 & -\kappa & 0 \\ 0 & 1 & 0 \\ 0 & 0 & 1 \end{bmatrix} \begin{bmatrix} \sigma_{11} & \sigma_{12} & \sigma_{13} \\ \sigma_{21} & \sigma_{22} & \sigma_{23} \\ \sigma_{31} & \sigma_{32} & \sigma_{33} \end{bmatrix} \begin{bmatrix} 1 & 0 & 0 \\ -\kappa & 1 & 0 \\ 0 & 0 & 1 \end{bmatrix} \tag{3.14}$$

from which $S_{12} = \sigma_{12} - k\sigma_{22}$. However, in the hypothesis of plane stress the normal component of the traction on inclined surfaces (σ_{22}) and σ_{33} are equal to zero (Nunes & Moreira, 2013). As a result, σ_{12} coincides with S_{12}. Finally, the updated square of differences between theoretical and experimental stress values becomes

$$\begin{aligned} Error = &\sum_{i=1}^{N} \left[\left(S_{\theta\theta_i} - S_{\theta\theta_i}^{exp} \right) \right]^2 + \sum_{i=1}^{N} \left[\left(S_{ZZ_i} - S_{ZZ_i}^{exp} \right) \right]^2 \\ &+ \sum_{i=1}^{N} \left[\left(S_{\theta Z_i} - S_{\theta Z_i}^{exp} \right) \right]^2 + \sum_{i=1}^{N} \left[\left(S_{\theta R_i} - S_{\theta R_i}^{exp} \right) \right]^2 + \sum_{i=1}^{N} \left[\left(S_{ZR_i} - S_{ZR_i}^{exp} \right) \right]^2 \end{aligned} \tag{3.15}$$

assuming all simple shear stress values equal. Hence, a_i parameters are obtained fitting the circumferential, axial and shear stress-strain responses.

Finally, the convexity conditions (Fan & Sacks, 2014; Holzapfel, 2006; Pandit *et al.*, 2005; Sun & Sacks, 2005) for the obtained parameters have been verified to ensure material stability, physically meaningful and unambiguous mechanical behaviour. A strict local convexity of the strain-energy function means that the matrix containing its second derivatives with respect to $E_{\theta\theta}$ and E_{ZZ} is positive definite (Holzapfel, 2006). Hence, the contours of constant W are convex. As a result of the convexity requirement,

the possible ranges of the model parameters for the strain energy density function are restricted (Ma *et al.*, 2007).

In order to assess this demand, contours of the strain-energy function against the circumferential and axial strain are plotted.

Chapter 4

Experimental Results

The current chapter shows all the mechanical responses acquired from the experimental tests as a direct application of the methodology reported in Chapter 3. Aiming to focus on the mechanical tensile response obtained immediately after the pre-conditioning process, the loading-unloading paths are not displayed. Therefore, the mechanical behaviour in the toe-region can be easily appreciated.
Firstly, the characterization of the rubber, carried out to corroborate details of the whole experimental protocol (e.g. sample preparation, pre-conditioning, measurement,...), is presented in Section 4.1, while the responses associated to the aortic tissue are reported in Section 4.2. Finally, the mechanical behaviour emerged from planar biaxial tensile tests is showed in Section 4.3.

4.1 Uniaxial tests on rubber strips and dumb-bells

A carbon filled material has been selected to make a trial run of the experimental protocol before testing the aortic tissue. Hence, such rubber is not intended to match the biological behaviour, but just the general hyper-elastic response. As previously described in Section 3.1 samples have been cut in two different shapes: strips and

standard dumb-bells.

Strips have been pre-conditioned for 5 cycles at 7 different frequencies (0.05 Hz, 0.2 Hz, 0.3 Hz, 0.6 Hz, 1 Hz, 1.2 Hz and 1.6 Hz) and stretched until rupture. In addition, a control test without pre-conditioning has been performed. As shown in Figure 4.1, stress-strain responses achieved by the strips appear to be heterogeneous.

The range of maximum stress recorded is subjected to big variations, in the range 1.46 MPa – 5 MPa. Furthermore it appears that specific f_P, such as 0.2 Hz, 0.6 Hz and above 1.2 Hz, generate a quite repeatable behaviour, reducing the scatter between the lowest and the highest maximum stress value to just 20%. Such scatter for $f_P = 0.05Hz$ and in absence of pre-conditioning exceeds 100%.

In each plot, the stiffness and strain values associated to σ_{avg}, which is calculated for each test as half of the $min\{\sigma_1^{max}, \sigma_2^{max}, \ldots, \sigma_n^{max}\}$ n being the number of samples, were considered for ANOVA evaluations. As a result, no sensible variation (p = 0.634) in the curve stiffness evaluated for σ_{avg} was observed. Differently, the strain obtained in the absence of pre-conditioning is significantly different (p = 0.005) compared to pre-conditioning frequencies $f_P \geq 1$ Hz.

In each subplot of Figure 4.1, two specific responses are selected to be fit by different strain-energy functions: an upper band (continuous black line) and a lower band (continuous blue line). The fitting parameters calculated by Abaqus for each of these responses are listed in Table 4.1. As can be observed, some of the selected stress-strain data could not be fitted by Arruda-Boyce constitutive model, thus they are indicated as *unstable*. Further details about such behaviour are reported in Section 6.1.1.

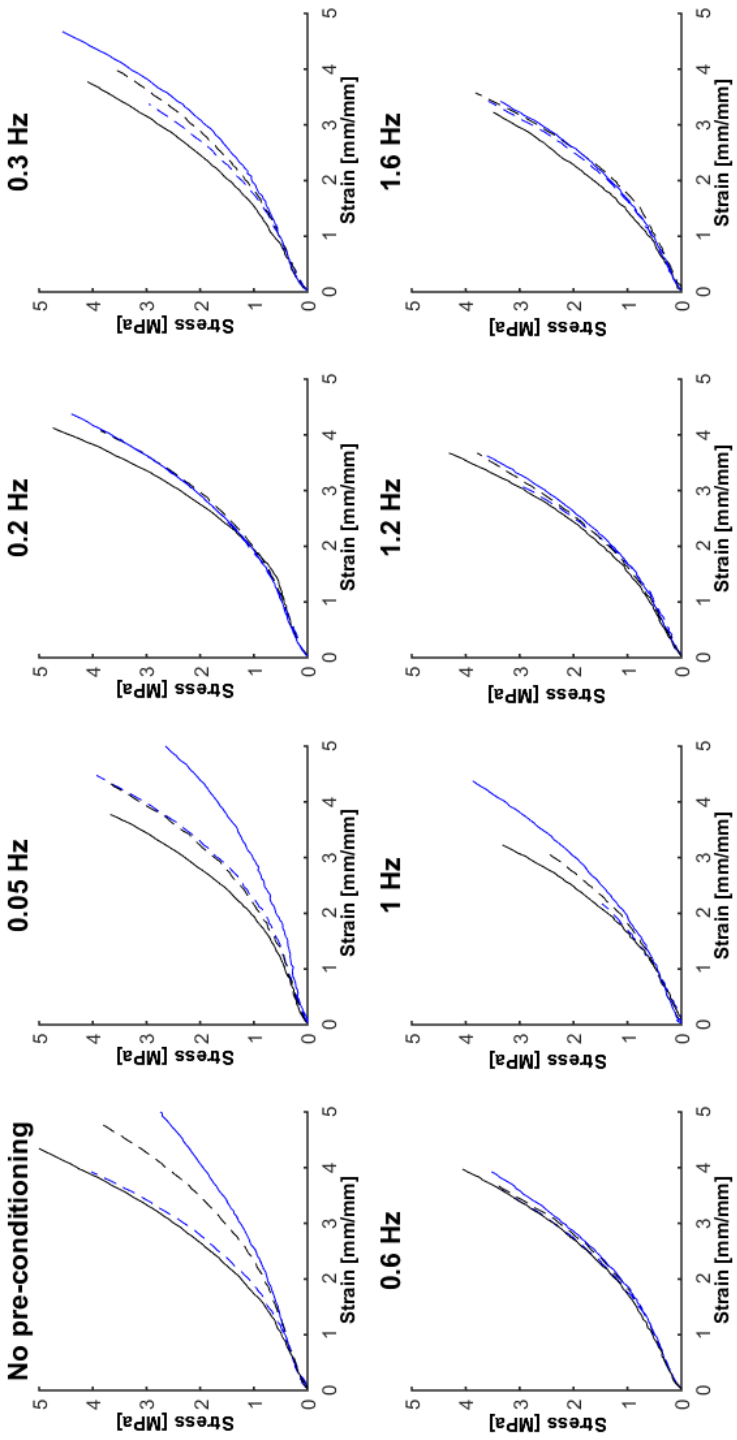

Figure 4.1 Filtered uniaxial stress-strain response of rubber strips, pre-conditioned for 5 cycles at selected frequencies. Four samples have been tested for each test. Data obtained from no pre-conditioning, 0.2 Hz, 0.6 Hz and 1.6 Hz have been imported in the FE model.

Pre-conditioning frequency [Hz]	Strain-energy function												
	Ogden						Neo-Hooke	Yeoh			Arruda-Boyce		
	μ_1 [Pa]	α_1	μ_2 [Pa]	α_2	μ_3 [Pa]	α_3	C_{10} [Pa]	C_{10} [Pa]	C_{20} [Pa]	$C_{30} =$ [Pa]	μ [Pa]	μ_0 [Pa]	λ_m
0 •	5880525.3	-2.1	355567.8	2.5	-6225486.9	-2.5	142788.1	89751.3	2841.3	-13.6	*unstable*		
0	-281362.1	2.6	346486.5	3.1	158565.8	-0.9	165894.2	104536.9	8475.3	-35.1	250829.1	271888.1	2.8
0.05 •	5320231.6	-3.3	397346.1	3.2	-5809670.9	-3.8	75481.9	34495.5	13807.5	-218.1	103529.9	121167.9	2.1
0.05	2769246.6	-2.6	303822.4	2.8	-3150067.1	-3.4	65840.6	35107.7	4366.4	-39.9	*unstable*		
0.2 •	9922130.0	-3.1	316250.3	3.4	-10163613.1	-3.5	151814.7	105903.7	4408.2	114.0	220169.9	241961.9	2.6
0.2	4164447.4	-3.0	263776.6	3.2	-4261152.0	-3.5	171436.7	122362.3	4331.1	37.2	259278.9	278386.1	3.0
0.3 •	2293997.7	-3.1	379917.0	3.0	-2645869.8	-3.7	158143.4	88691.8	13494.8	-193.7	231269.2	256679.3	2.5
0.3	384536.1	-4.1	439265.4	5.2	-848251.6	-10.4	156561.9	109115.3	4308.4	13.5	238143.3	254260.4	3.1
0.6 •	2134070.2	-3.4	342634.7	3.2	-2353451.2	4.4	165340.5	117896.0	5748.7	26.4	245242.4	268391.2	2.7
0.6	-248177.4	4.5	22024.5	5.5	778856.3	-8.0	181568.8	132554.5	4227.1	40.2	273185.2	294098.1	3.0
1 •	-704904.9	-0.8	1886.9	6.3	1195968.2	-4.3	192314.6	138235.0	7649.6	73.7	275976.7	309361.6	2.4
1	-2866580.3	-2.4	1519.8	5.8	3143285.4	-3.2	131040.2	74326.9	7592.1	-65.8	194175.1	209952.5	2.9
1.2 •	1984548.8	0.2	74362.4	3.9	-2131573.1	-0.8	88428.5	40083.6	16411.5	-289.6	*unstable*		
1.2	-4972170.4	-2.2	842.8	6.8	5391296.6	-3.0	173720.5	100958.6	11198.3	-86.3	*unstable*		
1.6 •	197593.7	2.8	16453.1	4.7	15927.7	-1.8	163611.1	107541.2	10649.9	-78.0	236482.7	265412.5	2.4
1.6	-160998.9	-1.7	-1333560.2	4.2	3012330.8	-8.3	200347.0	122804.3	8486.8	-32.4	*unstable*		

Table 4.1 Fitting parameters estimated by Abaqus for selected stress-strain curves plotted in Figure 4.1.
• indicates the stiffest response.

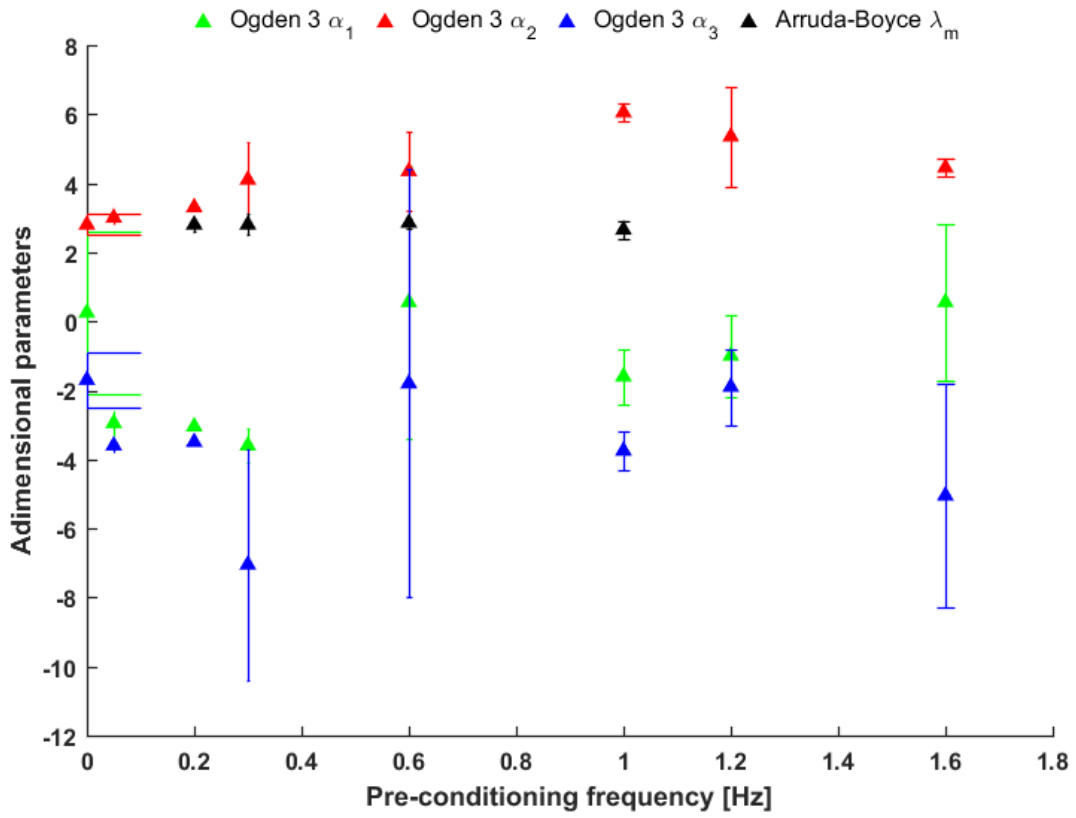

Figure 4.2 Mean (marker) and standard deviation (error bar) calculated for the adimensional fitting parameters listed in Table 4.1.

In order to appreciate how the listed parameters change with the f_P, the mean and the standard deviation have been calculated. Among the adimensional parameters, a significant change in the standard deviation can be observed for α_3 of Ogden model ($3^{rd} order$) in Figure 4.2. Neither the mean values neither the standard deviation of adimensional parameters can elucidate the reason why stress-strain responses are more repeatable at certain frequencies. Although different order of magnitude can be observed in terms of standard deviation, similar considerations are reserved to the other parameters plotted in Figure 4.3. The largest scatter is achieved by Ogden μ_3.

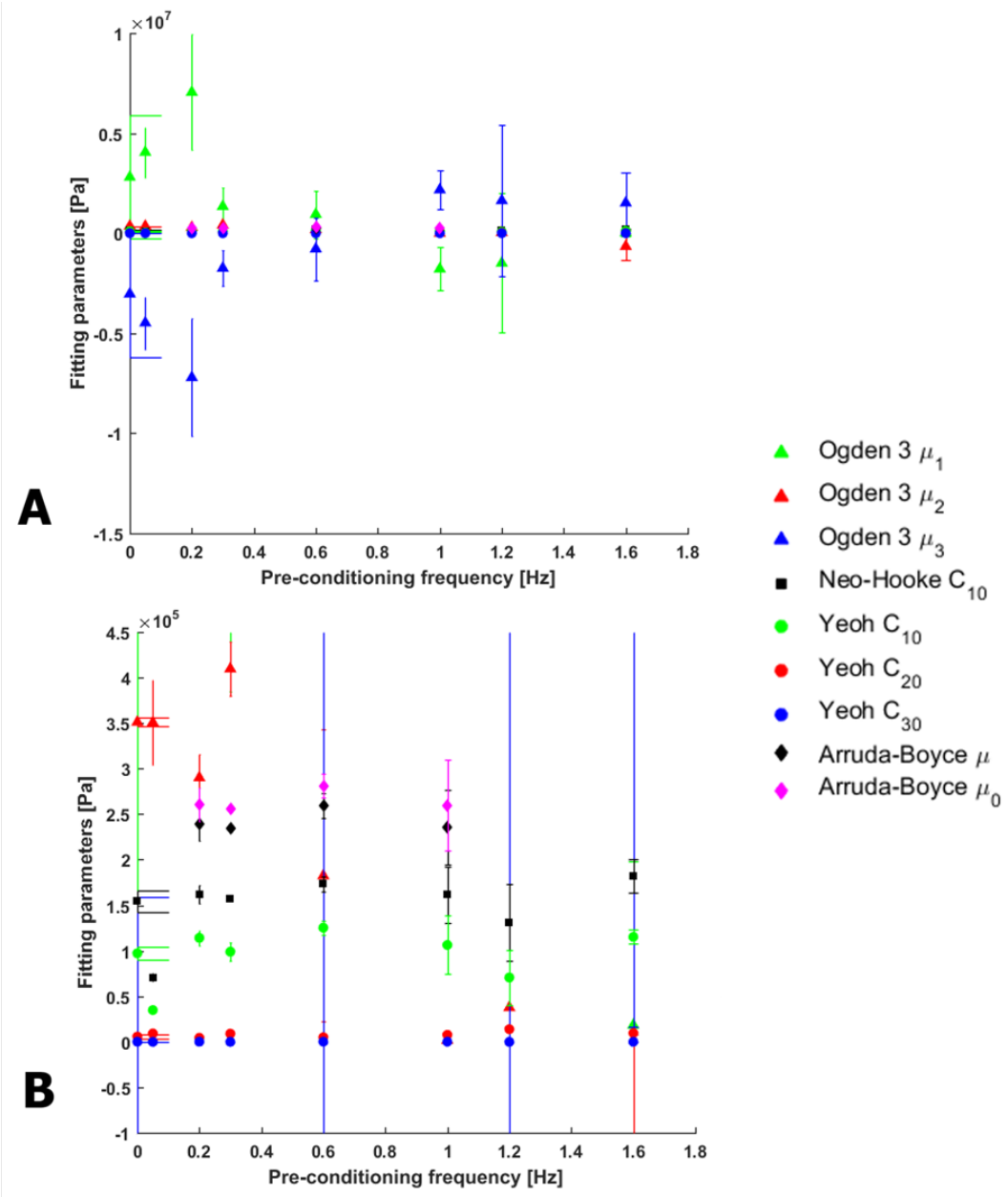

Figure 4.3 Mean (marker) and standard deviation (error bar) calculated for the fitting parameters listed in Table 4.1. Since standard deviation exhibit different order of magnitude, a zoom in of plot A is given in plot B.

Dumb-bells have been tested in order to explore the effect of a geometric variation on experimental data collection, using the same experimental setup and methodology adopted for the strips (Section 3.2.2). Stress values appear mostly scattered, except for some particular frequencies (i.e. 1 Hz) where stress-strain curves are well overlapped (Figure 4.4).

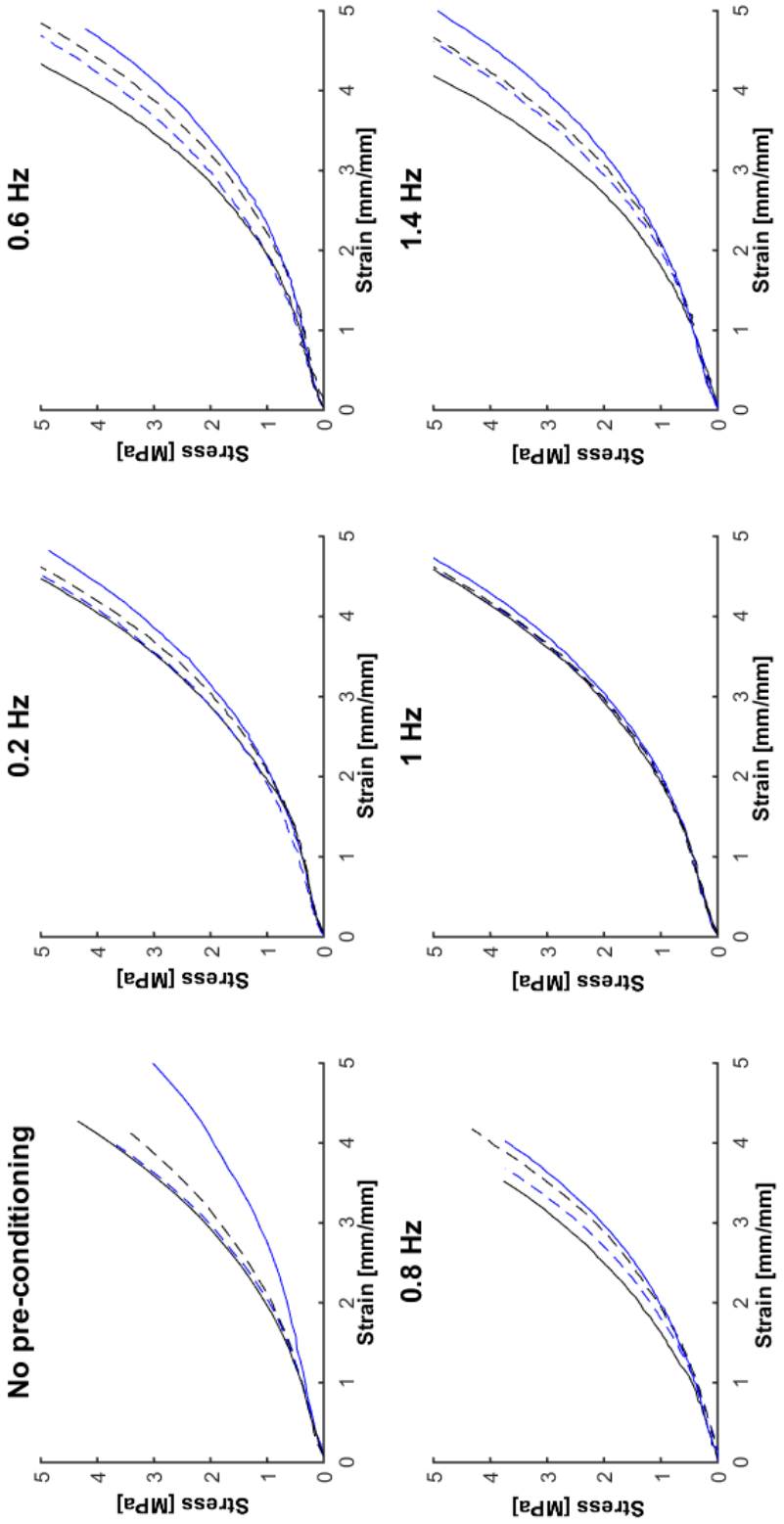

Figure 4.4 Filtered uniaxial stress-strain response of rubber dumb-bells, pre-conditioned for 5 cycles at selected frequencies. Four samples have been tested for each test. Data obtained from no pre-conditioning, 0.2 Hz, 0.8 Hz and 1 Hz have been imported in the FE model.

Pre-conditioning frequency [Hz]	Strain-energy function													
	Ogden 3^{rd} order						Neo-Hooke		Yeoh			Arruda-Boyce		
	μ_1 [Pa]	α_1	μ_2 [Pa]	α_2	μ_3 [Pa]	α_3	C_{10} [Pa]	C_{10} [Pa]	C_{20} [Pa]	$C_{30} =$ [Pa]	μ [Pa]	μ_0 [Pa]	λ_m
0 •	-187618.2	-0.1	2481.1	5.6	533820.7	-5.2	164700.3	110998.3	5523.8	25.3	244774.4	264861.5	2.9
0	838387.9	-2.5	540207.8	2.9	-1524253.6	-4.9	102061.7	60065.4	3928.7	-21.8	*unstable*		
0.2 •	7674410.4	-3.0	266923.2	3.3	-7901284.7	-3.4	128060.4	75576.3	7594.0	-13.8	*unstable*		
0.2	1328794.3	-3.5	175030.9	3.4	-1352910.1	-4.2	140259.5	91814.8	5007.9	5.9	213275.4	228541.0	3.1
0.6 •	3711759.0	-3.0	398963.1	3.1	-4192346.1	-3.8	113986.1	63475.2	8617.7	-32.7	*unstable*		
0.6	-299861.3	3.6	139868.1	4.1	685162.9	-5.8	164317.3	133496.9	672.4	77.3	251657.0	265976.4	3.4
0.8 •	60596.9	-2.6	271835.0	4.3	-317262.4	-9.2	104127.7	56383.1	18120.4	-346.8	*unstable*		
0.8	15895.6	3.2	3.9	9.1	231502.0	-6.7	141655.9	86198.8	6760.7	-14.9	204750.3	224025.3	2.7
1 •	112728.6	0.3	67641.7	3.8	65424.2	-0.2	165131.5	110130.6	4482.5	21.4	*unstable*		
1	799637.6	0.6	108837.1	3.6	-1121568.0	-3.0	89115.5	35094.4	9063.5	-65.4	128946.6	142399.7	2.6
1.4 •	-427803.9	4.9	24814.6	5.8	1023273.8	-9.4	156642.6	96251.6	5962.8	11.8	228770.0	247259.9	2.9
1.4	-4939507.8	-1.8	4261.2	5.4	5191204.2	-2.4	99841.1	47636.9	6865.7	-15.5	*unstable*		

Table 4.2 Fitting parameters estimated by Abaqus for selected stress-strain curves plotted in Figure 4.4.
• indicates the stiffest response.

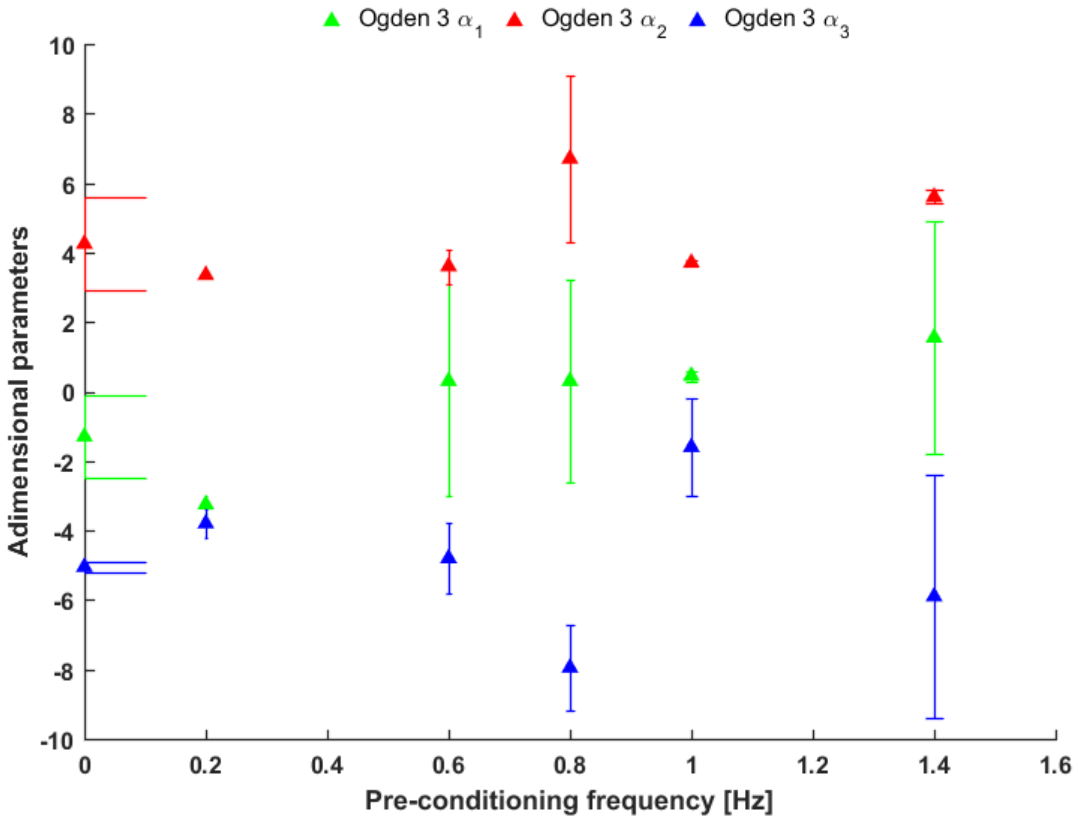

Figure 4.5 Mean (marker) and standard deviation (error bar) calculated for the adimensional fitting parameters listed in Table 4.2.

The ANOVA tests on the stiffness, evaluated at σ_{avg}, reveal that the presence of pre-conditioning generates statistically different (p = 0.0022) material elastic response. Similarly to the strips, a statistical evidence ($p = 1.17 \cdot 10^{-7}$) is observed analysing the strain values associated to σ_{avg}.

Similarly to analyses conducted for strips data sets, the fitting parameters estimated for the upper band (continuous black line) and the lower band (continuous blue line) of dumb-bells responses are listed in Table 4.2. The mean values calculated for Ogden adimensional parameters (Figure 4.5) are closer when the stress-strain results are more overlapped, the f_P being 1 Hz. However, such feature is not confirmed by the remaining parameters shown in Figure 4.6, as the minimum scatter is obtained for the f_P being 0.8 Hz.

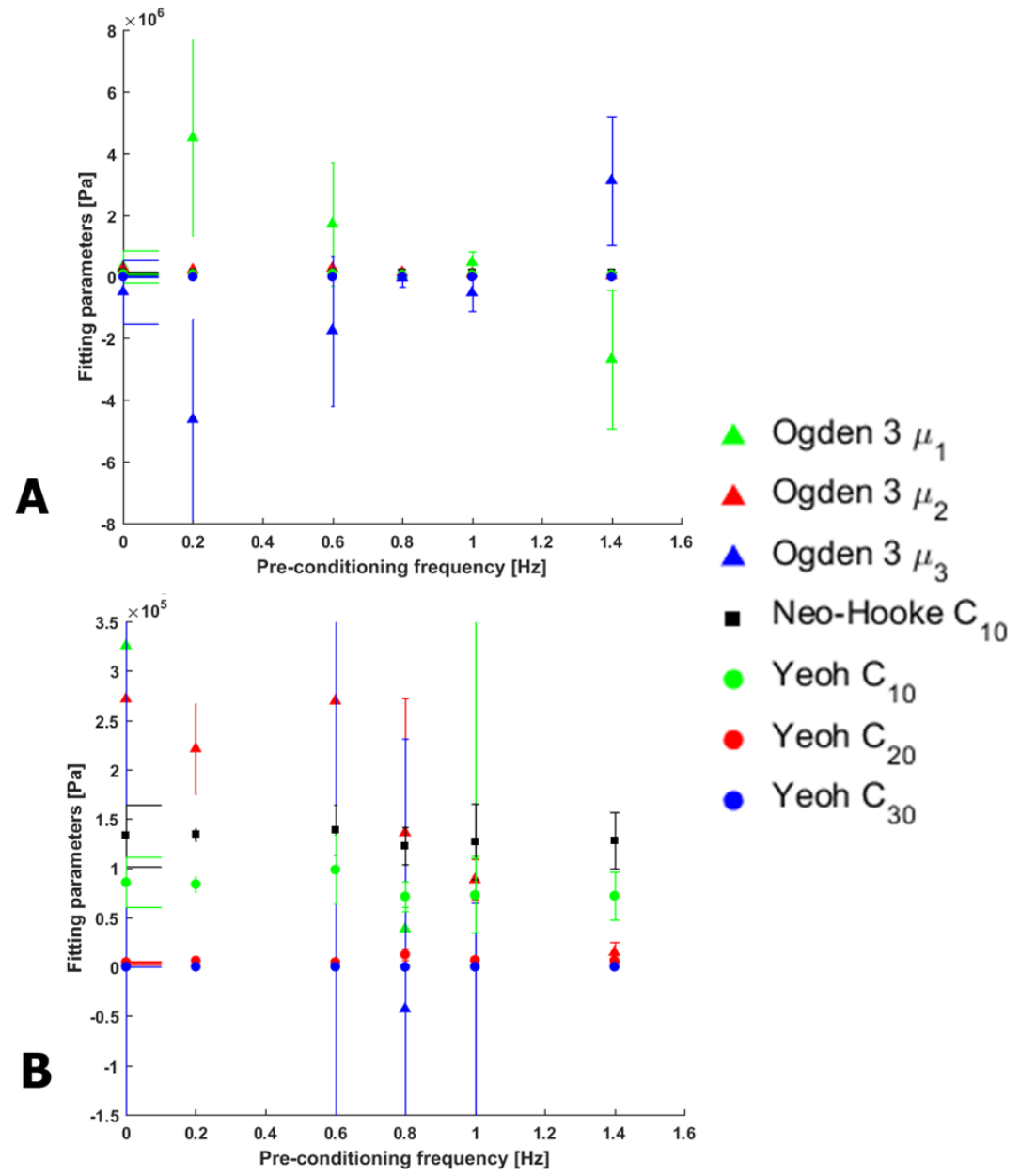

Figure 4.6 Mean (marker) and standard deviation (error bar) calculated for the fitting parameters listed in Table 4.2. Since standard deviation exhibit different order of magnitude, a zoom in of plot A is given in plot B.

Observations

In both sample shapes (strip and dumb-bell), the absence of pre-conditioning systematically generates less reproducible results, with a large range of stresses for the same interval of strains (Figs. 4.1 and 4.4).

Comparing strips (Figure 4.1) and dumb-bells (Figure 4.4) results obtained at the same f_P (0.2 Hz, 0.6 Hz and 1 Hz), ultimate stress and strain values appear greater for dog-bone shaped samples.

No clear relation between the scatter of fitting parameters (Figure 4.2, 4.3, 4.5, 4.6) and the repeatability of stress-strain responses can be highlighted. However, further considerations about the quality of the fitting will be explored in Section 6.1.1.

The explanation of how f_P might affect the mechanical characterization of the material remains unclear. Hence, this requires further investigations to a microscopic level that are beyond the scope of this work. However, according to the Brownian motion theory, natural frequency generates an unique response of molecules (Gent, 2001). Alternatively, in cluster size studies of pre-conditioned samples, a particular frequency distinguishes rigid from fragile behaviour (Bhowmick, 2008). Besides these hypotheses, no theoretical explanation has been found to the repeatable macroscopic behaviour observed only at certain frequencies.

4.2 Uniaxial tests on aortic tissue

The porcine aortas have been freshly harvested from a local slaughterhouse and frozen within 4 hours from sacrifice. The samples belonged to two different aortic districts: the thoracic and abdominal aorta. Six specimens, for each circumferential and longitudinal direction, have been cut by means of the standard metal dye, obtaining the typical dog-bone shape. Such samples have been pre-conditioned for 5 cycles at 1.2 Hz and 2 Hz and stretched at a constant cross-head speed of 0.2 mm/s. In addition, a control test without pre-conditioning has been performed. The strain acquisition has been carried out during tensile tests through a video-extensometer.

4.2.1 Abdominal samples

The reduced diameter of the abdominal aorta did not allow samples to be cut in the circumferential direction. Hence, only the longitudinal direction has been explored. In Figure 4.7, the curves display the common non linear elastic behaviour of the aortic wall.

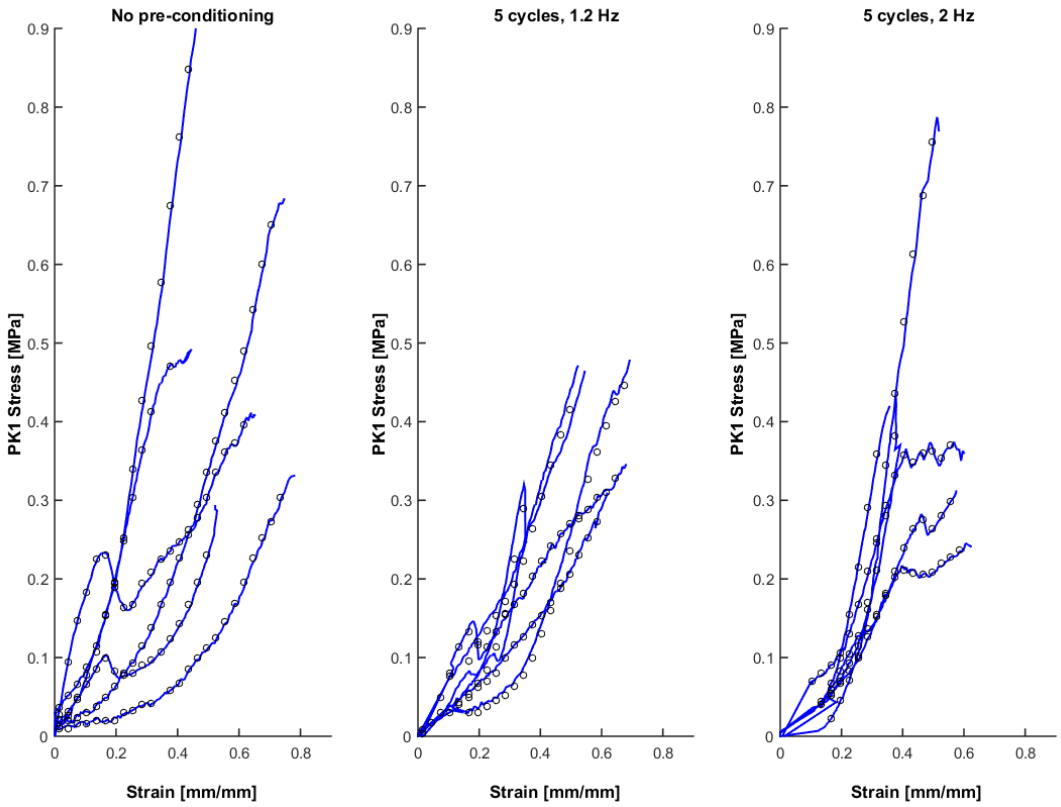

Figure 4.7 Uniaxial stress-strain response of abdominal dumb-bells, pre-conditioned for 5 cycles at selected frequencies. Data filtered by custom made script (black circles) have been imported in the FE model.

Abdominal stress-strain responses appear to be highly heterogeneous. The range of maximum stress recorded is highly variable, in the range 0.25 MPa – 0.9 MPa.

Pre-conditioning frequency [Hz]	Strain-energy function													
	Ogden					Neo-Hooke		Yeoh			Arruda-Boyce			
	μ_1 [Pa]	α_1	μ_2 [Pa]	α_2	μ_3 [Pa]	α_3	C_{10} [Pa]	C_{10} [Pa]	C_{20} [Pa]	$C_{30} =$ [Pa]	μ [Pa]	μ_0 [Pa]	λ_m
0 •	-33714854.9	-3.1	16711896.8	-1.4	17246453.8	-4.9	172337.7	104526.4	541259.2	-246599.0	*unstable*		
0	-553291.2	2.6	412634.3	2.6	246849.0	-10.9	34466.8	24912.3	3319.1	21545.8	*unstable*		
1.2 •	-7892705.3	-3.0	1348998.7	-1.4	7040232.9	-4.9	144734.0	145280.7	-96394.3	206176.1	285708.8	290955.2	5.8
1.2	-2732312.5	-2.5	1124521.8	-0.4	1788700.0	-4.8	82217.9	61827.2	80452.7	-48796.3	*unstable*		
2 •	568201.5	2.0	79144.4	4.0	-314808.9	-2.0	203400.4	175899.5	93047.8	-45711.0	401459.2	409250.3	5.6
2	-2732312.5	-2.5	1124521.8	-0.4	1788700.0	-4.8	82217.9	61827.2	80452.7	-48796.3	*unstable*		

Table 4.3 Fitting parameters estimated by Abaqus for selected stress-strain curves plotted in Figure 4.7.
• indicates the stiffest response.

Despite no repeatable behaviour being observed in any of the three tests, the stress-strain curves obtained in absence of pre-conditioning appear to cover a wider range of stress compared to other cases. As an example, selecting a strain value of 0.4, the stress range in absence of pre-conditioning is 0.068 - 0.76 MPa, for f_P being 1.2 Hz is 0.12 - 0.32 MPa and for f_P being 2 Hz is 0.21 - 0.4 MPa.

A limited number of samples display an evident non-monotonic response: around a strain value of 0.2 the stress suddenly drops. Since this feature is followed by an increase in both strain and stress amount, such behaviour could be interpreted as failure of a number of fibres within the sample. However, the subsequent collagen recruitment overcomes that alike failure.

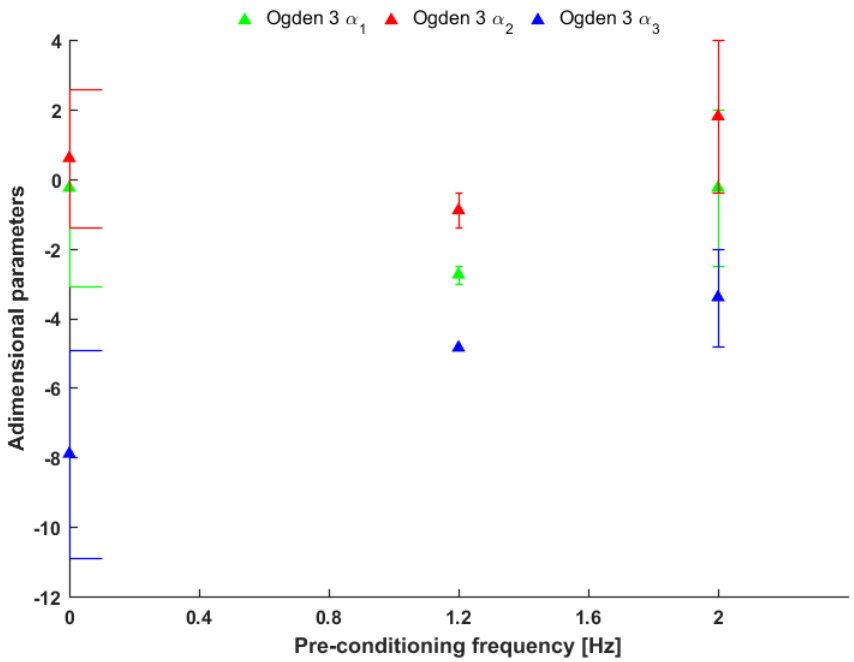

Figure 4.8 Mean (marker) and standard deviation (error bar) calculated for the adimensional fitting parameters listed in Table 4.3.

The stiffest and the softest response obtained for each f_P (Figure 4.7) have been selected to be fitted by constitutive models. As a result, the coefficients are listed in Table 4.3. However, a faster comparison is offered in Figure 4.8 and 4.9. The adimensional coefficients are significantly less scattered for f_P being 1.2 Hz (Figure 4.8). Differently,

comparing the other parameters in Figure 4.9, the model coefficients are closer when f_P is 2 Hz.

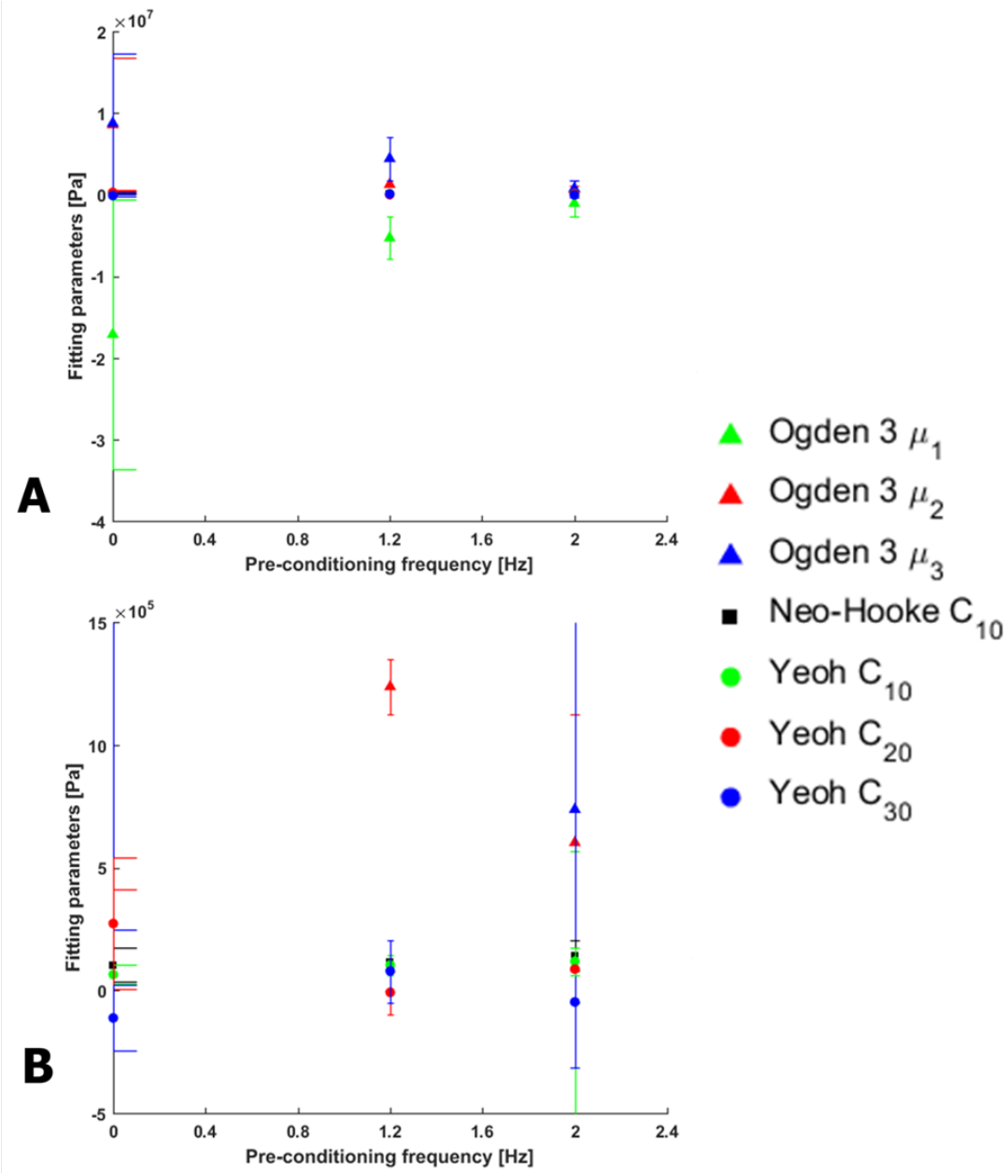

Figure 4.9 Mean (marker) and standard deviation (error bar) calculated for the fitting parameters listed in Table 4.3. Since standard deviation exhibit different order of magnitude, a zoom in of plot A is given in plot B.

Observations

Non-aneurysmal abdominal aorta walls have been rarely tested by means of uniaxial tensile tests. The results obtained in the present study can be compared with the responses obtained by Raghavan et al. (Raghavan *et al.*, 1996) for human infrarenal aorta. Athough maximum strain achieved is comparable to results in Figure 4.7, they reported a considerably higher stress of about 1.75 MPa. Such value, obtained by means of a completely different experimental protocol, may be affected mostly by the thickness measurement performed by means of a dial caliper. Similarly, Xiong et al. (Xiong *et al.*, 2008) tested samples of abdominal aorta retrieved from human cadaveric organ donors. Despite the figure captions appear not entirely clear, the maximum stress achieved are centred around the value of 1 MPa in the longitudinal direction. Their tests were performed after a different storage (4°C) and adopting a completely different protocol from the present investigation. Therefore, the values presented in Figure 4.7 appear lower in terms of stress levels, since tests could not be carried out up to rupture. However, the maximum strain achieved 0.6 is in agreement with Xiong et al. (Xiong *et al.*, 2008). Differently, Sokolis et al. (Sokolis *et al.*, 2002) obtained a wider range of strain. Although calculations are needed to compare their response from porcine aorta with Figure 4.7, they recorded about double the maximum strain. Further calculations show that the maximum stress they report is about 0.8 MPa, which has been rarely observed in this work (Figure 4.7).

4.2.2 Thoracic circumferential samples

The responses obtained from dumb-bell samples cut from thoracic aorta in the circumferential direction are displayed in Figure 4.10. The maximum stress values reached during such tests are included in a quite large range: 0.25 MPa – 1 MPa.

A surprising repeatable behaviour is observed when a f_P of 1.2 Hz is applied to the sam-

ples, as responses appear quite overlapped compared to other tests. However, selecting a strain value of 0.4, the stress range in the absence of pre-conditioning is 0.07 - 0.26 MPa, for f_P being 1.2 Hz is 0.53 - 0.77 MPa and for f_P being 2 Hz is 0.11 - 0.36 MPa. No visible difference between the absence of pre-conditioning and tests performed after a 2 Hz cycling can be observed.

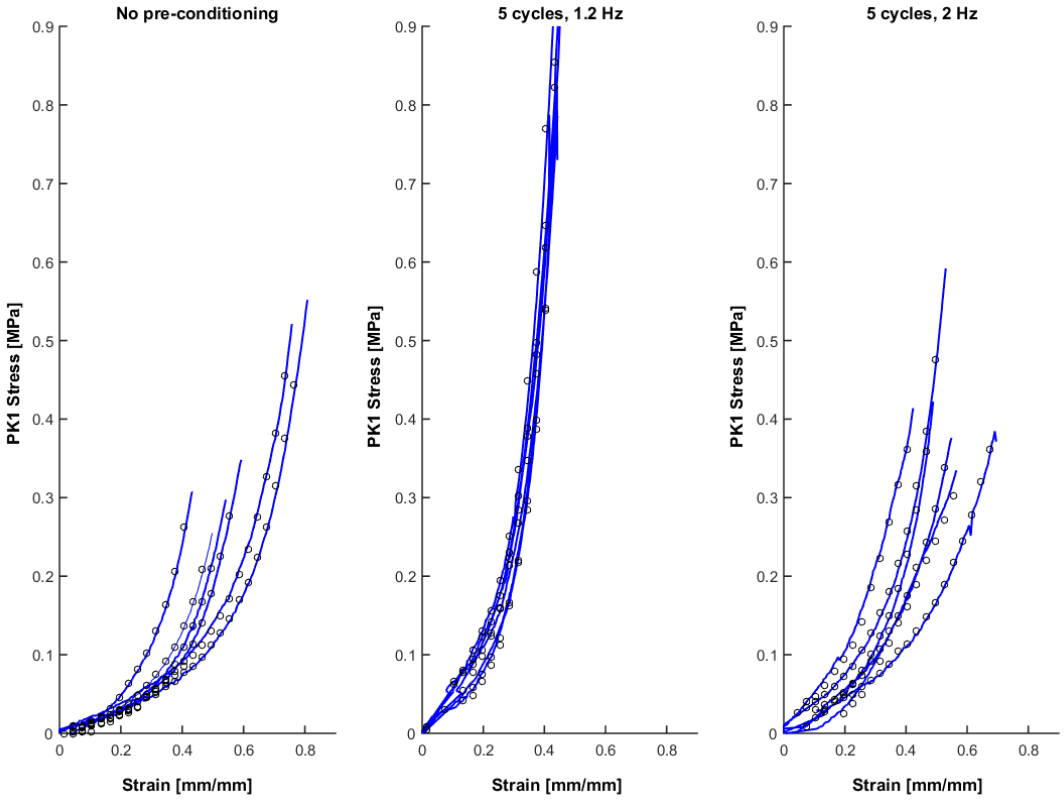

Figure 4.10 Uniaxial stress-strain response of thoracic circumferential dumb-bells, pre-conditioned for 5 cycles at selected frequencies. Data filtered by custom made script (black circles) have been imported in the FE model.

Analogously to abdominal samples, the stiffest and the softest mechanical responses (Figure 4.10) have been fitted to different constitutive models. The estimated coefficients are listed in Table 4.4. The least scattered values of adimensional parameters are observed at f_P being 2 Hz. The unusual behaviour shown at 1.2 Hz (Figure 4.10) relates to the closest mean values, however the standard deviation is significant. In contrast, Ogden remaining parameters, as well as Yeoh ones, are more scattered at 1.2 Hz (Figure 4.12).

Pre-conditioning frequency [Hz]	Strain-energy function													
	Ogden					Neo-Hooke		Yeoh			Arruda-Boyce			
	μ_1 [Pa]	α_1	μ_2 [Pa]	α_2	μ_3 [Pa]	α_3	C_{10} [Pa]	C_{10} [Pa]	C_{20} [Pa]	$C_{30} =$ [Pa]	μ [Pa]	μ_0 [Pa]	λ_m
0 •	-2845951.4	-5.4	1228710.3	-3.1	1696818.1	-9.3	34330.5	16240.8	131142.1	45445.1	*unstable*		
0	19513.0	8.3	2.5	24.4	30654.7	-2.1	35796.6	26133.7	6909.7	20647.2	*unstable*		
1.2 •	-5975573.0	17.3	4749953.9	17.5	1351683.6	15.7	97244.5	69246.5	177854.1	752810.3	192080.1	196551.9	5.2
1.2	-6143886.1	-5.4	1613871.3	-4.0	4685332.2	-7.6	40933.3	24250.6	93349.6	148253.6	*unstable*		
2 •	-3681020.0	2.0	2117255.1	4.0	1762432.1	-2.0	101292.9	84034.8	31221.4	227231.1	200033.4	204210.8	5.4
2	-564742.2	8.7	524840.3	8.9	112400.8	5.3	56046.5	39389.4	19548.7	18902.5	*unstable*		

Table 4.4 Fitting parameters estimated by Abaqus for selected stress-strain curves plotted in Figure 4.10.
• indicates the stiffest response.

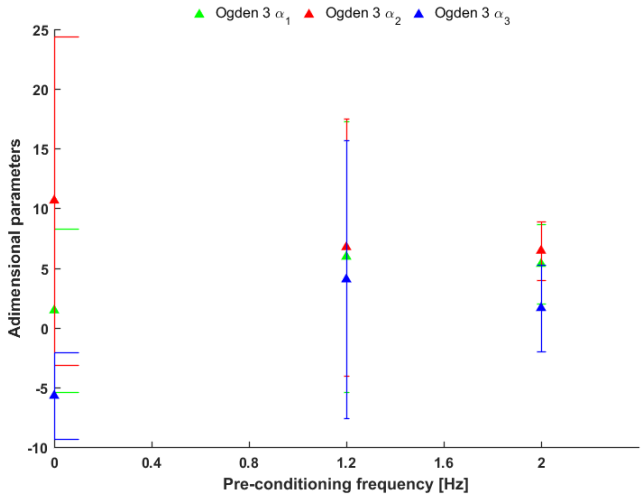

Figure 4.11 Mean (marker) and standard deviation (error bar) calculated for the adimensional fitting parameters listed in Table 4.4.

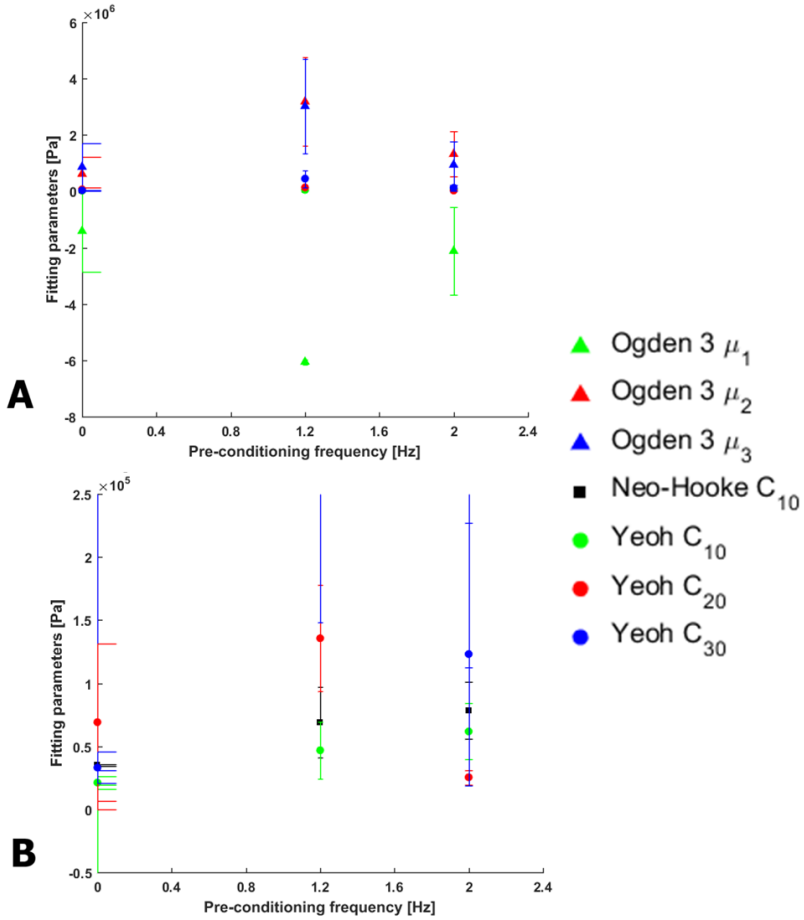

Figure 4.12 Mean (marker) and standard deviation (error bar) calculated for the fitting parameters listed in Table 4.4. Since standard deviation exhibit different order of magnitude, a zoom in of plot A is given in plot B.

4.2.3 Thoracic longitudinal samples

The behaviour of the longitudinal thoracic samples is reported in Figure 4.13. The maximum stress values recorded for thoracic longitudinal sample ranges between 0.1 MPa and 0.5 MPa.

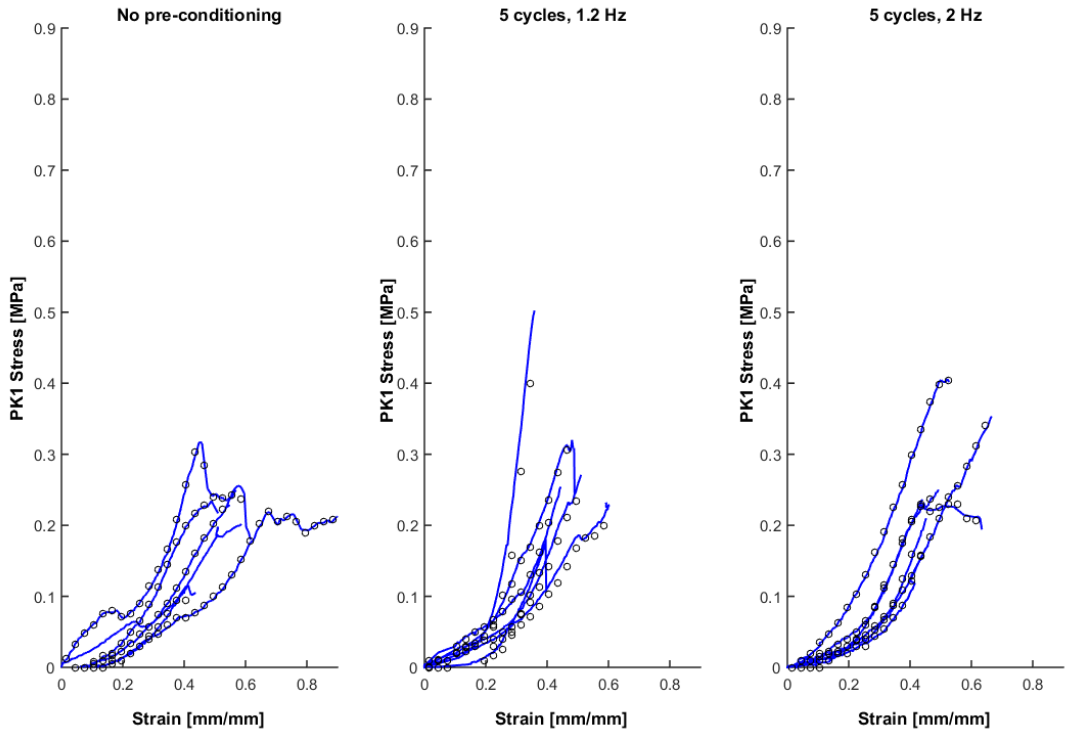

Figure 4.13 Uniaxial stress-strain response of thoracic longitudinal dumb-bells, pre-conditioned for 5 cycles at selected frequencies. Data filtered by custom made script (black circles) have been imported in the FE model.

Despite no repeatable behaviour can be observed in any of the three tests, stress-strain curves obtained in the absence of pre-conditioning cover a wider range of stress compared to other cases. As an example, selecting a strain value of 0.4, the stress range in the absence of pre-conditioning is 0.07 - 0.25 MPa, for f_P being 1.2 Hz is 0.14 - 0.23 MPa and for f_P being 2 Hz is 0.12 - 0.29 MPa.

Pre-conditioning frequency [Hz]	Strain-energy function													
	Ogden					Neo-Hooke		Yeoh			Arruda-Boyce			
	μ_1 [Pa]	α_1	μ_2 [Pa]	α_2	μ_3 [Pa]	α_3	C_{10} [Pa]	C_{10} [Pa]	C_{20} [Pa]	$C_{30} =$ [Pa]	μ [Pa]	μ_0 [Pa]	λ_m
0 •	-31880695.6	4.4	14495917.3	5.2	17675593.7	3.4	94215	120115.9	-250744.9	469839.2	185992.4	188698.4	6.5
0	1594367.5	-0.1	42.5	20.7	-1690790.9	-2.1	13101.7	-3623.6	71800.6	-23506.4	*unstable*		
1.2 •	-5262727.3	-2.5	1918373.9	0.02	3478178.8	-5.4	48939.5	20710.8	131408.3	11114.5	*unstable*		
1.2	-1954260.7	11.7	1830946.0	11.7	307554.8	-25.0	45526.6	43974.7	-46727.5	141243.7	*unstable*		
2 •	-1061570.1	1.4	2509674.8	2.3	-1393255.8	1.4	95721.5	46878.9	199169.3	-88779.1	*unstable*		
2	-4617701.9	-1.8	1681069.2	0.2	3054994.7	-4.1	41481.3	17358.3	64680.8	2126.7	*unstable*		

Table 4.5 Fitting parameters estimated by Abaqus for selected stress-strain curves plotted in Figure 4.13.
• indicates the stiffest response.

Fitting parameters obtained for the stiffest and the softest response are listed in Table 4.5. The adimensional parameters are compared in Figure 4.14: the minimum scatter is clearly related to f_P being 2 Hz. Similarly, the remaining parameters are significantly closer at the same frequency and comparable to f_P being 1.2 Hz (Figure 4.15).

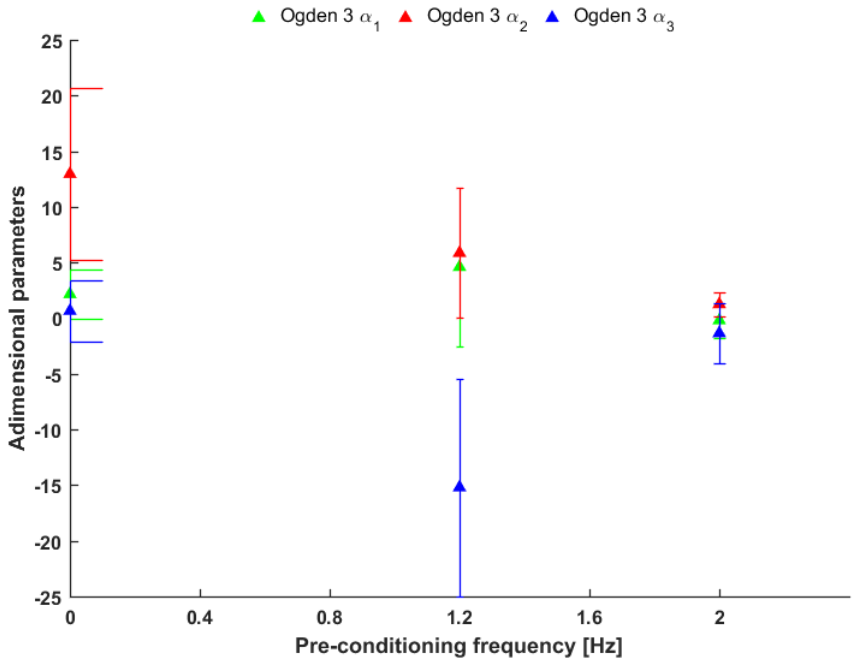

Figure 4.14 Mean (marker) and standard deviation (error bar) calculated for the adimensional fitting parameters listed in Table 4.5.

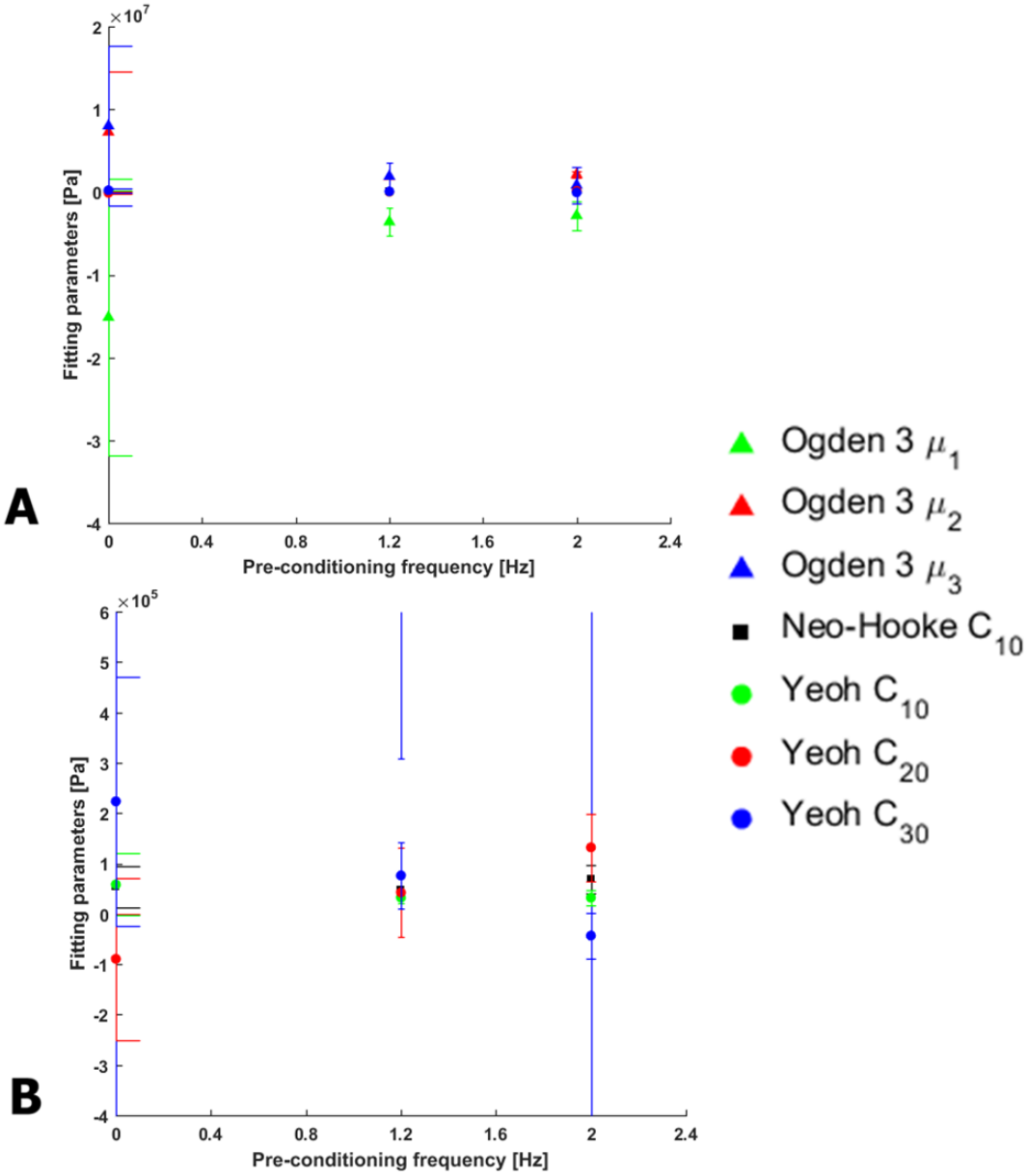

Figure 4.15 Mean (marker) and standard deviation (error bar) calculated for the fitting parameters listed in Table 4.5. Since standard deviation exhibit different order of magnitude, a zoom in of plot A is given in plot B.

Observations

The analyses conducted on fitting parameters show that the highest f_P generates the least scattered coefficients for the thoracic samples (Figure 4.11, 4.12, 4.14 and 4.15). Thoracic results, displayed in Figure 4.10 and 4.13, may be compared with the most recent mechanical characterization of Pena et al. (Peña *et al.*, 2015). Their Cauchy

stress-stretch plots show a maximum stress, mean value of all samples, of about 0.14 MPa in the circumferential direction and 0.16 MPa in the longitudinal one. Such values, converted into engineering stress, have been reached for analogous strain levels during the present research, but a significant wider range of results has been covered (Figure 4.10). Although the same definition of zero load point has been adopted, they performed a remarkably different pre-conditioning stage, consisting in three cycles carried out at increasing load values.

4.3 Equi-biaxial tests on aortic tissue

Similarly to uniaxial tests, the biaxial mechanical behaviour of the porcine aortas has been investigated for the thoracic and abdominal districts. For each of them six square samples (20 mm x 20 mm), aligned along the circumferential and longitudinal direction, have been prepared and tested in load control (Figure 4.16).

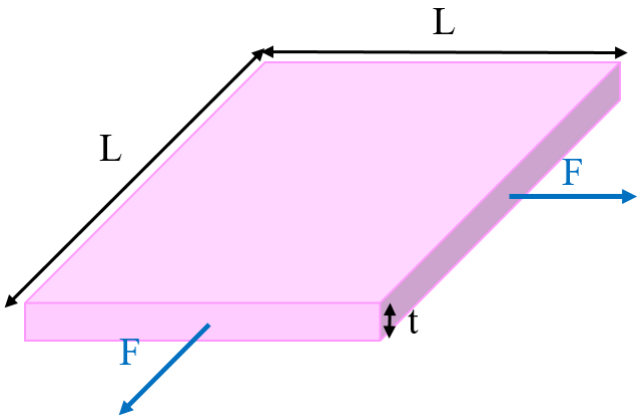

Figure 4.16 Equi-biaxial tests apply the same force (F) along each direction of the square sample. However, the stress-strain response for an anisotropic material is expected to be different depending on the direction.

The Green-Lagrange strain field has been mapped for each specimen through DIC processing. The first Piola-Kirchhoff stress has been evaluated over the specific thickness

of each sample, which has been estimated in the undeformed configuration. Despite the same value of stress being expected, the aortic anisotropy generates slightly different stress-strain responses along each direction.

4.3.1 Abdominal samples

Abdominal results, displayed in Figure 4.17, highlight the wall anisotropy. The longitudinal direction appears generally stiffer compared to the circumferential one (Figure 4.18). However, the response observed below strain 0.1 occurs to be substantially isotropic.

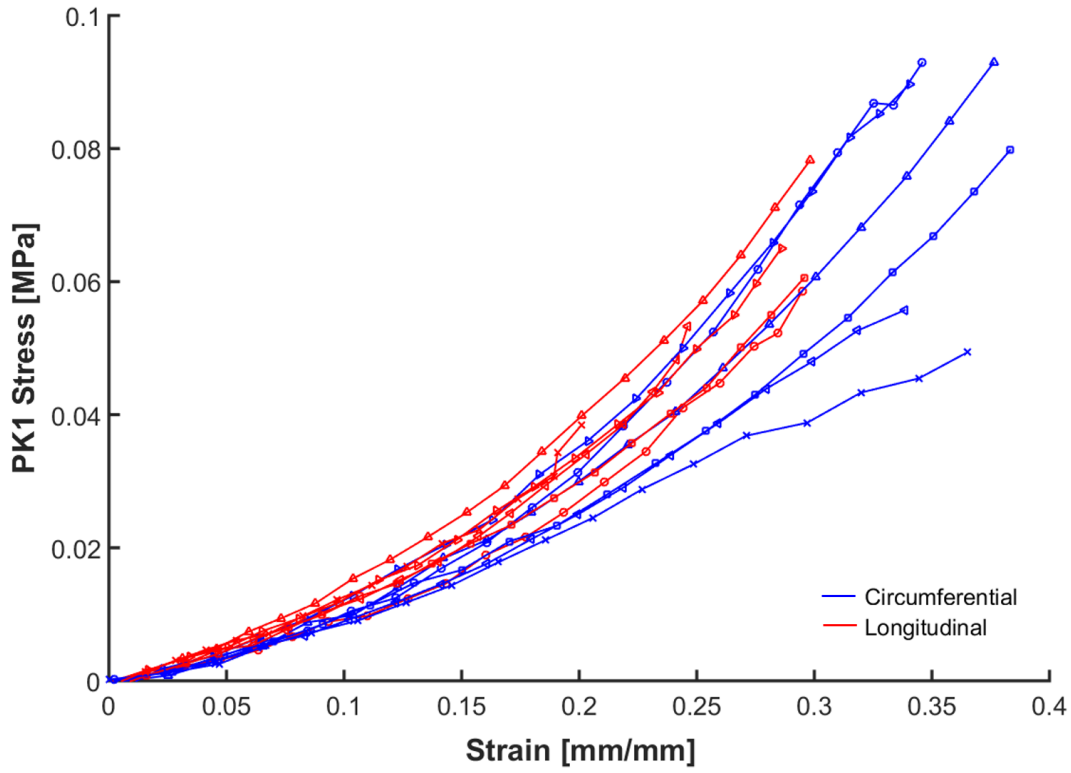

Figure 4.17 Biaxial stress-strain response of abdominal aorta, previously pre-conditioned for 5 cycles. Markers couple the longitudinal (red) and circumferential (blue) response obtained from the same sample.

In terms of maximum stress levels reached, the longitudinal constituent exhibits lower stress values compared to the circumferential one. Overall such values range from

0.05 to 0.09 MPa. Among the same sample, the minimum difference between the circumferential and longitudinal stress is 0.002 MPa. In terms of strain, highest values range from 0.24 to 0.38. However, for none of the sample the difference in strain between the two directions exceeds 0.09.

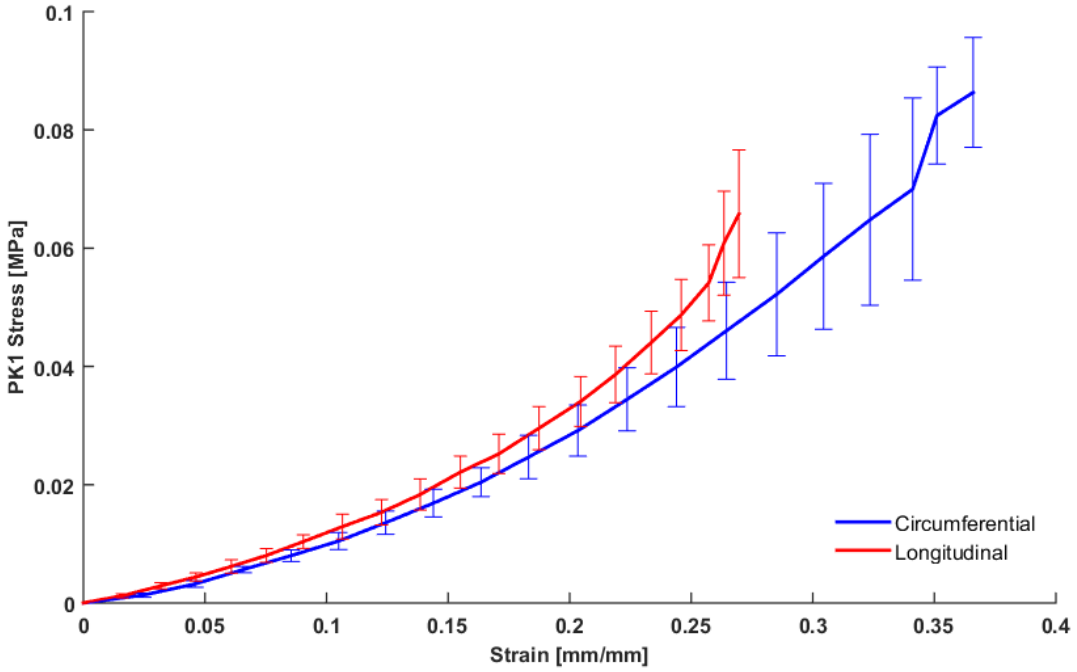

Figure 4.18 Biaxial stress-strain response of abdominal aorta. Each line averages the values of all 6 samples tested, while errorbars show the standard deviation.

Observations

The mechanical response obtained from abdominal aorta (Figure 4.17) is comparable to the work of Vande Geest et al. (Vande Geest *et al.*, 2006) in terms of stress, being the maximum in both circumferential and axial direction approximately 0.08 MPa. In contrast, their work highlights that strain levels never exceed 0.15. This reduced distensibility compared to Figure 4.17 may be explained because of the different pre-conditioning protocol (9 cycles) and considering that they harvested the tissue samples from human autopsy. Although the anisotropy is not substantial, the ratio between peak Green strain values shows that the axial direction appears generally stiffer than the

circumferential one in the healthy abdominal aorta. Such result is in agreement with this chapter findings (Figure 4.17).

4.3.2 Thoracic samples

Thoracic responses, reported in Figure 4.19, confirm the anisotropic behaviour of the aorta. Once again, the circumferential component represents the softest one, reaching higher stress and strain values compared to the longitudinal one. However, the longitudinal constituent exhibits a stiffer behaviour (Figure 4.20).

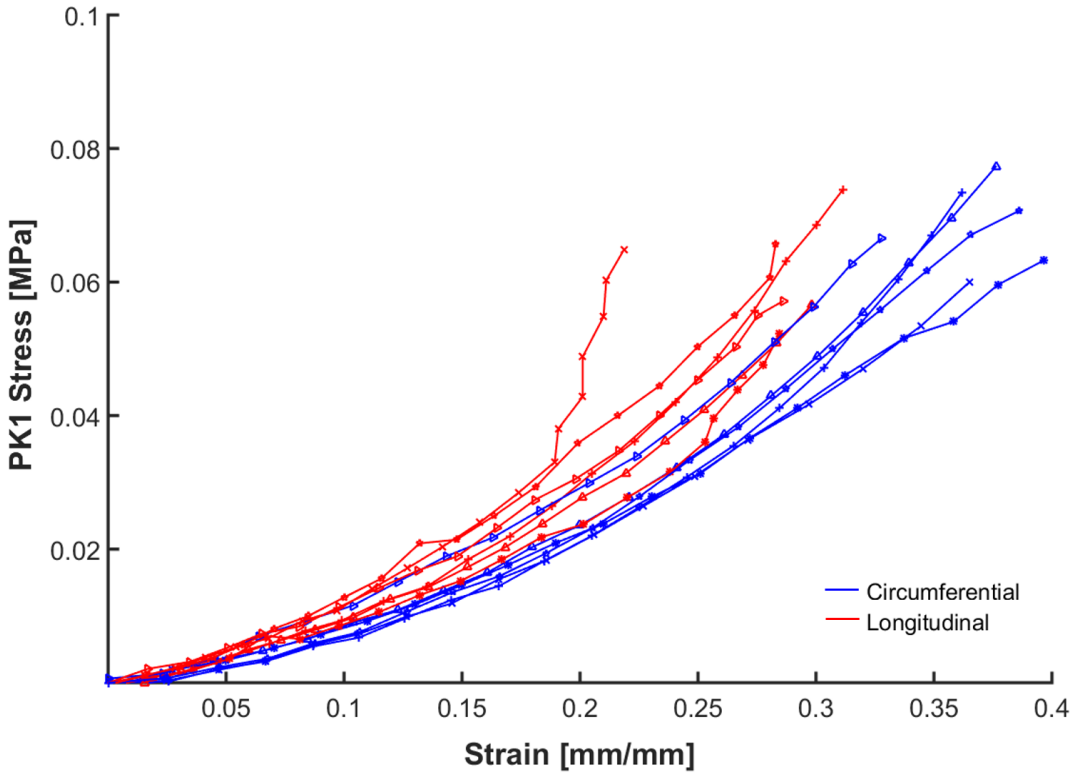

Figure 4.19 Biaxial stress-strain response of thoracic aorta, previously pre-conditioned for 5 cycles. Markers couple the longitudinal (red) and circumferential (blue) response obtained from the same sample.

Overall maximum stress levels range from 0.05 to 0.08 MPa. However, among the same sample, the scatter between the circumferential and longitudinal stress does not

exceed 0.02 MPa. In terms of strain, highest values range from 0.21 to 0.38. Such gap represents the maximum achieved within a sample, while the minimum difference recorded is 0.05.

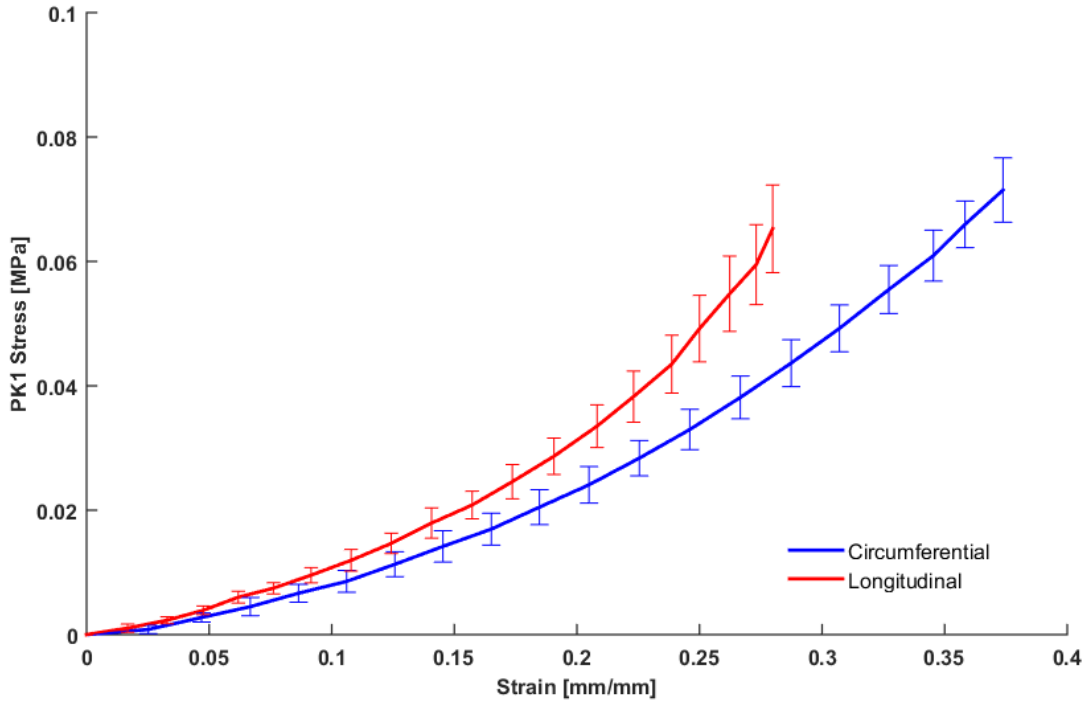

Figure 4.20 Biaxial stress-strain response of thoracic aorta. Each line averages the values of all 6 samples tested, while errorbars show the standard deviation.

Observations

Although a load controlled equi-biaxial test similar to the present study has been performed, Pena et al. (Peña *et al.*, 2015) found that for thoracic samples the circumferential direction is evidently stiffer than the longitudinal one. Thus, results presented by Pena et al. find no clear justification, since responses in Figure 4.19 show the longitudinal component to be generally stiffer. In addition, they report a reduced distensibility for analogous maximum stress levels (0.08 MPa). They adopted a stress rate of 2 kPa/s for 35mm x 35mm samples, which is, for their thickest specimen, equal to the value specified in Chapter 3 (0.2 N/s). A slower speed rate could certainly not justify their inferior level of strain and the use of a warm bath during the tests could unlikely be

responsible for such behaviour.

4.4 Comparisons of experimental data

Uniaxial responses collected for abdominal (Figure 4.7) and thoracic (Figures 4.10 and 4.13) porcine aortas are compared in Figure 4.21, taking into account the stiffest and softest curves.

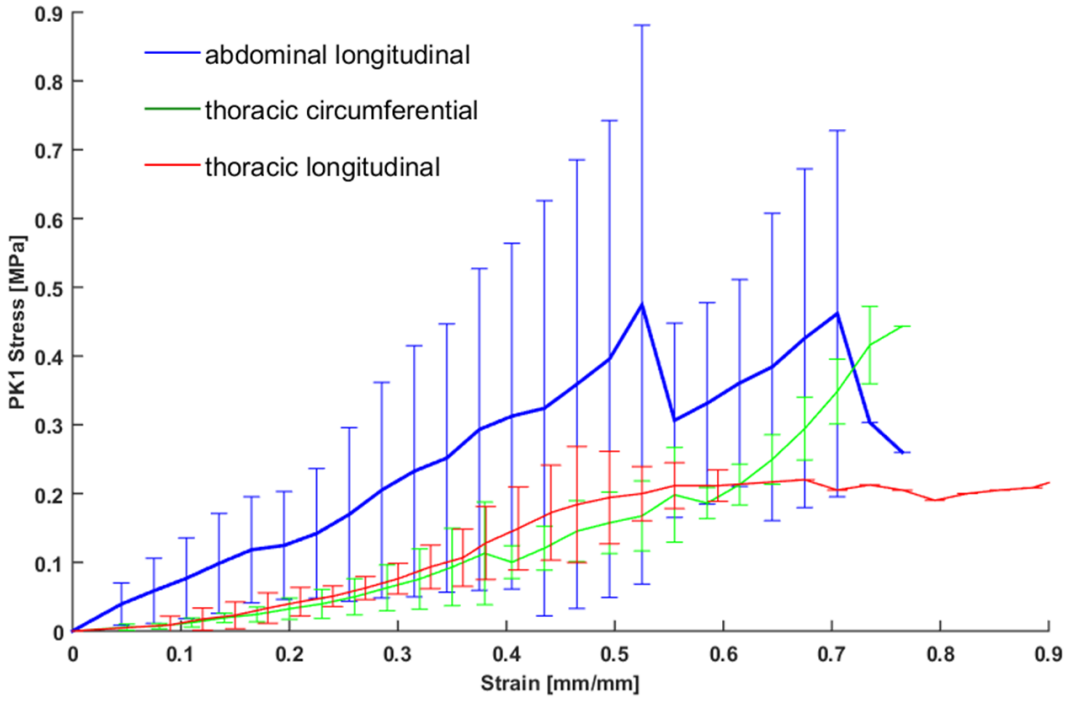

Figure 4.21 Comparison of uniaxial stress-strain responses of porcine aorta: abdominal aorta in the axial direction (blue), thoracic aorta in circumferential (green) and longitudinal (red) direction. Each line averages the values of all 6 samples tested, while errorbars show the standard deviation.

Abdominal responses cover a much wider range both in terms of stress and strain compared to thoracic ones. Focusing on softest behaviours, no difference can be appreciated up to strain 0.67, over which responses diversify: while the thoracic circumferential (green) increases the stress exponentially, the corresponding axial component (red)

reaches a plateau. On the other end, stiffest thoracic responses differ only in the range of strain 0 - 0.2, displaying a different concavity (Figure 4.21).

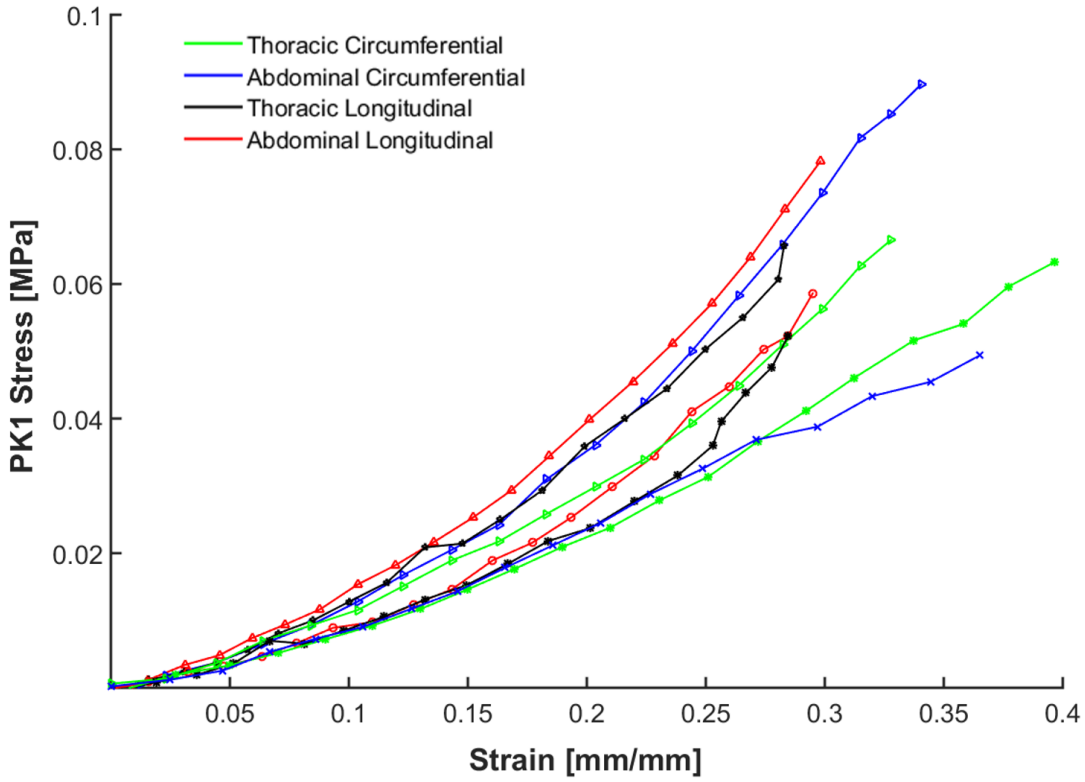

Figure 4.22 Comparison of biaxial stress-strain responses of porcine aorta: thoracic aorta in circumferential (green) and longitudinal (black) direction, abdominal aorta in the circumferential (blue) and axial direction (red).

Since the biomechanical response of aortic tissue to uniaxial loading conditions is insufficient for the characterization of its three-dimensional mechanical behaviour (Vande Geest *et al.*, 2006), planar biaxial tests have been carried out. Superimposing the biaxial response of abdominal and thoracic porcine aortas no pronounced differences can be appreciated (Figure 4.22). In order to compare the limits, only the stiffest and softest curves are reported.

In terms of circumferential components, abdominal responses cover a wider range of stress compared to the thoracic. Furthermore, thoracic results cover the softest area of abdominal results. Looking at the longitudinal behaviours, abdominal stress strain

curves appear generally stiffer than the thoracic. In this case, the amplitude of stress ranges are quite similar.

Finally, as additional outcome of this experimental campaign, an interesting analogy between the uniaxial and biaxial tensile tests is available. While uniaxial tests allow greater deformations of the sample, biaxial tests restrain considerably the range of stress and strain that the sample may experience.

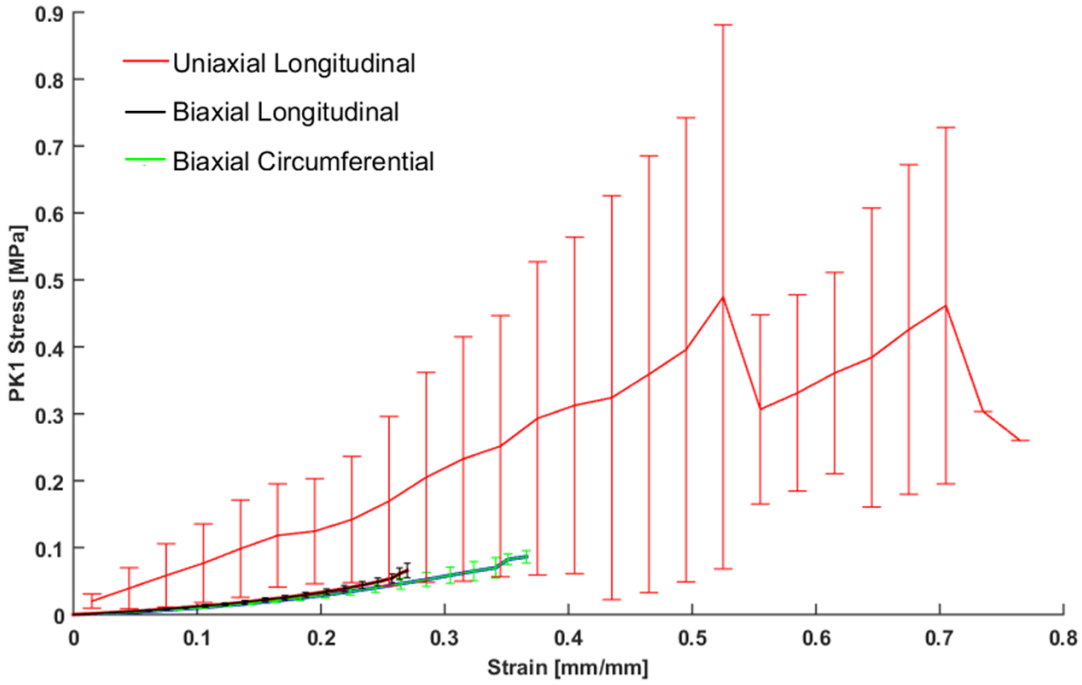

Figure 4.23 Comparison of uniaxial (red) and biaxial stress-strain responses of abdominal aorta. Each line averages the values of all 6 samples tested, while errorbars show the standard deviation.

This effect is quite clear in Figure 4.23, where abdominal responses are compared. Dog-bone shaped samples along the axial direction (red) cut out the circumferential response, thus maximum stress of 0.5 MPa has been recorded (Figure 4.23). Differently, an equi-biaxial test performed on a square specimen ensure that both components are subjected to the same stress. Hence, anisotropy effects are limited.

Similarly, thoracic behaviours obtained from uniaxial tests display a different magnitude in terms of stress and strains compared to biaxial tests. Furthermore, the longitudinal component appears softer than the circumferential as a result of uniaxial deformations. On the contrary, such axial component becomes predominant during biaxial tests, where it exhibits a generally stiffer behaviour (Figure 4.24).

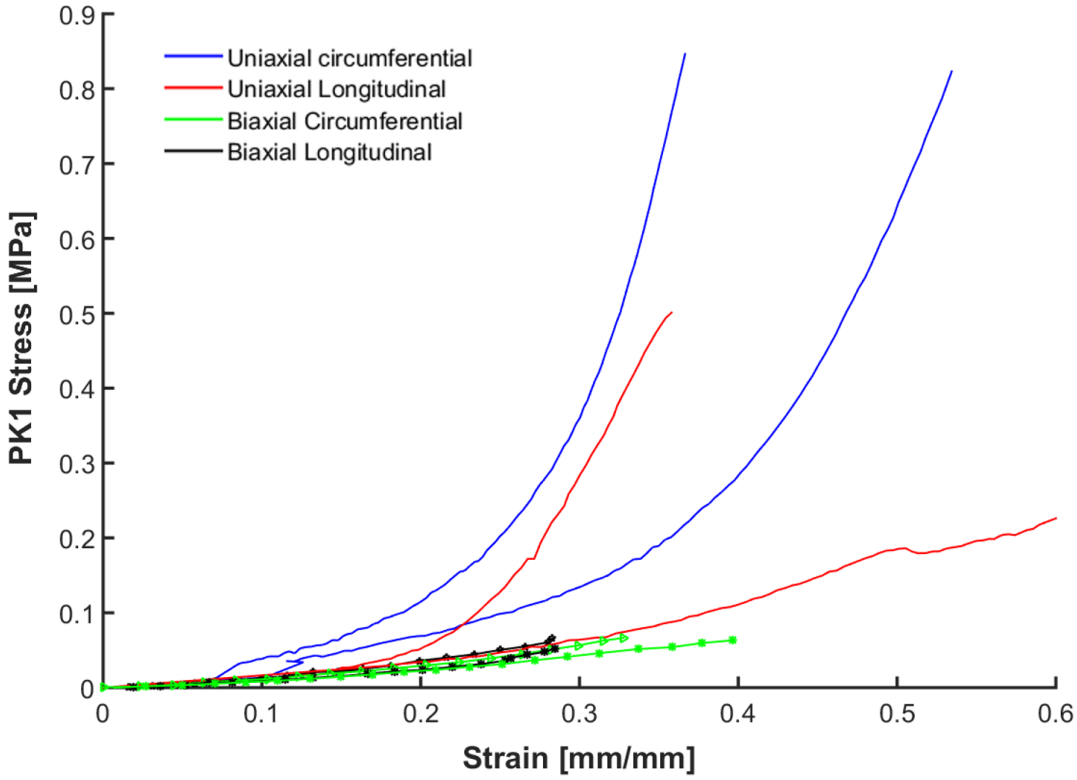

Figure 4.24 Comparison of uniaxial and biaxial stress-strain responses of thoracic aorta.

Concluding, uniaxial tests are remarkably simpler to perform compared to biaxial examinations. However, characterizations of dumb-bells show considerably stiffer mechanical responses, larger strain and higher stress than square samples. Furthermore the anisotropic behaviour of the thoracic aorta is not highlighted by comparing uniaxial outcomes (Figure 4.21), while it looks clear looking at biaxial results (Figure 4.22). It is worth emphasizing that biaxial tensile tests executed in force control are challenging and can be performed only by certain facilities. Thus, great efforts were needed to

collect carefully the experimental responses listed in the present Chapter aiming to design accurate finite element models.

Chapter 5

Computational models

The formation of aortic aneurysm resembles, from the mechanical point of view, the problem encountered in structural engineering of the plastic deformation, permanent bulging, and subsequent rupture of a tube under the effect of a continuous oscillatory internal pressure (Lasheras, 2007). However, in the case of arteries, the problem to be analyzed is more intricate, since the walls are composed of a complex anisotropic structure (Humphrey, 2002). Therefore, the present chapter reports the details of FE models designed to approach the problem of aneurysm formation. Two main approaches are presented: isotropic (Section 5.2) and anisotropic (Section 5.3) modelling.

First of all, a cylindrical geometry modelling a generic rubber-like material is reported in Section 5.2.1. Thus, experimental data-set obtained from rubber trials, shown in Section 4.1, are imported into the model to quantify the effect of different experimental features, such as f_P. The second model (Section 5.2.2) is intended as a simplified aorta, with the geometry still being cylindrical. Since material properties derive from uniaxial tensile test, this model is isotropic and studies two different aspects: a physiologic cardiac activity and the bulging instigation.

In Section 5.3, a sequence of four models is presented to detail a challenging implementation of FE anisotropic models. The thoracic and abdominal mechanical responses

taken into account are based on the biaxial tensile tests.

5.1 Preliminary assumptions

An arterial wall in the unloaded configuration is not stress free (Chuong & Fung, 1986; Vaishnav & Vossoughi, 1987). The role of the so called *residual stresses* can be revealed by making a radial cut in a ring segment of an artery: as the cut ring springs open, the resulting arc- shaped specimen approaches the stress-free state. Such residual stresses give rise to residual strains.

However, these stress levels are not large in comparison with the *in vivo* stress in the arterial wall (Vaishnav & Vossoughi, 1987). Furthermore, uniaxial and biaxial testing (Section 3.2) remove the sample curvature, and do not take into consideration the residual stress characterized by the opening of an unpressurized aortic segment when it is cut longitudinally (Labrosse *et al.*, 2009). Labrosse *et al.* (2009) also observed no appreciable differences in material constants whether or not residual stress was taken into account. In a classic thick-walled cylinder under pressure, the circumferential and longitudinal stresses are expected to be highest at the lumen, and decrease radially. In the case of a pressurized cylinder with residual stress, it is excepted that residual stresses decrease the stress gradient across the wall under pressurization (Labrosse *et al.*, 2009). The quantification of this aspect is not accounted for among the objectives of the present study.

Previous studies assumed the stress in the load-free configuration, in which the arterial wall is not subjected to any loads, to be negligible (Georgakarakos *et al.*, 2010; Raghavan & Vorp, 2000; Wang *et al.*, 2002). The same assumption has been made for models presented in the following sections.

Further assumptions on the aortic wall structure were taken. Although aorta consists of three layers (Section 1.1.3), only a single layer (Badel *et al.*, 2011; Doyle *et al.*,

2007; Lee *et al.*, 2014; Maher *et al.*, 2012a) has been modelled in the present study. Such originates directly from the experimental methodology, since layers have not been tested separately (Section 3.1). Thus, the overall response of the aortic samples has been assigned to the computational model of the wall. In addition, the wall micro-structure has been assumed homogeneous, as its histology has not been investigated during the experimental testing.

Finally, no contact with the spine and organs was simulated.

5.2 Isotropic models

In literature, arteries are widely modelled as hollow tubes (Alhayani *et al.*, 2013, 2014; Avril *et al.*, 2010; Badel *et al.*, 2011). Among these, the simplification of healthy aortic geometry in cylindrical models has been previously adopted (Scotti *et al.*, 2008; Zhao *et al.*, 2008).

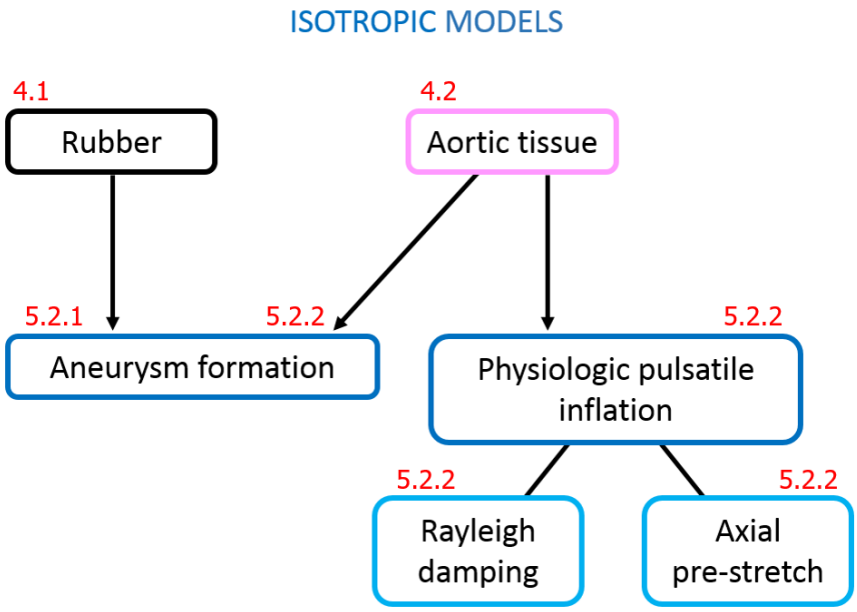

Figure 5.1 Schematic outline of the FE analyses performed for rubber and aortic material properties by means of isotropic models. Red numbers indicate the Sections in which experimental data have been presented (Chapter 4) and each model is detailed. Data obtained from aortic tissue have been used to perform two different analyses (blue boxes). Two approaches (light blue boxes) were attempted to simulate the physiologic pulsatile inflation.

Besides, isotropic modelling is based on experimental data collected from uniaxial tensile tests and post-processed. Such simplified design is a valuable step in carrying out preliminary buckling evaluations by means of the Riks algorithm. A graphical outline of the isotropic models that will be introduced in the subsequent sections is displayed in Figure 5.1.

5.2.1 Modelling a rubber tube

The main aim of the simulations based on rubber mechanical responses is to highlighting the influence of pre-conditioning frequency adopted during the experimental session on the measured mechanical properties of the tissue. In order to simulate the inflation of a cylindrical distensible tube, a circular tube is created using Abaqus (Dassault Systèmes S.A., France), in accordance with a typical geometry extensively used in literature Shi and Moita (Shi & Moita, 1996) to assess aneurysm formation (Bucchi & Hearn, 2013b). Thus, dimensions of the distensible tube are: external radius 10 mm, thickness 1 mm and length 200 mm. Four node shell elements with reduced integration (S4R) (Gonçalves *et al.*, 2008; Lopes *et al.*, 2007) are adopted to mesh the tube with a radius equal to 9.5 mm, representing the radius of the middle plane between the internal and external cylindrical surface.

A mesh sensitivity study is carried out to prove independence of results from the adopted discretization, and at the same time to optimize the computational cost. The coarsest mesh (Mesh 1) is formed by 8 elements along the circumference and 44 elements along the longitudinal direction, for a total number of 352 elements. Subsequent mesh refinements are obtained doubling elements in both directions. Hence, Mesh 2 is constituted by 1408 elements, Mesh 3 by 5632 elements and the finest Mesh 4 by 22528 elements (Figure 5.2).

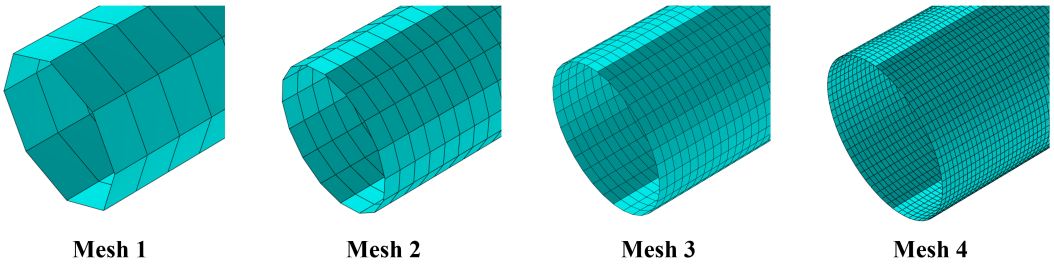

Figure 5.2 Mesh sensitivity study. Four different refinements are evaluated to understand which one generates results independent from the discretization.

As boundary conditions, both tube ends are fully constrained (suppressing displacements and rotations). In order to analyse eventual elastic instability during inflation, the modified Riks method, previously introduced in Section 2.4.3, is adopted. This algorithm provides a load proportional factor (LPF) to be interpreted as a multiplier of the initial arbitrary load (pressure) applied to the lumen surface, being 1 kPa for this model. Below the maximum LPF, the model deforms uniformly. The peak, instead, represents the critical pressure that causes the aneurysm formation, hence instability. The experimental data imported in the model are fitted using strain-energy functions reviewed in Section 2.2.2: Ogden, Neo-Hookean, Arruda-Boyce and Yeoh.

As conclusion of the mesh sensitivity study, the critical pressure values have been evaluated for three strain-energy functions: Ogden 2^{nd} order, Neo-Hookean and Arruda Boyce. As showed in Figure 5.3, Mesh 3 appears as the best compromise between computational costs and results, as the predicted critical pressure value differs 0.4% to the amount computed for the finest mesh.

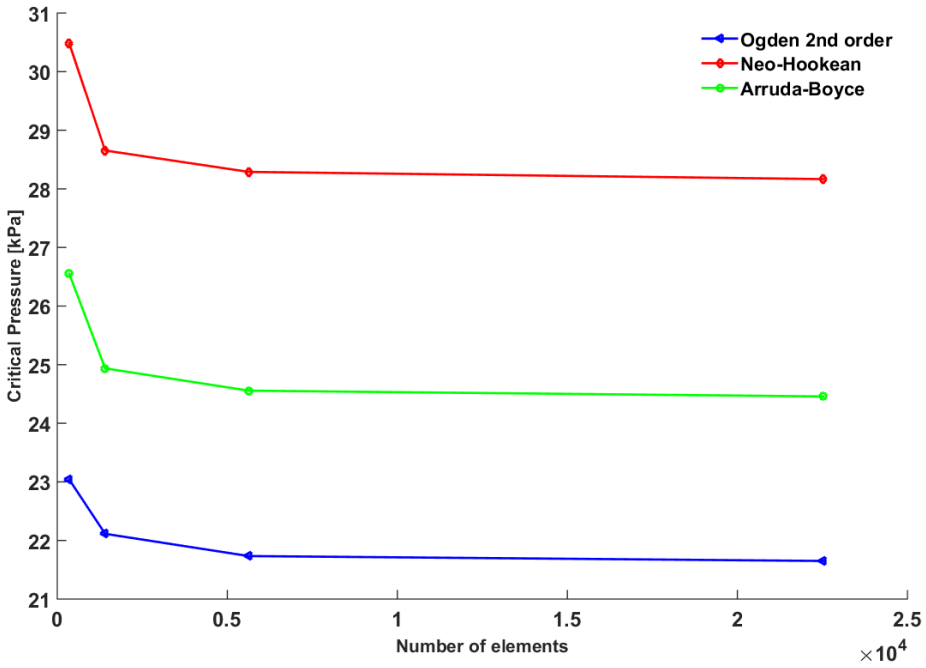

Figure 5.3 Critical pressure values evaluated for three strain-energy functions as part of the mesh sensitivity study. Mesh 3 (5632 elements) produces quite similar results to Mesh 4 (22528 elements).

5.2.2 Modelling an idealized aorta

Similarly to the previous model, the aortic geometry is simplified to a hollow cylinder with radius equal to 10 mm (Wang & Parker, 2004) to represent the middle plane section and length 200 mm. Such geometry is adopted for both the thoracic and abdominal segment. Hence two models with identical geometry and different material properties are analysed. The thickness of each model has been assumed to be the average value estimated from experimental tests: 2.5 mm for the thoracic and 1.64 mm for the abdominal aorta. Such values have been obtained by means of the optical methodology presented in Section 3.3.

A mesh sensitivity was carried out (Figure 5.4), keeping an element aspect ratio of about 1. A final mesh of 3264 elements (32 elements in circumferential direction and 102 elements in longitudinal direction) was selected. Once again, a four node shell elements with reduced integration (S4R) were adopted to mesh the geometry (Badel

et al., 2013; Raghavan & Vorp, 2000).

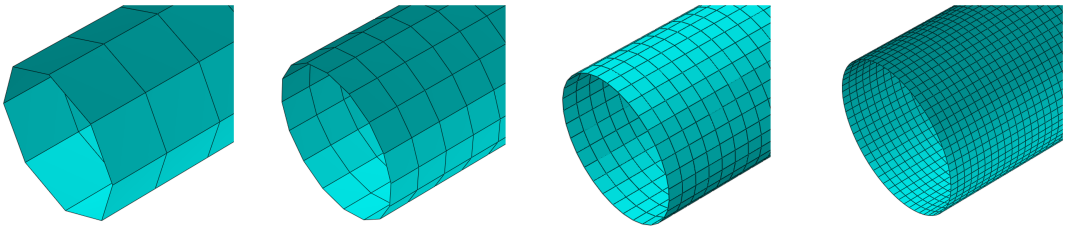

Figure 5.4 Mesh sensitivity study. Four different refinements are evaluated to understand which one generates results independent from the discretization.

Similarly to the previous rubber model, the critical pressure has been explored: Mesh 3 appears to be the best discretization, as reported in Table 5.1.

The isotropic modelling of the aortic wall is based on the fitting of experimental data collected from uniaxial tensile tests. Hence, the fitting is attempted by several strain-energy functions: Ogden, Neo-Hookean, Arruda-Boyce, Yeoh and Marlow.

Mesh	Number of elements	Critical pressure [kPa]
1	208	13.0025
2	816	12.08
3	3264	11.916
4	13056	11.877

Table 5.1 Critical pressure values evaluated for Neo-Hookean strain-energy function as part of the mesh sensitivity study.

Applying a physiologic load on idealized geometry

The physiologic model aims at exploring the effect of experimental thickness measurement on radial displacement (or deformation) and stress distribution in healthy conditions. Such analysis represents a typical preliminary stage to study arterial in-

stability (Badel *et al.*, 2013). Two FEM approaches have been explored to model a stable aortic response under physiologic pulsatile inflation: the first is based on the introduction of Rayleigh damping, the second applies a pre-stretch to the model.

Rayleigh damping The equation of motion of a linear dynamic system can be written as

$$M\ddot{x} + C\dot{x} + Kx = f \tag{5.1}$$

where M, C and K are the mass, damping and stiffness matrices and x and f are displacement and force vectors, respectively. Due to the problems of obtaining a system's damping information, there is no practical way of forming the physical damping matrix by using the finite element method even though damping exists in most mechanical systems or structures. A common approach is represented by the Rayleigh, decomposed as:

$$C = \alpha M + \beta K \tag{5.2}$$

where α and β are arbitrary constant coefficients (Liu & Gorman, 1995). In FEM, damping is a material property specified as part of the material definition. The α factor introduces damping forces caused by the absolute velocities of the model and so simulates the idea of the model moving through a viscous ether, so that any motion of any point in the model causes damping. Such a damping factor gives a damping contribution proportional to the mass matrix for an element. The β factor introduces damping proportional to the strain rate, which can be thought as damping associated with the material itself. Although viscous effect can be captured better by fluid-dynamic studies, Rayleigh damping represents an attempt to take into account the visco-elastic nature of the aortic wall in this study.

Since the model may have quite general nonlinear response, the concept of stiffness

proportional damping must be generalized, since it is possible for the tangent stiffness matrix to have negative eigenvalues (which would imply negative damping). To overcome this problem, β is interpreted in Abaqus as a viscous component, which creates an additional damping stress. This damping stress is added to the stress caused by the constitutive response at the integration point when the dynamic equilibrium equations are formed, but it is not included in the stress output (Dassault Systèmes, 2014).

Mass proportional damping factor α	**Stiffness proportional damping factor** β
0.0005	0.001
0.001	0.002
0.01	0.01
0.01	0.02
0.01	0.1
0.02	0.01
0.03	0
0.1	0.01
1	0
2	0
5	0
9	0
10	0
10	0.001

Table 5.2 Combinations of Rayleigh damping coefficients attempted to describe aortic tissue in Abaqus.

Firstly, a transient dynamic model was conceived. In order to avoid excessive circumferential and longitudinal fluctuations during the cardiac cycle, Rayleigh damping has

been applied to model the energy dissipation.

Despite the Rayleigh approach counts damping weighting coefficients proportional to the mass (α) and stiffness (β) matrix (Bathe, 1996), some studies preferred to take into account only the coefficient α (Conway *et al.*, 2012; Tezduyar *et al.*, 2008). However, the adopted values for arterial models are rarely published and not justified by any experimental evidence: Tezduyar et al. apparently assigned a value of 0.006 s^{-1} to α (Tezduyar *et al.*, 2008).

Therefore, in this first approach, several combinations of coefficient values have been explored, as reported in Table 5.2.

Axial pre-stretch The other approach is based on the physiologic evidence that arteries *in situ* are pre-stretched in the axial direction (Horný *et al.*, 2014; Learoyd & Taylor, 1966). The implementation of such boundary condition is consistent with other recent numerical studies (Alhayani *et al.*, 2013; Badel *et al.*, 2013). In this study a pre-stretch $\lambda = 1.09$ (Learoyd & Taylor, 1966) was applied to model physiologic boundary conditions.

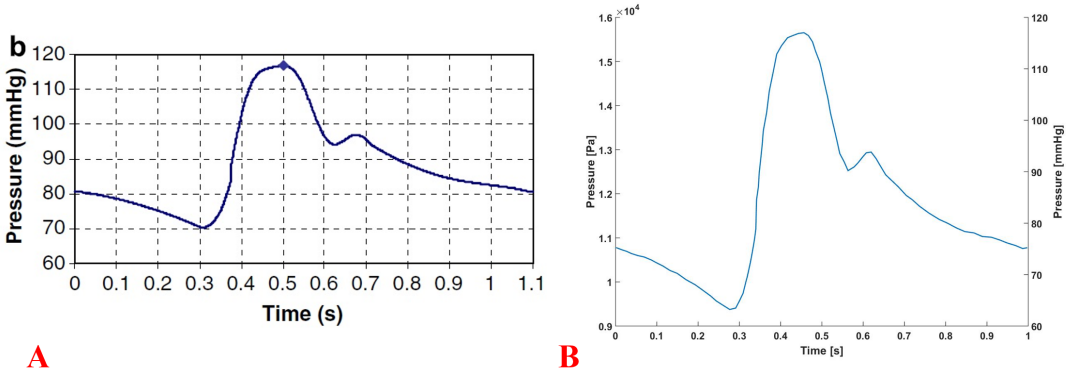

Figure 5.5 Physiologic pressure waveform reported by Scotti et al. (Scotti *et al.*, 2008) (A), extracted and normalized on 1 second in Matlab (B). The minimum pressure is 70 mmHg, the maximum is about 117 mmHg.

The application of the pulsatile cycle is obtained by a slow inflation of the aorta up to the diastolic pressure value (80 mmHg). The pressure waveform adopted (Scotti *et al.*,

2008) was normalized to a 1 second period for cycle to simulate 60 bpm (Figure 5.5). In order to compare the predictions of radial displacements and wall stress, two numerical analyses have been conducted for the pulsatile cycle: quasi-static (periodic pulsatile pressure) and dynamic. The outcome of such model is presented in Section 6.1.3.

Aneurysm formation

A supra-physiologic state (Schmidt *et al.*, 2015) is used to study the case of aneurysm formation. Differently from the physiologic model, no axial pre-stretch was applied to simulate the worst case scenario: the pre-stretch, normally ensuring arterial stability (Rachev, 2009), rapidly decreases with ageing (Horný *et al.*, 2014). This condition is relaxed in order to increase the likelihood to predict aortic buckling, hence both ends were fully constrained. An internal inflating pressure of 1 kPa was applied.

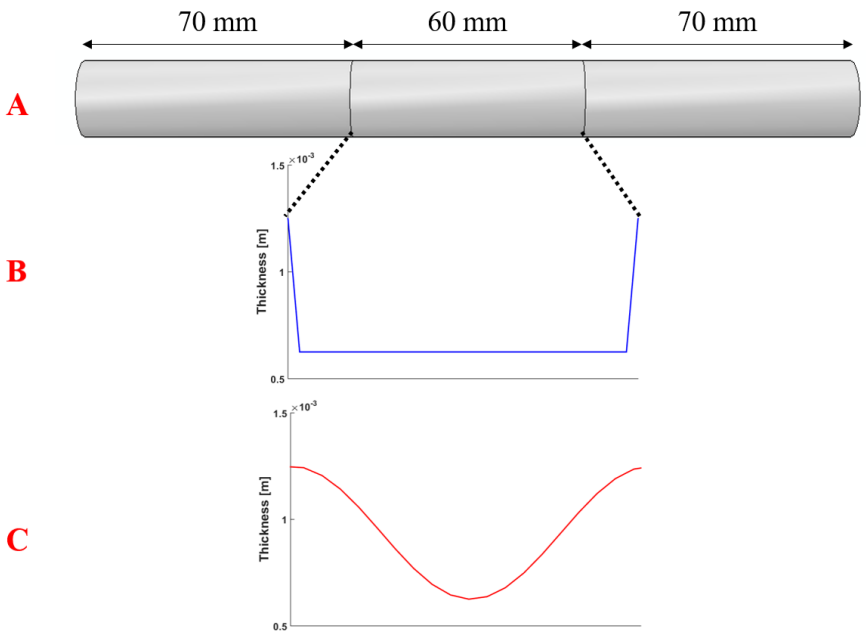

Figure 5.6 Schematic of artificial local imperfections introduced in the FE model of aorta. Both alterations affect the middle part (A) of the geometry. In order to study possible effects on aneurysm formation, an abrupt (B) or smoothed (C) imperfection reduces locally the thickness of the model.

Although several simulations are performed on a geometry characterized by homogeneous thickness, further analyses explore the presence of a geometrical imperfection affecting wall thickness. Thus, artificial local macroscopic imperfections were introduced in the computational model to understand whether geometrical alterations are critical for aneurysm formation.

Particularly, an abrupt axysimmetrical ring imperfection (Lopes *et al.*, 2007) in the central part of the aorta was produced, reducing by 50% the thickness of the shell in the central part of the aortic model (Figure 5.6 B). In order to figure out whether the profile of the alteration may affect the results, the ring imperfection has been subsequently smoothed assuming a sine shape (Figure 5.6 C). Finally, the existence of a threshold, below which aneurysm may be predicted in a healthy thoracic aorta presenting local thickness reduction, has been investigated.

5.3 Anisotropic models of aorta

Among the anisotropic models available in literature, reviewed in Section 2.2.3, Fung strain-energy function has been selected. Differently from the HGO model, Fung strain-energy function focuses on the phenomenological aortic behaviour, neglecting fibres orientation. The dispersion and angles of fibres require microscopic analyses that are beyond the aim of this research. Furthermore, the application of the Fung model, to which limited attention is reserved in the state of art, to study aneurysm formation represents one of the novelties of the present work.

The material properties assigned to the Fung orthotropic formulation in Abaqus are based on the parameters obtained from the fitting procedure described in Section 3.3.1. In Abaqus, the generalized Fung strain-energy potential has the following form:

$$W = \frac{C}{2}\left[e^{Q(E)} - 1\right] + \frac{1}{D}\left(\frac{J_{el}^2 - 1}{2} - \ln J_{el}\right) \tag{5.3}$$

where C and D are temperature-dependent material parameters and J_{el} is the elastic volume ratio. The initial bulk modulus K_0 depends on the initial deviatoric elasticity tensor **D** as follows

$$K_0 = \frac{2}{D}. \tag{5.4}$$

In order to define full incompressibility, *hybrid* formulation (Section 2.4) has been adopted and D parameter has been set as nil for all the following models (Dassault Systèmes, 2014).

Such anisotropic modelling has been applied to four different geometries, intended as four steps of increasing complexity. This approach aims at building a systematic and reliable methodology to face the challenges presented by Fung modelling. In addition, the four geometries allow a comparison of the results with isotropic models described in Section 5.2.2.

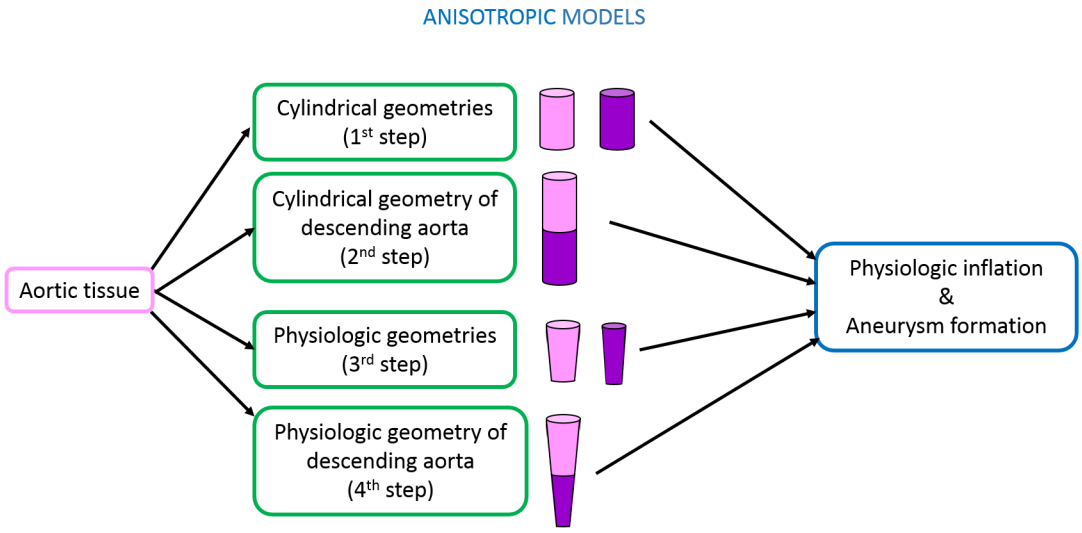

Figure 5.7 Schematic outline of the FE analyses performed for anisotropic models of aorta. Pink geometries are characterized by material properties of thoracic aorta, while purple ones refer to abdominal aorta.

Two analyses are performed on all the following models.
Firstly, a static inflation up to 16 kPa ($\sim$ 120 mmHg) is performed while both ends are fully constrained. Secondly, an aneurysm formation is instigated by means of the modified Riks method (Section 2.4.3). An internal inflating pressure of 1 kPa is applied and the same boundary conditions employed for the static inflation are assigned. A graphical outline of the anisotropic models that will be introduced in the subsequent sections is displayed in Figure 5.7.

Differently from isotropic models, *solid* elements instead of *shell* ones are selected as preliminary tests showed an increased stability of these simulations. Such considerations appear to be in agreement with Abaqus recommendations (Dassault Systèmes, 2014). Hence, 8-node linear brick elements, featuring *reduced* integration with hourglass control and *hybrid* with constant pressure (C3D8RH), mesh the geometries (Alhayani *et al.*, 2013; Badel *et al.*, 2011).
Since the present work does not focus on the gradient of stress generated across the wall, a single element was assigned for each model across the arterial wall. In addition, although rarely in literature the number of elements for each direction are reported, Takizawa et al. (Takizawa *et al.*, 2010) observed comparable results using one or two layers of elements.

5.3.1 Cylindrical geometries

As the first step of the anisotropic modelling, the simplified cylindrical geometry described in Section 5.2.2 is adopted for both the thoracic and abdominal segment. Thus, two models of identical geometry and different material properties are generated. In both cases the internal diameter measures 20 mm. As reported for the isotropic aortic design, a specific thickness, assumed constant along each model, is assigned to the

abdominal (1.64 mm) and thoracic (2.5 mm) segment.

A mesh of 3264 C3D8RH elements (32 elements in circumferential direction and 102 elements in longitudinal direction) is generated.

5.3.2 Cylindrical geometry: descending aorta

The second step in the Fung modelling process uses the same material properties adopted in the previous design coupled into a single model. Therefore a new cylindrical geometry, intended as a simplification of a descending aorta, is obtained: the material properties of the upper segment refer to the thoracic and the behaviour of the inferior sector to the abdominal aorta. However, the total length (335 mm) is smaller compared to the sum of the previous models (200 mm each). Such choice will be explained in Section 5.3.4.

Previous cylindrical geometries report a constant thickness, specific for each segment. In order to avoid a geometric abrupt discontinuity along the junction between the aortic districts, the value earlier assigned to the abdominal simplified geometry is adopted for this current model. In other words, the thickness in this case is equal to 1.64 mm along the whole model.
A mesh of 6732 C3D8RH elements (32 elements in circumferential direction and 210 elements in longitudinal direction) is generated.

On the other hand, the discontinuity of material properties appears not easily avoidable. The main objective of the present modelling step is to increase the complexity of the material response: the specific mechanical behaviours, collected with up-to-date experimental techniques, are contiguous in the model. Furthermore, joining two different

and specific biological responses is an aspect rarely addressed in literature, that appears novel for the Fung formulation.

5.3.3 Physiologic geometries

The third step of the anisotropic modelling process takes into account different geometric features. Although these models remain a simplification of the real aorta, the geometry appears of increased complexity and closer to *in vivo* structure.

Two realistic models are conceived using data originally tabulated by Noordergraaf (Noordergraaf, 1956) and successively updated, for the lower abdominal aorta, by Westerhof et al. (Westerhof *et al.*, 1969). Recently, Wang & Parker (Wang & Parker, 2004) adjusted such dimensions to produce a realistic human arterial tree. Thus, the values of length, diameter and wall thickness adopted for the design of the present thoracic model refer to Thoracic aorta I and II (Wang & Parker, 2004). Analogously, data for the abdominal model are taken from Abdominal aorta I to IV details (Wang & Parker, 2004).

Therefore, differently from previous models, each aortic district is now distinguished by different length and diameter. Furthermore the thickness is no longer constant along each design. A mesh of 5728 C3D8RH elements (32 elements in circumferential direction and 179 elements in longitudinal direction) is generated for the abdominal aorta, while 1920 C3D8RH elements (32 elements in circumferential direction and 60 elements in longitudinal direction) are employed for the thoracic segment.
Once again, specific material properties are assigned to each model.

5.3.4 Physiologic geometry: descending aorta

As the fourth and last step in the anisotropic modelling methodology a realistic human descending aorta is conceived. This model is generated joining the physiologic geometries described in the previous step (Section 5.3.3) and based on published data.

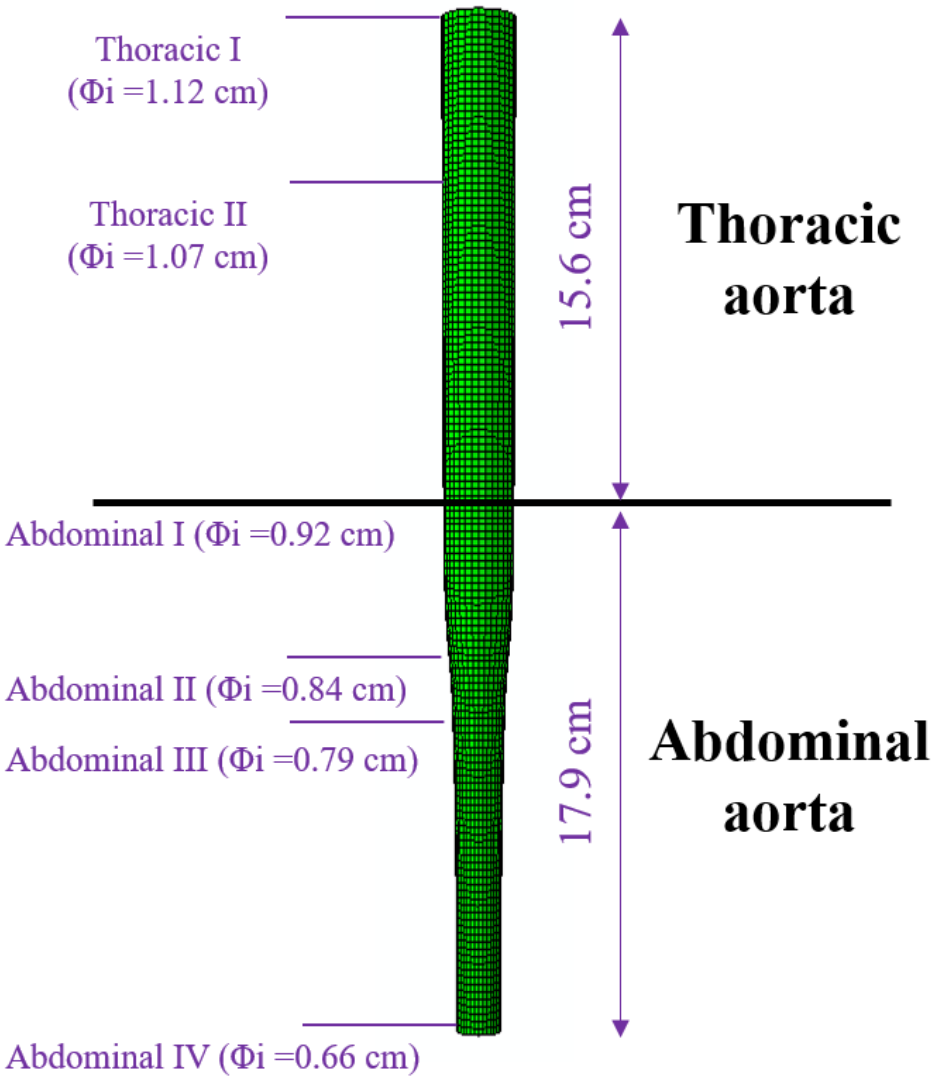

Figure 5.8 Model of descending aorta: the upper district refers to the thoracic aorta, the lower one to the abdominal aorta. Dimensions refer to published data (Noordergraaf, 1956; Wang & Parker, 2004; Westerhof *et al.*, 1969); Φ*i* indicates the internal diameter.

The design is displayed in Figure 5.8, where the decreasing diameter from thoracic to abdominal district can be appreciated. The total length, equal to 335 mm, has been adopted in the previous model of cylindrical descending aorta (Section 5.3.2). A mesh of 5874 C3D8RH elements is generated.

Similarly to Section 5.3.2, the discontinuity of material properties is present.

Chapter 6

Computational Results

The evaluation of whether a supra-physiological pressure would lead to aneurysm formation is accounted among the novelties of this thesis. Such macro-structural prediction has been based on accurate aortic wall mechanical properties. Therefore, the hyper-elastic behaviours presented in Chapter 4 have been imported in FE models to find out the critical point at which a bulge formation is predicted.

In Section 6.1 all the numerical results derived from the isotropic model, based on uniaxial mechanical properties, are reported. Among such responses, the impact of the pre-conditioning frequency (f_P) on rubber behaviour is detailed by means of FE models in Section 6.1.1. Analogous analyses based on aortic tissue behaviour are presented in Section 6.1.2. In Section 6.1.3, the effect of the sample thickness measurement on FE simulations is detailed investigating, in an idealized model of the aorta, either the physiologic behaviour or the aneurysm formation. The predictions obtained by means of the anisotropic models, taking into account the biaxial response of the aorta, are presented in Section 6.2. Finally, all numerical results are discussed in Section 6.3.

6.1 Predictions obtained from isotropic models

The first model has been designed to assess the response of an isotropic simplified geometry. Therefore, filtered stress-strain responses have been imported and fitted by several SEF in Abaqus (Dassault Systèmes S.A., France). Such material has been adopted to describe a hollow cylinder geometry, which details are reported in Section 5.2.

6.1.1 Rubber design

The impact of f_P on the critical pressure prediction is shown in Table 6.1 for the strips and Table 6.2 for the dumb-bells.

The fitting procedure of stress-strain data has been carried out in Abaqus. The material properties estimated to be unstable over the specified range of strain for a certain constitutive model are marked as *unstable* in the following tables. The Drucker stability criterion (Cadge & Prior, 1999) checks over a single element that the stiffness matrix of an incompressible material is positive definite. Such requirement ensures that a positive work is done to deform the modelled material. In this context, Abaqus provides a convenient tool (*Evaluate*) to assess how the experimental data could fit different material formulations. The coefficients necessary for the specified strain energy functions are calculated to compare the behaviour predicted by the material model and the experimental data. Hence, the software detects material instability.

Differently, whether the material has been assessed as stable, the absence of a critical pressure is designated as *no aneurysm*, meaning that the aneurysm is not formed. Whether an aneurysm is predicted, a bulge is formed as reported in Figure 6.1.

Numerical predictions associated to strips data-set show that Neo-Hookean strain-energy function always predicts the highest level of instability, while the Ogden models estimate the lowest values. The absence of pre-conditioning enlarges by far the range of critical pressures (15.2 kPa – 28.3 kPa), which corresponds to a $\Delta P = Pmax - Pmin = 13.1$ kPa.

The use of 0.2 Hz of pre-conditioning reduces this range (20.2 kPa-29.3 kPa), $\Delta P = 9.1$ kPa. Furthermore, this trend is even more appreciable for 0.6 Hz or 1.6 Hz that produce a pressure difference of $\Delta P = 7.4$ kPa and $\Delta P = 6.5$ kPa respectively (Table 6.1).

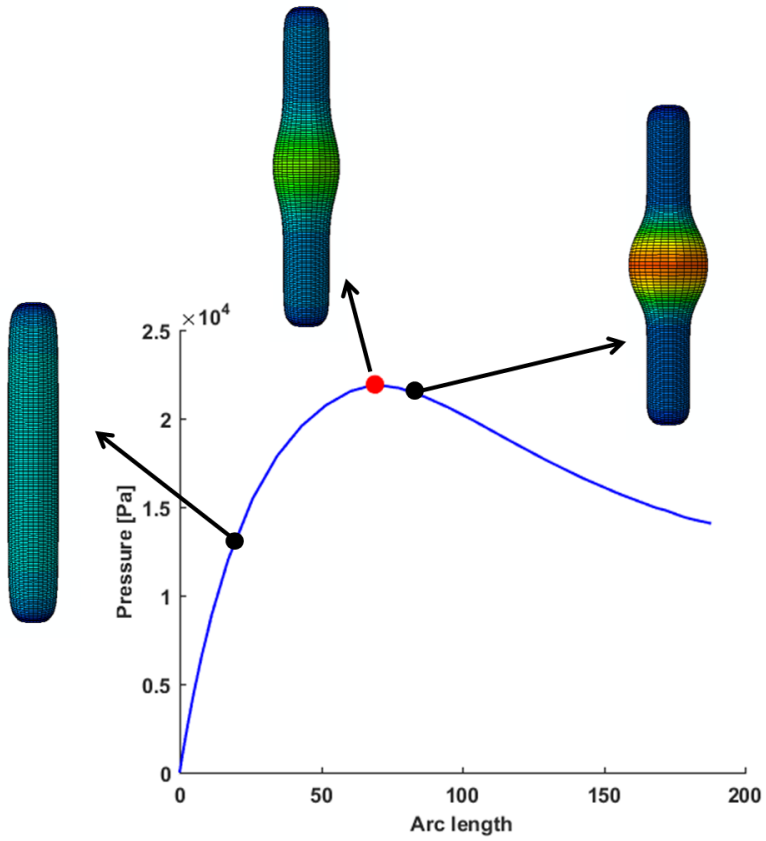

Figure 6.1 Stages of aneurysm formation predicted after an uniform static inflation of a rubber cylindrical model. The critical pressure is indicated by the red dot.

An analogous trend is observed in simulations based on dumb-bells stress-strain behaviour, as confirmed in Figure 6.2. Dumb-bells experimental responses are fitted by a larger number of strain-energy functions compared to other frequencies of pre-conditioning (Table 6.2). The maximum pressure difference of $\Delta P = 10.7$ kPa is observed in absence of pre-conditioning, in the range 17.4 kPa – 28.2 kPa. The scatter of critical pressure values is progressively reduced with the increasing of f_P, reaching the minimum difference $\Delta P = 5.8$ kPa (22.5 kPa – 28.2 kPa) at 1 Hz (Table 6.2).

Strain-energy function	**Pre-conditioning frequency**					
	0 Hz		0.2 Hz		0.6 Hz	1.6 Hz
	Stiffest	Softest	Stiffest	Softest		
Ogden1st order	15.275	*no aneurysm*	*no aneurysm*	20.316	20.892	*no aneurysm*
Ogden2nd order	*unstable*	*no aneurysm*	20.215	23.111	21.734	21.489
Ogden3rd order	*unstable*	*no aneurysm*	*unstable*	*unstable*	*unstable*	*unstable*
Neo-Hooke	24.447	28.392	25.931	29.327	28.290	27.951
Arruda-Boyce	*unstable*	24.640	22.233	25.014	24.567	25.009
Yeoh	17.358	*no aneurysm*	*no aneurysm*	24.325	*no aneurysm*	*no aneurysm*

Table 6.1 Critical pressure values [kPa] calculated with the specified strain energy functions. The experimental data were obtained after strip pre-conditioning performed at the showed frequencies. *Unstable* indicates lack of stability as predicted during the fitting procedure, *no aneurysm* specifies that no peak pressure was reached. For 0 Hz and 0.2 Hz the stiffest (first column) and softest (second column) stress-strain response were taken into account. Conversely, an average curve was chosen for 0.6 Hz and 1.6 Hz.

Strain-energy function	**Pre-conditioning frequency**						
	0 Hz		0.2 Hz		0.8 Hz		1 Hz
	Stiffest	Softest	Stiffest	Softest	Stiffest	Softest	
Ogden1st order	*no aneurysm*	*no aneurysm*	*no aneurysm*	*no aneurysm*	*no aneurysm*	*no aneurysm*	*no aneurysm*
Ogden2nd order	*no aneurysm*	*unstable*	15.346	18.080	*unstable*	*no aneurysm*	23.542
Ogden3rd order	*unstable*	*unstable*	*unstable*	*unstable*	*unstable*	*unstable*	23.676
Neo-Hooke	28.167	17.445	21.925	23.998	17.812	24.249	28.250
Arruda-Boyce	23.512	*unstable*	*unstable*	20.504	*unstable*	20.473	*unstable*
Yeoh	*no aneurysm*	*no aneurysm*	*no aneurysm*	*no aneurysm*	*no aneurysm*	*no aneurysm*	22.472

Table 6.2 The critical pressure values [kPa] of dumb-bell samples, calculated with several models similarly to Table 1. The effect of a different sample shape can be evaluated comparing the pre-conditioning frequencies 0 Hz and 0.2 Hz. *Unstable* indicates lack of stability as predicted during the fitting procedure, *no aneurysm* specifies that no peak pressure was reached. For 0 Hz, 0.2 Hz and 0.8 Hz the stiffest (first column) and softest (second column) stress-strain response were taken into account. Conversely, an average curve was chosen for 1 Hz.

Despite different pressure differences are observed, the ANOVA tests deny any statistical evidence of the f_P adopted to pre-cycle strips (p = 0.7) or dumb-bells (p = 0.3) samples.

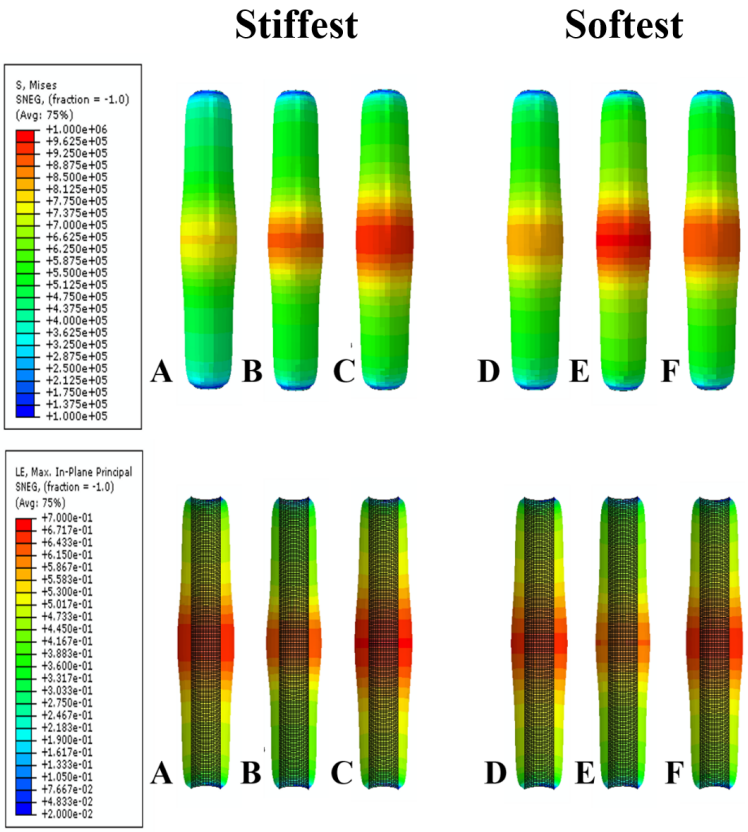

Figure 6.2 Comparison of different aneurysm shapes predicted just after the pressure reaches a critical point. The adopted test data are referred to strips pre-conditioned at 0.2Hz, selecting two different stress-strain curves: the stiffest and the softest. The stiffest stress-strain response used: A) Ogden second order, B) Neo-hooke, C) Arruda-Boyce. The softest stress-strain response used: D) Ogden second order, E) Neo-hooke, F) Arruda-Boyce. The first row of results reports von Mises stress, whereas the second row shows the logarithmic strain values superimposed to the undeformed configuration.

The effect of specific strain-energy functions on the prediction of aneurysm formation in terms of shape (deformations), radial strains and stress levels is displayed in Figure 6.2. The compared configurations are generated just after the critical pressure is attained. In detail, models A, B and C refer to the stiffest response obtained at 0.2 Hz. It appears that the largest bulge is predicted for the Arruda-Boyce model (C). Similarly, models D,

E and F belong to the softest behaviour at the same frequency. Once again, the largest bulge is obtained with the Arruda-Boyce model (F). The radial stretch values are listed in Table 6.3.

However, it has been observed that the largest bulge (Table 6.3) in not instigated by the highest critical pressure (Table 6.1).

Strain-energy function	**Radial stretch**	
	Stiffest	Softest
Ogden 2^{nd} order	9.49	10.9
Neo-Hooke	9.15	9.5
Arruda-Boyce	9.6	12.6

Table 6.3 Comparison of radial stretch values [mm] predicted one step after the pressure reaches a critical point. These values refer to aneurysm shapes displayed in Figure 6.2.

A statistical comparison between the maximum displacement instigated immediately after the formation of the bulge has been conducted. Among results depending on strips experimental behaviour, no meaningful difference between displacement values is observed (p = 0.62). On the other end, the displacements computed in the model based on the stress-strain response of dumb-bells show a clear effect of the $f_P = 1$. Results referred to 1 Hz are statistically dissimilar (p = 0.01) from $f_P = 0.2$ Hz and from the control test.

Observations

Results presented in the present Section appears to be novel, since they evaluate the influence of the pre-conditioning frequency, adopted during the experimental characterization, on the critical pressures computed by the FE model.

For both strip and dumb-bell shape, the maximum scatter of critical pressures is achieved

when samples are not pre-conditioned (Table 6.1 and 6.2).

As an additional remark, it appears clear that strain-energy functions, fitting the experimental data, affect the FE results. The softest stress-strain experimental response obtained after a pre-conditioning at 0.2 Hz is reported in Figure 6.3. This data-set is fitted by five different strain-energy functions: Arruda-Boyce, Neo-Hooke, Yeoh, Ogden 1^{st} order and Ogden 2^{nd} order (Table 6.4).

Strain-energy function	**Fitting parameters**
Ogden 1^{st} order	$\mu = 193613.5$ [Pa]; $\alpha = 3$;
Ogden 2^{nd} order	$\mu_1 = 43014.2$ [Pa]; $\alpha_1 = 4.1$ $\mu_2 = 209780.2$ [Pa]; $\alpha_2 = 1.4$;
Neo-Hooke	$C_{10} = 171436.6$ [Pa]
Arruda-Boyce	$\mu = 259278.9$ [Pa]; $\mu_0 = 278386.105$ [Pa]; $\lambda_m = 3$
Yeoh	$C_{10} = 122362.3$ [Pa]; $C_{20} = 4331.1$ [Pa] $C_{30} = 37.2$ [Pa]

Table 6.4 Fitting parameters estimated by Abaqus for each strain-energy function plotted in Fig. 6.3 are reported. Ogden 3^{rd} order resulted unstable.

Despite the stability computed by Abaqus in the range displayed, comparing the plot in Figure 6.3 and numerical results in Table 6.1 for the softest response at 0.2 Hz, it seems that the highest critical pressure is associated to the stiffest stress-strain fitting below strain 1, given by the Neo-Hookean model. However, it is worth notice that such mathematical model provides the poorest fitting of the experimental data-set, compared to the others. Therefore, the magnitude of numerical results appears affected by the selection of model fitting the stress-strain response.

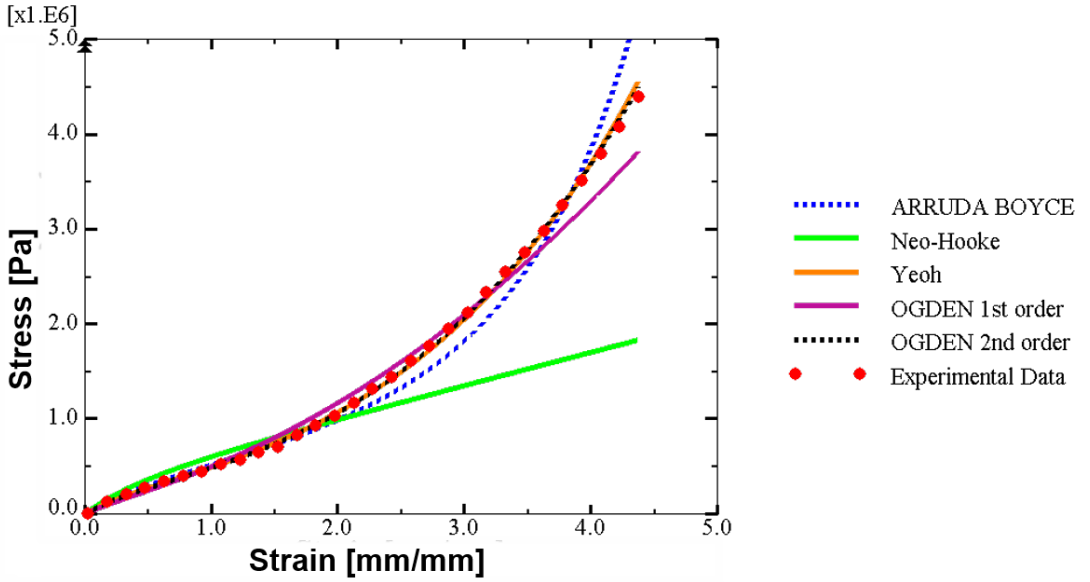

Figure 6.3 Experimental data (red dots), collected from a strip pre-conditioned at 0.2 Hz, fitted by different strain-energy functions in Abaqus. Ogden 3^{rd} order resulted unstable.

In literature, the modified Riks method has already been employed to study the formation of a local bulge along a rubber tube, the focus was on the effect of the axial extension ratio on critical pressure values (Gonçalves *et al.*, 2008). In addition, the influence of the local and global imperfections on critical pressure has been addressed (Lopes *et al.*, 2007). The influence of certain mesh elements, strain-energy functions, boundary conditions and tube geometry on numerical predictions have been explored by Bucchi & Hearn (Bucchi & Hearn, 2013b).

6.1.2 Aortic design: aneurysm formation

Similarly to the computational results presented for rubber material in the previous section, the role of f_P on the critical pressure prediction is presented in Table 6.5 for the abdominal samples and Table 6.6 and 6.7 for the thoracic ones. The softest and the stiffest experimental responses have been selected for each frequency. Once again, the word *unstable* indicates that the curve fitting procedure in Abaqus, declares the material

to be unstable over the specified range of strain. Whether no bulge or critical pressure is predicted the expression *no aneurysm* is encountered. Figure 6.4 clarifies the possible outcomes of the numerical analysis.

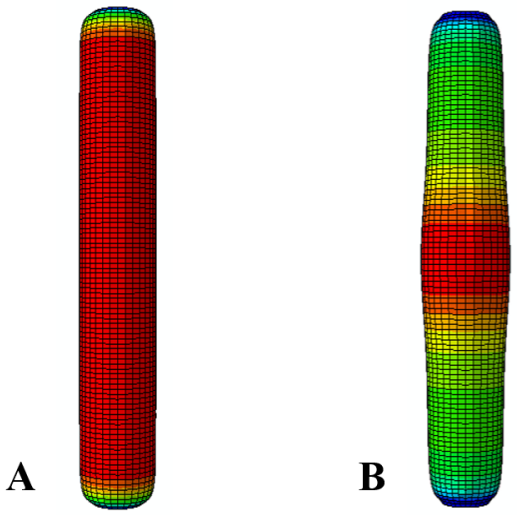

Figure 6.4 Two possible numerical outcomes of static inflation performed with Riks modified method. A) The simplified aortic segment is uniformly inflated, but *no aneurysm* is predicted. B) Following an initial stage of uniform inflation, the formation of a bulge is computed in the middle of the model.

Numerical results show that a critical pressure is always computed for a Neo-Hookean SEF. However, significant differences are generally observed between the stiffest and the softest curves of each test.

In the majority of cases, abdominal results show that no aneurysm is expected to be formed by such healthy tissues. The minimum range of critical pressures, whether available, is computed for the stiffest response obtained at 1.2 Hz, being $\Delta P = Pmax - Pmin = 0.34$ kPa. Conversely, the absence of pre-conditioning maximises this range (5.9 kPa – 29.5 kPa). The stiffest stress-strain response related to a pre-conditioning of 2 Hz reported the major number of SEFs predicting aneurysm formation (Table 6.5). The scatter of these values is of $\Delta P = 11.6$ kPa.

Strain-energy function	**Pre-conditioning frequency**					
	0 Hz		1.2 Hz		2 Hz	
	Stiffest	Softest	Stiffest	Softest	Stiffest	Softest
Ogden1st order	*no aneurysm*	*no aneurysm*	*no aneurysm*	*no aneurysm*	*no aneurysm*	*no aneurysm*
Ogden2nd order	*unstable*	*no aneurysm*	*no aneurysm*	*unstable*	*unstable*	*no aneurysm*
Ogden3rd order	*no aneurysm*	*no aneurysm*	*no aneurysm*	*unstable*	*unstable*	*no aneurysm*
Neo-Hooke	29.470	5.865	24.775	4.505	34.679	14.022
Arruda-Boyce	*unstable*	*unstable*	25.118	*unstable*	35.395	*unstable*
Yeoh	*no aneurysm*	*no aneurysm*	*no aneurysm*	*no aneurysm*	*no aneurysm*	*no aneurysm*
Marlow	*no aneurysm*	*no aneurysm*	*no aneurysm*	*no aneurysm*	46.303	*no aneurysm*

Table 6.5 Critical pressure values [kPa] calculated for abdominal longitudinal data with the specified strain energy functions. The experimental data were obtained after pre-conditioning performed at the showed frequencies. *Unstable* indicates lack of stability as predicted during the fitting procedure, *no aneurysm* specifies that no bulge was formed. The stiffest (first column) and softest (second column) stress-strain response were taken into account for each frequency.

Similarly, Arruda-Boyce SEF predicts aneurysm formation for the stiffer responses obtained from thoracic circumferential samples subjected to a pre-conditioning (Table 6.6). Despite the different f_P adopted, the stiffer responses report the same pressure difference of $\Delta P = 0.38$ kPa between the SEF fitting the experimental data. When a pre-conditioning is neglected, the critical pressures predicted are the lowest.
A different trend is observed for thoracic longitudinal samples (Table 6.7). Stress-strain responses obtained in the absence of pre-conditioning appear to predict the major number of critical pressures, in the range (2.2 kPa – 17.2 kPa). In addition, the minimum $\Delta P = 0.26$ kPa is computed for the softer response neglecting the pre-conditioning.
Despite different pressure differences being observed, the ANOVA tests deny any statistical evidence of the f_P adopted to pre-cycle abdominal (p = 0.34), thoracic circumferential (p = 0.18) or longitudinal (p = 0.86) samples.

Figure 6.5 illustrates how SEFs and the f_P value affect the prediction of aneurysm formation in term of shape displacements and stress levels. Elastic tubes are represented just after the critical pressure is attained. In detail, model A and B refer to the stiffest response obtained for thoracic circumferential samples at 1.2 Hz fitted by Neo-Hookean (A) and Arruda-Boyce (B) SEF respectively. It appears that the highest stress-levels and largest displacements are predicted for the Arruda-Boyce model (B). Similarly, models C and D belong to the stiffest behaviour at 2 Hz. However, no appreciable differences can be observed in the stress levels and displacements computed for Neo-Hookean (C) and Arruda-Boyce (D) SEF.

Strain-energy function	**Pre-conditioning frequency**					
	0 Hz		1.2 Hz		2 Hz	
	Stiffest	Softest	Stiffest	Softest	Stiffest	Softest
Ogden1st order	*no aneurysm*	*no aneurysm*	*no aneurysm*	*no aneurysm*	*no aneurysm*	*no aneurysm*
Ogden2nd order	*unstable*	*no aneurysm*	*no aneurysm*	*no aneurysm*	*no aneurysm*	*no aneurysm*
Ogden3rd order	*no aneurysm*	*no aneurysm*	*no aneurysm*	*no aneurysm*	*no aneurysm*	*no aneurysm*
Neo-Hooke	5.846	6.123	16.640	7.004	17.303	9.594
Arruda-Boyce	*unstable*	*unstable*	17.019	*unstable*	17.690	*unstable*
Yeoh	*no aneurysm*	*no aneurysm*	*no aneurysm*	*no aneurysm*	*no aneurysm*	*no aneurysm*
Marlow	*no aneurysm*	*no aneurysm*	*no aneurysm*	*no aneurysm*	*no aneurysm*	*no aneurysm*

Table 6.6 Critical pressure values [kPa] calculated for thoracic circumferential data with the specified strain energy functions. The experimental data were obtained after pre-conditioning performed at the showed frequencies. *Unstable* indicates lack of stability as predicted during the fitting procedure, *no aneurysm* specifies that no bulge was formed. The stiffest (first column) and softest (second column) stress-strain response were taken into account for each frequency.

Strain-energy function	**Pre-conditioning frequency**					
	0 Hz		1.2 Hz		2 Hz	
	Stiffest	Softest	Stiffest	Softest	Stiffest	Softest
Ogden1st order	17.2284	*no aneurysm*	*no aneurysm*	*no aneurysm*	*no aneurysm*	*no aneurysm*
Ogden2nd order	*no aneurysm*	2.49381	*unstable*	*no aneurysm*	*unstable*	*unstable*
Ogden3rd order	*no aneurysm*	*unstable*	*no aneurysm*	*no aneurysm*	*unstable*	*no aneurysm*
Neo-Hooke	16.127	2.237	8.376	7.754	16.388	6.776
Arruda-Boyce	16.2855	*unstable*	*unstable*	*unstable*	*unstable*	*unstable*
Yeoh	*no aneurysm*	*unstable*	*no aneurysm*	*no aneurysm*	*no aneurysm*	*no aneurysm*
Marlow	*no aneurysm*	*no aneurysm*	*no aneurysm*	*no aneurysm*	*no aneurysm*	*no aneurysm*

Table 6.7 Critical pressure values [kPa] calculated for thoracic longitudinal data with the specified strain energy functions. The experimental data were obtained after pre-conditioning performed at the showed frequencies. *Unstable* indicates lack of stability as predicted during the fitting procedure, *no aneurysm* specifies that no bulge was formed. The stiffest (first column) and softest (second column) stress-strain response were taken into account for each frequency.

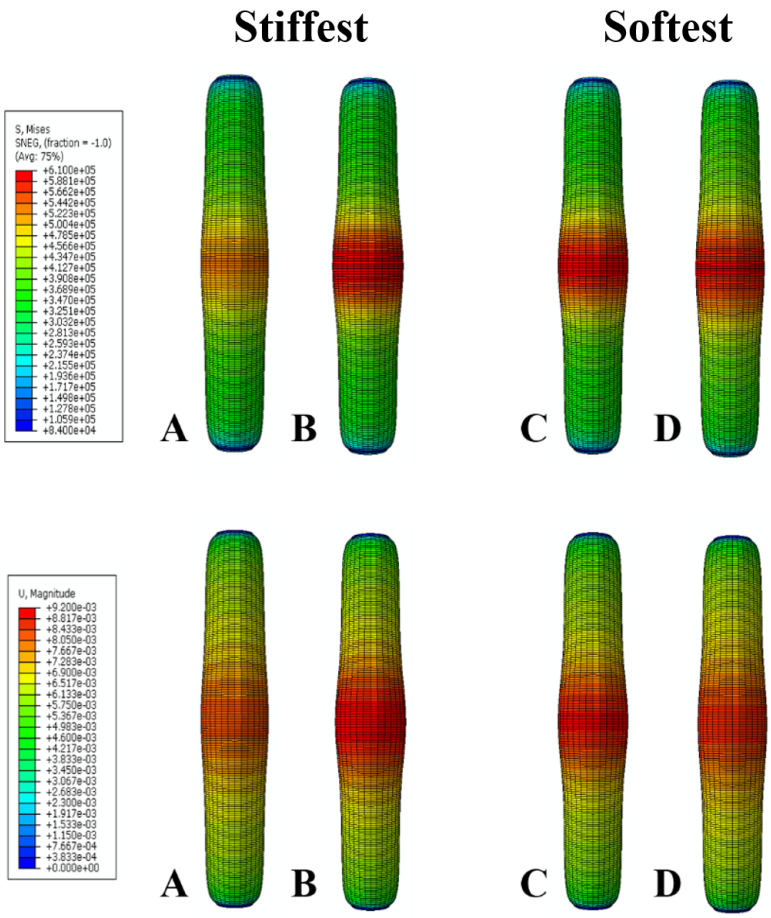

Figure 6.5 Comparison of different aneurysms predicted one step after the pressure reaches a critical point. The adopted test data are referred to samples pre-conditioned at 1.2 Hz (A, B) and 2 Hz (C, D). The stiffest stress-strain curves are adopted. Results from Neo-Hookean (A, C) and Arruda-Boyce (B, D) strain–energy functions are showed. The first row of results reports von Mises stress [Pa], whereas the second row shows the displacement values [m].

Although von Mises stress is an axis-independent scalar frequently used as an indicator of material failure in classical engineering analyses, it is extensively used to assess the maximum stress in the biomechanical field (Humphrey & Holzapfel, 2012). Since von Mises stress is quite often reported to map prediction of aneurysm growth (Shang *et al.*, 2015), repair (Wang & Li, 2011) and rupture (Raghavan & Vorp, 2000; Rodríguez *et al.*, 2008; Scotti & Finol, 2007; Wang *et al.*, 2002), it has also been adopted in this work to describe the bulge initiation.

Observations

Numerical analyses based on aortic tissue behaviour rarely predicted aneurysm formation. It is worth noticing that biological responses appear more challenging to fit compared to rubber material, as reported in Figure 6.6. Although the third order of Ogden strain-energy function generally shows the best fitting among the others, no critical pressure was ever computed for it (Table 6.5, 6.6 and 6.7). As an example, the fitting parameters for an abdominal data-set (Figure 6.6) are reported in Table 6.8.

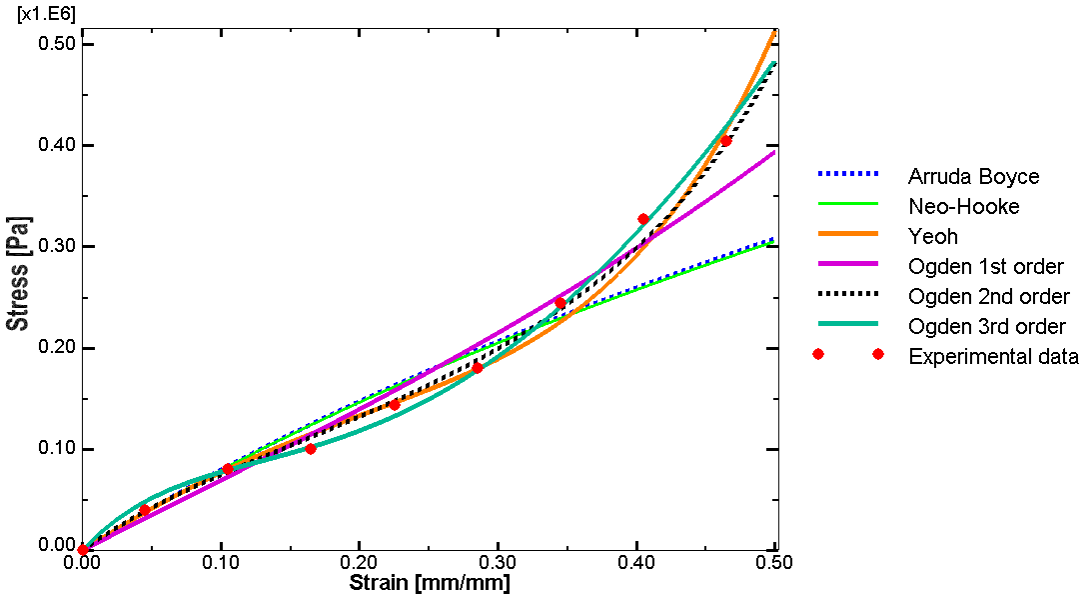

Figure 6.6 Experimental data (red dots), collected from an abdominal sample pre-conditioned at 1.2 Hz, fitted by different strain-energy functions in Abaqus.

The only strain-energy function able to predict regularly a buckling mode and a bulge appearance is the Neo-Hookean one. Such model has been adopted for analogous analyses by Alhayani et al. (Alhayani *et al.*, 2013). However, they did not explicitly report any critical pressure value, being more interested in analysing the relation between axial stretch and critical pressure values. In literature, no other FE study addressed the supra-physiological loading as a possible cause of aneurysm generation.

Fu et al. (Fu *et al.*, 2012) suggested that the initial formation of aneurysms can be modelled as a bifurcation phenomenon. However, their analytical studies, based on

literature data, predicted no bifurcations for rabbit carotid modelled by Holzapfel and unrealistic bifurcation pressures for abdominal aortic tissues modelled by Choi & Vito's strain-energy function.

Strain-energy function	**Fitting parameters**
Ogden 1^{st} order	$\mu = 236575.1$ [Pa]; $\alpha = 4.3$;
Ogden 2^{nd} order	$\mu_1 = 750.9$ [Pa]; $\alpha_1 = 19.3$ $\mu_2 = 333872.2$ [Pa]; $\alpha_2 = -10.3$
Ogden 3^{rd} order	$\mu_1 = -782705.3$ [Pa]; $\alpha_1 = -3.01$ $\mu_2 = 1348998.7$ [Pa]; $\alpha_2 = -1.4$ $\mu_3 = 7040232.9$ [Pa]; $\alpha_3 = -4.9$
Neo-Hooke	$C_{10} = 144734.02$ [Pa]
Arruda-Boyce	$\mu = 285708.8$ [Pa]; $\mu_0 = 290955.2$ [Pa]; $\lambda_m = 5.7$
Yeoh	$C_{10} = 145280.6$ [Pa]; $C_{20} = -96394.2$ [Pa] $C_{30} = 206176.1$ [Pa]

Table 6.8 Fitting parameters estimated by Abaqus for each strain-energy function plotted in Fig. 6.6 are reported.

6.1.3 Aortic design: the role of sample thickness on numerical predictions

The present analysis aims to explore the impact of the experimental thickness estimation on FE predictions, as no standard or common practice is available for such measurement. In the following paragraphs, the outcomes associated to a sample-specific thickness are compared with results obtained from different width measurements. Thus, two main

analyses are carried out on an idealized geometry modelled by means of isotropic aortic behaviour: a physiologic loading and aneurysm instigation. An overall summary of this study procedure is presented in Figure 6.7.

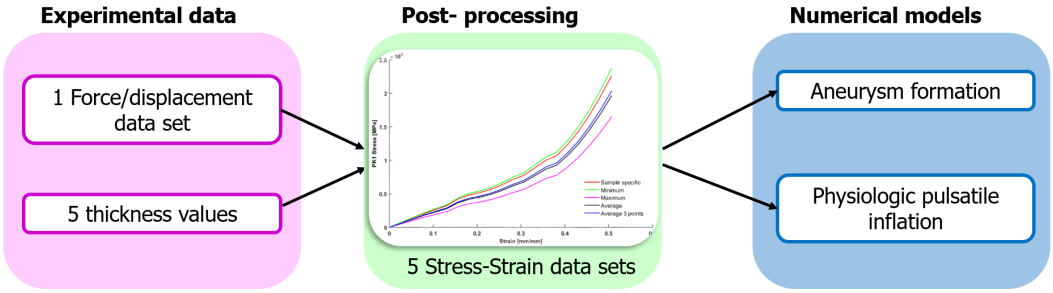

Figure 6.7 Summary of the steps taken to evaluate the role of sample thickness on numerical outcomes.

Thickness values

The application of the optical method, proposed in Section 3.3, estimated a sample-specific thickness (average of all values in the region of interest) of 2.22 mm for the thoracic and 1.67 mm for the abdominal aorta. Out of six samples tested for each aortic district, the average stress-strain response has been selected. Hence, thickness values above refer to such specimens. In addition, thickness values of thoracic samples range from a minimum of 2.12 mm to a maximum of 3.05 mm, the average of all specimens being 2.56 ± 0.34 mm. The measurement of the thickness averaging only three distinct points, within the ROI of the selected sample, determined a thickness value of 2.47 mm. These three points have been consistently chosen, being the ends and the middle point of the ROI.

Abdominal samples thickness values extend from a minimum of 1.28 mm to a maximum of 2.18 mm, the average of all specimens being 1.64 ± 0.37 mm. The average of three points in the ROI of the selected sample has been estimated to be 1.8 mm.

Applying a physiologic time-dependent load on idealized geometry

Despite the number of attempts performed to carry out a transient dynamic analysis including Rayleigh damping to the aortic model, no reliable simulations were completed, as excessive circumferential fluctuations were often generated. For instance, whether a high value of mass proportional damping was assigned (e.g. $\alpha = 2$, $\beta = 0$), instabilities arose from the end of the second cardiac cycle: the aorta appears to fluctuate around the axial axis. On the other hand, a low mass proportional damping insured a complete stability of the aorta (e.g. $\alpha = 0.01$, $\beta = 0.02$). However, it is difficult to assess whether such damping is representative of physiologic conditions, since no experimental observations have been found regarding the soft tissue in the literature.

On the other hand, the application of the pre-stretch to the aortic model has been successful in avoiding excessive oscillations, as reported in Figure 6.8. It was noticed that the initial transient is needed to avoid oscillations that otherwise appear at the beginning of the periodic pressure wave (Figure 6.8 A). Responses in terms of radial displacement (Figure 6.8 B) and von Mises stress (Figure 6.8 C) recorded for a node in the middle of the aortic model show the instantaneous behaviour of the aorta and the absence of instabilities.

In addition, no significant difference has been appreciated in the comparison of the transient and the quasi-static analyses, due to the minimum scatter of radial displacement ($< 10^{-9}m$) and von Mises stress (0.516 kPa) in correspondence of inflating pressure peaks. However, some oscillations may occasionally be observed at the end of the 3^{rd} cycle during dynamic simulations. The effect of the sample thickness on quasi-static predictions is captured in Table 6.9 for the thoracic part and in Table 6.10 for the abdominal part of the aorta.

The choice of constitutive models has been limited in the present analysis to those providing the best fitting of uniaxial mechanical responses and the most stable numer-

ical behaviour. As a result, the maximum radial displacement and wall stress values calculated in the central part of the model can be compared (Table 6.9 and 6.10).

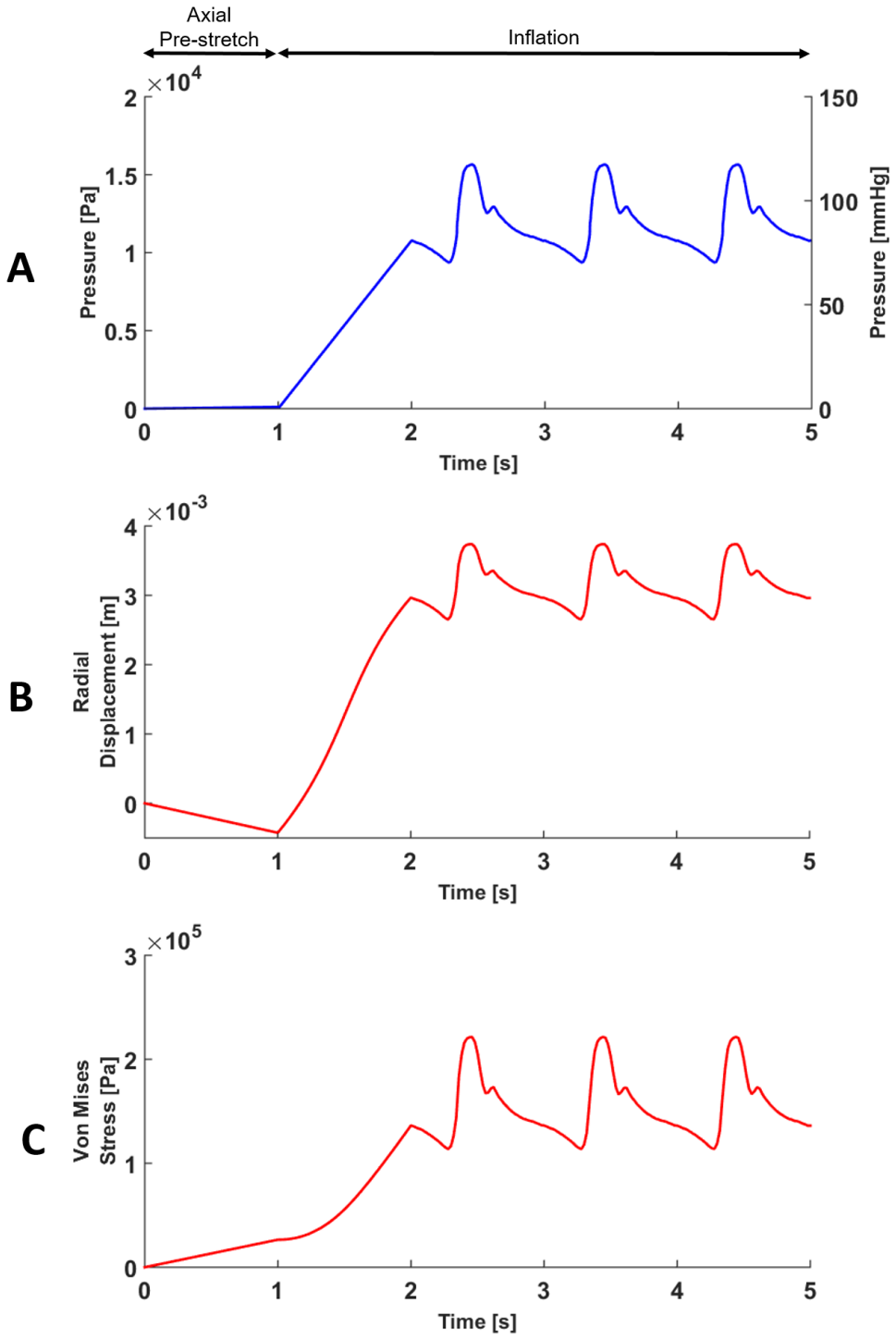

Figure 6.8 Pressure waveform inflating the FE model of aorta consisting in a ramp and three cycles (A). A pre-stretch is applied during the first second. Radial displacement of a node placed in the mid of the FE model, as a result of the inflating pressure (B). Resulting von Mises stress of the same node (C).

Strain-energy function	Minimum of all samples (0.00212 m)		Sample specific (0.00222 m)		Average of three points (0.00247 m)		Average of all points (0.00256 m)		Maximum of all points (0.00305 m)	
	R_d[m]	σ[kPa]	R_d[m]	σ[kPa]	R_d[m]	σ[kPa]	R_d[m]	σ[kPa]	R_d[m]	σ[kPa]
Ogden2nd order	0.00469	269	0.00478	274	0.00498	285	0.00505	289	0.00538	317
Yeoh	0.00365	219	0.00374	222	0.00395	228	0.00402	231	0.00435	242
Marlow	0.00363	218	0.00371	221	0.00391	227	0.00397	229	0.00435	242

Table 6.9 The effect of sample thickness on the maximum radial displacement (R_d) and maximum von Mises stress (σ) predicted by the FE model of thoracic aorta, subjected to a physiologic cardiac activity. The listed strain-energy functions assured the best fitting of the experimental data and a stable numerical outcome.

Strain-energy function	Minimum of all samples (0.00128 m)		Average of all points (0.00164 m)		Sample specific (0.00167 m)		Average of three points (0.0018 m)		Maximum of all points (0.00218 m)	
	R_d[m]	σ[kPa]	R_d[m]	σ[kPa]	R_d[m]	σ[kPa]	R_d[m]	σ[kPa]	R_d[m]	σ[kPa]
Yeoh	0.00436	370	0.00516	414	0.00522	418	0.00545	431	0.00603	466
Marlow	0.00434	369	560	441	0.00573	449	0.00637	490	/	/

Table 6.10 The effect of sample thickness on the maximum radial displacement (R_d) and maximum von Mises stress (σ) predicted by the FE model of abdominal aorta, subjected to a physiologic cardiac activity. The listed strain-energy functions assured the best fitting of the experimental data. Unstable numerical outcome due to oscillations is indicated by "/".

Aneurysm formation

The impact of any experimental feature on FE simulations appears even more delicate when it comes to predictions of diseases, such as aneurysm formation. In particular, the correlation between the sample thickness measurements and critical pressures instigating the bulging appearance represents one of the novelties of the present work.
Since no accurate definition of aneurysm formation, in terms of FE modelling, has been found, it is important to specify a definition. The formation of aneurysm is accepted under the fulfilment of the following two conditions: Riks solver predicts an instability and a bulge is observed in the model. Typically, the bulge is identified by the wall stress values in the central part of the aorta appearing considerably higher compared to the rest of the model.
The influence of sample thickness in the instigation of an aneurysm is explored for both the thoracic and abdominal aorta. Considering the thoracic FE model has a constant thickness (also referred as *homogeneous*), the only SEF that predicts aneurysm formation is the Neo-Hookean. Differently, the abdominal model shows an aneurysm to be instigated also whether Marlow SEF is adopted to reproduce the experimental data. The critical pressure values computed are reported in Table 6.11.

The application of the artificial ring imperfection on the aortic model, as addressed in Section 5.2.2, leads to a substantial change in predictions for the thoracic model, since aneurysm formation is now predicted by Marlow SEF. Therefore, it has been decided to investigate the existence of a threshold, below which aneurysm may be predicted in a healthy thoracic aorta presenting local thickness reduction. The critical pressure values computed for an abrupt or smoothed ring imperfection are shown in Table 6.12. Further simulations between -30% and -25% of thickness reduction generated no clear outcomes. Therefore, in order to define a safe threshold, it appears that a minimum

reduction of 30%, compared to the thickness of the model ends, is required to observe aneurysm formation in the thoracic aorta.

Strain-energy function	**Minimum of all samples (0.00128 m)**	**Average of all points (0.00164 m)**	**Sample specific (0.00167 m)**	**Average of three points (0.0018 m)**	**Maximum of all points (0.00218 m)**
Marlow	27.61	21.55	21.16	*No aneurysm*	16.21

Table 6.11 Critical pressure values [kPa] predicted to form aneurysm in a homogeneous FE geometry of abdominal aorta, which behaviour is evaluated for five different sample thickness values. *No aneurysm* indicates that no aneurysm is predicted.

Localized thickness reduction	**Minimum of all samples (0.00212 m)**	**Sample specific (0.0022 m)**	**Average of three points (0.00247 m)**	**Average of all points (0.00256 m)**	**Maximum of all points (0.00305 m)**
Ring imperfection -50%	24.55	23.44	21.08	20.34	17.06
Smooth imperfection -50%	28.53	27.22	24.48	23.61	19.82
Smooth imperfection -40%	33.13	31.65	28.45	27.45	23.04
Smooth imperfection -30%	39.27	37.51	33.73	32.52	27.30
Smooth imperfection -25%	*No aneurysm*	*No aneurysm*	*No aneurysm*	*No aneurysm*	*No aneurysm*

Table 6.12 Critical pressure values [kPa] predicted to form aneurysm in a not homogeneous model of thoracic aorta, which behaviour is evaluated for five different sample thickness values. A geometrical ring imperfection is introduced to reduce the thickness in the middle of the FE model. Marlow strain-energy function is adopted in all cases. *No aneurysm* indicates that no aneurysm is predicted.

However, the role of the percentage of reduction on the maximum von Mises stress values seems to not be relevant, as reported in Figure 6.9.

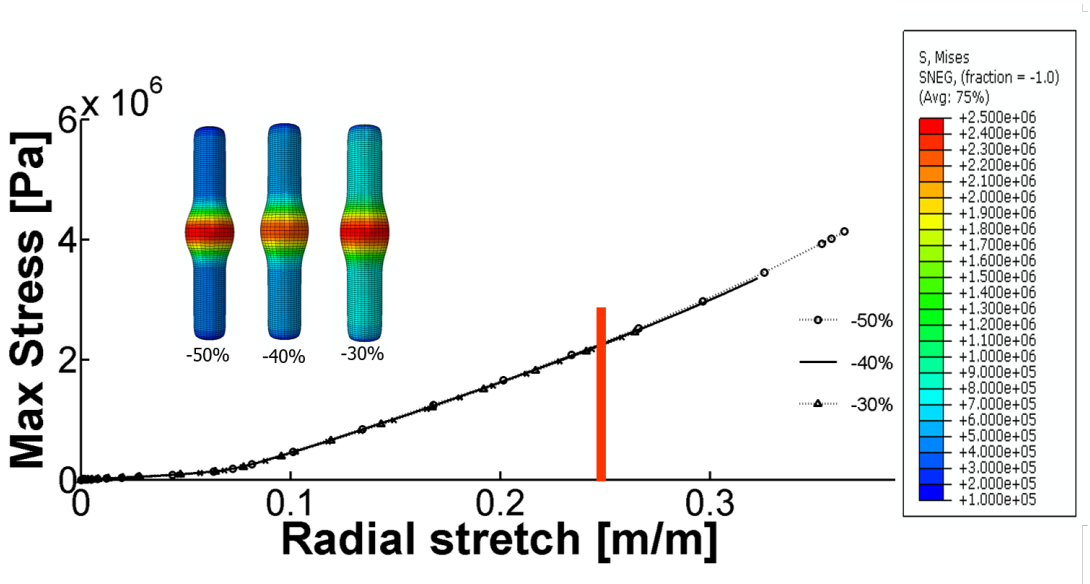

Figure 6.9 Von Mises stress achieved in the central part of the thoracic model vs Radial stretch. Three different percentages of ring imperfection artificially introduced in the central part of the model are compared. Snapshots compare the global deformation predicted for the radial stretch value indicated by the red line.

The impact of the sample thickness on the predicted peak wall stress in the thoracic model is shown in Figure 6.10. Above a radial stretch of 0.1 the scatter between the sample thickness is directly proportional to the scatter of the stress values.

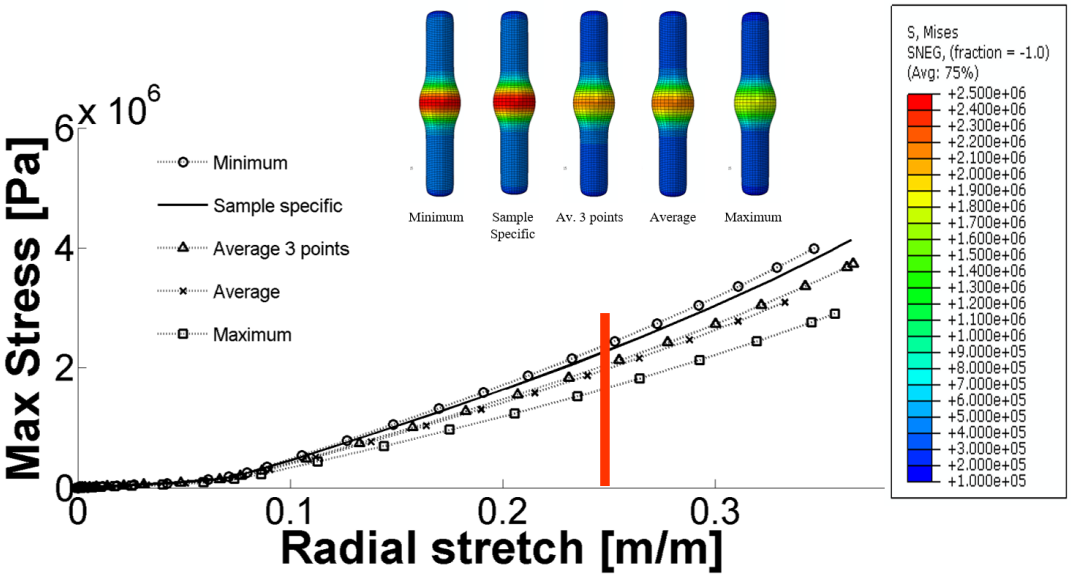

Figure 6.10 Von Mises stress achieved in the central part of the thoracic model vs Radial stretch for different sample thickness values. Snapshots compare the global deformation predicted for the radial stretch value indicated by the red line.

The critical pressure values computed for the abdominal model affected by the ring imperfection (Table 6.13) appear subjected to a reduction of about 50% compared to the corresponding homogeneous model (Table 6.11).

Localized thickness reduction	**Minimum of all samples (0.00128 m)**	**Average of all points (0.00164 m)**	**Sample specific (0.00167 m)**	**Average of three points (0.0018 m)**	**Maximum of all points (0.00218 m)**
Ring imperfection -50%	13.23	10.34	10.16	9.41	7.76

Table 6.13 Critical pressure values [kPa] predicted to form aneurysm in a not homogeneous model of abdominal aorta, which behaviour is evaluated for five different sample thickness values. A geometrical ring imperfection is introduced to reduce the thickness in the middle of the FE model.

Furthermore, the effect of the sample thickness on the inflating pressure in the thoracic and abdominal models can be appreciated in Figure 6.11. Pressure values have been extracted in different stages (radial stretches), being the last one proximal to the plateau computed by Riks solver. The plateau corresponds to the value of critical pressure instigating the aneurysm formation. It appears consistent for each radial stretch value that pressure decrease with increasing sample thickness. The scatter between the pressures associated to the minimum (green) and the maximum (yellow) sample thickness increases with radial stretch. In addition, comparing the results obtained for the thoracic (A) and abdominal (B) segments at $\lambda_R = 0.2$, the scatter for the abdominal model is almost a third of the thoracic one.

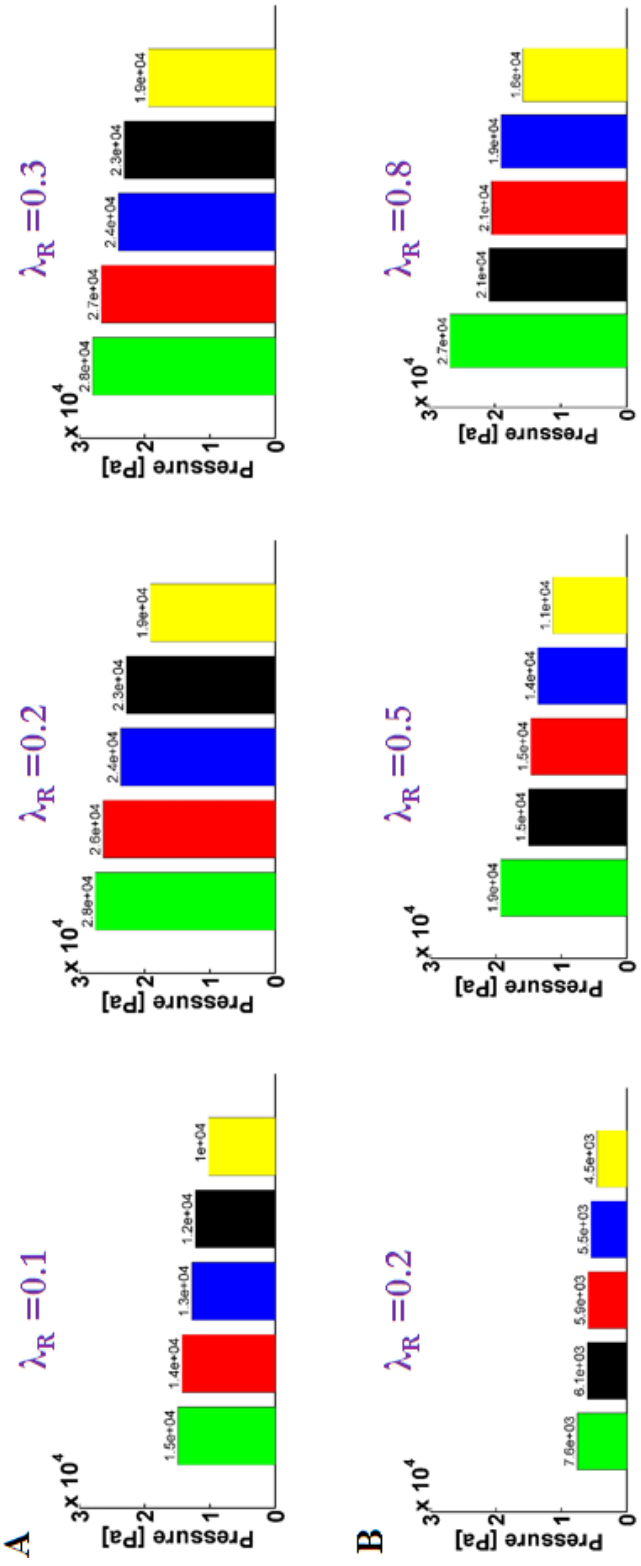

Figure 6.11 Sample thickness role on the pressure inflating the thoracic (A) and abdominal (B) aortic model. Three values of radial stretch have been selected for each model. Each bar colour is specific for a sample thickness value: the minimum of all samples (green), the average of all samples (black), the maximum of all samples (yellow), the sample specific (red) and and the average of three random points (blue).

Observations

The quasi-static model, recently adopted by Pierce et al. (Pierce *et al.*, 2015), has been preferred, as computational costs are reduced and higher stability is reached compared to the dynamic analyses.

The pre-stretch approach generates a minimum variation of the radial displacement in response to the systolic peak. Conversely, wall stress peaks are more pronounced and one order of magnitude higher than the pressure inflating the aorta. The effect of sample thickness on numerical predictions is clearly reflected in maximum radial stretch and wall stress values calculated for the thoracic aorta: both values increase with enlarging sample thickness (Tables 6.9 and 6.10). An higher value of sample thickness leads to a softer stress-strain behaviour of the tissue. Therefore, higher radial deformations are produced. Similar results are generated by Yeoh and Marlow constitutive models. An analogous trend is observed in the abdominal physiologic model (Table 6.10).

The FE model for aneurysm formation in a homogeneous abdominal aorta computes critical pressure values inversely proportional to the sample thickness (Table 6.11). As a result, the model associated with the maximum sample thickness value expects that a physiologic pressure may instigate an aneurysm formation ($\sim$ 122mmHg). Aneurysm formation is expected for the healthy thoracic aorta exclusively along a local geometrical thinning, modelled in this work as an axisymmetric ring. The trend observed in the physiological model is confirmed, since a direct and consistent effect of the sample specific thickness can be appreciated in Table 6.12 and Figure 6.11. Also, critical pressure values appear to decrease with increasing degree of thinning. This outcome is supported by the abdominal results that report a reduction in pressure value directly proportional to the reduction in thickness (Table 6.13). However, while the sample thickness is affecting the wall stress values (Figure 6.10), the reduction of the geometrical thickness in the thoracic model seems irrelevant in the wall stress predictions (Figure 6.9). It is

worth notice though that pressure generating such stress-stretch behaviour do not match, being the increment size variable.

6.2 Predictions obtained from anisotropic models of aorta

Fung orthotropic formulation is available among the anisotropic models in Abaqus. This model, rarely adopted compared to HGO strain-energy function, has been preferred for the present study due to its phenomenological nature (Section 5.3).

Experimental data, collected from biaxial tensile tests (Section 4.3), have been post-processed by Matlab scripts, as detailed in Section 3.3.1. The quality of the fitting is affected by the requirement that all Fung parameters need to be strictly positive (Holzapfel, 2006). Such condition has been imposed among the options of *lsqcurvefit* function and the Levenberg-Marquardt method has been selected. Convergence, however, could not be reached up to the requested tight tolerance. Thus, a sub-optimal fitting was accepted after two millions of iterations. The fitting coefficients generated from this procedure are listed in Table 6.14 for the abdominal tissue and in Table 6.15 for the thoracic one. The complexity of such fitting consists in taking into account three different stress-strain curves, which refer to the circumferential, axial and shear response. The inclusion of the shear response, analytically determined (Section 3.3.1), will be justified and discussed in Chapter 7. The parameter C, multiplying the exponential function in the Fung strain-energy function (Section 2.2.3), has dimension of a stress. Thus, the values estimated for C appear comparable for the fitting of abdominal and thoracic responses. A significant variability among abdominal data sets is limited to parameters a_5 and a_6 (Table 6.14). On the other side, a much wider variability is observed for thoracic data sets, except a_9 and C (Table 6.15).
The experimental data and associated fitting are plotted in Figure 6.12 for the abdominal tissue and in Figure 6.13 for the thoracic one.

Fung parameter	**Fitting coefficient**		
	Set 1	Set 2	Set 3
a_1	0.81	1.03	1.41
a_2	0.74	0.68	0.64
a_3	1.41	1.64	1.84
a_4	0.43	0.39	0.64
a_5	0.000035	0.059	0.25
a_6	0.0006	0.194	0.4
a_7	0.9	0.77	0.72
a_8	1.23	1.43	1.63
a_9	1.23	1.43	1.63
C	73277.87	63874.05	63122.66

Table 6.14 Coefficients obtained fitting the experimental mechanical response of abdominal aorta subjected to biaxial tensile tests. Each set refers to different experimental responses. Parameter C is expressed in Pa, while a_i are dimensionless.

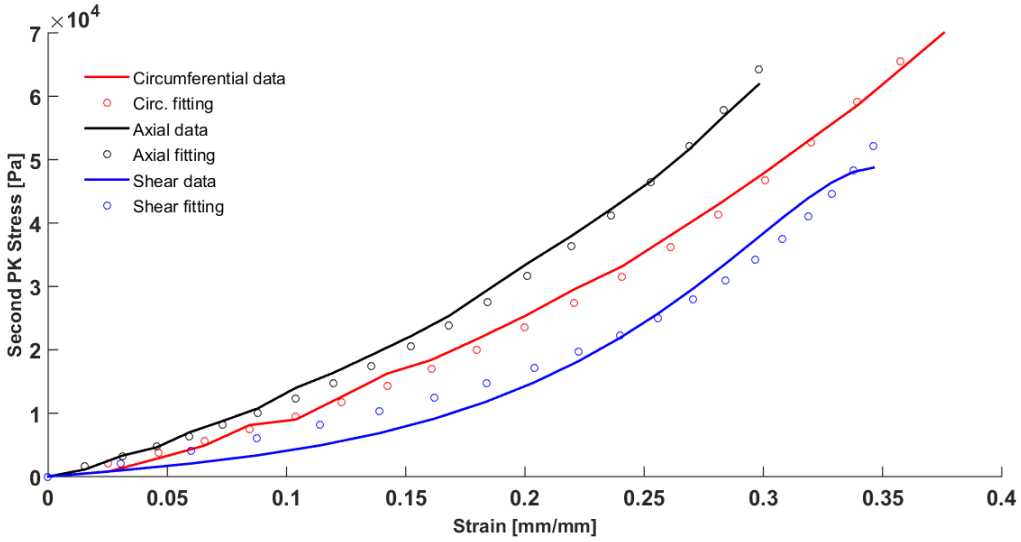

Figure 6.12 Fitting (circles) of stress-strain mechanical responses (lines) for abdominal aortic tissue, referring to Set 1 of Table 6.14. Circumferential (red) and axial (black) behaviour have been obtained from biaxial tensile tests. Shear (blue) data have been determined analytically.

Fung parameter	**Fitting coefficient**		
	Set 1	Set 2	Set 3
a_1	0.45	0.072	0.39
a_2	0.53	0.11	0.28
a_3	3.19	6.01	1.84
a_4	0.09	0.44	0.34
a_5	0.0003	0.0002	0.022
a_6	0.002	0.0000000001	0.000039
a_7	0.51	0.79	0.48
a_8	7.58	3.05	3.65
a_9	0.13	0.19	0.33
C	73131.96	70570.02	83325.44

Table 6.15 Coefficients obtained fitting the experimental mechanical response of thoracic aorta subjected to biaxial tensile tests. Each set refers to different experimental responses. Parameter C is expressed in Pa, while a_i are dimensionless.

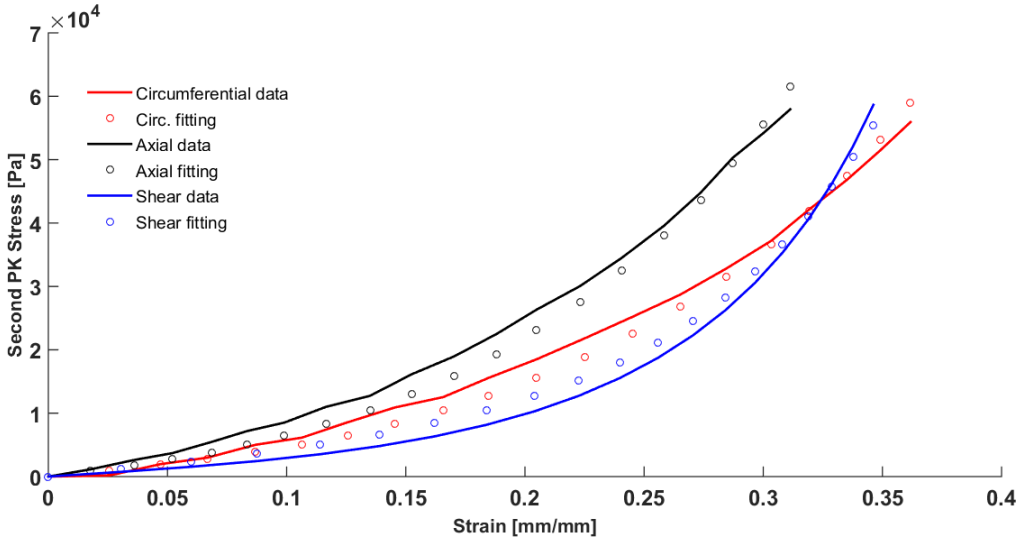

Figure 6.13 Fitting (circles) of stress-strain mechanical responses (lines) for thoracic aortic tissue, referring to Set 1 of Table 6.15. Circumferential (red) and axial (black) behaviour have been obtained from biaxial tensile tests. Shear (blue) data have been determined analytically.

A variety of recommendations is available in literature to verify Fung material stability and its physically meaningful mechanical behaviour (Fan & Sacks, 2014; Holzapfel, 2006; Pandit *et al.*, 2005; Sun & Sacks, 2005).

The convexity has been checked visually by plotting the contours representing states of constant energy of the Fung strain-energy function (Holzapfel, 2006) based on the coefficients listed in Tables 6.14 and 6.15. Such projections are usually displayed onto the Green-Lagrange strain planes (Holzapfel, 2006; Holzapfel *et al.*, 2000; Sun & Sacks, 2005). Hence, Figure 6.14 reports the isoenergetic curves generated for the fitting of the abdominal aorta behaviour.

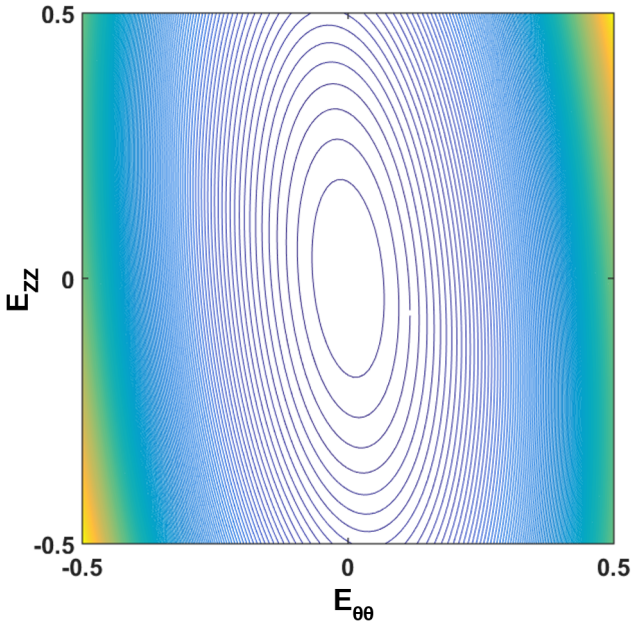

Figure 6.14 Convexity check of Fung strain-energy function for abdominal material properties, based on coefficients of Set 1 listed in Table 6.14.

Similarly, the convexity associated to the set of coefficients determined for the thoracic aorta has been verified, as displayed in Figure 6.15.

Set 1 from Table 6.14 and 6.15 were selected to describe the material properties in the following geometries. These data sets refer indeed to average stress-strain responses observed among the sample tested.

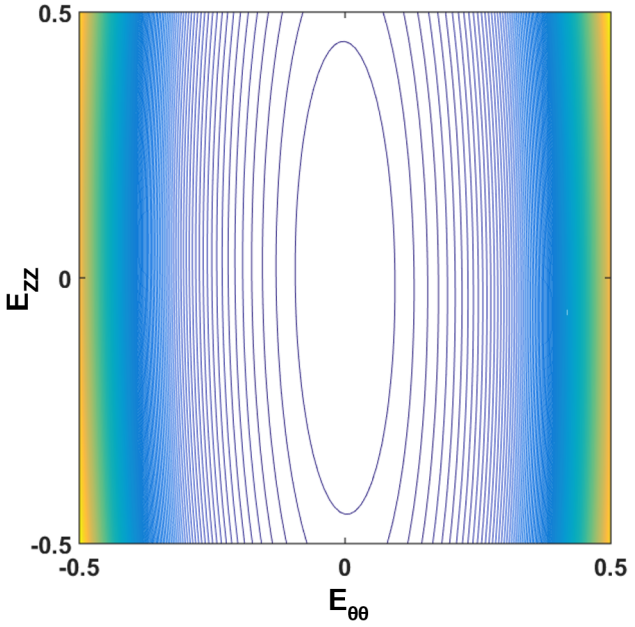

Figure 6.15 Convexity check of Fung strain-energy function for thoracic material properties, based on coefficients of Set 1 listed in Table 6.15.

6.2.1 Cylindrical geometries

Two cylindrical models, meshed by C3D8RH elements, have been designed as part of the first step into the Fung modelling progress of the present work (Figure 5.7). Identical in diameter and length, these models differ by the thickness, assumed constant along each geometry and greater for the thoracic district compared to the abdominal one (Section 5.3.1). This feature is based on experimental measurements shown in Section 6.1.3.

The static inflation, simulating a systolic peak ($\sim$ 120 mmHg), generated higher wall stress values for the abdominal model compared to the thoracic one. In detail, the maximum von Mises stress value and the displacement magnitude predicted are reported in Table 6.16.

Model	Max von Mises stress [MPa]	Displacement magnitude [mm]
Abdominal	0.25	7.1
Thoracic	0.31	8

Table 6.16 Stress and displacement magnitude values predicted for abdominal and thoracic anisotropic model of aorta subjected to a static inflation of 16 kPa. Geometries are simplified as cylindrical.

It it worth recalling that fully constrained boundary conditions were applied (Section 5.3), thus no radial stretch is allowed at the model ends. Although the displacement magnitude appears uniform along the abdominal model, the central part of the thoracic one looks slightly less stretched compared to the rest of the vessel. This feature could be explained by a major displacement along the axial direction, which is affecting the overall displacement field (U) in the central region.

The modified Riks algorithm does not predict any bulging appearance. Thus, no aneurysm is expected for any of these cylindrical geometries which anisotropic material properties are described by Fung strain-energy function.

6.2.2 Cylindrical geometry: descending aorta

The second model, intended as a step towards more complex designs, shows the coupling of abdominal and thoracic anisotropic material properties. The novelty of this model consists, indeed, into assigning a peculiar Fung formulation to the corresponding segment of the aorta. Hence, in this model of the descending aorta, the upper half of the model behaves as a thoracic sample (Section 4.3.2), while the inferior part responds as abdominal aortic tissue (Section 4.3.1), both subjected to biaxial tensile tests.

Aiming to proceed gradually towards a physiologic model, at this step no substantial geometric transformation is introduced: the geometry is kept cylindrical with a constant

thickness (Section 5.3.2).

Wall stress values predicted for the static inflation appear higher in the thoracic district, the peak being equal to 0.335 MPa. As shown in Figure 6.16, an abrupt discontinuity in stress values is reported in the central part of the model, where different material properties connect (Section 5.3.2).

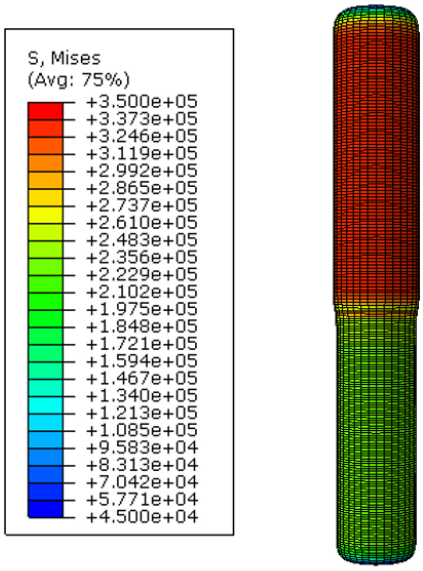

Figure 6.16 von Mises stress [Pa] predicted for an anisotropic model of descending aorta subjected to a static inflation of 16 kPa. The upper half of the cylindrical geometry is modelled by thoracic material properties, while abdominal material properties are assigned to the inferior half.

As expected, no abrupt discontinuity is observed for displacement magnitude values, as no geometric disruption has been introduced. The central part appears stretched up to 18 mm around the junction area, being also free from the boundary conditions effect. Thus, it appears that this cylindrical geometry, coupling different material properties, allows a displacement magnitude which is more than doubled compared to separate responses (Section 6.2.1).

On the other hand, the present model does not predict any different outcome in terms of aneurysm instigation compared to cylindrical geometries. No critical pressure and bulge appearance are computed.

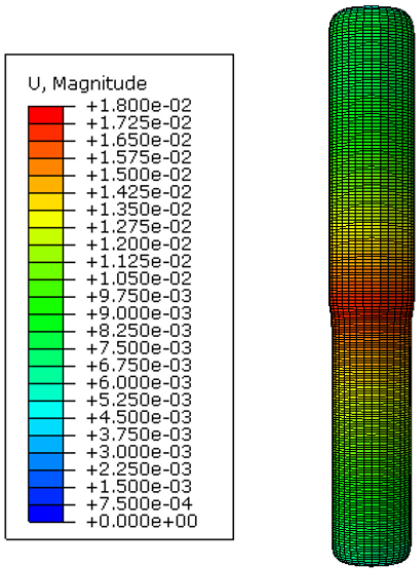

Figure 6.17 Displacement magnitude [m] predicted for an anisotropic model of descending aorta subjected to a static inflation of 16 kPa. The upper half of the cylindrical geometry is modelled by thoracic material properties, while abdominal material properties are assigned to the inferior half.

6.2.3 Physiologic geometries

The third step in the modelling process of anisotropic aorta appears crucial, since the geometry has been changed (Figure 5.7). Cylindrical models are replaced by geometries close to human physiology, based on published data (Noordergraaf, 1956; Wang & Parker, 2004; Westerhof *et al.*, 1969). Thus, the thickness and the diameter of the models decrease continuously from the top of the thoracic segment to the bottom of the abdominal one, where the aorta splits into the iliac arteries.

Compared to previous anisotropic models, no changes in loading, boundary conditions, mesh elements or material properties have been introduced.

The static inflation appears challenging, since the analysis diverges. A list of approaches

will be presented in the next Section 6.2.4. At this stage, a classical Newton-Raphson procedure to perform non-linear elastic static analysis has been deemed inadequate. Hence, the analysis has been carried out with the Riks algorithm. As a result, no aneurysm formation is predicted in either aortic district, in analogy to previous cases. However, a pressure of 15.1 kPa ($\sim$ 113 mmHg), the highest value taken into account by the algorithm for the abdominal model, generates a von Mises stress of 0.47 MPa, as displayed in Figure 6.18.

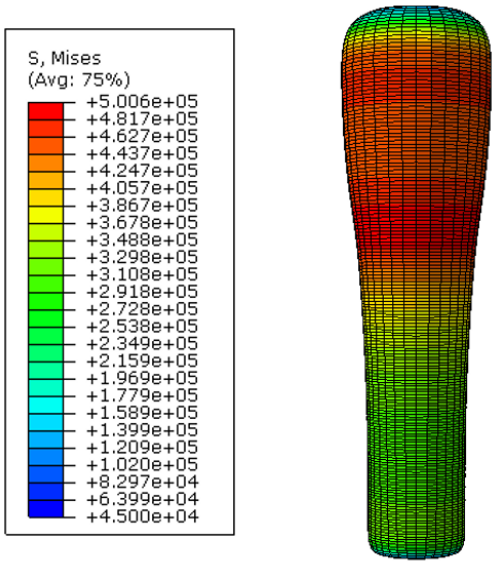

Figure 6.18 von Mises stress [Pa] predicted for a physiologic anisotropic model of abdominal aorta subjected to a pressure of 15.1 kPa. Such stress distribution has been predicted during Riks analysis.

It may appear contradictory that the superior part of the model, characterized by larger diameter and thickness, reaches an higher value of stress compared to the inferior part. Such result can be explained, as an example, by the equation of circumferential Cauchy stress of a loaded tube (Schulze-Bauer *et al.*, 2002)

$$\sigma_{\theta\theta} = p\left(\frac{r}{h} - 1\right) \tag{6.1}$$

where p is the transmural pressure. The outer radius (r) and the wall thickness (h) refer to the deformed configuration. Applying a pressure of 15.1 kPa, the thickness is reduced by half compared to the initial load-free configuration uniformly along the model. Although a greater displacement magnitude is observed in the inferior part of the model (Figure 6.19), the radius r remains larger in the superior part. Thus, major wall stress values are computed in the upper region of the abdominal aorta.

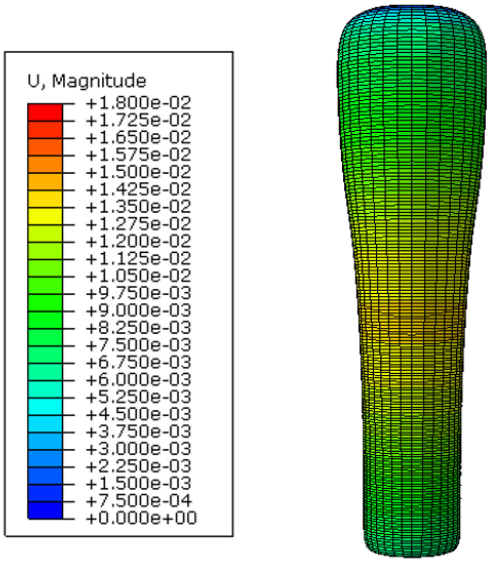

Figure 6.19 Displacement magnitude [m] predicted for a physiologic anisotropic model of abdominal aorta subjected to a pressure of 15.1 kPa. Such stress distribution has been predicted during Riks analysis.

A pressure of 12.3 kPa ($\sim$ 92 mmHg), the highest value taken into account by the Riks algorithm for the thoracic model, generates a von Mises stress of 0.47 MPa, as shown in Figure 6.20. Despite a limited reduction of diameter and thickness occurs in the geometry, the stress (Figure 6.20) and displacement magnitude (Figure 6.21) distribution appear uniform as observed in cylindrical models (Section 6.2.1).

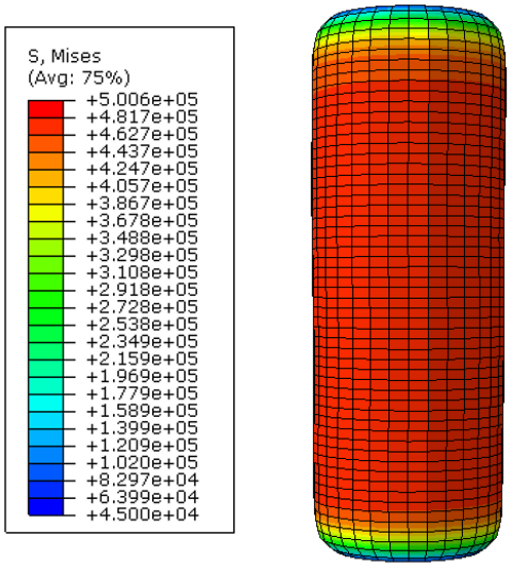

Figure 6.20 von Mises stress [Pa] predicted for a physiologic anisotropic model of thoracic aorta subjected to a pressure of 12.3 kPa. Such stress distribution has been predicted during Riks analysis.

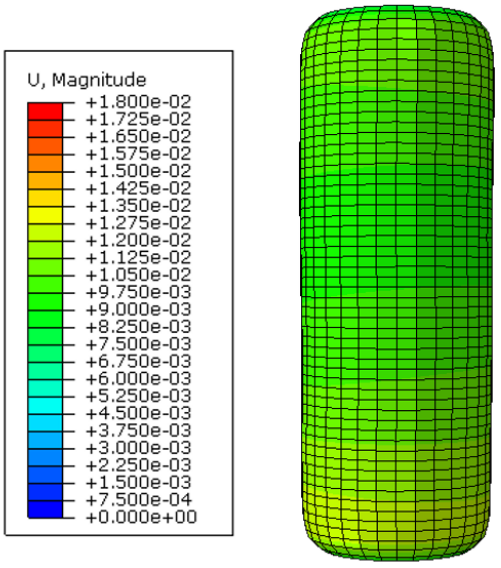

Figure 6.21 Displacement magnitude [m] predicted for a physiologic anisotropic model of thoracic aorta subjected to a pressure of 12.3 kPa. Such stress distribution has been predicted during Riks analysis.

6.2.4 Physiologic geometry: descending aorta

As last step of the anisotropic modelling process based on Fung formulation, a physiologic model of the descending aorta has been generated. The geometry, displayed in Figure 5.8, has been obtained joining the designs analysed in the previous Section 6.2.3. This model appears to be novel in the state of art for its geometry and for the material properties, based on experimental tests (Section 4.3) and described by means of the Fung orthotropic strain-energy function.

Similarly to the previous step (Section 6.2.3), where the thoracic and abdominal segment have been analysed separately, the static inflation of the current model diverges after half of the loading is applied. It is worth emphasizing that no changes in loading, boundary conditions, mesh elements or material properties have been introduced compared to the cylindrical model of descending aorta (Section 6.2.2). The geometry represents the only feature that has been altered, in order to take into account a design closer to the physiology.

An impressive amount of attempts and huge efforts were required to solve this problem, since no complete and clear knowledge is available in the state of art neither in Abaqus manual. In the following Chapter 7, it will be fully discussed how published studies about Fung formulation lack important details. Furthermore, limited suggestions are available in the Abaqus manual about Fung modelling, hence, the work described in the present Section has been particularly arduous.
First of all, different element types have been considered to mesh the geometry, keeping unaltered all the other parameters, such as boundary conditions, load application and number of elements. Thus, the following element types have been investigated:

- 8-node linear brick, reduced integration with hourglass control (C3D8R)
- 8-node linear brick, incompatible modes, hybrid with linear pressure (C3D8IH)

- 20-node quadratic brick, reduced integration, hybrid with linear pressure (C3D20RH).

As a result, divergence was experienced even earlier than using C3D8RH elements. Mesh refinements were not helpful either: along the thickness of the geometry up to 3 elements have been used.
Therefore, keeping the original mesh (C3D8RH) unaltered, boundary conditions, different from fully constrained ends, have been explored. Aiming to avoid any boundary setting inconsistent with physiologic conditions, configurations accounting pins, encastre and axial displacements have been unsuccessfully attempted.

Convergence has been reached by a single combination of element type and boundary conditions: C3D8IH elements mesh the geometry which ends are allowed to expand radially. In detail, no axial stretch is allowed, while radial displacement of geometry ends is permitted. In addition, no movement is allowed to the axis of the geometry.
Incompatible mode elements (C3D8I and the corresponding hybrid elements) are first-order elements that use full integration and, thus, have no hourglass modes. These elements are somewhat more expensive than the regular first-order displacement elements; however, they are significantly more economical than second-order elements. However, Abaqus guide recommends incompatible elements to improve the bending behaviour of regular displacement elements (Dassault Systèmes, 2014).
Thus, it may be concluded that such elements deal better with possible instabilities arising from these specific material properties.

The wall stress distribution predicted for static inflation is displayed in Figure 6.22. In this case, a cut view (Figure 6.22 B) is provided to highlight appreciably higher stress values on the internal surface: von Mises stress levels appear doubled on the lumen wall (Figure 6.22 B) compared to the external one (Figure 6.22 A). Furthermore, similarly to

results obtained in the previous steps (Section 6.2.3), wall stress values decrease from thoracic aorta to the bottom of the abdominal one.

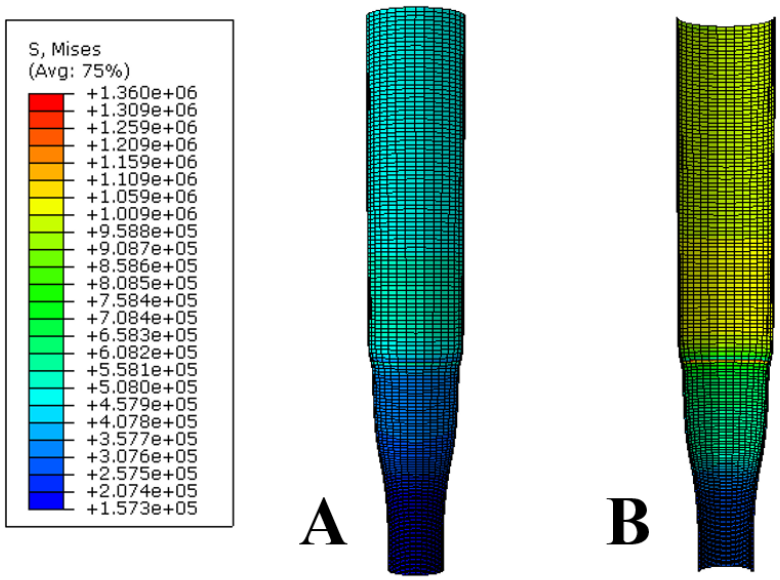

Figure 6.22 von Mises stress [Pa] predicted for an anisotropic model of descending aorta subjected to a static inflation of 16 kPa. The upper region of the cylindrical geometry is modelled by thoracic material properties, while abdominal material properties are assigned to the inferior region. Higher stress levels are experienced on the internal surface of the geometry (B) compared to the external one (A).

An additional cut view is provided to appreciate at the same time the stress distribution and the global deformation of the model compared to the undeformed configuration (Figure 6.23).

Large deformations are predicted applying a systolic pressure to the present physiologic model of descending aorta. The diameter of the model in the final configuration (Figure 6.24) appears almost doubled, being the maximum radius of the undeformed abdominal district 2.2 cm.

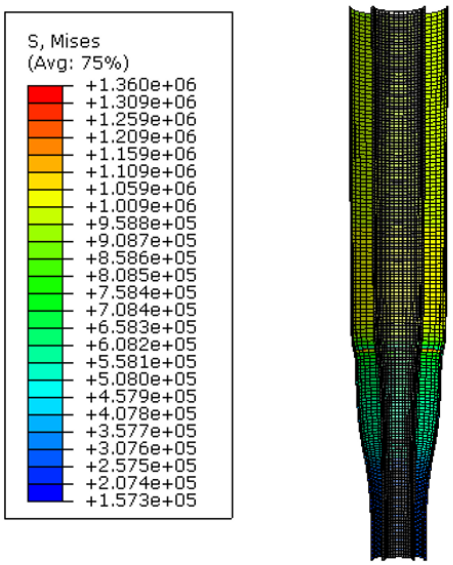

Figure 6.23 Cut view of the anisotropic model of descending aorta. The undeformed configuration appears superimposed to the wall stress field [Pa] of the final configuration.

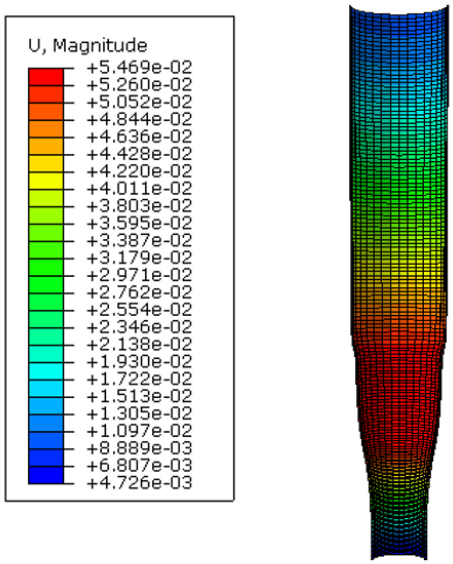

Figure 6.24 Displacement magnitude [m] predicted for an anisotropic model of descending aorta subjected to a static inflation of 16 kPa. The superior part of the geometry is modelled by thoracic material properties, while abdominal material properties are assigned to the inferior region.

Observations

Comparing the cylindrical (Section 6.2.2) and physiologic (Section 6.2.4) models of descending aorta, higher wall stress values are reached, in both cases, in the thoracic district compared to the abdominal one. While the stress field is almost uniform in both thoracic regions and in the abdominal region of the cylindrical model, the stress in the physiologic abdominal aorta covers a range of approximately 0.2 MPa. This aspect is suggested to be mainly a direct effect of the geometry, due to the decreasing diameter and thickness. In addition, wall stress values appear about 0.15 MPa higher in the thoracic physiologic model (Figure 6.22 A) compared to the thoracic cylindrical one (Figure 6.16).

Larger deformations are achieved in the physiologic model (Figure 6.24), where the maximum displacement magnitude is three times higher than the maximum predicted for the cylindrical model. The reasons for such difference consist in the different material modelling and geometry. Furthermore, while the abdominal segment accounts the highest stretch in the physiologic model, the stretch peak in the cylindrical model is expected along the junction between the aortic segments. This feature can be explained keeping in mind the different boundary conditions: fully constrained ends of the cylindrical model allow the larger stretch in the middle of the model. On the other end, radial displacement was permitted in the physiologic model.

6.3 Isotropic and anisotropic models: a comparison

The artery constitutive behaviour has been defined closer to being isotropic than anisotropic by Alhayani et al. (Alhayani *et al.*, 2013). However, the material properties they adopted are speculative, not fully supported by the literature. On the contrary, Schmidt et al. (Schmidt *et al.*, 2015) highlighted significant differences between the

simulations using an isotropic and an anisotropic model of a strongly idealized artery. In the present research, a more physiologic design (Section 5.3) and a Fung orthotropic model, based on biaxial data (Section 4.3) and pure shear (Section 3.3.1), has been evaluated to investigate the aneurysm appearance as a result of supra-physiological inflation.

A further novelty of the present work consists of comparing the isotropic response obtained from such physiologic model with the anisotropic one reported in Section 6.2.4. Therefore, the geometry described in Figure 5.8 has been characterized by isotropic material properties for the thoracic and abdominal segment respectively. Such isotropic behaviours have been previously adopted in Section 6.1.3: data referring to sample specific thickness have been selected. In addition and similarly to thickness study (Section 6.1.3), Marlow strain-energy function describes such data obtained from uniaxial tensile tests.
Once again, C3D8IH elements mesh the geometry which ends are allowed to expand radially while, no axial stretch is allowed.

The static inflation, intended to simulate a systolic pressure load, generates stress values comparable in both models on the external wall surface (Figure 6.25). However, a consistent difference can be observed in the cut view, where lumen stress values appear consistently lower in the isotropic model compared to the anisotropic one (Figure 6.26).

In the isotropic model displacement magnitude does not exceed 1.2 mm (Figure 6.27), while in the anisotropic model the deformation appears an order of magnitude larger, as the maximum is about 5 cm.

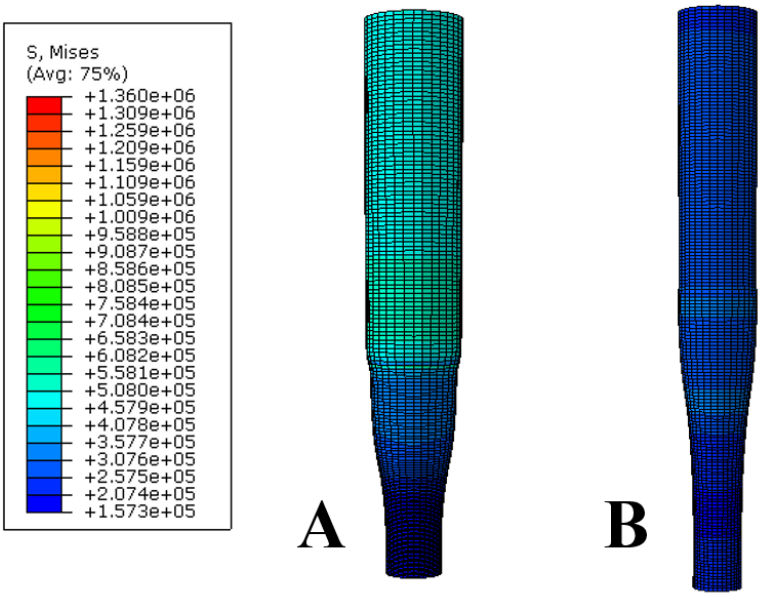

Figure 6.25 Comparison of von Mises stress [Pa] predicted for an anisotropic (A) and isotropic (B) model of descending aorta subjected to a static inflation of 16 kPa. The superior district of the geometry is modelled by thoracic material properties, while abdominal material properties are assigned to the inferior district.

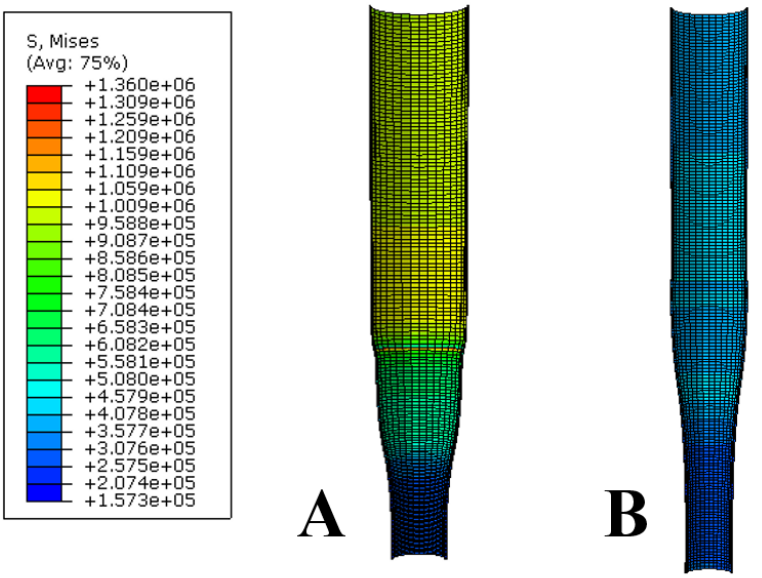

Figure 6.26 Comparison of von Mises stress [Pa] predicted for an anisotropic (A) and isotropic (B) model of descending aorta subjected to a static inflation of 16 kPa. The cut view highlights the lumen surface.

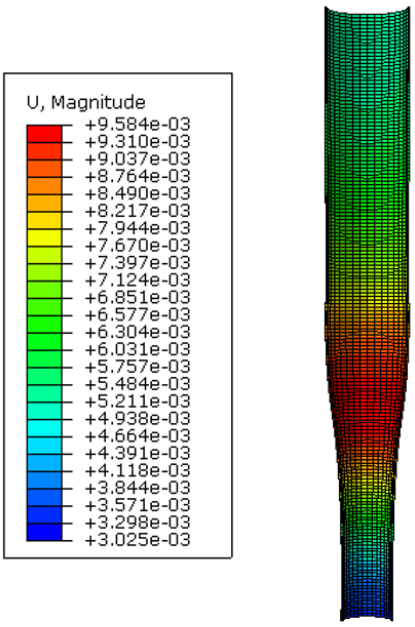

Figure 6.27 Displacement magnitude [m] predicted for an isotropic model of descending aorta subjected to a static inflation of 16 kPa. The superior part of the geometry is modelled by thoracic material properties, while abdominal material properties are assigned to the inferior region.

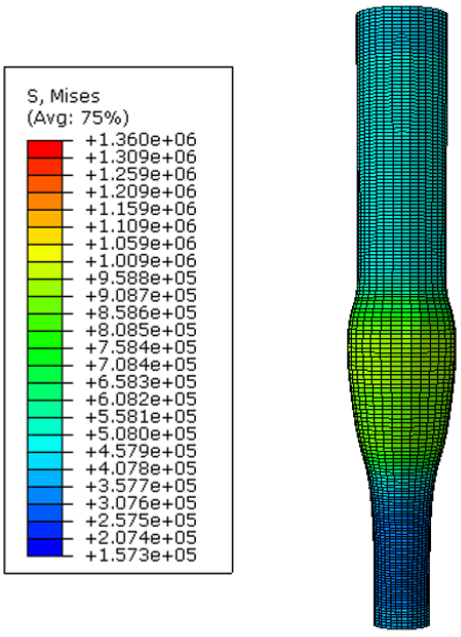

Figure 6.28 von Mises stress [Pa] predicted for aneurysm formation in a isotropic model of descending aorta. The upper district of the geometry is modelled by thoracic material properties, while abdominal material properties are assigned to the inferior district.

Comparing the maximum von Mises stress predicted for the static inflation, the anisotropic model shows about 52% higher values than the isotropic one on the external wall. Even more, the displacement magnitude predicted is about 5 times larger in the anisotropic model.

However, the most relevant difference between the isotropic and the anisotropic model is predicted by Riks modified algorithm. While no bulge formation has been computed for the anisotropic model (Section 6.2.4), a critical pressure of 22.8 kPa ($\sim$ 171 mmHg) predicts aneurysm appearance in the isotropic model. The formation is expected in the superior part of the abdominal aorta, where wall stress values exceeds 1.1 MPa, as shown in Figure 6.28.

Despite the bulging formation, displacement magnitude predicted for such supra-physiologic pressure (Figure 6.29) appear inferior to the deformation expected by the anisotropic model at systolic pressures (Figure 6.24).

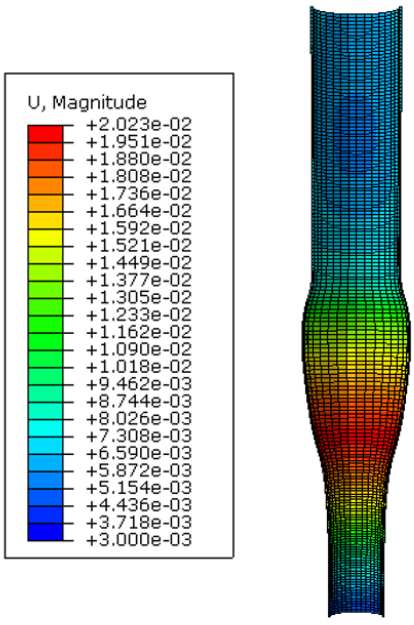

Figure 6.29 Displacement magnitude [m] predicted for aneurysm formation in a isotropic model of descending aorta. The superior district of the geometry is modelled by thoracic material properties, while abdominal material properties are assigned to the inferior district.

Concluding, material properties strongly affect the FE predictions, since the Fung orthotropic model generates quite different predictions compared to the isotropic one. Such difference is even enhanced in the aneurysm prediction, as only the isotropic model predicts an aneurysm formation.

Chapter 7

Discussion & Conclusions

The novelties of the present work range from the experimental procedure to the computational modelling of aortic behaviour.

In order to study the aneurysm formation, the mechanical characterization of the healthy porcine aortas has been accomplished by means of uniaxial and biaxial tensile tests. Given the multitude of experimental procedures present in literature and reviewed in Chapter 2, the first objective of this research was to define a complete up-to-date protocol to extract reliable material properties from aortic tissues. Such methodology has been validated first on a carbon filled rubber material. It is worth emphasizing that this material was chosen because of its hyper-elastic response, its large availability in the laboratory and its simple management. No claim is made that the adopted rubber can match the biological response of the aorta.

As a consequence of the study conducted on rubber, aortic samples have been cut only in dog-bone shape to ensure a standard preparation procedure. Furthermore, in order to investigate whether the f_P may have an effect on aortic tissue similar to what has been experienced for rubber, it has been chosen to test three cases for each district: 1.2 Hz (analogous to 70 bpm), 2 Hz (120 bpm) and the absence of pre-conditioning.

Among the novelties of the experimental procedure, an optical approach to measure

the sample thickness has been proposed in Section 3.3. The thickness study (Section 6.1.3) evaluated the impact of the five different methodologies to measure the sample thickness on numerical models. As a result, the scatter between the minimum and the maximum thickness values taken into account for each thoracic and abdominal aorta is less than 1 mm. However, the sample-specific measures do not necessarily correspond to the average outcome of the five methodologies since they are below or equal to the median of the range.

Experimental results for aortic tissue, presented in Chapter 4, are hardly comparable with published data, due to considerable differences in sample preparation and mechanical testing. As detailed in *Observations* sections, substantial differences have been spotted with Peña et al. (Peña *et al.*, 2015) mechanical characterizations. Despite a general agreement with other published data (Vande Geest *et al.*, 2006; Xiong *et al.*, 2008) has been observed, a complete match of responses appears impossible due to biological variability and disparate protocols.

The analogy between aneurysm formation and bulging bifurcation of inflated cylinders, simplifying arterial geometry, has previously been investigated by Rodriguez & Merodio (Rodríguez & Merodio, 2011). Therefore, cylindrical geometries have been widely used in the present work to generate isotropic or anisotropic aortic models (Chapter 6) based on experimental data (Chapter 4).

Isotropic results, reported in Section 6.1.2, seem to suggest that no aneurytical bulge should be expected from supra-physiological inflation of healthy thoracic or abdominal aorta modelled as perfect cylinders. Although several SEF do not predict any aneurysm appearance, the adoption of Neo-Hookean SEF always computes a bulge formation. Single elastin fibres are responsible of the arterial compliant response and they exhibit Neo-Hookean mechanical behaviour. However, the overall non-linear behaviour cannot be described by such a constitutive model (Watton *et al.*, 2009). Similarly, Kyriacou & Humphrey (Kyriacou & Humphrey, 1996) expressed their concern about the adoption

of Neo-Hookean SEF to describe soft tissue behaviour. This is why results of Neo-Hookean simulations are not presented as demonstration of aneurysm formation.
As detailed in Section 6.1.3, whether a healthy isotropic aortic mechanical behaviour is modelled by Marlow SEF, a substantial localized thickness reduction occurs to be necessary to instigate the aneurysm formation in thoracic aorta. Such SEF avoids the curve fitting, that may introduce artefacts on the acquired aortic material response, ensuring a controllable mechanical behaviour beyond the range of data (Marlow, 2003). In order to define a safe guideline, it appears that a minimum reduction of 30%, compared to the thickness of the model ends, is required to observe aneurysm formation in the thoracic aorta (Table 6.12). The effects of local imperfection on the critical pressure has been investigated by Lopes et al. (Lopes *et al.*, 2007) for latex material, but no analogous work has been retrieved for arterial tissue. Hence, this analysis appears to be novel and its results relevant, since the wall thickness is defined crucial to evaluate solely the aneurysm risk of rupture (Lasheras, 2007) in literature.
Despite the same cylindrical geometry has been modelled, different material properties have been assigned to obtain the outcomes listed in Section 6.1.2 and in Section 6.1.3. In the first case, the stiffest and softest experimental responses were selected, leading to no bulging prediction in either aortic district. In the second case, an average stress-strain response has been chosen, leading to aneurysm prediction in abdominal aorta even in the absence of local imperfections. Thus, the impact of a specific stress-strain response appears consistent.

The state of art, reviewed in Section 2.3.2, suggests that uniaxial and planar biaxial tests should be sufficient to achieve a complete characterisation of the aortic tissue and to model its anisotropic behaviour by means of the Fung SEF. However, so far no work published a complete set of 9 parameters (Equation 2.27) to fit soft tissue behaviour.
Schulze-Bauer et al. (Schulze-Bauer *et al.*, 2002) reported 4 parameters to fit the response of human femoral arteries subjected to inflation tests. In 2003, Schulze-Bauer &

Holzapfel (Schulze-Bauer & Holzapfel, 2003) modelled already published clinical data of thoracic aorta, oblivious of the cross-sectional area, by means of 4 Fung parameters. Sun & Sacks (Sun & Sacks, 2005) meant to produce clear guidelines to build a Fung model in Abaqus. However, they published only 7 parameters. Pandit et al. (Pandit *et al.*, 2005) published 4 coefficients to fit the experimental data obtained from inflation tests performed on porcine left anterior descending artery. In 2006, vande Geest et al. (Vande Geest *et al.*, 2006) were unable to fit the experimental data with a 4 parameter Fung elastic model. Differently, Horny et al. (Horný *et al.*, 2006) fitted the responses of inflation tests on human thoracic aorta by means of 4 Fung parameters. However, they added a Neo-Hookean term to the SEF. Ma et al. (Ma *et al.*, 2007) claim that their Abaqus model of cerebral aneurysm is modelled by 5 Fung parameters. In 2010, Avril et al. (Avril *et al.*, 2010) modelled in Abaqus the inflation of human arteries, publishing only 4 parameters. Vychytil et al. (Vychytil *et al.*, 2010) reported the 9 parameters equation, but they published only 6 coefficients with no assumption for the shear terms. Bellini et al. (Bellini *et al.*, 2011) reported 4 parameters to fit responses of planar biaxial tests conducted on porcine duodenum, jejunum and ileum. Recently, Lee et al. (Lee *et al.*, 2014) published 7 parameters for porcine carotid arteries.

The present work arises no doubt that 4 Fung parameters are sufficient to obtain an excellent fit of biaxial tests results. In addition, the 3 parameters referred to shear are generally neglected in literature. Since no shear is generated during a simple inflation test, such parameters were initially disregarded in this work. However, it has been noticed that a complete material description requires 9 positive parameters for the orthotropic model. Thus, it appears not clear why no complete set of coefficients have been published so far, since they are necessary to run the FE model.

Therefore, results in Tables 6.14 and 6.15 represent a considerable novelty.

Anisotropic results, reported in Section 6.2, seem to suggest that no aneurysm could be predicted either in a cylindrical or more physiologic geometry, having no thickness

imperfection. Hence, such outcomes appear in agreement with isotropic models findings (Section 6.1.2). However, the comparison between isotropic and anisotropic material properties on the physiologic geometry (Section 6.3) revealed a substantial difference: aneurysm formation was predicted only for isotropic material properties. It is worth noticing that such isotropic material properties predicted aneurysm formation even in the cylindrical geometry (Section 6.1.3). Once again, the role of material properties appears crucial to FE outcomes. In addition, consistent differences in stress and strain values have been noticed as a result of static inflation at a systolic pressure.
Such findings appear in contrast with Ramachandran *et al.* (2012), who claimed that the modelling choices (Fung-type or isotropic) have minimal impact on wall tension evaluation. Similarly, Alhayani *et al.* (2013) observed that the formation of the bulge in the anisotropic (HGO) model appeared analogous to the one predicted in the isotropic design. However, their material properties were partially arbitrary.

7.1 Limitations

The main limitations of the current work need to be highlighted.

Being considered the most similar to the human one, experimental tests have been conducted on porcine aortic tissue. Hence, experimental tests on human tissue could lead to different outcomes.

Several analyses have been performed on FE aortic geometries simplified as a cylinder. Although, the physiologic design appears closer to *in vivo* structure, no arteries connected to the aorta have been considered. In addition, the anisotropic model has been based on data published by Wang & Parker (2004), where the diameters are different from dimensions indicated by O' Gara (2003). As has been observed during the present

work, a different geometry may lead to different predictions.

Despite its three layers structure, the aorta has been modelled by a single layer. The focus of the present study is on the macro-structural response and not on specific layers.

Since no dedicated facility was available and no time could be allocated for more experimental tests, the shear response, needed for anisotropic FE models, has been estimated analytically. Thus, such results could differ from what could be observed in an experimental campaign alike the study just presented by Sommer *et al.* (2016), who investigated the shear properties of diseased thoracic aorta.

Finally, predictions on physiologic geometry based on isotropic material properties couple only longitudinal responses, since uniaxial tests could not be performed on abdominal aortas in the circumferential direction. Therefore, the role of collagen in the *adventitia* layer could be enhanced, while the role of smooth muscle (circumferentially oriented) in the *media* reduced.

7.2 Future work

Future developments of the present study may involve different aspects, ranging from the experimental practice to the computational models.

Experimental analyses Since *synthetic* shear tests have been conducted in this study, a natural development would be to carry out such tests. Thus, experimental shear tests could be performed on porcine tissue to gain a complete insight of its mechanical behaviour. As a consequence, Fung parameters could be recalculated to determine the 9 coefficients and spot any difference with the values presented in this work.
Furthermore, an inflation test could be useful to investigate how the results differ from

equi-biaxial outcomes. Hence, two cameras will be needed to compute the strain map by means of DIC. Such analysis would explore whether the different load application changes the radial direction involvement.

Computational models Several further numerical analyses may be conducted designing different FE geometries. First of all the descending aorta may be modelled even closer to *in vivo* structure, introducing for example the arterial branches. Each ramification constitutes indeed a discontinuity of the aortic wall. In addition, the pressure distribution is expected to be different. Such branches may be introduced as part of the idealized model or from patient specific geometry. The present study had no access to MRI scan, which may clearly increase the level of complexity and fidelity of the FE model.

The model of descending aorta could also be extended to take into account the role of the main bifurcation on the stress analysis: iliac arteries originating from the extremity of abdominal aorta could be added to the present model. Thus, the aneurysm prediction may lead to different outcomes. In addition, a comparison of the stress and strain values may evaluate how approximated is the design without the main bifurcation.

7.3 Conclusions

The main aim of the present study consisted of analysing the macro-structural behaviour of the aorta with particular attention on aneurysm formation. Given that several works are generally focussed on rupture prediction, the formation of the bulging has received limited attention in literature.

An extensive experimental campaign has been conducted performing uniaxial and equi-biaxial tensile tests on porcine aortic tissue. In order to acquire reliable material properties, a complete protocol, based on up-to-date techniques, has been detailed. A

consistent variability of hyperelastic responses has been observed.
Mechanical responses have been post-processed by a number of custom made Matlab scripts and imported to FE models.
Several computational analyses have been performed to evaluate the impact of experimental methodology on numerical predictions. Among the experimental features examined the pre-conditioning frequency, the sample shape and the sample thickness measurement are accounted. As a result, each detail of the experimental protocols affects the tissue mechanical response and is reflected into computational results.

Furthermore, numerous FE analyses investigated the effect of computational features on numerical outcomes. The role of two main aspects has been explored: the geometric design and the material properties modelling.
Firstly, the role of the geometry is highlighted in the four steps conceived to generate a physiologic aortic model, which structure is anisotropic. Comparing the cylindrical and physiologic geometry, the same material properties generate considerable different values of wall stress and radial stretch. Furthermore, each design requires specific boundary conditions and mesh element.
Secondly, the fitting of experimental responses appears definitely crucial for numerical predictions. Among isotropic models, several strain-energy functions have been compared: each formulation leads to a different fitting and hence to unique numerical outcomes. Moreover, consistent differences in wall stress and radial stretch result from the comparison between isotropic and Fung anisotropic models.

Concluding, the present study suggests that aneurysm formation in healthy models of aortas is unlikely to be caused by supra-physiologic pressure loading. Whether an aneurysm is predicted in the descending aorta, it is suggested that the abdominal district is more prone to show the bulge compared to the thoracic one.

Bibliography

Aaronson, P.I., Ward, J.P.T., & Connolly, M.J. (2012). *The Cardiovascular System at a Glance*. Wiley-Blackwell, Malden, 4th edition.

Aggarwal, S., Qamar, A., Sharma, V., & Sharma, A. (2011). Abdominal aortic aneurysm: A comprehensive review. *Experimental and Clinical Cardiology*, 16(1), 11–15.

Alhayani, A.A., Giraldo, J.A., Rodríguez, J.F., & Merodio, J. (2013). Computational modelling of bulging of inflated cylindrical shells applicable to aneurysm formation and propagation in arterial wall tissue. *Finite Elements in Analysis and Design*, 73, 20–29.

Alhayani, A.A., Rodríguez, J.F., & Merodio, J. (2014). Competition between radial expansion and axial propagation in bulging of inflated cylinders with application to aneurysms propagation in arterial wall tissue. *International Journal of Engineering Science*, 85, 74–89.

Anjum, A. & Powell, J.T. (2012). Is the incidence of abdominal aortic aneurysm declining in the 21st century? Mortality and hospital admissions for England & Wales and Scotland. *European journal of vascular and endovascular surgery : the official journal of the European Society for Vascular Surgery*, 43(2), 161–6.

Anjum, A., von Allmen, R., Greenhalgh, R.M., & Powell, J.T. (2012). Explaining the decrease in mortality from abdominal aortic aneurysm rupture. *The British journal of surgery*, 99(5), 637–45.

Arruda, E.M. & Boyce, M.C. (1993). A three-dimensional constitutive model for the large stretch behavior of rubber elastic materials. *Journal of the Mechanics and Physics of Solids*, 41(2), 389–412.

ASM, I. (2004). *Tensile Testing*. ASM International, United States of America, 2nd edition.

Avril, S., Badel, P., & Duprey, A. (2010). Anisotropic and hyperelastic identification of in vitro human arteries from full-field optical measurements. *Journal of biomechanics*, 43(15), 2978–85.

Badel, P., Avril, S., Lessner, S., & Sutton, M. (2011). Mechanical identification of hyperelastic anisotropic properties of mouse carotid arteries. *Mechanics of Biological Systems and Materials*, 2(c), 11–17.

Badel, P., Rohan, C.P.Y., & Avril, S. (2013). Finite Element simulation of buckling-induced vein tortuosity and influence of the wall constitutive properties. *Journal of the Mechanical Behavior of Biomedical Materials*, 26, 119–126.

Bailly, L., Deplano, V., Lemercier, a., Boiron, O., & Meyer, C. (2014). New experimental protocols for tensile testing of abdominal aortic analogues. *Medical Engineering and Physics*, 36(6), 800–804.

Bailly, L., Geindreau, C., Orgéas, L., & Deplano, V. (2012). Towards a biomimetism of abdominal healthy and aneurysmal arterial tissues. *Journal of the mechanical behavior of biomedical materials*, 10, 151–65.

Balzani, D. (2006). *Polyconvex Anisotropic Energies and Modeling of Damage Applied to Arterial Walls*. Ph.D. thesis, Duisburg-Essen.

Bathe, K.J. (1996). *Finite Element Procedures*. Prentice Hall, New Jersey.

Bathe, K.J. (2001). The inf - sup condition and its evaluation for mixed finite element methods. *Computer and Structures*, 79, 243–252.

Bathe, K.J., Ramm, E., & Wilson, E.L. (1975). Finite element formulations for large deformation dynamic analysis. *International Journal for Numerical Methods in Engineering*, 9, 353–386.

Beatty, M.F. & Krishnaswamy, S. (2000). Theory of stress-softening in incompressible isotropic materials. *Journal of the Mechanics and Physics of Solids*, 48(9), 1931–1965.

Bellini, C., Glass, P., Sitti, M., & Di Martino, E.S. (2011). Biaxial mechanical modeling of the small intestine. *Journal of the mechanical behavior of biomedical materials*, 4(8), 1727–40.

Bhowmick, A.K. (2008). *Current topics in elastomeric research*. CRC Press, Boca Raton.

Brady, A.R., Fowkes, F.G.R., Greenhalgh, R.M., Powell, J.T., Ruckley, C.V., & Thompson, S.G. (2000). Risk factors for postoperative death following elective surgical repair of abdominal aortic aneurysm : results from the UK Small Aneurysm Trial. *British Journal of Surgery*, 87, 742–749.

British Heart Foundation (2014). Cardiovascular Disease Statistics.

Brown, R. (2006). *Physical testing of rubber*. Springer, New York, 4th edition.

BS 903-1 (1995). Physical testing of rubber. Part 1: Guide to the selection and use of methods of test for rubber.

BS ISO (2012). Tissue paper and tissue products.

Bucchi, A. & Hearn, G.E. (2013a). Predictions of aneurysm formation in distensible tubes: Part A Theoretical background to alternative approaches. *International Journal of Mechanical Sciences*, 71, 1–20.

Bucchi, A. & Hearn, G.E. (2013b). Predictions of aneurysm formation in distensible tubes: Part B Application and comparison of alternative approaches. *International Journal of Mechanical Sciences*, 70, 155–170.

Cadge, D. & Prior, A. (1999). Finite element modelling of three-dimensional elastomeric components. In D. Boast & V.A. Coveney (Eds.), *Finite element analysis of elastomers*. Professional Engineering Publishing, London, 187–205.

Carrera, E. (1994). A study on arc-length-type methods and their operation failures illustrated by a simple model. *Computers & Structures*, 50(2), 217–229.

Chapelle, D. & Bathe, K.J. (2011). *The Finite Element Analysis of Shells – Fundamentals*. Springer, Berlin, 2nd edition.

Choudhury, N., Bouchot, O., Rouleau, L., Tremblay, D., Cartier, R., Butany, J., Mongrain, R., & Leask, R.L. (2009). Local mechanical and structural properties of healthy and diseased human ascending aorta tissue. *Cardiovascular pathology : the official journal of the Society for Cardiovascular Pathology*, 18(2), 83–91.

Chow, M.J. & Zhang, Y. (2011). Changes in the mechanical and biochemical properties of aortic tissue due to cold storage. *The Journal of surgical research*, 171(2), 434–42.

Chuong, C.J. & Fung, Y.C. (1986). On Residual Stresses in Arteries. *Journal of Biomechanical Engineering*, 108(2), 189.

Cloonan, A.J., O'Donnell, M.R., Lee, W.T., Walsh, M.T., De Barra, E., & McGloughlin, T.M. (2012). Spherical indentation of free-standing acellular extracellular matrix membranes. *Acta biomaterialia*, 8(1), 262–73.

Conway, C., Sharif, F., McGarry, J.P., & McHugh, P.E. (2012). A Computational Test-Bed to Assess Coronary Stent Implantation Mechanics Using a Population-Specific Approach. *Cardiovascular Engineering and Technology*, 3(4), 374–387.

Cox, M.A.J., Driessen, N.J.B., Boerboom, R.A., Bouten, C.V.C., & Baaijens, F.P.T. (2008). Mechanical characterization of anisotropic planar biological soft tissues using finite indentation: experimental feasibility. *Journal of biomechanics*, 41(2), 422–9.

Crick, S.J., Sheppard, M.N., Ho, S.Y., Gebstein, L., & Anderson, R.H. (1998). Anatomy of the pig heart : comparisons with normal human cardiac structure. *Journal anatomy*, 193, 105–119.

Crisfield, M. (1981). A fast incremental/iterative solution procedure that handles "snap-through". *Computers & Structures*, 13(1-3), 55–62.

Dassault Systèmes, S. (2014). Abaqus Analysis User's Guide.

Davies, P.F. & Tripathi, S.C. (1993). Mechanical stress mechanisms and the cell. An endothelial paradigm. *Circulation research*, 72(2), 239–245.

Delfino, a., Stergiopulos, N., Moore, J.E., & Meister, J.J. (1997). Residual strain effects on the stress field in a thick wall finite element model of the human carotid bifurcation. *Journal of biomechanics*, 30(8), 777–786.

Di Martino, E.S., Bohra, A., Vande Geest, J.P., Gupta, N., Makaroun, M.S., & Vorp, D.A. (2006). Biomechanical properties of ruptured versus electively repaired abdominal aortic aneurysm wall tissue. *Journal of vascular surgery*, 43(3), 570–6.

Diani, J., Fayolle, B., & Gilormini, P. (2009). A review on the Mullins effect. *European Polymer Journal*, 45(3), 601–612.

Doyle, B.J., Callanan, A., & McGloughlin, T.M. (2007). A comparison of modelling techniques for computing wall stress in abdominal aortic aneurysms. *Biomedical engineering online*, 6, 38.

Doyle, B.J., Corbett, T.J., Callanan, A., Walsh, M.T., Vorp, D.A., & McGloughlin, T.M. (2009a). An experimental and numerical comparison of the rupture locations of an abdominal aortic aneurysm. *Journal of endovascular therapy: an official journal of the International Society of Endovascular Specialists*, 16(3), 322–35.

Doyle, B.J., Corbett, T.J., Cloonan, A.J., O'Donnell, M.R., Walsh, M.T., Vorp, D.A., & McGloughlin, T.M. (2009b). Experimental modelling of aortic aneurysms: novel applications of silicone rubbers. *Medical engineering & physics*, 31(8), 1002–12.

Duprey, A., Khanafer, K., Schlicht, M., Avril, S., Williams, D., & Berguer, R. (2010). In Vitro Characterisation of Physiological and Maximum Elastic Modulus of Ascending Thoracic Aortic Aneurysms Using Uniaxial Tensile Testing. *European Journal of Vascular and Endovascular Surgery*, 39(6), 700–707.

Erbel, R. & Eggebrecht, H. (2006). Aortic dimensions and the risk of dissection. *Heart*, 92(1), 137–42.

Fan, R. & Sacks, M.S. (2014). Simulation of planar soft tissues using a structural constitutive model: Finite element implementation and validation. *Journal of Biomechanics*, 47(9), 2043–2054.

Fitzpatrick, J.C., Clark, P.M., & Capaldi, F.M. (2010). Effect of decellularization protocol on the mechanical behavior of porcine descending aorta. *International journal of biomaterials*, 2010, 1–11.

Fu, Y.B., Pearce, S.P., & Liu, K.K. (2008). Post-bifurcation analysis of a thin-walled hyperelastic tube under inflation. *International Journal of Non-Linear Mechanics*, 43(8), 697–706.

Fu, Y.B., Rogerson, G., & Zhang, Y. (2012). Initiation of aneurysms as a mechanical bifurcation phenomenon. *International Journal of Non-Linear Mechanics*, 47(2), 179–184.

Fung, Y.C. (1993). *Biomechanics: Mechanical Properties of Living Tissues*. Springer, New York.

Fung, Y.C., Fronek, K., & Patitucci, P. (1979). Pseudoelasticity of arteries and the choice of its mathematical expression Pseudoelasticity of arteries and the choice of its mathematical expression of Applied Mechanics. *The American Physiological Society*, 237, H620–H631.

Galbraith, G.G., Skalak, R., & Chien, S. (1998). Shear stress induces spatial reorganization of the endothelial cell cytoskeleton. *Cell Motility and the Cytoskeleton*, 40(4), 317–330.

Gao, Z. & Desai, J.P. (2010). Estimating zero-strain states of very soft tissue under gravity loading using digital image correlation. *Medical image analysis*, 14(2), 126–37.

García, A., Peña, E., Laborda, A., Lostalé, F., De Gregorio, M.a., Doblaré, M., & Martínez, M.a. (2011). Experimental study and constitutive modelling of the passive mechanical properties of the porcine carotid artery and its relation to histological analysis: Implications in animal cardiovascular device trials. *Medical engineering & physics*, 33(6), 665–76.

Garcia, M., Ruiz, O., & Lopez, C. (2005). Hyperelastic Material Modeling. Technical report.

Gasser, C.T., Auer, M., Labruto, F., Swedenborg, J., & Roy, J. (2010). Biomechanical rupture risk assessment of abdominal aortic aneurysms: model complexity versus predictability of finite element simulations. *European journal of vascular and endovascular surgery: the official journal of the European Society for Vascular Surgery*, 40(2), 176–85.

Gasser, C.T., Nchimi, A., Swedenborg, J., Roy, J., Sakalihasan, N., Böckler, D., & Hyhlik-Dürr, A. (2014). A Novel Strategy to Translate the Biomechanical Rupture Risk of Abdominal Aortic Aneurysms to their Equivalent Diameter Risk: Method and Retrospective Validation. *European Journal of Vascular and Endovascular Surgery*, 47(3), 288–295.

Gent, A.N. (1996). A New Constitutive Relation for Rubber. *Rubber Chemistry and Technology*, 69(1), 59–61.

Gent, A.N. (2001). *Engineering with Rubber: How to Design Rubber Components*. Hanser, Munich, 2nd edition.

Georgakarakos, E., Ioannou, C.V., Kamarianakis, Y., Papaharilaou, Y., Kostas, T., Manousaki, E., & Katsamouris, a.N. (2010). The Role of Geometric Parameters in the Prediction of Abdominal Aortic Aneurysm Wall Stress. *European Journal of Vascular and Endovascular Surgery*, 39(1), 42–48.

Giannakoulas, G., Giannoglou, G., Soulis, J., Farmakis, T., Papadopoulou, S., Parcharidis, G., & Louridas, G. (2005). A computational model to predict aortic wall stresses in patients with systolic arterial hypertension. *Medical Hypotheses*, 65(6), 1191–1195.

Giannoglou, G., Giannakoulas, G., Soulis, J., Chatzizisis, Y., Perdikides, T., Melas, N., Parcharidis, G., & Louridas, G. (2006). Predicting the Risk of Rupture of Abdominal Aortic Aneurysms by Utilizing Various Geometrical Parameters: Revisiting the Diameter Criterion. *Angiology*, 57(4), 487–494.

Gonçalves, P., Pamplona, D., & Lopes, S. (2008). Finite deformations of an initially stressed cylindrical shell under internal pressure. *International Journal of Mechanical Sciences*, 50(1), 92–103.

Greenhalgh, R.M., Brown, L.C., Kwong, G.P.S., Powell, J.T., & Thompson, S.G. (2004). Comparison of endovascular aneurysm repair with open repair in patients with abdominal aortic aneurysm (EVAR trial 1), 30-day operative mortality results: randomised controlled trial. *Lancet*, 364(9437), 843–848.

Guyton, C. & Hall, J.E. (2000). *Textbook of Medical Physiology*. Elsevier Health Sciences, Philadelphia, 10th edition.

Hallett Jr., J.W. (2000). Management of abdominal aortic aneurysms. *Mayo Clin Proc*, 75(2012), 395–399.

Han, H.C. (2007). A Biomechanical Model of Artery Buckling. *Journal of biomechanics*, 40(16), 3672–3678.

Hellenthal, F.a.M.V.I., Pulinx, B., Welten, R.J.T.J., Teijink, J.a.W., van Dieijen-Visser, M.P., Wodzig, W.K.W.H., & Schurink, G.W.H. (2012). Circulating biomarkers and abdominal aortic aneurysm size. *The Journal of surgical research*, 176(2), 672–8.

Heron, M. (2015). Deaths: Leading Causes for 2012. *National Vital Statistics Reports*, 64(10), 1–94.

Herrmann, L.R. (1965). Elasticity equations for incompressible and nearly incompressible materials by a variational theorem. *AIAA Journal*, 3(10), 1896–1900.

Hinnen, J.W., Koning, O.H.J., Visser, M.J.T., & Van Bockel, H.J. (2005). Effect of intraluminal thrombus on pressure transmission in the abdominal aortic aneurysm. *Journal of vascular surgery*, 42(6), 1176–1182.

Holzapfel, G.A. (2000). *Nonlinear solid mechanics. A continuum approach for engineering.* John Wiley & Sons Ltd, Chichester (UK), 1st edition.

Holzapfel, G.A. (2006). Determination of material models for arterial walls from uniaxial extension tests and histological structure. *Journal of theoretical biology*, 238(2), 290–302.

Holzapfel, G.A., Gasser, C.T., & Ogden, R.W. (2000). A new constitutive framework for arterial wall mechanics and a comperative study of material models. *Journal of Elasticity*, 61, 1–48.

Holzapfel, G.A., Gasser, C.T., & Ogden, R.W. (2004). Comparison of a multi-layer structural model for arterial walls with a fung-type model, and issues of material stability. *Journal of biomechanical engineering*, 126(April 2004), 264–275.

Holzapfel, G.A., Gasser, C.T., & Stadler, M. (2002). A structural model for the viscoelastic behavior of arterial walls: Continuum formulation and finite element analysis. *European Journal of Mechanics - A/Solids*, 21(3), 441–463.

Holzapfel, G.A., Sommer, G., Gasser, C.T., Regitnig, P., & Gerhard, A. (2005). Determination of layer-specific mechanical properties of human coronary arteries with nonatherosclerotic intimal thickening and related constitutive modeling. *American journal of physiology. Heart and circulatory physiology*, 289(5), H2048–2058.

Horný, L., Netusil, M., & Vonavkova, T. (2014). Axial prestretch and circumferential distensibility in biomechanics of abdominal aorta. *Biomechanics and Modeling in Mechanobiology*, 13(4), 783–799.

Horný, L., Žitný, R., Chlup, H., & Macková, H. (2006). Identification of the material parameters of an aor- tic wall. *Bulletin of Applied Mechanics*, 2(8), 173–181.

Humphrey, J.D. (2002). *Cardiovascular Solid Mechanics: Cells, Tissues, and Organs*. Springer, New York.

Humphrey, J.D. & Holzapfel, G.A. (2012). Mechanics, Mechanobiology, and Modeling of Human Abdominal Aorta and Aneurysms. *Journal of biomechanics*, 45(5), 805–14.

Iliopoulos, D.C., Deveja, R.P., Kritharis, E.P., Perrea, D., Sionis, G.D., Toutouzas, K., Stefanadis, C., & Sokolis, D.P. (2009). Regional and directional variations in the mechanical properties of ascending thoracic aortic aneurysms. *Medical engineering & physics*, 31(1), 1–9.

Isaksen, J.G., Bazilevs, Y., Kvamsdal, T., Zhang, Y., Kaspersen, J.H., Waterloo, K., Romner, B., & Ingebrigtsen, T. (2008). Determination of wall tension in cerebral artery aneurysms by numerical simulation. *Stroke*, 39, 3172–3178.

ISO 37 (2005). Rubber, vulcanized or thermoplastic. Determination of tensile stress-strain properties.

ISO 4664 (1998). Rubber - Guide to the determiantion of dynamic properties.

Jerabek, M., Major, Z., & Lang, R. (2010). Strain determination of polymeric materials using digital image correlation. *Polymer Testing*, 29(3), 407–416.

Karduna, a.R., Halperin, H.R., & Yin, F.C. (1997). Experimental and numerical analyses of indentation in finite-sized isotropic and anisotropic rubber-like materials. *Annals of biomedical engineering*, 25(6), 1009–16.

Karthikesalingam, A., Holt, P.J., Vidal-Diez, A., Ozdemir, B.A., Poloniecki, J.D., Hinchliffe, R.J., & Thompson, M.M. (2014). Mortality from ruptured abdominal aortic aneurysms: clinical lessons from a comparison of outcomes in England and the USA. Technical Report 9921.

Kawabata, S., Matsuda, M., Tei, K., & Hawai, H. (1981). Experimental Survey of the Strain Energy Density Function of Isoprene Rubber Vulcanizate. *Macromolecules*, 14, 154–162.

Khan, S., Verma, V., Verma, S., Polzer, S., & Jha, S. (2015). Assessing the potential risk of rupture of abdominal aortic aneurysms. *Clinical Radiology*, 70(1), 11–20.

Kim, J. & Baek, S. (2011). Circumferential variations of mechanical behavior of the porcine thoracic aorta during the inflation test. *Journal of biomechanics*, 44(10), 1941–7.

Kobielarz, M. & Jankowski, L.J. (2013). Experimental characterization of the mechanical properties of the abdominal aortic aneurysm wall under uniaxial tension. *Journal of theoretical and applied mechanics*, 51, 949–958.

Krehbiel, J.D. & Berfield, T.A. (). Applying Digital Image Correlation to Biological Materials. Technical report, Beckman Institute for Advanced Science and Technology at Illinois, Urbana, Illinois (US).

Kyriacou, S. & Humphrey, J.D. (1996). Influence of size, shape and properties on the mechanics of axisymmetric saccular aneurysms. *Journal of Biomechanics*, 29(8), 1015–1022.

Labrosse, M.R., Beller, C.J., Mesana, T., & Veinot, J.P. (2009). Mechanical behavior of human aortas: Experiments, material constants and 3-D finite element modeling including residual stress. *Journal of Biomechanics*, 42(8), 996–1004.

Lally, C., Reid, a.J., & Prendergast, P.J. (2004). Elastic behavior of porcine coronary artery tissue under uniaxial and equibiaxial tension. *Annals of biomedical engineering*, 32(10), 1355–1364.

Lasheras, J.C. (2007). The Biomechanics of Arterial Aneurysms. *Annual Review of Fluid Mechanics*, 39(1), 293–319.

Learoyd, B.M. & Taylor, M.G. (1966). Alterations with Age in the Viscoelastic Properties of Human Arterial Walls. *Circulation Research*, 18(3), 278–292.

Lee, A.Y., Han, B., Lamm, S.D., Fierro, C.a., & Han, H.C. (2012). Effects of elastin degradation and surrounding matrix support on artery stability. *AJP: Heart and Circulatory Physiology*, 302(4), H873–H884.

Lee, A.Y., Sanyal, A., Xiao, Y., Shadfan, R., & Han, H.C. (2014). Mechanical instability of normal and aneurysmal arteries. *Journal of Biomechanics*, 47(16), 3868–3875.

Lee, J.S., Frasher, Wallace G., J., & Fung, Y.C. (1967). Two dimensional finite deformation experiments on dog's arteries and veins. Technical report, California University, San Diego.

Lillie, M.a., Shadwick, R.E., & Gosline, J.M. (2010). Mechanical anisotropy of inflated elastic tissue from the pig aorta. *Journal of biomechanics*, 43(11), 2070–8.

Liu, M. & Gorman, D. (1995). Formulation of Rayleigh damping and its extensions. *Computers & Structures*, 57(2), 277–285.

Lopes, S., Gonçalves, P., & Pamplona, D. (2007). Influence of initial geometric imperfections on the stability of thick cylindrical shells under internal pressure. *Communications in numerical methods in engineering*, 23, 577–597.

Luo, W., Hu, X., Wang, C., & Li, Q. (2010). Frequency- and strain-amplitude-dependent dynamical mechanical properties and hysteresis loss of CB-filled vulcanized natural rubber. *International Journal of Mechanical Sciences*, 52(2), 168–174.

Ma, B., Lu, J., Harbaugh, R.E., & Raghavan, M.L. (2007). Nonlinear anisotropic stress analysis of anatomically realistic cerebral aneurysms. *Journal of biomechanical engineering*, 129(February 2007), 88–96.

Maher, E., Creane, A., Lally, C., & Kelly, D.J. (2012a). An anisotropic inelastic constitutive model to describe stress softening and permanent deformation in arterial tissue. *Journal of the mechanical behavior of biomedical materials*, 12, 9–19.

Maher, E., Early, M., Creane, A., Lally, C., & Kelly, D.J. (2012b). Site specific inelasticity of arterial tissue. *Journal of biomechanics*, 45(8), 1393–9.

Marlow, R.S. (2003). A general first-invariant hyperelastic constitutive model. In J.J.C. Busfield & A.H. Muhr (Eds.), *Constitutive models for rubber III*. Taylor & Francis, Lisse, 157–160.

Matsumoto, T., Fukui, T., Tanaka, T., Ikuta, N., Ohashi, T., Kumagai, K., Akimoto, H., Tabayashi, K., & Sato, M. (2009). Biaxial Tensile Properties of Thoracic Aortic Aneurysm Tissues. *Journal of Biomechanical Science and Engineering*, 4(4), 518–529.

Mello, J.M.D., Orsi, A.M., Padovani, C.R., Maria, S., Matheus, M., & Eleutério, M.L. (2004). Structure of the aortic wall in the guinea pig and rat. *Brazilian Journal of morphological Sciences*, 21, 35–38.

Meng, H., Swartz, D.D., Wang, Z., Hoi, Y., Kolega, J., Metaxa, E.M., Szymansky, M.P., & Yamamoto, J. (2006). A Model System for Mapping Vascular Responses to Complex Hemodynamics at Arterial Bifurcations In Vivo. *Neurosurgery.*, 59(5), 1094–1101.

Meng, H., Tutino, V.M., Xiang, J., & Siddiqui, a. (2014). High WSS or Low WSS? Complex interactions of hemodynamics with intracranial aneurysm initiation, growth, and rupture: Toward a unifying hypothesis. *American Journal of Neuroradiology*, 35(7), 1254–1262.

Meng, H., Wang, Z., Hoi, Y., Gao, L., Metaxa, E.M., Swartz, D.D., & Kolega, J. (2007). Complex Hemodynamics at the Apex of an Arterial Bifurcation Induces Vascular Remodeling Resembling Cerebral Aneurysm Initiation. *Stroke*, 38(6), 1924–1931.

Messphysiks Material testing GmbH (). Video extensometer ME 46. Visual strain with digital image processing.

Mohan, D. & Melvin, J.W. (1982). Failure properties of passive human aortic tissue I - Uniaxial tension tests. *Journal of biomechanics*, 15, 887–902.

Mooney, M. (1940). A Theory of Large Elastic Deformation. *Journal of Applied Physics*, 11(9), 582.

Moreira, D. & Nunes, L. (2013). Comparison of simple and pure shear for an incompressible isotropic hyperelastic material under large deformation. *Polymer Testing*, 32(2), 240–248.

National Health Service (2014). Abdominal Aortic Aneurysm Screening Programme.

Nichols, M., Townsend, N., Scarborough, P., & Rayner, M. (2014). Cardiovascular disease in Europe 2014: epidemiological update. *European Heart Journal*, 35(42), 2950–2959.

Nienaber, C.A. & Fattori, R. (Eds.) (1999). *Diagnosis and Treatment of Aortic Diseases*. Springer Science & Business Media.

Noordergraaf, A. (1956). *Physical Basis of Ballistocardiography*. Excelsior, S-Gravenhage.

Nordon, I.M., Hinchliffe, R.J., Holt, P.J., Loftus, I.M., & Thompson, M.M. (2009). Review of Current Theories for Abdominal Aortic Aneurysm Pathogenesis. *Vascular*, 17(05), 253.

Nunes, L.C.S. & Moreira, D.C. (2013). Simple shear under large deformation: Experimental and theoretical analyses. *European Journal of Mechanics, A/Solids*, 42, 315–322.

O' Gara, P.T. (2003). Aortic Aneurysm. *Circulation*, 107, e43–e45.

Ogden, R.W. (1972). Large deformation isotropic elasticity - on the correlation of theory and experiment for incompressible rubberlike solids. *Royal society*, 326(1567), 565–584.

Ogden, R.W. (1997). *Non-linear Elastic Deformations*. Dover Publications.

Ogden, R.W., Saccomandi, G., & Sgura, I. (2004). Fitting hyperelastic models to experimental data. *Computational Mechanics*, 34(6), 484–502.

O'Leary, S.a., Doyle, B.J., & McGloughlin, T.M. (2014). The impact of long term freezing on the mechanical properties of porcine aortic tissue. *Journal of the Mechanical Behavior of Biomedical Materials*, 37, 165–173.

Ozdemir, B.A., Karthikesalingam, A., Sinha, S., Poloniecki, J.D., Vidal-Diez, A., Hinchliffe, R.J., Thompson, M.M., & Holt, P.J.E. (2015). Association of hospital structures with mortality from ruptured abdominal aortic aneurysm. *British Journal of Surgery*, 102(5), 516–524.

Palanca, M., Tozzi, G., & Cristofolini, L. (2015). The use of digital image correlation in the biomechanical area: a review. *International Biomechanics*, 3(1), 1–21.

Pan, B., Qian, K., Xie, H., & Asundi, A. (2008). On errors of digital image correlation due to speckle patterns. In X. He, H. Xie, & Y. Kang (Eds.), *International Conference on Experimental Mechanics*, volume 7375. 73754Z1–73754Z7.

Pan, B., Qian, K., Xie, H., & Asundi, A. (2009). Two-dimensional digital image correlation for in-plane displacement and strain measurement: a review. *Measurement Science and Technology*, 20(6), 062001.

Pandit, A., Lu, X., Wang, C., & Kassab, G.S. (2005). Biaxial elastic material properties of porcine coronary media and adventitia. *American journal of physiology. Heart and circulatory physiology*, 288(6), H2581–H2587.

Parker, J.R. (2010). *Algorithms for Image Processing and Computer Vision*, volume 29. John Wiley & Sons, Indianapolis.

Peña, J.A., Martínez, M.A., & Peña, E. (2015). Layer-specific residual deformations and uniaxial and biaxial mechanical properties of thoracic porcine aorta. *Journal of the Mechanical Behavior of Biomedical Materials*, 50, 55–69.

Pierce, D.M., Maier, F., Weisbecker, H., Viertler, C., Verbrugghe, P., Famaey, N., Fourneau, I., Herijgers, P., & Holzapfel, G.A. (2015). Human thoracic and abdominal aortic aneurysmal tissues: Damage experiments, statistical analysis and constitutive modeling. *Journal of the Mechanical Behavior of Biomedical Materials*, 41, 92–107.

Rachev, A. (2009). A theoretical study of mechanical stability of arteries. *Journal of biomechanical engineering*, 131(5), 051006 1–10.

Raghavan, M.L., Hanaoka, M.M., Kratzberg, J.A., de Lourdes Higuchi, M., & da Silva, E.S. (2011a). Biomechanical failure properties and microstructural content of ruptured and unruptured abdominal aortic aneurysms. *Journal of biomechanics*, 44(13), 2501–2507.

Raghavan, M.L., Kratzberg, J., Castro de Tolosa, E.M., Hanaoka, M.M., Walker, P., & da Silva, E.S. (2006). Regional distribution of wall thickness and failure properties of human abdominal aortic aneurysm. *Journal of biomechanics*, 39(16), 3010–3016.

Raghavan, M.L., Lin, K., Ramachandran, M., Nadareishvili, A., Amelon, R., & Lu, J. (2011b). Planar radial extension for constitutive modeling of anisotropic biological soft tissues. *International Journal of Structural Changes in Solid*, 3(2), 23–31.

Raghavan, M.L. & Vorp, D.A. (2000). Toward a biomechanical tool to evaluate rupture potential of abdominal aortic aneurysm : identification of a finite strain constitutive model and evaluation of its applicability. *Journal of Biomechanics*, 33, 475–482.

Raghavan, M.L., Webster, M.W., & Vorp, D.A. (1996). Ex vivo biomechanical behavior of abdominal aortic aneurysm: assessment using a new mathematical model. *Annals of biomedical engineering*, 24(5), 573–82.

Ramachandran, M., Laakso, A., Harbaugh, R.E., & Raghavan, M.L. (2012). On the role of modeling choices in estimation of cerebral aneurysm wall tension. *Journal of Biomechanics*, 45(16), 2914–2919.

Rein, C.M., Cardenas, J.C., & Church, F.C. (2011). The controversial role of the urokinase system in abdominal aortic aneurysm formation and rupture. *Arteriosclerosis, thrombosis, and vascular biology*, 31(12), 2769–71.

Rickaby, S.R. & Scott, N.H. (2013). Multicyclic modelling of softening in biological tissue. *IMA Journal of Applied Mathematics*, 1–19.

Riks, E. (1979). An incremental approach to the solution of snapping and buckling problems. *International Journal of Solids and Structures*, 15(7), 529 – 551.

Rivlin, B.Y.R.S. & Saunders, D.W. (1951). Large elastic deformations of isotropic materials. VII. Experiments on the deformation of rubber. *Philosophical Transactions of the Royal Society A: Mathematical, Physical and Engineering Sciences*, 243(865), 251–288.

Rodríguez, J.F. & Merodio, J. (2011). A new derivation of the bifurcation conditions of inflated cylindrical membranes of elastic material under axial loading. Application to aneurysm formation. *Mechanics Research Communications*, 38(3), 203–210.

Rodríguez, J.F., Ruiz, C., Doblaré, M., & Holzapfel, G.A. (2008). Mechanical stresses in abdominal aortic aneurysms: influence of diameter, asymmetry, and material anisotropy. *Journal of biomechanical engineering*, 130(2), 021023 1–10.

Rouet, L., Ardon, R., Rouet, J.m., Long, A., Rouet, L., Ardon, R., Rouet, J.m., Dufour, C., Rouet, L., Ardon, R., Rouet, J.m., & Mory, B. (2010). Semi-automatic abdominal aortic aneurysms geometry assessment based on 3D ultrasound. In *IEEE Ultrasonics Symposium*. San Diego, US, 201–204.

Rowley, N.J., Dawson, E.a., Birk, G.K., Cable, N.T., George, K., Whyte, G., Thijssen, D.H.J., & Green, D.J. (2011). Exercise and arterial adaptation in humans: uncoupling localized and systemic effects. *Journal of applied physiology*, 110, 1190–1195.

Roy, C.S. (1881). The Elastic Properties of the Arterial Wall. *The journal of Physiology*.

Rudarakanchana, N. & Jenkins, M. (2014). Management of abdominal aortic aneurysms in the UK. *British journal of hospital medicine*, 75(10), 395–399.

Sahakaro, K. & Beraheng, S. (2008). Reinforcement of maleated natural rubber by precipitated silica. *Journal of Applied Polymer Science*, 109(6), 3839–3848.

Sakalihasan, N., Limet, R., & Defawe, O.D. (2005). Abdominal aortic aneurysm. *Lancet*, 365(9470), 1577–89.

Sandford, R.M., Bown, M.J., London, N.J., & Sayers, R.D. (2007). The Genetic Basis of Abdominal Aortic Aneurysms: A Review. *European Journal of Vascular and Endovascular Surgery*, 33(4), 381–390.

Sasso, M., Palmieri, G., Chiappini, G., & Amodio, D. (2009). Frequency Dependent Mechanical Behaviour of Elastomers Under Uniaxial Cyclic Loading. In *SEM Annual Conference*.

Scanlon, V.C. & Sanders, T. (2011). *Essentials of Anatomy and Physiology*. Davis Company, F. A., Philadelphia, 6th edition.

Schmidt, T., Pandya, D., & Balzani, D. (2015). Influence of isotropic and anisotropic material models on the mechanical response in arterial walls as a result of supra-physiological loadings. *Mechanics Research Communications*, 64, 29–37.

Schriefl, A.J., Zeindlinger, G., Pierce, D.M., Regitnig, P., & Holzapfel, G.A. (2012). Determination of the layer-specific distributed collagen fibre orientations in human thoracic and abdominal aortas and common iliac arteries. *Journal of the Royal Society, Interface*, 9, 1275–1286.

Schulze-Bauer, C.a.J. & Holzapfel, G.A. (2003). Determination of constitutive equations for human arteries from clinical data. *Journal of biomechanics*, 36(2), 165–9.

Schulze-Bauer, C.a.J., Regitnig, P., & Holzapfel, G.A. (2002). Mechanics of the human femoral adventitia including the high-pressure response. *American journal of physiology. Heart and circulatory physiology*, 282(6), H2427–H2440.

Schurink, G., M. Aarts, N., Wilde, J., van Baalen, J., Chuter, T., Kool, L., & van Bockel, J. (1998). Endoleakage after stent-graft treatment of abdominal aneurysm: Implications on pressure and imaging—an in vitro study. *Journal of Vascular Surgery*, 28(2), 234–241.

Schweizerhof, K. & Wriggers, P. (1986). Consistent linearization for path following methods in nonlinear fe analysis. *Computer Methods in Applied Mechanics and Engineering*, 59(3), 261–279.

Scott, R.A.P. (2002). The Multicentre Aneurysm Screening Study (MASS) into the effect of abdominal aortic aneurysm screening on mortality in men: a randomised controlled trial. *Lancet*, 360(9345), 1531–1539.

Scott, R.A.P., Tisi, P.V., Ashton, H.A., & Allen, D.R. (1998). Abdominal aortic aneurysm rupture rates: a 7-year follow-up of the entire abdominal aortic aneurysm population detected by screening. *Journal of vascular surgery*, 28(1), 124–128.

Scotti, C.M. & Finol, E.a. (2007). Compliant biomechanics of abdominal aortic aneurysms: A fluid-structure interaction study. *Computers and Structures*, 85(11-14), 1097–1113.

Scotti, C.M., Jimenez, J., Muluk, S.C., & Finol, E.A. (2008). Wall stress and flow dynamics in abdominal aortic aneurysms: finite element analysis vs. fluid-structure interaction. *Computer methods in biomechanics and biomedical engineering*, 11(3), 301–322.

Segers, P. & Verdonck, P. (2000). Role of tapering in aortic wave reflection: hydraulic and mathematical model study. *Journal of Biomechanics*, 33(3), 299–306.

Seibert, B., Tummala, R.P., Chow, R., Faridar, A., Mousavi, S.a., & Divani, A.a. (2011). Intracranial aneurysms: Review of current treatment options and outcomes. *Frontiers in Neurology*, 2(45), 1–11.

Selvadurai, A.P.S. & Yu, Q. (2006). On the indentation of a polymeric membrane. *Proceedings of the Royal Society A: Mathematical, Physical and Engineering Sciences*, 462(2065), 189–209.

Shang, E.K., Nathan, D.P., Woo, E.Y., Fairman, R.M., Wang, G.J., Gorman, R.C., Gorman, J.H., & Jackson, B.M. (2015). Local wall thickness in finite element models improves prediction of abdominal aortic aneurysm growth. *Journal of Vascular Surgery*, 61(1), 217–223.

Shergold, O.A., Fleck, N.A., & Radford, D. (2006). The uniaxial stress versus strain response of pig skin and silicone rubber at low and high strain rates. *International Journal of Impact Engineering*, 32(9), 1384–1402.

Shi, J. & Moita, G.F. (1996). The post-critical analysis of axisymmetric hyper-elastic membranes by the finite element method. *Computer Methods in Applied Mechanics and Engineering*, 7825(96), 265–281.

Shojima, M. (2004). Magnitude and Role of Wall Shear Stress on Cerebral Aneurysm: Computational Fluid Dynamic Study of 20 Middle Cerebral Artery Aneurysms. *Stroke*, 35(11), 2500–2505.

Sokolis, D.P., Boudoulas, H., & Karayannacos, P.E. (2002). Assessment of the aortic stress-strain relation in uniaxial tension. *Journal of biomechanics*, 35(9), 1213–1223.

Sokolis, D.P., Kefaloyannis, E.M., Kouloukoussa, M., Marinos, E., Boudoulas, H., & Karayannacos, P.E. (2006). A structural basis for the aortic stress-strain relation in uniaxial tension. *Journal of biomechanics*, 39(9), 1651–1662.

Sommer, G. (2010). *Mechanical Properties of Healthy and Diseased Human Arteries*. Ph.D. thesis, Graz University of Technology, Graz.

Sommer, G., Sherifova, S., Oberwalder, P.J., Dapunt, O.E., Ursomanno, P.A., DeAnda, A., Griffith, B.E., & Holzapfel, G.A. (2016). Mechanical strength of aneurysmatic and dissected human thoracic aortas at different shear loading modes. *Journal of Biomechanics*.

Stemper, B.D., Yoganandan, N., Stineman, M.R., Gennarelli, T.A., Baisden, J.L., & Pintar, F.a. (2007). Mechanics of fresh, refrigerated, and frozen arterial tissue. *The Journal of surgical research*, 139(2), 236–42.

Sugita, S. & Matsumoto, T. (2013). Novel biaxial tensile test for studying aortic failure phenomena at a microscopic level. *Biomedical engineering online*, 12(1), 1–13.

Sun, W. & Sacks, M.S. (2005). Finite element implementation of a generalized Fung-elastic constitutive model for planar soft tissues. *Biomechanics and modeling in mechanobiology*, 4(2-3), 190–199.

Sun, W., Sacks, M.S., & Scott, M.J. (2005). Effects of Boundary Conditions on the Estimation of the Planar Biaxial Mechanical Properties of Soft Tissues. *Journal of Biomechanical Engineering*, 127, 709 – 715.

Sussman, T. & Bathe, K.J. (1987). A finite element formulation for nonlinear incompressible elastic and inelastic analysis. *Computers & Structures*, 26(I), 357–409.

Sussman, T. & Bathe, K.J. (2009). A model of incompressible isotropic hyperelastic material behavior using spline interpolations of tension – compression test data. *Communications in numerical methods in engineering*, 25, 53–63.

Taber, L.A. (2004). *Nonlinear theory of elasticity. Applications in Biomechanics*. World Scientific, Singapore.

Takizawa, K., Christopher, J., Tezduyar, T.E., & Sathe, S. (2010). Space–time finite element computation of arterial fluid–structure interactions with patient-specific data. *International Journal for Numerical Methods in Biomedical Engineering*, 26, 101–116.

Tanaka, T.T. & Fung, Y.C. (1974). Elastic and inelastic properties of the canine aorta and their variation along the aortic tree. *Journal of Biomechanics*, 7(4), 357–370.

Taylor, C. & Hood, P. (1973). A numerical solution of the Navier-Stokes equations using the finite element technique. *Computers & Fluids*, 1(1), 73–100.

Tezduyar, T.E., Sathe, S., Schwaab, M., & Conklin, B.S. (2008). Arterial fluid mechanics modeling with the stabilized space – time fluid – structure interaction technique. *International Journal for Numerical Methods in Fluids*, (54), 901–922.

Tong, J., Cohnert, T., Regitnig, P., & Holzapfel, G.A. (2011). Effects of age on the elastic properties of the intraluminal thrombus and the thrombus-covered wall in abdominal aortic aneurysms: biaxial extension behaviour and material modelling. *European journal of vascular and endovascular surgery : the official journal of the European Society for Vascular Surgery*, 42(2), 207–19.

Torii, R., Oshima, M., Kobayashi, T., Takagi, K., & Tezduyar, T.E. (2006). Fluid-structure interaction modeling of aneurysmal conditions with high and normal blood pressures. *Computational Mechanics*, 38, 482–490.

Treloar, L.R.G. (1943). Stress strain data for vulcanised rubber under various types of deformation. *Transactions of the Faraday Society*, 40, 59–70.

Treloar, L.R.G. (2005). *The physics of rubber elasticity.* Clarendon Press, Oxford, 3rd edition.

Truesdell, C. (1963). Remarks on Hypo-Elasticity. *Journal of Research of the National Bureau of Standards*, 67(3), 141–143.

Truesdell, C. & Noll, W. (1965). *The Non-Linear Field Theories of Mechanics*. Springer Science & Business Media, Berlin, 3rd edition.

Vahapoglu, V., Karadeniz, S., & Yazici, I. (2011). Uniaxial Tensile Testing of Rubber-Like Materials. *Experimental Techniques*, 35(1), 17–23.

Vaishnav, R.N. & Vossoughi, J. (1987). Residual stress and strain in aortic segments. *Journal of Biomechanics*, 20(3), 235–239.

Vande Geest, J.P., Sacks, M.S., & Vorp, D.A. (2006). The effects of aneurysm on the biaxial mechanical behavior of human abdominal aorta. *Journal of biomechanics*, 39(7), 1324–1334.

Vic (2007). Vic-3D.

Virues Delgadillo, J.O. (2010). Effect of freezing on the passive mechanical properties of arterial samples. *Journal of Biomedical Science and Engineering*, 03(07), 645–652.

Voitle, E., Hofmann, W., & Cejna, M. (2015). Aortic emergencies diagnosis and treatment: a pictorial review. *Insights Imaging*, 6, 17–22.

Volokh, K.Y. (2008). Multiscale Modeling of Material Failure : From Atomic Bonds to Elasticity with Energy Limiters. *International Journal for Multiscale Computational Engineering*, 6(5), 393–410.

Vossoughi, J. & Tözeren, A. (1998). Determination of an effective shear modulus of aorta. *Russian Journal of Biomechanics*, 1–2, 20–36.

Vychytil, J., Moravec, F., Kochová, P., Kuncová, J., & Švíglerová, J. (2010). Modelling of the mechanical behaviour of porcine carotid artery undergoing inflation-deflation test. *Applied and computational mechanics*, 4, 251–262.

Wang, D.H.J., Makaroun, M.S., Webster, M.W., & Vorp, D.A. (2002). Effect of intraluminal thrombus on wall stress in patient-specific models of abdominal aortic aneurysm. *Journal of vascular surgery*, 36(3), 598–604.

Wang, J.J. & Parker, K.H. (2004). Wave propagation in a model of the arterial circulation. *Journal of biomechanics*, 37(4), 457–70.

Wang, X. & Li, X. (2011). Fluid-structure interaction based study on the physiological factors affecting the behaviors of stented and non-stented thoracic aortic aneurysms. *Journal of Biomechanics*, 44(12), 2177–2184.

Watton, P.N., Ventikos, Y., & Holzapfel, G.A. (2009). Modelling the mechanical response of elastin for arterial tissue. *Journal of Biomechanics*, 42(9), 1320–1325.

Website 1, . (). Https://radiologysigns.wordpress.com/2012/08/18/volume-rendered-ct-angiogram-of-an-abdominal-aortic-aneurysm/.

Website 2, . (). Https://my.clevelandclinic.org/services/heart/heart-blood-vessels/aorta.

Weisbecker, H., Pierce, D.M., Regitnig, P., & Holzapfel, G.A. (2012). Layer-specific damage experiments and modeling of human thoracic and abdominal aortas with non-atherosclerotic intimal thickening. *Journal of the Mechanical Behavior of Biomedical Materials*, 12, 93–106.

Westerhof, N., Bosman, F., De Vries, C.J., & Noordergraaf, A. (1969). Analog studies of the human systemic arterial tree. *Journal of Biomechanics*, 2(2), 121–143.

Wolinsky, H. & Glagov, S. (1969). Comparison of Abdominal and Thoracic Aortic Medial Structure in Mammals. *Circulation Research*, 25(6), 677–686.

Wriggers, P. (2010). *Nonlinear Finite Element Methods*. Springer-Verlag, Berlin.

Xiong, J., Wang, S.M., Zhou, W., & Wu, J.G. (2008). Measurement and analysis of ultimate mechanical properties, stress-strain curve fit, and elastic modulus formula of human abdominal aortic aneurysm and nonaneurysmal abdominal aorta. *Journal of vascular surgery*, 48(1), 189–95.

Yeoh, O.H. (1993). Some forms of the strain energy function for rubber. *Rubber Chemistry and Technology*, 66, 754–771.

Zeinali-Davarani, S., Chow, M.J., Turcotte, R., & Zhang, Y. (2013). Characterization of biaxial mechanical behavior of porcine aorta under gradual elastin degradation. *Annals of biomedical engineering*, 41(7), 1528–38.

Zemanek, M., Bursa, J., & Detàk, M. (2009). Biaxial tension tests with soft tissues of arterial wall. *Engineering mechanics*, 16(1), 3–11.

Zhang, D. & Arola, D.D. (2004). Applications of digital image correlation to biological tissues. *Journal of biomedical optics*, 9(4), 691–699.

Zhao, A.R., Field, M.L., Digges, K., & Richens, D. (2008). Blunt trauma and acute aortic syndrome: a three-layer finite-element model of the aortic wall. *European Journal of Cardio-thoracic Surgery*, 34(3), 623–629.

Zhao, M. (2008). On Nonlinear Buckling and Collapse Analysis using Riks Method. In *Abaqus Users' Conference*. Illinois.

Zhou, J. & Fung, Y.C. (1997). The degree of nonlinearity and anisotropy of blood vessel elasticity. *Proceedings of the National Academy of Sciences of the United States of America*, 94(26), 14255–14260.

Zou, Y. & Zhang, Y. (2012). Mechanical evaluation of decellularized porcine thoracic aorta. *Journal of Surgical Research*, 175(2), 359–368.

Appendix

Planar biaxial tensile tests

Computational models are quite advantageous to improve the design of experimental tests. In the present research, the planning of biaxial tests has been carefully considered due to the variety of methods available in literature, reviewed in Section 2.3.2.
Therefore, aiming to determine the sample size and to compare different configurations to hold the sample during the testing procedures, preliminary computational evaluations have been carried out.

Methodology

Since two different approaches are generally adopted to clamp the sample (Section 2.3.2), this static analysis aims to compare their effect on the stress field achieved in same region of interest (red square, Figure A1). Initially, a planar biaxial tensile test carried out by means of hooks is modelled as reported in Figure A1.

Although the schematic represents the use of 4 hooks on each side, also the configuration having 6 hooks on each edge is analysed. Symmetric boundary conditions are imposed to model only a quarter of the specimen, excluding a minimum border needed to hold the sample (Figure A1). In the hypothesis of the hook diameter being 0.6 mm, the traction force, applied to each hook insertion, is distributed among 6 neighbour nodes to model a more realistic configuration. A force of 0.889 N is assigned to each node in the 6 hooks configurations. Finally, a mesh of 3136 shell elements (S4R) is generated.

The second approach takes into account the use of two grips equally spaced on each sample side (Figure A2).
Differently from the hooks configuration, the entire quarter of the sample is designed and meshed by 5776 S4R elements. However, the action of each grip, modelled as a surface traction of 2 MPa, is limited to the blue frame reported in Figure A1. Such high values of force, in the hooks case, and pressure, in the grip case, aim to model a limit configuration.
The aortic material is modelled as isotropic, based on experimental data obtained from uniaxial tests performed on samples cut from the thoracic aorta in the circumferential direction (Section 4.2). Such stress-strain responses are fitted by Ogden 3^{rd} order strain-energy function.

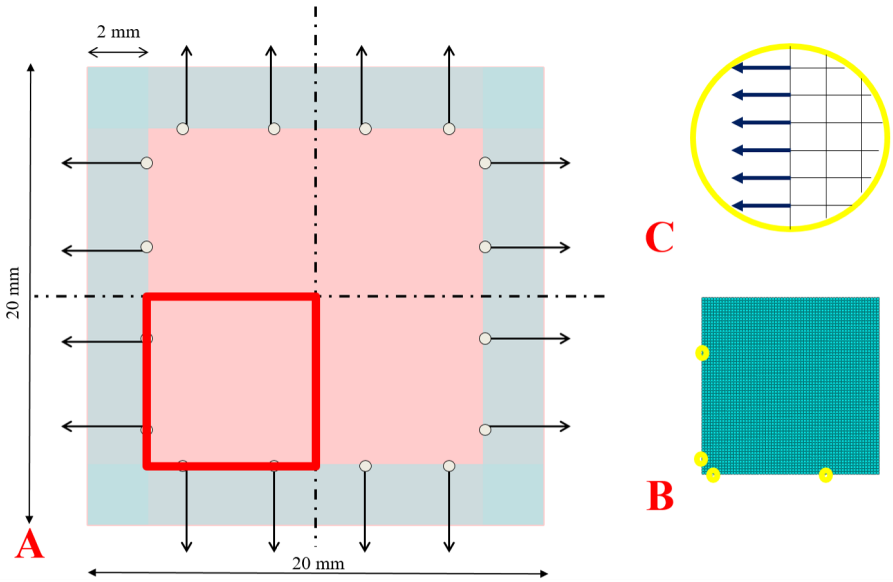

Figure A1 Schematic of biaxial tensile test carried out by using 4 hooks on each side of the sample (A). A minimum frame (light blue), 2 mm wide, has been estimated to hold firmly the sample. Hooks insertions (circles) are equally spaced. Given the symmetry, a quarter of this schematic (red square) has been modelled in Abaqus (B). Yellow circles, which indicate hooks insertions, are zoomed in C. The force applied to each insertion is distributed among 6 neighbour nodes.

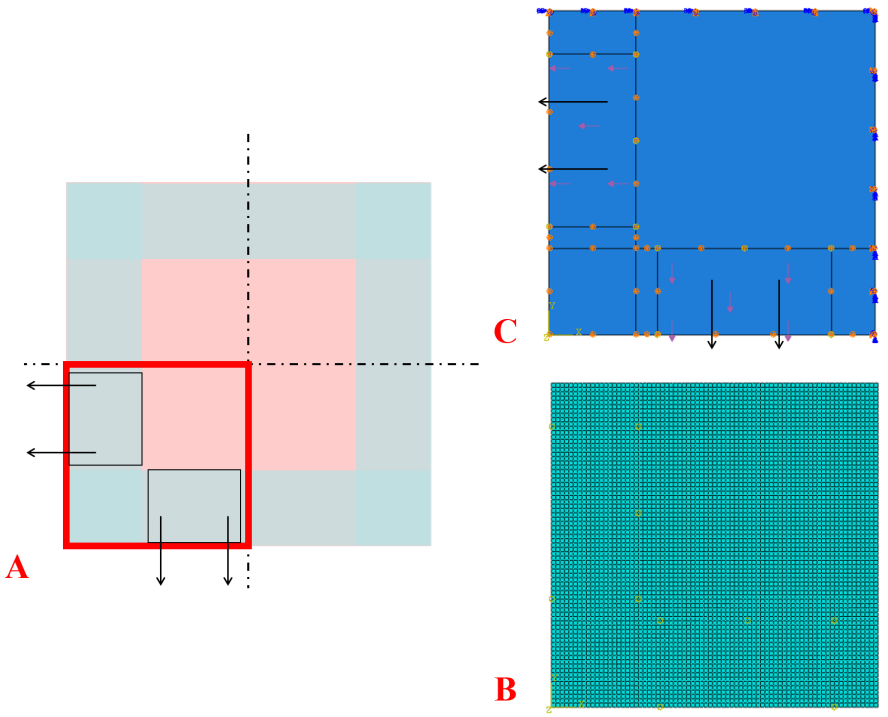

Figure A2 Schematic of biaxial tensile test carried out by using two grips equally spaced on each sample side (A). Given the symmetry, a quarter of this schematic (red square) has been modelled in Abaqus (B). A uniformly distributed pressure is applied on grips surface (C).

Results

Preliminary computational analyses have been carried out to determine details of the biaxial testing protocol, such as sample size and clamping configurations. First investigations compared different sizes of square samples (1 cm, 1.5 cm and 2 cm), hooked to be stretched during a planar test. As a result, a size of 2 cm is preferred, being big enough to avoid any boundary effects in the central region of the sample. The influence of hooks and grips is compared in Figure A3.

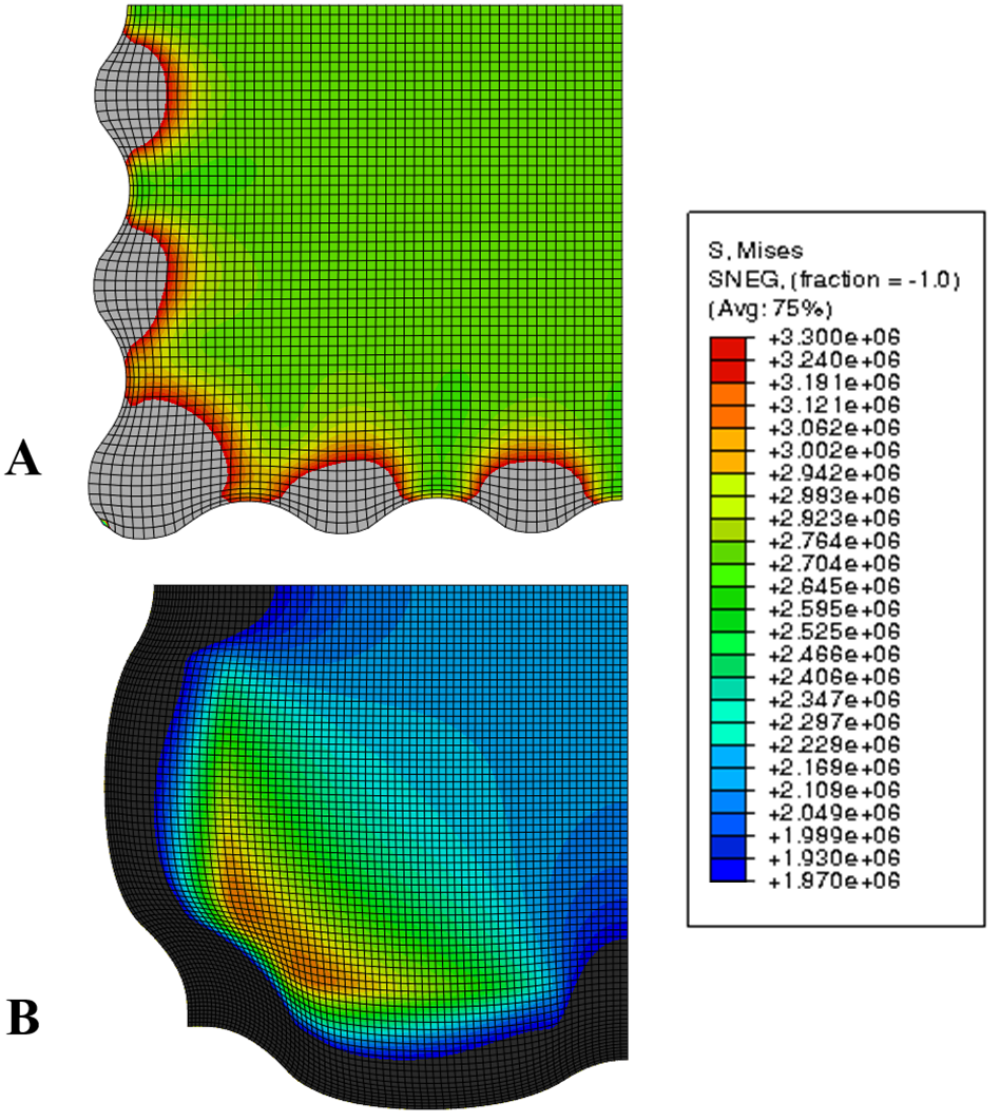

Figure A3 The effect of hooks (A) and grips (B) on the stress field achieved during biaxial tensile test. Given the symmetry of the test, only a quarter of a square aortic sample is modelled.

The analysis taking into account the hooks excluded a frame border of the sample (Figure A1) in order to focus on the central region of interest. Differently, the surface traction of the grips required the entire sample quarter. As a result, the stress field

generated by the use of hooks (Figure A3 A) appears far more uniform compared to grips action (Figure A3 B). The standard deviation calculated for the central region of the sample are, indeed, 58 kPa when hooks are adopted and 133 kPa when grips are preferred. Boundary effects cause by grips produce a gradient of stress reaching almost the central region of the sample. The mean stress values reached in the area of interest are 2.7 MPa in the case of hooks and 2.2 MPa in the case of grips.

Observations

Computational analyses on the planar biaxial tests fully justify the experimental methodology detailed in Section 3.2.4. Although such analyses do not take into account the squeezing of the material and its anisotropic behaviour, similar findings have been published by Sun et al. (Sun *et al.*, 2005). They concluded that suture-based approaches are best suited for biaxial mechanical tests of biological materials, since four suture attachments are sufficient for stress field uniformity.

Certificate of Ethics Review

Project Title:	Investigation of formation and development of aneurysm
User ID:	678090
Name:	Serena de Gelidi
Application Date:	10/12/2015 13:42:04

You must download your certificate, print a copy and keep it as a record of this review.

It is your responsibility to adhere to the University Ethics Policy and any Department/School or professional guidelines in the conduct of your study including relevant guidelines regarding health and safety of researchers and University Health and Safety Policy.

It is also your responsibility to follow University guidance on Data Protection Policy:

- General guidance for all data protection issues
- University Data Protection Policy

You are reminded that as a University of Portsmouth Researcher you are bound by the UKRIO Code of Practice for Research; any breach of this code could lead to action being taken following the University's Procedure for the Investigation of Allegations of Misconduct in Research.

Any changes in the answers to the questions reflecting the design, management or conduct of the research over the course of the project must be notified to the Faculty Ethics Committee. Any changes that affect the answers given in the questionnaire, not reported to the Faculty Ethics Committee, will invalidate this certificate.

This ethical review should not be used to infer any comment on the academic merits or methodology of the project. If you have not already done so, you are advised to develop a clear protocol/proposal and ensure that it is independently reviewed by peers or others of appropriate standing. A favourable ethical opinion should not be perceived as permission to proceed with the research; there might be other matters of governance which require further consideration including the agreement of any organisation hosting the research.

GovernanceChecklist
A1-BriefDescriptionOfProject: Mechanical testing of porcine tissue to set a computational model aimed to study aneurysm formation.
A2-Faculty: Technology
A3-VoluntarilyReferToFEC: No
A5-AlreadyExternallyReviewed: No
B1-HumanParticipants: No
HumanParticipantsDefinition
B2-HumanParticipantsConfirmation: Yes

C6-SafetyRisksBeyondAssessment: No
SafetyRisksBeyondAssessmentWarning
D2-PhysicalEcologicalDamage: No
PhysicalEcologicalDamageWarning
D4-HistoricalOrCulturalDamage: No
HistoricalOrCulturalDamageWarning
E1-ContentiousOrIllegal: No
ContentiousOrIllegalWarning
E2-SociallySensitiveIssues: No
SociallySensitiveWarning
F1-InvolvesAnimals: No
InvolvesAnimalsWarning
F2-HarmfulToThirdParties: No
HarmfulToThirdPartiesWarning
G1-ConfirmReadEthicsPolicy: Confirmed
G2-ConfirmReadUKRIOCodeOfPractice: Confirmed
G3-ConfirmReadConcordatToSupportResearchIntegrity: Confirmed
G4-ConfirmedCorrectInformation: Confirmed

Dissemination

Presentations

- 12^{th} – 16^{th} Jul 2015
  Oral presentation at 25^{th} Congress of the International Society of Biomechanics (ISB 2015) in Glasgow.
- 5^{th} – 8^{th} Jul 2015
  Oral presentation at 21^{st} Congress of the European Society of Biomechanics (ESB 2015) in Prague.
- 27^{th} Apr 2015
  Seminar at the Magdi Yacoub Institute (Imperial College) in Harefield.
- 25^{th} – 28^{th} Aug 2013
  Oral presentation at 19^{th} Congress of the European Society of Biomechanics (ESB 2013) in Patras.

Posters

- 1^{st} July 2014
  Research Day, Faculty of Technology (University of Portsmouth). *Aneurysm formation: from experimental tests to computational models*
- 10^{th} June 2013
  Research Day, Faculty of Technology (University of Portsmouth). *Aneurysm formation: Experimental protocol.* Awarded best poster.

Publications

- de Gelidi S., Tozzi G., Bucchi A., 2016. The Role of Pre-Conditioning Frequency in the Experimental Characterization of Hyper-Elastic Materials as Models for Soft Tissue Applications. *International Journal of Applied Mechanics* 08 (05), 1650066 1–20.
- de Gelidi S., Tozzi G., Bucchi A. (under review with *Materials Science & Engineering C*). The effect of thickness measurement on numerical arterial models.
- de Gelidi S., Rahmani B., Burriesci G., Bucchi A.(under review with *Journal of the Mechanical Behavior of Biomedical Materials*). Equi-biaxial characterisation of porcine aortic tissue: an up-to-date protocol.